APPROVAL SHEET

Title of dissertation: SHEDDING NEW LIGHT ON MAGNETIC ACCRETION: A Comprehensive Study of the X-Ray Emission in Accreting Pulsars

Name of Candidate: Diana Monica Cheatham
Doctor of Philosophy, 2017

Dissertation and Abstract Approved: _____

Dr. Markos Georganopoulos
Associate Professor
Department of Physics

Date Approved: _____

ABSTRACT

Title of dissertation: SHEDDING NEW LIGHT ON MAGNETIC ACCRETION: A Comprehensive Study of the X-Ray Emission in Accreting Pulsars

Diana Monica (Marcu) Cheatham,
Doctor of Philosophy, 2017

Dissertation directed by: Dr. Katja Pottschmidt
Department of Physics, UMBC/CRESST

Neutron stars are evolutionary remnants of massive stars. They are extremely compact and challenge many of our current theories of the existence of matter at densities similar to that of the atomic nucleus. Highly magnetic neutron stars are known as pulsars. Many X-ray pulsars radiate due to the accumulation of material from a companion star in a binary system. This accretion process in the presence of an extreme magnetic field results in the formation of plasma funnels at the pulsar's magnetic poles. The X-ray continuum is produced inside these extremely hot accretion columns. The magnetic fields of pulsars can be measured directly from the cyclotron resonant scattering feature sometimes observed in their X-ray spectra. To this day, the accreting pulsar continua have been described using standard phenomenological models that provide no physical insight. However, in the past few years, physically descriptive models have been under development.

For the work presented in this dissertation, I analyzed data from the

Japanese X-ray observatory, *Suzaku*. I first performed a detailed temporal and standard spectral analysis of the accreting pulsar XTE J1946+274. Building on that, I conducted a self-consistent study of the X-ray emission of a sample of nine accreting pulsars. The first step involved fitting a cutoff power-law model to the X-ray spectral of all sources. The second step involved testing the application of a newly implemented physical model to the same pulsar sample, and thereby obtaining physical descriptions of the accretion column structure and geometry. The physical parameters obtained include the radius, plasma (electron) temperature, and ratios of different Comptonization effects inside the accretion column. By comparing the physical and phenomenological spectral fit results, I provided the first observational proof that the plasma temperature inside the accretion column is related to the degree of curvature of the X-ray continuum. Lastly, I describe the remarkable self-consistency of the pulsar sample study by showing that the plasma temperature inside the accretion column, estimated from the thermal broadening effect of the cyclotron line, is consistent with the temperatures described by the physical model.

To summarize, considerable progress has been made in recent years regarding the development of physical models describing the accretion process onto a highly magnetic neutron stars. I successfully applied a new model implementation and provided the first direct connection between physical parameters of the accretion process (magnetic field strength, plasma temperature, plasma density, mass accretion rate) and the X-ray continuum spectral shape.

SHEDDING NEW LIGHT ON MAGNETIC ACCRETION:
A Comprehensive Study of the X-Ray Emission in Accreting Pulsars

by

Diana Monica (Marcu) Cheatham

Dissertation submitted to the Faculty of the Graduate School of the
University of Maryland, Baltimore County in partial fulfillment
of the requirements for the degree of
Doctor of Philosophy
2017

Advisory Committee:
Associate Professor Markos Georganopoulos
Dr. Katja Pottschmidt
Professor James Franson
Dr. Michael T. Wolff
Assistant Professor Eileen Meyer
Associate Professor Laszlo Takacs

To my beloved uncle Johnny,

Wish you could have been here!

ACKNOWLEDGMENTS

Presenting this dissertation has been a life-long goal for me, however, this would not have been possible without the help of many people over the years. I would like to briefly summarize all the people that have helped, supported, and inspired me, not just during my years as a graduate student, but even from before I had the opportunity to move to the U.S. to pursue a career in physics and astrophysics. I will begin with my mentors, advisers, professors, and collaborators, and I will continue with my friends and family.

I would like to thank the person without whom this project would not have been possible, my mentor, Dr. Katja Pottschmidt, thank you for your expert advice, support, and encouragement throughout the past eight years! I would also like to thank Professor Jörn Wilms, who has been a second mentor for me.

I would like to send a special thank you to Professor Ian George, who has supported and helped me with my classes, exams, and projects during my first years as a graduate student. I want to thank Dr. Michael T. Wolff for all his help, for developing and implementing the spectral model used in this project, and being part of my committee. I would like to thank the members of my committee, Professor Markos Georganopoulos, Professor James Franson, Professor Eileen Meyer, and Professor Laszlo Takacs. Thank you for being part of this project and helping me finalize my work. I would also like to thank my Physics Graduate Program Director at UMBC, Professor Tod Pittman, for all his guidance and advice over the years.

I really want to thank Lynne Griffith for all the help involving grants, immigration forms, tax forms, and all the paperwork over the years, I would not have been able to make it this far without your help! I also want to thank Dr. Steve Sturner for coming to my test talks and with whom I have enjoyed our long conversations commuting to GSFC.

Over the past few years I have been lucky to be part of a large collaboration, therefore, I would like to thank my colleagues from Bamberg, Germany, and from the ADAP and MAGNET collaboration: Amy Gottlieb, Dr. Matthias (Kühnel) Bissinger, Dr. Sebastian Müller, Sebastian Falkner, Dr. Fritz-Walter Schwarm, Dr. Victoria Grinberg, Dr. Paul Hemphill, Dr. Peter Becker, Dr. Kent Wood, Ralf Ballhausen, and Dr. Anne Lohfink. You have all been wonderful colleagues and it has been an absolute pleasure working with you all!

I want to especially thank my undergraduate adviser from George Mason University, Professor Joseph Weingartner, for his amazing guidance and help during my first years in the U.S. and in college. Also from GMU, I wish to thank Professor Karen Sauer for being an amazing professor and teaching me scientific writing, and Professor Shobita Satyapal along with Dr. Rachel Dudik, who were the first to introduce me to scientific research.

I would also like to mention teachers and professors from Romania that have helped me achieve my dream of studying physics and astrophysics in the U.S.. First, my physics teachers and professors in high school, Mr. and Mrs. Ioniţă, thank you for all your help and patience, I would not have made it this far without you! Second, my incredible math teachers, Mrs. Măinescu and Mr. Ştefănescu, my wonderful English teachers, Ileana Pârvu, without whom I would never have been able to pass the SATs, and Elena Deftu ("Teacher"), who started teaching me English when I was only five years old and advised my parents to put me in school early. I want to thank my piano teachers, Daniela Mocioc and Iuliana Pavel, for filling my life, mind, and soul with the beauty of music.

Out of all the people that have inspired and helped me over the years, I want to especially thank Mrs. Elena Petcan, my first physics teacher, who was such an amazing and caring teacher, and who took a special interest in me when I was only 14 years old. She tutored me and inspired me so much that at that tender age I had already decided to make physics a large part of my future. I will forever be grateful and I hope I would have made you proud!

None of this would have ever been possible without my parents, Doina and Nicky Marcu. Your love, support, patience, trust, and many other qualities that I could fill a book with, have made me who I am today and what I have been able to achieve. You have sacrificed so much for me, and although I will never be able to repay in any way everything that you have ever done for me, my greatest hope is that I have made you proud.

About ten years ago I was lucky to meet an amazing man, who, little did I know back then, would become my life partner and my biggest supporter. Thank you, Allen DeVere Cheatham for being there for me at all times, loving and supporting me throughout the past few years. I could not be any happier, you have brought so much happiness into my life, and without you I would never have made it! I love you and thank you for being such a wonderful husband!

I want to thank my mother and father in law, Carole and David Cheatham, for welcoming me so warmly into their family, supporting, and encouraging me, proof-reading my work, and being incredibly helpful. I appreciate everything that you have done for me and I am lucky to have you in my life. For all their support, I would also like to thank my brothers and sister in law, Aaron, Adam, and Karli Cheatham.

I thank my grandma, Silvia Niculescu (Buni), who calls me every other week to check on me and has been an inspiration for strength. I also want to thank my uncle, Ion Niculescu (Johnny), who was such a wonderful person, all heart, cared for me greatly, and was always so proud of his little niece.

I want to thank my amazing friends, Petre, Cerasela, and Radu Ianoş, for all the good times: from skiing trips, to hiking, tennis games, canasta, and all our hangouts. I also thank my friends Emma, Costin Craciunescu and their family for always checking up on me and supporting me over the years.

I also thank my friends Katie and Sam Cook, and Stacie and Robert Dodson for their support and friendship since the first week of college in August 2006. I want to thank my friend and colleague, Dr. Erin Balsamo, for all her support and motivation and willingness to get together to study for our common goal. Also for our Saturday study sessions at Starbucks, I want to thank my friend John Huggins.

For all her support, and encouragement, I want to thank my best friend, Alina Nicu. I really miss you and our conversations and I hope to see again!

Lastly, I would like to thank Ms. Heather Burns, who contributed to a fellowship for women in science at George Mason University. Without your help during my senior year, I would not have been able to graduate. I will forever be grateful for the life-changing opportunity you have offered me!

The material in Chapter 7 is a reprint of Marcu-Cheatham, D. M.; Pottschmidt, K.; Kühnel, M.; Müller, S.; Falkner, S.; Caballero, I.; Finger, M. H.; Jenke, P. J.; Wilson-Hodge, C. A.; Frst, F.; Grinberg, V.; Hemphill, P. B.; Kreykenbohm, I.; Klochkov, D.; Rothschild, R. E.; Terada, Y.; Enoto, T.; Iwakiri, W.; Wolff, M. T.; Becker, P. A.; Wood, K. S.; Wilms, J., 2015, "The Transient Accreting X-Ray Pulsar XTE J1946+274: Stability of X-Ray Properties at Low Flux and Updated Orbital Solution", published in the *Astrophysical Journal* (ApJ, 815, 44). The dissertation author is the primary investigator of this publication.

The material in Chapter 8 is being preparared to be submitted for publication as Marcu-Cheatham, D. M., Pottschmidt, K., Wolff, M. T.; Gottlieb, A. M.; Hemphill, P. B.; Ballhausen R.; Falkner, S.; Schwarm, F.-W.; Fürst, F.; Becker, P. A.; Wood, K. S.; Wilms, J., 2017, "Comprehensive Empirical and Physical Study of the X-ray Spectra of Accreting Pulsars with Suzaku", in the *Monthly Notices of the Royal Astronomical Society*. The dissertation author is the primary investigator of this manuscript.

For these research projects I myself conducted all analyses and prepared all paper and manuscript material – with the exception of Chapter 7.3.3, "Orbit Determination" –, under the supervision of my thesis advisor Dr. Katja Pottschmidt (UMBC).

I performed the complete data reduction and all spectral modeling. For each source I consolidated the results and compared them to previous studies. My spectral modeling of Centaurus X-3 built on initial work by GSFC/UMBC intern Amy Gottlieb. My spectral modeling using the new physical continuum model implementation was done providing regular feedback to and receiving regular feedback from Dr. Michael T. Wolff (NRL), the creator of the model.

Of the temporal analysis presented for XTE J1946+274 I performed the evaluation of the hardness changes as well as the pulse period determination and the energy-resolved pulse profile analysis. The orbit determination presented in Chapter 7.3.3 was performed by Dr. Matthias Kühnel (now Bissinger) at the Dr. Karl Remeis-Observatory at University of Erlangen-Nuremberg (Bamberg, Germany).

For both projects I compiled the material for scientific discussion (e.g., parameter correlation plots, comparison data) and wrote the interpretation of the results and conclusions which I developed collaboratively with and under the supervision of Dr. Katja Pottschmidt, Prof. Jörn Wilms (FAU, Germany), and Dr. Michael T. Wolff. Feedback and suggestions were provided by the co-authors, primarily in regular telephone conferences and through comments on the draft manuscripts.

TABLE OF CONTENTS

LIST OF TABLES

LIST OF FIGURES

1

Introduction

This dissertation presents a study of the production of high-energy radiation near astrophysical objects under extreme physical conditions. In particular, this work focuses on modeling the X-ray emission produced as a result of the gradual accumulation of very hot matter/plasma onto compact objects with very high magnetic fields. Magnetic accretion is a highly complex process that pushes the limits of our understanding of the behavior of matter in the presence of magnetic and gravitational fields that are on the order of a trillion times larger than those of our planet. These extreme physical conditions can neither be reproduced in laboratories, nor have they even been observed in our solar system.

Plasma energized by large gravitational and magnetic fields can reach temperatures on the order of $10^6 - 10^9\,\mathrm{K}$, which are high enough to produce predominantly X-rays and sometimes even γ-rays through several radiative processes. This study expands upon the analysis of X-ray radiation emitted by very hot plasmas accreted onto highly magnetic neutron stars (pulsars).

My work builds upon the following major discoveries in the fields of physics and astrophysics. In 1895 Wilhelm Conrad Röntgen discovered X-rays, a highly energetic form of electromagnetic radiation (light). A few decades later, Sir James Chadwick discovered the neutron (Chadwick, 1932), a sub-atomic particle with no

electric charge, which forms the atomic nucleus along with protons. Two years later, Baade & Zwicky (1934) proposed the idea of a neutron star forming during a supernova, i.e., a cataclysmic explosion which occurs at the end of the evolutionary stages of a massive star, and in particular that *"in the supernova process, mass in bulk is annihilated"*. Decades later, Hewish & Okoye (1965) found *"evidence of an unusual source of high radio brightness temperature in the Crab Nebula"*. Based on subsequent findings by Staelin & Reifenstein (1968) and Lovelace et al. (1968), we now know that what Hewish & Okoye (1965) observed was emission from the neutron star located at the center of the Crab nebula (see Figure 1.1), which formed during the famous supernova in 1054. Pacini (1967) was the first scientist to suggest that the fast rotation of a compact object with a large magnetic field (such as a highly magnetized neutron star) may result in regular periodic bursts of radiation, i.e., pulsations. The first isolated pulsar, PSR B1919+21, was found from observations of radio emissions by Anthony Hewish's graduate student, Jocelyn Bell (Hewish et al., 1968), and Hewish received the Nobel Prize in Physics in 1974 for this discovery. In the late 60's, X-ray Astronomy was quickly becoming a new field of astrophysical studies, as the first cosmic X-ray detector was deployed on the rocket *USAF* Arobee 150 in 1962. For a few years, the observed X-ray emission was mainly that from the Sun. That was until the first extrasolar X-ray source, Scorpius X-1, was discovered by Shklovsky (1967). Shortly thereafter, Giacconi et al. (1971) discovered the first X-ray-emitting pulsar, Centaurus X-3. After studying the X-ray variability in the data from the *Uhuru* X-ray satellite, Schreier et al. (1972) stated: *"We interpret this effect as due to an occulting binary system. The changes in intensity are then due to the occultation of the X-ray source by a large massive companion and the sinusoidal variations of the 4.8 s pulsations are due to Doppler effect."* This description became the canonical picture of binary X-ray pulsars (Ghosh, 2007).

Although accreting pulsars were first discovered over four decades ago,

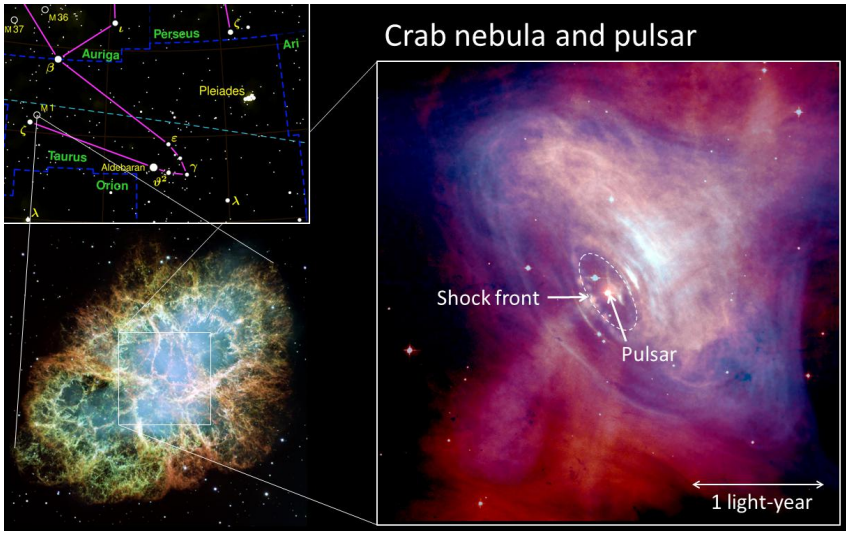

Figure 1.1: The top left image shows the Taurus constellation. The bottom left image shows a closer view of the Crab nebula, obtained by the Hubble space telescope. The image on the right side shows a combination of visible light (red) and X-rays (blue) with the pulsar located in the center (Bernold Feuerstein/Max-Planck-Institut für Kernphysik, source: NASA, http://idwf.de/-BxMtBA, Fig. 1).

the physics behind magnetic accretion is still not well understood. Therefore, this work focuses on improving our understanding of this phenomenon through a comprehensive spectral analysis using both standard and state-of-the art modeling techniques. In Chapter 2, I describe the relevant stages of stellar evolution, as well as neutron star formation and structure. In Chapter 3, I discuss the main properties of X-ray binaries, the determination of the orbital parameters of a neutron star in a binary system, and the processes of mass transfer within these systems. Chapter 4 contains a description of the radiative processes that play a role in the process of accretion onto a neutron star. Properties of the accretion process onto a highly magnetic pulsar and the details of X-ray emission from the neutron star accretion column are described in Chapter 5. My primary data source for this study was the X-ray satellite, *Suzaku*, as presented in Chapter 6, where I also briefly discuss other X-ray instruments that were relevant for the analysis. Chapter 7 presents a detailed spectral and temporal study of the accreting

pulsar XTE J1946+274, which introduces our standard broadband spectral modeling techniques. This chapter is based on the paper "The Transient Accreting X-Ray Pulsar XTE J1946+274: Stability of X-Ray Properties at Low Flux and Updated Orbital Solution", published in the *Astrophysical Journal* (Marcu-Cheatham et al., 2015, ApJ, 815, 44). Chapter 8 builds upon the study of XTE J1946+274, and represents a larger and more comprehensive spectral analysis of nine bright accreting pulsars, with an emphasis on testing a new physical model implementation (described in Chapter 5). This chapter is based on the paper manuscript "Comprehensive Empirical and Physical Study of the X-ray Spectra of Accreting Pulsars with Suzaku" (Marcu-Cheatham et al., 2017, in prep.). Lastly, in Chapter 9, I summarize the results and conclusions of this study along with providing an outlook on possible future projects.

2

Neutron Stars: Origin and Properties

2.1 Stellar Evolution

In this section, I summarize how stars form and evolve. I also discuss how neutron stars can be produced at the end of stellar evolution. Most of the information presented in this section is based on Hansen et al. (2004), Prialnik (2000), and Carroll & Ostlie (1996).

2.1.1 Star Formation

In the Inter-Stellar Medium (ISM) there exist high-density molecular clouds composed mainly of hydrogen (H) and helium (He). Stars are born within these types of interstellar "dust" clouds. Sir James Jeans (1902) first determined that the high densities of the molecular clouds make them gravitationally unstable. When a cloud is no longer in hydrostatic equilibrium, the gravitational pressure of its enclosed mass becomes higher than its internal gas pressure causing the cloud to gravitationally collapse into a protostellar cloud. The cloud must have a minimum

mass of

$$M_J \simeq \left(\frac{5kT}{G\nu m_{\rm H}}\right)^{3/2} \left(\frac{3}{4\pi\rho_0}\right)^{1/2}, \tag{2.1}$$

where k is the Boltzmann constant, T is the temperature of the cloud, G is the gravitational constant, ν is the mean molecular weight of the cloud, $m_{\rm H}$ the mass of a hydrogen atom, and ρ_0 is the initial mass density of the cloud. This is also known as the Jeans mass criterion (Jeans, 1902).

As the cloud contracts into a protostar (or proto-stellar cloud), gravitational energy is released, and the cloud temperature increases. Initially, within the protostar, convection processes dominate the energy transport. However, as its temperature and density continue to increase, the protostar becomes optically thick to its own radiation and radiative processes become dominant. At this stage the protostellar cloud becomes a pre-main sequence star. The collapse still continues as the temperature and density become high enough to "ignite" the fusion of protons into He nuclei. The energy released due to fusion eventually provides enough pressure to counter and stop further gravitational collapse. This force balance is known as hydrostatic equilibrium, i.e.,

$$\frac{{\rm d}P}{{\rm d}r} = -G\frac{M\rho}{r}, \tag{2.2}$$

where ${\rm d}P/{\rm d}r$ is the pressure gradient inside the star at the radius r from the center of the star, and M and ρ are the stellar mass and density, respectively. The result is a self-sustaining, H-to-He burning sphere, which is known as a main-sequence star. The Sun in our Solar System was born in a similar way 4.6 billion years ago as a result of a collapsing cloud inside a solar nebula. It is noteworthy that helium was the first element discovered outside of Earth. He emission was first detected by Jules Janssen in the chromosphere spectrum of the Sun during a solar eclipse in 1868 (Kochhar, 1991), therfore, the element was named after the Titan Sun god in the Greek mythology, Helios (Thomson, 1871).

For stars with a mass $< 1.3\,M_\odot$[1], for which the core temperatures are $4-15\times10^6\,\mathrm{K}$ (Reid & Hawley, 2005, p.83), the H-to-He fusion reaction that sustains a star from gravitational collapse occurs through what is known as the proton-proton (PP) chain. It is a series of chain reactions in which four ${}^1_1\mathrm{H}$ form a ${}^4_2\mathrm{He}$ atom,

$$4\,{}^1_1\mathrm{H} \rightarrow {}^4_2\,\mathrm{He} + 2\mathrm{e}^+ + 2\nu_\mathrm{e} + 2\gamma, \tag{2.3}$$

where e^+ is a positron (electron antiparticle), ν_e is an electron neutrino, and γ is a gamma-ray photon. The total energy released is $26.732\,\mathrm{MeV}$, out of which $\sim$2% is carried out of the star by the neutrinos. The positrons annihilate with electrons and release two gamma-ray photons,

$$\mathrm{e}^+ + \mathrm{e}^- \rightarrow 2\gamma, \tag{2.4}$$

where γ represents a photon with an energy of $0.511\,\mathrm{MeV}$, i.e., the rest mass of an electron. The resulting radiation energy from PP chain reactions provides the thermal pressure necessary to sustain a low-mass star against gravitational collapse.

For stars with masses $> 1.3\,M_\odot$, in which the temperatures are $> 15\times10^6\,\mathrm{K}$, the Carbon-Nitrogen-Oxygen (CNO) cycle becomes an addition source of H-to-He burning (Salaris & Cassisi, 2005, p.117) . In this process carbon, nitrogen, and oxygen isotopes are used as catalysts in a six-stage fusion chain reaction. The end result is

$$4\,{}^1_1\mathrm{H} + 2\mathrm{e}^- \rightarrow {}^4_2\,\mathrm{He} + 2\mathrm{e}^+ + 2\mathrm{e}^- + 2\nu_\mathrm{e} + 3\gamma, \tag{2.5}$$

where the positrons and electrons annihilate into gamma-ray photons. The overall reaction releases the same amount of energy, $26.732\,\mathrm{MeV}$, as the PP chain reaction. In our Sun, approximately 1.7% of the He produced is from the CNO cycle (Baaquie & Willeboordse, 2015, p.221).

[1]Note that $M_\odot$, $L_\odot$, and $R_\odot$ are astronomical units of measurements relative to the mass, luminosity, and radius of the Sun, respectively.

2.1.2 Stellar Classification

Main-sequence stars can be considered, to first order, to be blackbodies. Due to this property, their "color" provides the information needed to determine one of their most defining properties: their effective temperature. Wien's Displacement Law (Wien, 1897) describes how the wavelength at the peak of the blackbody emission flux is related to the effective temperature of the star ($T_{\rm eff}$) via

$$\lambda_{\rm max} = \frac{b}{T_{\rm eff}} \tag{2.6}$$

where b is Wien's displacement constant. More details on blackbody radiation can be found in Chapter 4.1.1.

The Harvard Spectral Classification (Habets & Heintze, 1981) is used to categorize main-sequence stars in the following order of decreasing temperature:

$$\mathrm{O} - \mathrm{B} - \mathrm{A} - \mathrm{F} - \mathrm{G} - \mathrm{K} - \mathrm{M}. \tag{2.7}$$

Figure 2.1 is an adaptation of the famous Hertzsprung-Russell (HR) diagram, which describes the relationship of the luminosities (or absolute magnitudes) and the spectral classes (or effective temperatures) of stars (Hertzsprung, 1909; Russell, 1914). Early-type stars are hot, luminous, have large masses and radii, and evolve more rapidly. For example, O-type stars have masses $> 16\,M_{\odot}$, luminosities $> 3 \times 10^4\,L_{\odot}$, and lifetimes on the order of $5 - 6 \times 10^6$ yr. In contrast, late-type stars are colder than early-type stars, they have smaller masses and radii, but they live for longer times since they evolve more slowly. For example, G-type stars with masses and luminosities similar to the Sun, have lifetimes of up to 15×10^9 yr. As a result, fewer early- than late- type stars exist.

As more stellar properties were discovered over subsequent years, more subcategories were added to this standard picture (Morgan et al., 1943; Keenan, 1985). Today, astronomers use the Yerkes Spectral Classification (Morgan et al.,

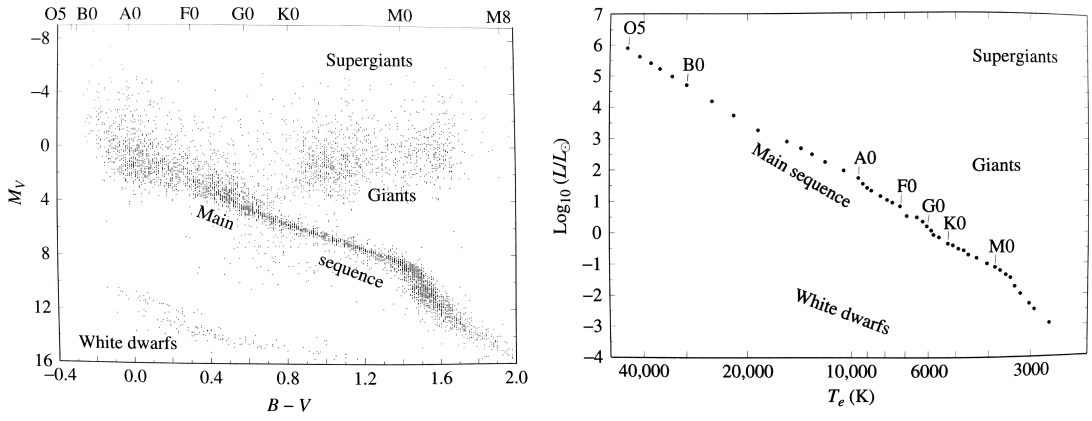

Figure 2.1: The Hertzsprung-Russell diagrams that describe the stellar distribution according to their properties. The left panel shows the absolute magnitude (M_V) versus the color index ($B-V$) of and spectral type (upper x-axis) of observed stars. The right panel shows a theoretical interpretation of the stellar luminosities versus their effective temperatures (Carroll & Ostlie, 1996, Fig. 8.11 and 8.12).

1943), in which Arabic and Roman numerals are added after the temperature class letter to distinguish among different spectral types and luminosity classes. The luminosity classes are: I for super-giants, II for bright giants, III for giants, IV for sub-giants V for main-sequence stars, VI for sub-dwarfs, and VII for white dwarfs (see Chapter 2.1.3 for post-main-sequence stellar evolution). For example, the Sun is categorized as a G2V type star, where G2 describes the spectral type and V describes the luminosity class.

2.1.3 Leaving the Main Sequence

A star is on the main sequence as long as H fuses into He in the core. When the H in the center starts to be exhausted, the star begins to change its structure: its core starts to contract and an external envelope forms and gradually expands. The star gradually moves from core-nuclear burning to shell-nuclear burning (Kippenhahn & Weigert, 1990, p.292). When all of the H in the core has fused into He, the star becomes a red giant with a slowly-growing He core, while in the shell, the remaining H fuses into He. This He is captured by the core, causing an

increase in mass. During this process, the core reaches the same temperature as the surrounding H-burning shell ($\sim 5 \times 10^7$ K). As its mass increases, the He-core becomes convective. Helium burning begins when the core has a mass of $\sim 0.45\, M_\odot$. For very low-mass stars ($< 2\, M_\odot$), the high density of the He-core causes the electrons inside it to become degenerate, making degenerate pressure dominant over thermal pressure. Because of this, when He fusion stars, the temperature increases, without the core expanding. This results in a sudden burst of energy, which is known as a "helium flash". The core composition continuously changes as He gradually fuses into carbon (C) and oxygen (O). This results in a C-O core with an He outer layer surrounded by a H-burning shell enclosed in an H-rich envelope. Past this stage, stars evolve differently depending on their mass.

Low-mass stars ($< 8\, M_\odot$) have cold cores ($\sim 10^8$ K) and slow fusion rates. Low-mass stars evolve into giants as they reach the core He- or C-burning stages. After the He is exhausted, they evolve into intermediate-luminosity red giants. The star continues to burn, losing a large part of its mass. A strong stellar wind develops due to the high radiation pressure inside the envelope. As a result, low-mass stars eject their envelope, which becomes a planetary nebula that surrounds the C-O nucleus. Planetary nebulae (also known as stellar remnant nebulae) appear as bright structures, e.g., circular rings around a point source of light. The collapse of the remaining core continues until electron degeneracy pressure counteracts the gravitational force (Zel'dovich & Novikov, 1971, p.239). Figure 2.2 shows an example of the evolutionary path followed by a $5 M_\odot$-mass star on the HR diagram as its internal structure changes. The remaining stellar core sustained by electron degeneracy pressure is known as a "white dwarf" (Iben, 1965).

High-mass stars ($> 8\, M_\odot$) have higher core temperatures ($> 10^9$ K) than their low-mass counterparts. They undergo fusion more rapidly, making them more luminous but with shorter lifetimes than low-mass stars. According to the theory of single star evolution, high-mass stars evolve from the main sequence to the core He-

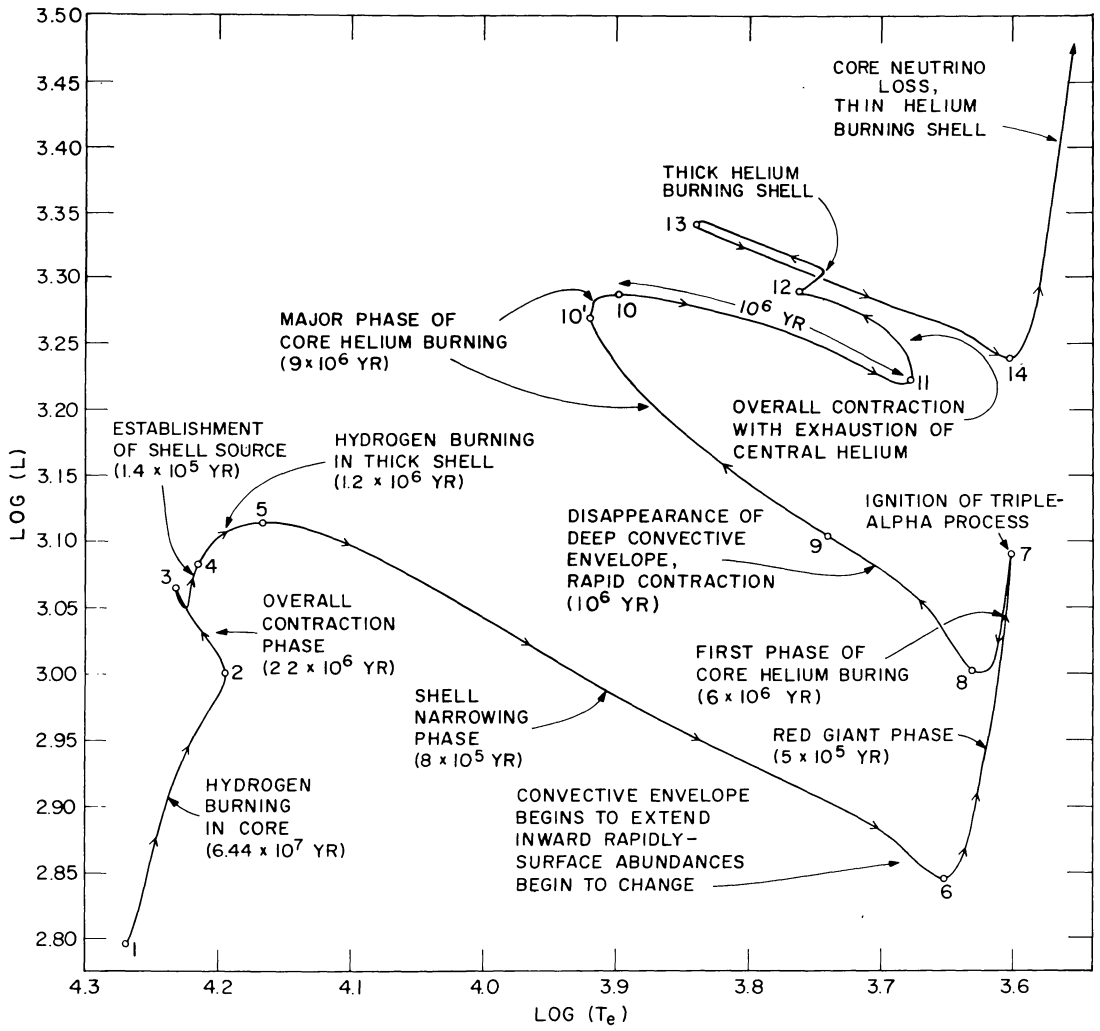

Figure 2.2: Adaptation of the Hertzsprung-Russel diagram showing the evolution of a $5\,M_\odot$ from the beginning of its main sequence to the giant phase (Iben, 1991, Fig. 2).

burning stage at a luminosity comparable to their main-sequence luminosity. They initially go through the same He-shell-burning and C-O-core-collapse stages as their low-mass counterparts. However, for high-mass stars, the core temperature continues to increase ($\sim 10^{10}$ K), and fusion of C and O results in the creation of increasingly heavier elements through He capture (e.g., see Arnett, 1996, p.311, for a review). The star develops an onion-type structure (Figure 2.3), with the heaviest element in the core and the lightest element (H) at the surface. Radiation pressure counteracts

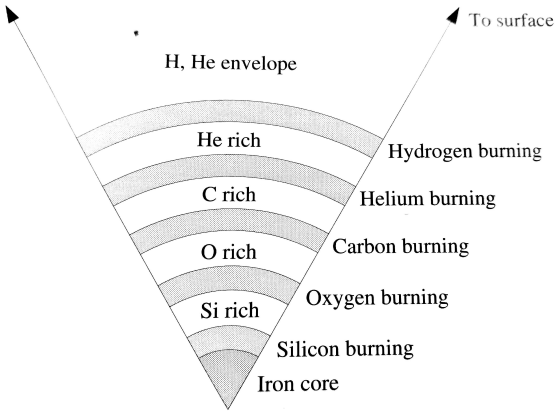

Figure 2.3: The onion-like layers of elements in a massive evolved star before its core collapse (Carroll & Ostlie, 1996, Fig. 13.14).

gravitational collapse until iron (Fe) starts being produced and the fusion slowly begins to exhaust. Heavier elements than Fe cannot be created because ^{56}Fe has the highest binding energy per nucleon of any element at those pressures (8.8 MeV), i.e., the fusion of Fe into elements with higher atomic numbers is an endothermic process, which would require an external energy supply. Once fusion has stopped, the stellar core resumes its collapse. The newly formed Fe core becomes too massive to be supported by electron degeneracy pressure and continues to collapse, causing the electrons to become relativistic. The internal pressure of the relativistic electron gas is what impedes further gravitational collapse. This electron pressure can be sustained until the electrons reach speeds close to that of the speed of light (c). This limit defines the Chandrasekhar mass, $M_{\rm Ch} = 1.4\,M_{\odot}$ (Chandrasekhar, 1931). If the stellar core is more massive than $M_{\rm Ch}$, the gravitational force exceeds the relativistic-electron pressure. The core continues to collapse as its density continues to increase and neutronization begins (see Chapter 2.2.1). During neutronization, a large number of neutrinos are produced. As the core finalizes its collapse, all the neutrinos escape[2] with sufficient energy and momentum to cause the envelope of the original star to be ejected. This is the dramatic phenomenon known as a type

[2]The sudden escape of the neutrinos is also known as a "neutrino burst".

II supernova (Burbidge et al., 1957; Colgate & White, 1966; Colgate, 1971). After the explosion, the compact object (collapsed stellar core) is left surrounded by the ejected material, also know as a supernova remnant. The remnant compact object is a neutron star, sustained by neutron degeneracy pressure, if the core mass is $1.4\,M_{\odot} < M_{\rm core} < 3.2\,M_{\odot}$ (see Chapter 2.2 for more details). Higher-mass cores cannot be sustained against their own gravity gravitational and collapse into a black hole.

2.2 Neutron Stars

2.2.1 Formation

For stellar cores with high enough pressures and densities (beyond the Chandrasekhar limit), protons, p, and electrons, e, combine to form neutrons, n, and electron neutrinos, $\nu_{\rm e}$, through electron capture,

$$\mathrm{p} + \mathrm{e}^{-} \rightarrow \mathrm{n} + \nu_{\rm e}. \tag{2.8}$$

This process is known as neutronization or inverse β-decay, and it causes the collapsing core temperature to decrease as the density increases to values as high as those of nuclear matter ($\sim 10^{15}\,\mathrm{g\,cm^{-3}}$). Once the temperature becomes low enough, the neutrinos escape the core all at once creating a shock that pushes the remaining outer layer, causing a strong supernova explosion (Baron & Cooperstein, 1990; Bethe, 1990). After the neutrinos escape, the remaining neutron-rich core left behind is a neutron star. Since neutrons are fermions and obey Pauli's exclusion principle, neutron degeneracy pressure will prevent further gravitational collapse.

The radius of a neutron star can be determined using the Tolman Oppenheimer Volkoff (TOV) equation (Tolman, 1939; Oppenheimer & Volkoff, 1939), which describes a neutron star in hydrostatic equilibrium while taking general relativistic

effects into account,

$$\frac{\mathrm{d}P}{\mathrm{d}r} = -\frac{G}{r^2}\left(\rho + \frac{P}{c^2}\right)\left(M + 4\pi r^3 \frac{P}{c^2}\right)\left(1 - \frac{2GM}{c^2 r}\right)^{-1}. \tag{2.9}$$

The neutron star's pressure, P, density, ρ, and mass, M, are functions of its radius, r, and G and c are the standard gravitational constant and speed of light, respectively. This equation results in an important mass-volume relationship for neutron stars: $MV =$ constant. Beyond the TOV mass ($3.2\,M_\odot$), the strong gravitational pressure is higher than the neutron degeneracy pressure. Therefore, a neutron star with a mass higher than $3.2\,M_\odot$ cannot be sustained by its internal pressure, and it will further collapse into a black hole. The TOV mass limit for neutron stars is analogous to the Chandrasekhar mass limit for white dwarfs.

2.2.2 Structure

Neutron stars challenge our current theories of the complex particle interactions that take place in the presence of the strong force (Quantum Chromodynamics, QCD). In order to solve the TOV equation, scientists are working on determining the correct Equation of State (EoS) that describes the extremely dense and cold interacting matter inside neutron stars. The EoS is a thermodynamic equation that describes the density of matter as a function of pressure, $\rho(P)$, under given physical conditions. For an in-depth recent review on the QCD thermodynamical process inside neutron stars see Fraga et al. (2016). Newton (2013) provides a more simplified description of the neutron star internal structure (see Figure 2.4). In the following, we summarize this theoretical picture.

Neutron stars have a very thin (a-few-millimeters-thick), thermally radiative plasma atmosphere. If the atmospheric thermal emission is strong enough to be observed, then one can study the neutron star surface temperatures and magnetic fields (Zavlin & Pavlov, 2002). Underneath the atmosphere, a neutron star has a

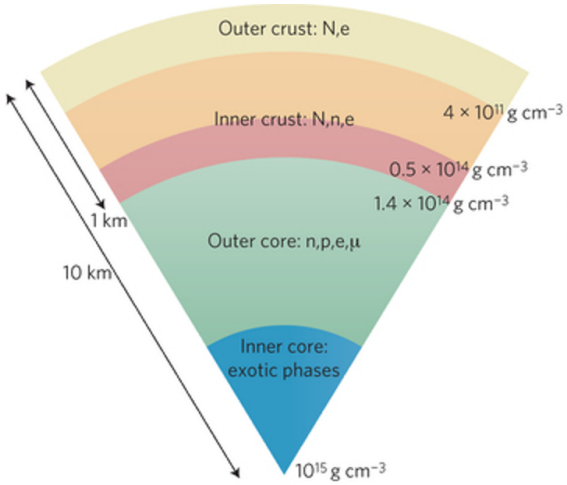

Figure 2.4: Schematic of the interior structure of a neutron star. The crust and outer core are composed of Fe nuclei (N), fluid neutrons (n), protons (p), electrons (p), and/or muons (μ). The inner core composition remains unclear and is speculated to be composed of exotic matter (Newton, 2013, Fig. 9a).

solid outer crust, consisting mainly of ^{56}Fe nuclei and free electrons. The outer crust is sustained by electron degeneracy pressure. Beneath this layer, there is an inner crust which drastically increases in density with depth (up to $0.5 \times 10^{14}\,\mathrm{g\,cm^{-3}}$). These densities are already beyond the highest densities that can be created in our laboratories. This inner crust layer is composed of a mixture of nuclei, electrons, and free neutrons. The outer and inner crusts together have a thickness of $\sim$1 km. Below the inner crust there is an outer core, where densities start at $\sim 1.4 \times 10^{14}\,\mathrm{g\,cm^{-3}}$ and continue increasing with depth. At these densities nuclei cannot exist. Instead, there is a mixture of fluid neutrons, protons, electrons, and muons. The stabilizing pressure is provided by the degenerate Fermi gas. The inner-most layer is the inner core, where densities are believed to reach up to $10^{15}\,\mathrm{g\,cm^{-3}}$, much higher than the density inside atomic nuclei ($\rho_{\mathrm{nuclear}} = 2.8 \times 10^{14}\,\mathrm{g\,cm^{-3}}$). The composition of the inner core is unknown as the physical conditions are far beyond what the current theories predict and what can be studied in laboratories. It is believed that exotic matter such as hyperons, deconfined quark matter, and color superconductivity[3]

[3]Hyperons are unstable baryons with masses higher than protons and neutrons. Deconfined quark

may exist at such high densities (Newton, 2013, and references therein).

The best available method of understanding the properties and structure of neutron stars is by determining their correct Equation of State (EoS). However, the biggest challenge that scientists are currently facing in this field is that there are no direct methods to measure either the densities or pressures inside of neutron stars. The alternative is to combine the theoretically-determined EoSs with the TOV equation (Equation. 2.9), and, thus, separate the EoS into two measurable, pressure-dependent properties: the neutron star mass, $M(\rho)$, and radius, $R(\rho)$. This makes it possible to use observational data to test the theoretical EoS models. For example, Figure 2.6 shows how a few observed neutron star masses compare to those predicted by various EoS theories. In these EoSs the maximum and minimum neutron star masses are determined from General Relativity and from stellar evolution theories, respectively. These models predict a tendency for the radius to decrease with increasing mass. In current models, the radius is expected to be 8–15 km for a neutron star with a mass higher than 1 $M_{\odot}$.

Although this method appears simplistic, measuring a neutron star's mass and radius is considerably complex and comes with a very high degree of uncertainty. For example, the thermal radiation emitted from the atmosphere can be used to estimate the radius, however, this emission is generally very weak and very difficult to detect. For isolated neutron stars, the mass can sometimes be determined through a timing analysis of the emitted radiation influenced by relativistic effects. Lattimer (2012) and Lattimer & Prakash (2001) provide reviews of techniques used to determine the masses and radii of neutron stars.

One can also study the emission produced through accretion, however, self-consistent pulsar accretion theories are still under development (Becker & Wolff, 2007; Farinelli et al., 2012; Ceccobello et al., 2014; Farinelli et al., 2016; Wolff et al., 2016; West et al., 2017). The neutron star mass can be determined from the orbital

matter describes a state in which quarks do not feel the strong force under extremely high energy densities. Color superconductivity is also related to the behavior of quark matter under very high densities.

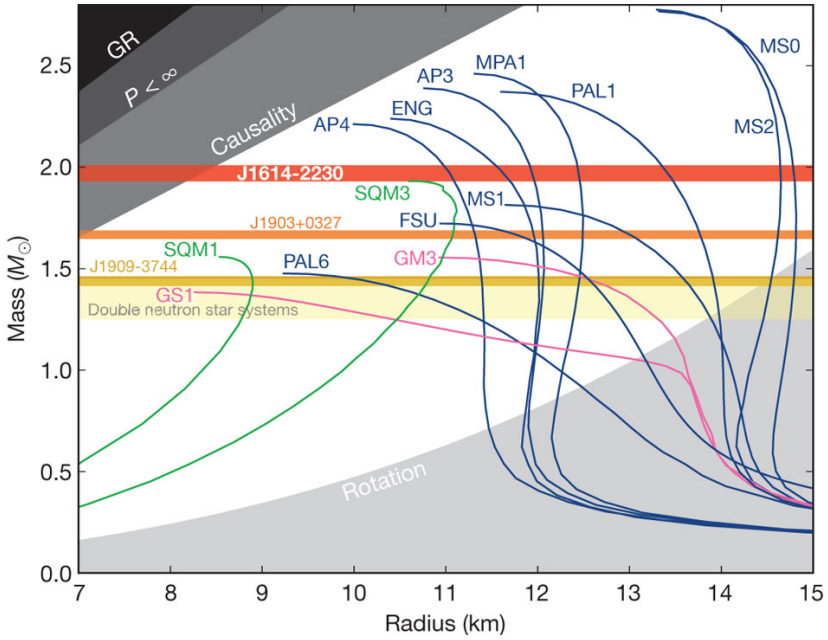

Figure 2.5: Theoretically predicted neutron star mass-radius correlations for different EoS models. The blue and pink curves represent hadronic models and the green curves represent strange quark matter models. The EOS names are described in Lattimer & Prakash (2001). The horizontal lines show mass constraints from pulsar observations of J1614−2230, J1903+0327, J1909−3744, and of double neutron star binaries. The top left regions are areas forbidden by general relativity, finite pressure, and causality as indicated. The lower right gray areas are constrained by the spin frequency of the fastest rotating pulsar PSR J1748-2446J. (Demorest et al., 2010, Fig. 3).

motion around a companion star. The caveat is that the uncertainties in distance and orbital motion measurements are generally very high. Although accreting pulsars are often in quiescence, they occasionally experience strong X-ray bursts, the study of which can provide some crucial physical properties. For example, Özel (2006) made a ground-breaking discovery when she studied a large thermonuclear X-ray burst from the X-ray binary EXO 0748−676. During this strong X-ray burst the neutron star atmosphere was "ignited" due to a high amount of accreted material. This "burning" atmosphere resulted in strong blackbody emission. This played a key role in Özel's study because the surface brightness and blackbody luminosity were both relatable to the mass and radius of the neutron star. With these results,

Özel was able to put constraints on the mass-radius relationship, thus, narrowing down the applicable EoS theories.

Overall, despite the large systematic uncertainties (from distance measurements to assumptions about the uniformity and structure of the atmosphere), the study of X-ray bursts in pulsar binaries has proven fruitful in the ongoing study of neutron star properties (see also Steiner et al., 2010; Kuśmierek et al., 2011). One caveat is that these types of X-ray bursts are seldom observed.

2.2.3 Neutron Stars in Isolation

Neutron stars can either be found as isolated sources or in binary systems with a star or another compact object, orbiting their common center of mass. Many neutron stars have very high magnetic (B) fields, the highest measured in the Universe, ranging from as low as $\sim 10^8$ G (Zavlin et al., 1996) and as high as $\sim 10^{15}$ G. Neutron stars with magnetic fields higher than 10^{13} G are known as magnetars (Duncan & Thompson, 1992). Highly magnetic neutron stars are also known as pulsars. The "pulsations" are due to the misalignment of the neutron star rotation and magnetic axes, which results in an observed "lighthouse effect". Isolated pulsars generally show strong radio and sometimes X-ray or gamma-ray emission (see Kaspi et al., 2006, for a detailed review). Particles in the neutron star atmosphere around the magnetic poles are accelerated and are channeled along the magnetic field lines. The non-thermal radiation created by these accelerated particles is beamed along the magnetic dipole field lines. This is known as Magnetic Dipole Radiation (MDR), see also Manchester & Taylor (1977, p.176), Shapiro & Teukolsky (1983, p.162), and Mészáros (1992, p.322). During this process, the neutron star loses kinetic energy and its rotation slows down. This is also known as magnetic braking. The emitted energy is

$$\dot{E} = I\omega\dot{\omega} = 4\pi^2 I \frac{\dot{P}}{P^3}, \tag{2.10}$$

where ω, I, and P are the angular velocity, moment of inertia, and pulse period of the neutron star, respectively. Pulsars radiating based on this mechanism are called rotation-powered. The magnetic field can also be calculated from the pulse period change, i.e., assuming the neutron star has a magnetic-dipole configuration, the magnetic field of a rotation-powered pulsar is given by

$$B_{\rm NS} = 3.2 \times 10^{19} (P\dot{P})^{1/2}\,{\rm G}. \tag{2.11}$$

An exotic category of isolated neutron stars are Anomalous X-ray Pulsars (AXP), which were first detected by Gregory & Fahlman (1981). Their energy source is not entirely understood as the slow rotation periods (6–12 s) do not explain the observed strong X-ray emission (Koyama et al., 1987). The current theories claim that AXPs are magnetars in which the decaying magnetic field results in the observed X-ray and gamma ray emission (Kaspi et al., 2006, and references therein). Another type of isolated neutron stars believed to be magnetars are Soft Gamma Repeaters (SGR), which exhibit irregular large bursts of X-rays and γ-rays (Zhang et al., 2000).

There is no complete explanation of why neutron stars have such high magnetic fields and work is ongoing determining the details of both the internal and external B(magnetic)-field structures (Turolla et al., 2015). The oldest and most straightforward theory that describes how neutron stars are born with high magnetic fields is the so-called "fossil" field theory (Ginzburg, 1964; Woltjer, 1964). The assumption is that the magnetic field of the neutron star progenitor is amplified by the conservation of magnetic flux during the stellar core collapse (see also Chapter 2.1.3). Assuming a star at the end of its main sequence has a collapsing core of radius $R_{\rm c}$, with a magnetic field $B_{\rm c}$, and results in the formation of a neutron

star of radius $R_{\rm NS}$, with a magnetic field $B_{\rm NS}$, then by conserving the magnetic flux,

$$\frac{\rm d}{{\rm d}t} B_{\rm c} R_{\rm c}^2 = 0 \Rightarrow B_{\rm NS} = B_{\rm c} \frac{R_{\rm c}^2}{R_{\rm NS}^2}. \tag{2.12}$$

There is still some uncertainty regarding whether the fossil theory provides the full explanation for why pulsars have high magnetic fields. For example, Bonanno et al. (2005) claim that dynamo effects (i.e., rotation, convection, and electric conductivity) within the progenitor star also need to be considered. On the other hand, Braithwaite & Spruit (2004) claim that the fossil theory can be used to explain even the magnetic fields of stellar remnants from white dwarfs to magnetars.

Pulsars rotate very rapidly, generally with spin periods of a few seconds. The famous Crab Pulsar (PSR B0531+21) is one of the fasted spinning isolated pulsars with a period of $\sim$33.5 ms (Becker & Aschenbach, 1995). The rapid rotation can be explained via the conservation of angular momentum. For a collapsing core with an angular velocity of $\omega_{\rm c}$ we can calculate the angular velocity of the resulting neutron star, ω, via

$$\frac{\rm d}{{\rm d}t} R_{\rm c}^2 \omega_{\rm c} = 0 \Rightarrow \omega = \omega_{\rm c} \frac{R_{\rm c}^2}{R^2} \tag{2.13}$$

where

$$\omega = \frac{2\pi}{P}, \tag{2.14}$$

and P is the pulse period of the neutron star. For collapsing stars with a stellar core of $\sim$1.4 $M_\odot$, the resulting neutron star pulse period is on the order of a few seconds, which is consistent with observations (Lyne et al., 1985).

2.2.4 Millisecond Pulsars

The fastest rotating neutron stars (with $P < 0.1$ s) are commonly known as "millisecond pulsars". About two thirds of them were discovered as isolated pulsars, while the rest are found in binary systems (see Lorimer, 2008, for a review). They are famous for being the most precise "clocks" in the Universe, much more

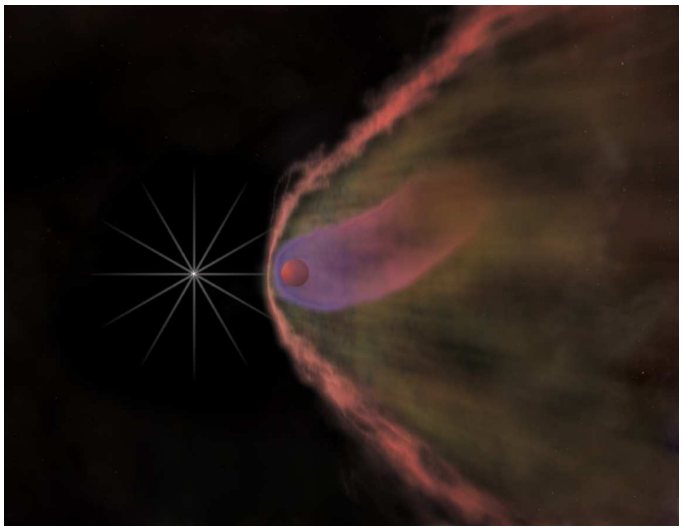

Figure 2.6: Artistic representation of the black-widow pulsar B1957+20. The white dot represents the pulsar with strong spin-generated winds blasting the companion, removing its material. The companion also has a wind that is much weaker than that of the neutron star, but the collision between the two winds results in the strong X-ray emission (red arc). This process can result in the companion being entirely evaporated (M.Weiss/NASA/CXC, Chandra X-Ray Observatory, 2003).

precise than the best atomic clocks on Earth.

Millisecond pulsars are thought to originate from binary systems in which the neutron star orbited a low-mass stellar companion (see Chapter 3 for more details on neutron stars in binary systems). Within these binary systems, material can be transferred from the stellar companion onto the neutron star. This accreted material exerts torques on the neutron star and the transferred angular momentum can increase the spin of the pulsar. Millisecond pulsars are the remnants of these types of systems after accretion has seized (see Bhattacharya & van den Heuvel, 1991; Tauris & van den Heuvel, 2006, and references therein for more information on the evolution of millisecond pulsars). For this reason, they are also known as "recycled" pulsars.

Two interesting categories of millisecond pulsars are black-widow and redback pulsars. These pulsars are found in binary systems with ablating companions, i.e., stellar companions that have lost a significant amount of their mass via "evapo-

ration" (irradiation-driven mass loss) and mass transfer to the neutron star (Chen et al., 2013), hence, the "cannibalistic" reference to black widow and redback spiders. Black-widow pulsars have the lowest-mass companions ($M_{\rm companion} \ll 0.1\,M_{\odot}$, i.e., brown dwarfs), and the redback-pulsar companions have slightly higher masses ($M_{\rm companion} \simeq 0.1 - 0.4\,M_{\odot}$, i.e., red dwarfs).

3

Neutron Stars in X-Ray Binaries

3.1 Types of Pulsar X-Ray Binaries

An X-Ray Binary (XRB) is a system composed of a star and a stellar remnant, each orbiting their center of mass, in which matter is transferred from the donor star on the compact object. Figure 3.1 shows an artistic representation of an X-ray binary. The donor is sometimes called an optical companion, as it mainly emits optical radiation. The compact object can be a white dwarf, a neutron star, or a black hole. Regardless of the type of the compact object, X-rays are produced as the transferred material is heated to high temperatures ($\sim 10^7$ K) through fueled by the release of gravitational potential energy.

XRBs are aome of the brightest X-ray sources in the sky. In the past few decades, the analyses of the data obtained from numerous X-ray space satellites have provided us with with an increasingly better understanding of these sources. Accretion onto neutron stars is an extreme phenomenon, characterized by high-temperature plasma interacting with very strong gravitational and magnetic forces.

X-Ray Binaries are most commonly classified as Low-Mass X-ray Binaries (LMXBs) or High-Mass X-ray Binaries (HMXBs). The optical companion in a LMXB is a low mass star ($\lesssim 2\, M_\odot$), such as an evolved red giant companion, or even a white dwarf. These optical companions have surface temperatures $< 10^4$ K.

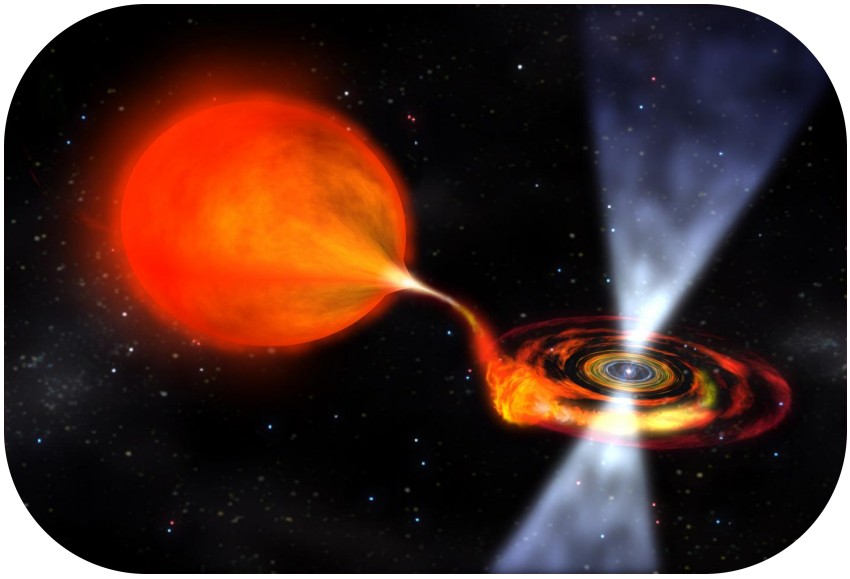

Figure 3.1: Artistic representation of an X-ray binary. Picture by Dana Berry/NASA.

LMXBs are thought to be old systems in which the compact object is a black hole or a weakly magnetic ($\leq 10^9$ G) neutron star. HMXBs are systems in which the donor is a young, massive star ($>6\,M_\odot$), i.e., of O or B spectral type. They have high surface temperatures ($> 10^4$ K), and are extremely bright (up to $10^6\,L_\odot$). Because O and B stars have shorter life spans, HMXBs are thought to be much younger than LMXBs. The compact objects in HMXBs are sometimes black holes, but more ofthen highly magnetic ($\geq 10^{12}$ G) neutron stars, which normally show strong pulsations. In the latter, the magnetic field of the pulsar is strong enough to disrupt the accretion flow (Davidson & Ostriker, 1973; Ghosh & Lamb, 1979a), i.e., the material is channeled along the magnetic field lines onto the surface of the neutron star. The neutron star magnetic field is much weaker in LMXBs and the material is accreted equatorially, as the accretion disk reaches close to the surface of the neutron star.

All accreting pulsars are X-ray pulsars (see Chapter 5 for details on the X-ray emission from the accretion column of these types of pulsars). The majority of accreting pulsars are found in HMBXs and only a few have been observed in

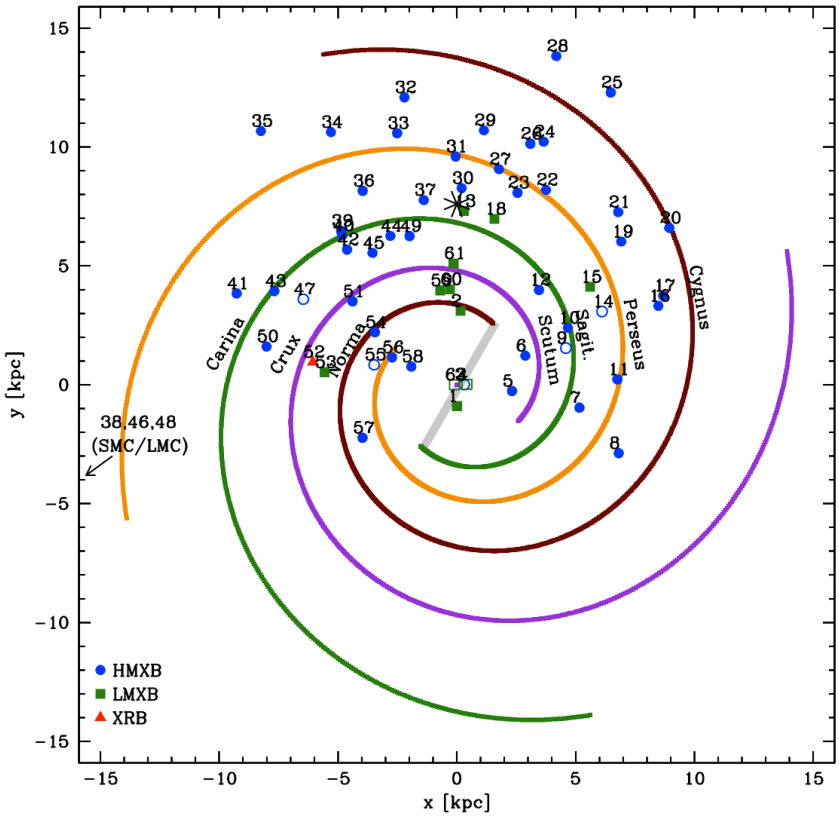

Figure 3.2: Position of currently known accreting X-ray pulsars in the galaxy. The Sun is labeled by the star (∗) symbol. The figure and data were provided by Arash Bodaghee, SSL, UC Berkeley, for the DokuWiki of the Dr. Karl Remeis-Observatory. The name of each numbered source can be found at http://www.sternwarte.uni-erlangen.de/wiki/doku.php?id=xrp:start.

LMXBs. Figure 3.2 shows the positions of currently known accreting X-ray pulsars in our galaxy. Accreting pulsars typically have pulse periods of a few seconds to minutes.

Table 3.1, modified from Table 7.2 in Charles & Seward (1995), lists the known types of XRBs, their components, and provides examples of known sources. For more general information on XRBs see Lewin et al. (1995).

Table 3.1. X-Ray Binaries

Type	Optical Companion	Compact Object	Accretion Disk	Examples
HMXB-SFXB	OB I-II	NS, BH	small	XTE J1739−302
HMXB	OB I-III	NS, BH	small	Cen X-3; Cyg X-1
HMXB-BeXB	Be	NS	small	A 0535+26
LMXB-SyXB	M-III	NS	small	GX 1+4
LMXB	A-F V	NS, BH	large	Her X-1; Cyg X-2
LMXB	K-M V	NS, BH	large	Sco X-1
LMXB	WD	NS	large	4U 1820-30

Note. — NS = neutron star; BH = black hole. In astronomy sources are generally named by constellations (Centaurus, Cygnus, Hercules, and Scorpius), or by its sky coordinates and discovery instrument: A for *Ariel*, U for *Uhuru*, and XTE for *The Rossi X-ray Timing Explorer*. The X-ray binary-type abbreviations are explained in Chapter 3.1 and 3.3. The stellar-type abbreviations are explained in Chapter 2.1.2 (modified Charles & Seward, 1995, Table 7.2).

3.2 Determination of Orbital Parameters

The pulse period of a neutron star in a binary system can be used to determine the parameters that describe the pulsar's orbit around its companion. From Kepler's first law, the orbit of a neutron star around its companion is an ellipse centered on the system's center of mass (CM). Determining the neutron star's position at any given time is a complex process, which involves the determination of the following orbital parameters:

- $P_{\rm orb}$, the time in which the neutron star completes one full orbit,
- a, the semi-major axis of the ellipse,
- e, the eccentricity of the ellipse,

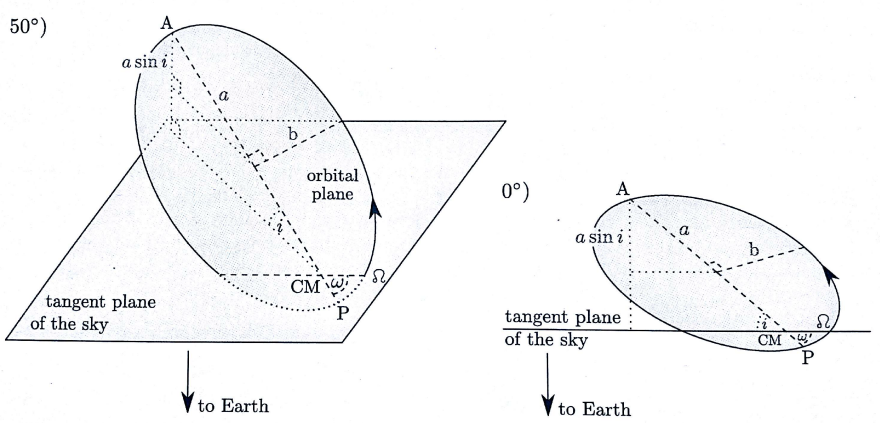

Figure 3.3: Schematic of the neutron star orbit in a binary system viewed at an angle of 50° (left panel) and 0° (right panel) relative to the tangent plane of the sky. See text for parameter description (Bissinger, 2016, Fig. 1.8).

- i, the inclination of the orbital plane,
- τ, the periastron time, i.e., when the components are closest during an orbit,
- ω, the longitude of the periastron of the orbit.

A schematic of the orbital geometry and parameters is shown in Fig. 3.3.

These parameters can be determined by studying the observed Doppler-shifted pulse period (Hilditch, 2001, p.169),

$$P_{\text{obs}}(t) = P(t)\left(1 + \frac{v(t)}{c}\right), \tag{3.1}$$

where $P(t)$ is the intrinsic pulse period of the neutron star as a function of time and $v(t)$ is the radial velocity, i.e., the time-dependent velocity of the neutron star in the observer's line of sight. The radial velocity is related to the orbital parameters via

$$v(t) = \frac{2\pi a \sin i}{P_{\text{orb}}\sqrt{1-e^2}}\left(\cos(\theta(t)+\omega) + e\cos\omega\right), \tag{3.2}$$

where θ is the true anomaly derived from Kepler's equation (Hilditch, 2001, p.37). Therefore, one needs to know how the neutron star's pulse period changes with time

in order to obtain the orbital parameters.

The intrinsic variations of the pulse period, $P(t)$, are a result of accretion torques exerted on the neutron star by the in-falling material or vice-versa. In the case of high luminosities ($\gtrsim 10^{35}\,\mathrm{erg\,s^{-1}}$), the pulse period of a neutron star decreases (i.e., the neutron star experiences a spin-up) due to the conservation of angular momentum from the in-falling material coupled with the magnetic field. The effect of the accretion torques was studied in detail by Ghosh & Lamb (1979b). They describe how the total exerted torque depends mainly on the material stresses (i.e., the angular momentum transfer which results in an overall negative torque), the magnetic stresses of the B-field on the in-flowing material, and viscous stresses inside the plasma were found to be negligible. The net effect of the accretion torques on the pulse period is

$$\dot{P} = -bP^2 L_{37}^{\alpha}, \tag{3.3}$$

where P is the measures instantaneous pulse period, L_{37} is the source luminosity measured at the same time as P in units of $10^{37}\,\mathrm{erg\,s^{-1}}$, and b is a constant. The luminosity exponent, α, describes either disk accretion ($\alpha = 6/7$) or wind/spherical accretion ($1 \leq \alpha \leq 7/3$). For low luminosities or very fast rotating pulsars, angular momentum is transferred from the neutron star to the accretion disk, thus, causing the neutron star to slow down, i.e., spin-down. For very low luminosities ($\lesssim 10^{34}\,\mathrm{erg\,s^{-1}}$) the neutron star can transfer enough angular momentum to the accretion disk to drive some of the material outwards. This is known as the propeller effect (Davidson & Ostriker, 1973; Illarionov & Sunyaev, 1975; Shakura, 1975).

The evolution of P_{obs} can be best determined from long-term X-ray monitoring observations and by applying the epoch folding technique to the X-ray lightcurves (see Chapter 5.4.3 for more details on epoch folding). $P(t)$ can be modeled via flux measurements (e.g., see the orbit determination of XTE J1946+274 in Chapter 7.3.3). $P_{\mathrm{obs}}(t)$ and, thus, the radial velocity $v(t)$ can be modeled iteratively and fitted with a suitable combination of orbital parameters. A detailed example of

this orbit determination procedure can be found in Marcu-Cheatham et al. (2015) where we improved the orbital parameters measurements for the accreting pulsar XTE J1946+274 by modeling its pulse period evolution (see Chapter 7 for more details).

It is important to note that in cases where the neutron star orbital parameters and the mass of the optical companion ($M_{\rm opt}$) are known (e.g., via spectral studies), the mass of the neutron star ($M_{\rm NS}$) can be derived via what is known as the mass function of the system (Hilditch, 2001, p.279), which is defined by

$$f(M) = \frac{(M_{\rm opt}\sin i)^3}{(M_{\rm NS}+M_{\rm opt})^2} = \frac{4\pi^2}{G}\frac{(a\sin i)^3}{P_{\rm orb}^2}\left(1-e^2\right)^{3/2}. \tag{3.4}$$

3.3 Mass Transfer in X-Ray Binaries

In addition to XRBs being categorized by either their donor star/optical companion (high- or low-mass stars), or their compact object (white dwarf, black hole, or neutron star), they can also be categorized according to the mechanism by which the material is transferred between the two components: (1) Roche-lobe overflow, (2) wind-driven transfer, or (3) Be circumstellar disk crossing. This section describes how these mass transfer mechanisms affect the accretion geometry close to the compact object. Some examples are shown in Table 3.1, while Table 8.1 lists all XRBs analyzed in this work. As an additional reference, Chapter A.1 shows the long-term flux measurements obtained with the *Swift*-BAT instrument of each of the XRBs used in this study, as the long-term behavior of the X-ray emission is related to the different types of mass transfer described in the following.

3.3.1 Roche-Lobe Overflow

Let us consider the coordinate system rotating with the binary. The gravitational potential acting on a particle is known as the Roche potential, Φ,

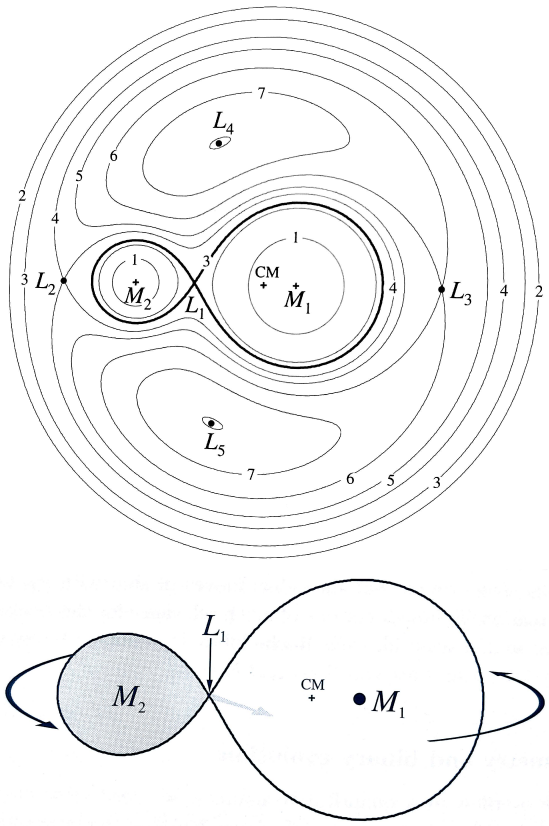

Figure 3.4: The top image shows a schematic view of the Roche potential in a binary system, in which the mass of one component (M_1) is four times larger than that of the other component (M_2). The CM represents the center of mass, and $L_1 - L_5$ represent Lagrangian points, i.e., locations at which an object is in force equilibrium. L_1 is the inner Lagrangian point, through which material is transferred. L_4 and L_5 are local potential minima and are also commonly known as "Trojan" asteroid points. The lines labeled 1–7 are equipotential lines of increasing value, where the thicker line (3) defines the Roche lobes of each component. The bottom image shows the component M_2 with a filled Roche lobe, from which mass overflows and is transferred to M_1 through the inner Lagrangian point L_1 (Frank et al., 2002, Fig. 4.3 and 4.4).

which, at the position $\vec{r}$, is given by

$$\Phi(\vec{r}) = -\frac{GM_1}{\vec{r} - \vec{r}_1} - \frac{GM_2}{\vec{r} - \vec{r}_2} - \frac{1}{2}\left(\vec{\omega} \times \vec{r}\right)^2, \tag{3.5}$$

where M_1, M_2, $\vec{r}_1$, and $\vec{r}_2$ are the masses and positions of the two co-rotating objects, and $\vec{\omega}$ is the angular frequency of the binary (Frank et al., 2002, p.50). This potential, shown in Figure 3.4, defines an area inside of which a particle is gravitationally bound to one of the objects. This area is known as the Roche lobe. The optical companion can be sufficiently evolved to fill and overflow its Roche lobe. If the envelope of the donor star expands beyond the inner Lagrangian point of the system, material is linearly transferred into the Roche volume of the compact object. Thus, the material is transferred through a mechanism known as Roche-lobe overflow (Figure 3.4). This type of material transfer is very efficient and the donor star experiences material-loss rates of $\sim 10^{-11} - 10^{-8} M_\odot$ yr^{-1} (Frank et al., 2002, p.58). The material flowing through the inner Lagrangian point has very high angular momentum. The conservation of this angular momentum forces the material to move along quasi-Keplerian orbits, thus, forming the accretion disk around the compact star. The viscous forces of the plasma lead to a reduction of the angular momentum in the inner regions of the disk causing the material to spiral in towards the compact object.

Roche-lobe overflow is generally observed in LMXBs and they represent a large part of the observed XRBs (see also Savonije, 1978). They typically have orbital periods $\lesssim$5 d. They are mostly transient systems in which the compact object is either a black hole or a neutron star, and their outbursts evolve through characteristic X-ray states over weeks or months. There are also some persistent sources that experience Roche-lobe overflow, such as binaries in which the compact object is a neutron star with a low magnetic field. HMXBs can experience Roche-lobe overflow to various degrees. The sources in this analysis that likely exhibit Roche-lobe overflow include 4U 1626−67, an ultra-compact [1] LMXB with a low-mass, degenerate optical companion (Levine et al., 1988; Chakrabarty, 1998). In addition, LMC X-4 and Cen X-3 (Lewin et al., 1995; Blondin & Owen, 1997), are two HMXBs

[1] 4U 1626−67 is characterized by a very short orbital period of 0.0292 d (Middleditch et al., 1981).

Figure 3.5: Artistic view of a binary system with a compact object accreting from the strong wind of its stellar companion. Credit: M.Weiss/NASA/Chandra X-ray Observatory (http://chandra.harvard.edu/photo/2007/m33x7/).

with O spectral type companions. LMC X-4 is also believed to be an example of a HMXB dominated by Roche-lobe overflow.

3.3.2 Wind-Driven Mechanism

The X-ray emission of the majority of HMXBs is variable but persistent due to undergoing strong wind-driven accretion (Figure 3.5). Stellar winds from high-mass stars are generally strong and driven by the radiation pressure in absorption lines (Frank et al., 2002, p.99). As a result, these winds can reach supersonic velocities. The strong gravitational field of the compact object can create shocks between wind streams, reducing the wind velocity and angular momentum. In these systems, the material can be accreted by the compact object spherically or through a small accretion disk formed due to the plasma's remaining angular momentum.[2]

[2]In the wind-driven accretion case the angular momentum is significantly lower than that in the Roche Lobe overflow case.

Despite the companion's very high wind-loss mass rate ($10^{-6} - 10^{-5} M_{\odot}$ yr^{-1}) compared to the Roche lobe overflow , the accretion is much less efficient with only 0.01–0.1% of the material being transferred to the compact object (Frank et al., 2002, p.73).

Wind-accreting binary systems typically have low eccentricities and we often observe eclipses due to the small orbital radii and periods of the NS (on the order of days, e.g., see Vela X-1 properties in Table 8.1). Also due to the proximity between the two stars, the mass accretion rate is generally larger (10^{-10}–$10^{-8}\, M_{\odot}$ yr^{-1}), making wind accretors some of the most luminous X-ray sources in our galaxy. Depending on their density, these stellar winds can absorb a significant amount of the soft X-ray emission from the pulsar, therefore, properties of the stellar wind can also be determined through studying the intrinsic absorption (and, also, fluorescent emission) observed in the X-ray spectrum (see Chapter 4.3 for more details on absorption and fluorescence).

Vela X-1 is the main wind-accreting pulsar studied for the project presented in this dissertation. It is composed on a pulsar deeply submerged in the supersonic wind of its B-type optical companion (Sidoli et al., 2015).

Supergiant Fast Xray Transients (SFXTs) are a recently discovered class of HMXBs (Sguera et al., 2006; Negueruela et al., 2006). These sources display very fast and bright X-ray flares with a duration of 100–10000 s. The very transient behavior is believed to be due to the stellar companion's wind being extremely inhomogeneous (Martínez-Núñez et al., 2017). Another recently discovered category of systems with strong wind emitters are known as highly obscured sources, which are strong X-ray sources that exhibit extremely high intrinsic absorption in both the X-ray and optical energy ranges (Chaty, 2008; Walter et al., 2015). Most SFXTs and the highly obscured systems were discovered by the *INTErnational Gamma-Ray Astrophysics Laboratory (INTEGRAL)* satellite (Walter et al., 2015).

Although LMXBs are known to be transient and experience Roche lobe

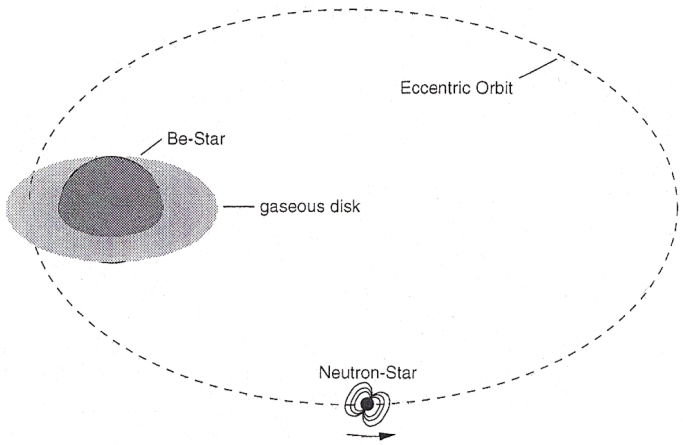

Figure 3.6: A Be XRB system in which the compact object (neutron star), passes through the Be-disk from which it accretes material (Kretschmar et al., 1996).

overflow and disk accretion, there is a small group of ∼10 known persistent LMXBs in which a neutron star orbits a low-mass M-type giant star with weak wind emission (Iben & Tutukov, 1996; Masetti et al., 2006). These are known as Symbiotic X-ray binaries (SyXBs). See Marcu et al. (2011) for an analysis of the hard X-ray band properties of the SyXB 3A 1954+319. In these sources, the compact object is completely embedded in the inhomogeneous stellar wind. This material has negligible angular momentum and does not form an accretion disk. Therefore, the material is accreted spherically, a mechanism known as Bondi-Hoyle accretion (Bondi & Hoyle, 1944).

3.3.3 Be Mechanism

A particular category of HMXBs are Be X-ray Binaries (BeXB), in which the optical companion is an un-evolved star of spectral type Oe to Be (Coe, 2000). These stars rotate very rapidly and eject material causing the formation of a "decretion" disk of material around the star. Be-type stars are characterized by the forbidden lines emitted from this circumstellar disk; therefore, "e" in "Be" stands for optical *e*mission lines (Struve, 1931). Strong X-rays are emitted when the compact

object enters the Be star's disk and accretes material from it (Figure 3.6). In BeXBs most compact objects are neutron stars (Belczynski & Ziolkowski, 2009) with wide ($P_{\rm orb}$∼20 − 200 d), and sometimes eccentric orbits (see Figure 3.6). BeXBs are usually transient sources which show two types of outbursts. Type I outbursts are regular, short, quasi-periodic, and they occur around periastron. Type II outbursts are very luminous and last for longer periods of time. During Type I outbursts, the accretion onto the neutron star is believed to be spherical, unlike the Type II outbursts, during which an accretion disk likely forms (Reig, 2007). Be stars have a short lifespan, BeXBs are believed to be young systems.

The majority of accreting pulsars analyzed for the project presented here are BeXBs. These are XTE J1946+274, 4U 0115+63, GX 304−1, and A 0535+26, which have Be-stellar companions, but also 1A 1118−61, which has an Oe-type companion. Chapter 7 focuses on the detailed temporal and spectral analysis of XTE J1946+274, while Chapter 8 contains a detailed spectral analysis of the larger pulsar sample.

3.4 The Corbet Diagram

The type of optical companion/mass-transfer mechanism in HMXBs is related to the pulse and orbital period of the neutron star (Corbet, 1986). As can be seen in Fig. 3.7, systems that exhibit the three different type of mass transfer mechanisms described in Chapter 3.3, occupy three different areas on pulse period versus orbital period diagram. These relationships can be used in the process of identifying optical companions/determine the mass-transfer mechanisms (Tomsick et al., 2011; Esposito et al., 2013) or other properties of XRBs (e.g., Chaty, 2013; Cheng et al., 2014; Enoto et al., 2014).

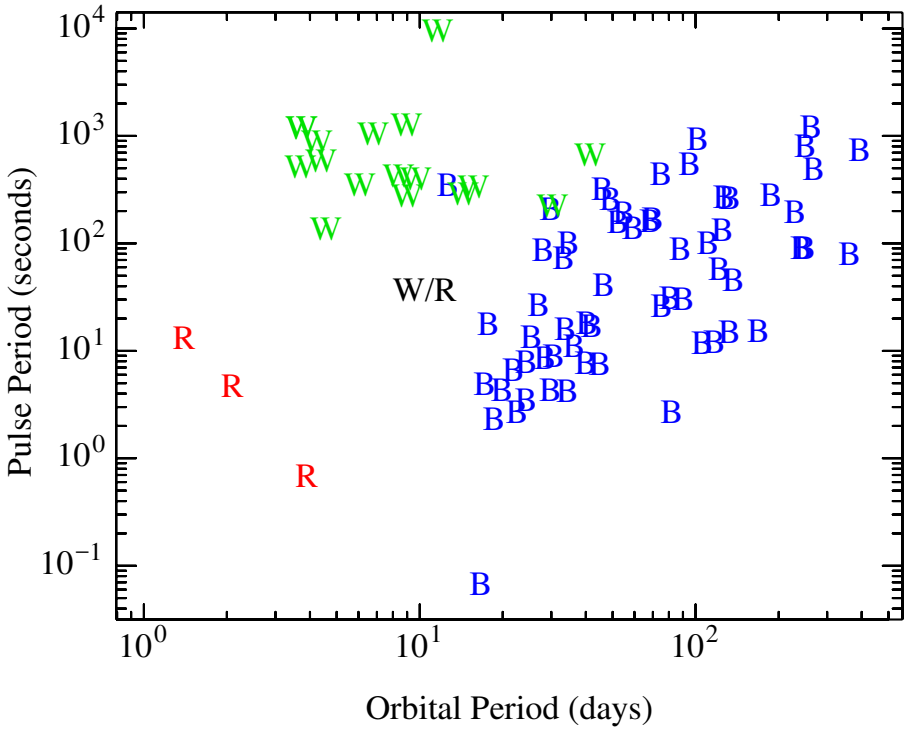

Figure 3.7: The Corbet diagram shows the pulse periods of neutron stars in HMXBs as a function of their respective orbital periods. The "R"s represent systems with Roche-lobe overflow, "W"s are wind accreting systems, and "B"s are BeXBs (Corbet, 1986; Coley, 2015, Corbet, priv. comm.).

4

Radiation Processes

4.1 Emission Processes

In this Chapter I describe the physical mechanisms which result in the bremsstrahlung, cyclotron, and blackbody radiation emitted during the accretion process onto a highly magnetic neutron star.

4.1.1 Blackbody Emission

Blackbody emission is radiation in thermal equilibrium with itself. Blackbody emission is an important astrophysical concept as it describes the spectral shape of stars and plays a role in accretion processes, as well.

Planck (1900) was the first to correctly describe the spectrum of a blackbody as it dependents on its temperature, T, i.e., the intensity radiated as a function of wavelength, λ, or frequency, ν, is

$$B_\nu(\nu, T) = \frac{2h\nu^3/c}{e^{h\nu/(kT)} - 1} \text{ or } B_\lambda(\lambda, T) = \frac{2hc^2/\lambda^5}{e^{hc/(\lambda kT)} - 1}, \tag{4.1}$$

where h is the Planck constant, k is the Boltzmann constant, and c is the speed of light.

The maximum intensity frequency (or wavelength) of a blackbody (i.e.,

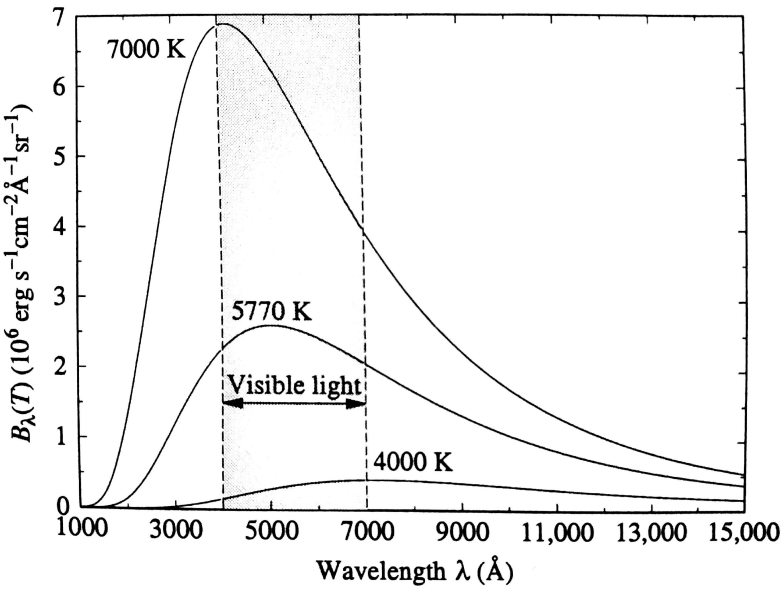

Figure 4.1: Blackbody spectrum as described by the Planck function $B_\lambda(T)$ (Carroll & Ostlie, 1996, Fig. 3.8).

the peak of the emission curve on Fig. 4.1) is described by Wien's Displacement Law (Wien, 1897) as

$$h\nu_{\max} = 2.82\,kT. \tag{4.2}$$

This is an important result which shows that the maximum radiated frequency/energy is directly related to the blackbody temperature. Another important property of blackbodies is that their temperature can also be determined from the total flux (F) via the Stefan-Boltzmann Law (Boltzmann, 1884),

$$F = \sigma T^4, \tag{4.3}$$

where σ is the Stefan-Boltzmann constant. Therefore, the total luminosity ($L_{\rm BB}$) of a blackbody with surface area $A_{\rm BB}$ is

$$L_{\rm BB} = A_{\rm BB}\sigma T^4. \tag{4.4}$$

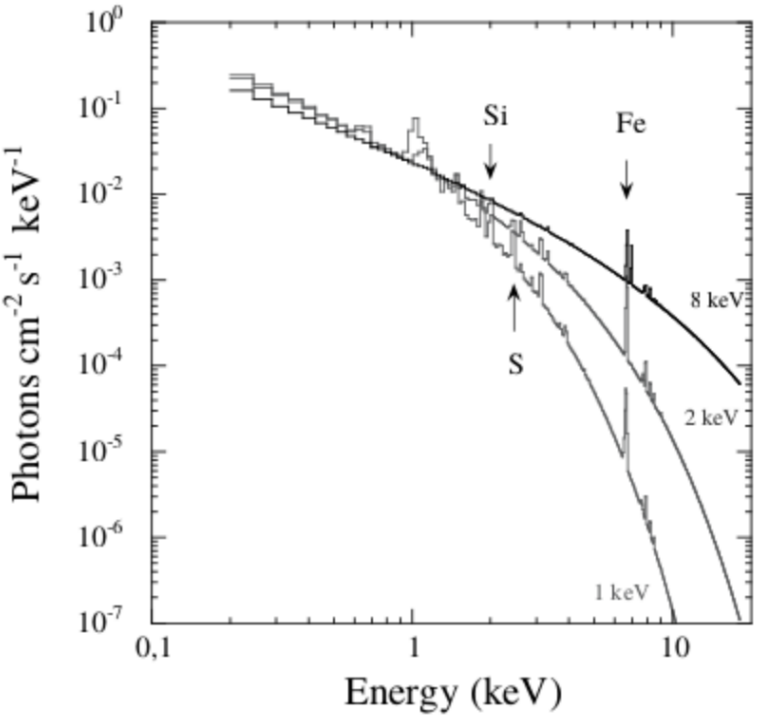

Figure 4.2: X-ray spectrum of thermal bremsstrahlung emission from a thin plasma of temperatures T =1, 2, and 8 keV with $Z = 35\%$ of the element abundance in the Sun. These are typical examples of X-ray spectra from Galaxy Clusters. Silicon (Si), sulfur (S), and iron (Fe) emission lines are labeled (Arnaud, 2005, Fig. 1).

Many accreting pulsars show signatures of low-temperature blackbody emission in their spectra. These types of emissions originate from outside the accretion column. In addition, blackbody radiation that undergoes inverse Compton scattering effects can also be produced inside the accretion column, playing a role in the hard X-ray continuum formation (see Chapter 5.4).

4.1.2 Bremsstrahlung Emission

The information presented in this section is based on Rybicki & Lightman (1979). In the late 1800's, Nicola Tesla found that electrons can be accelerated in the presence of a nucleus. The radiation resulting from a particle being accelerated due to the presence of a Coulomb field was called bremsstrahlung, German for

"braking radiation". In atomic physics, this phenomenon is also known as free-free (ff) emission.

In astrophysics bremsstrahlung radiation is often produced by electrons accelerated in the Coulomb field of a proton. For thermal plasmas (i.e., where electrons have a Maxwell-Boltzmann velocity distribution), this process is known as "thermal bremsstrahlung emission".

Assuming a thermal plasma in which moving electrons with electric charge -e, mass $m_{\rm e}$, and a density $n_{\rm e}$ interact with ions of charge Ze and density $n_{\rm i}$. The electrons would be deflected at small angles and the resulting bremsstrahlung emission, W, per unit time, dt, volume, dV, and frequency, dν, is

$$\frac{\mathrm{dW}}{\mathrm{d}t\mathrm{d}V\mathrm{d}\nu} = \frac{2^5\pi e^6 \mathrm{e}^6}{3m_{\rm e}c^3}\left(\frac{2\pi}{3m_{\rm e}k}\right)^{1/2} T^{-1/2} Z^2 n_{\rm e} n_{\rm i} e^{-h\nu/kT} \bar{g}_{\rm ff}, \tag{4.5}$$

where $\bar{g}_{\rm ff}$ is known as the velocity-averaged Gaunt factor. Therefore, the total power density of thermal bremsstrahlung emission is

$$j_{\rm ff} = \left(\frac{2\pi kT}{3m_{\rm e}}\right)^{1/2} \frac{2^5\pi e^6}{3hm_{\rm e}c^3} Z^2 n_{\rm e} n_{\rm i} \bar{g}_{\rm B}(T), \tag{4.6}$$

where $\bar{g}_{\rm B}(T) \approx 1.2$ is the frequency-averaged $\bar{g}_{\rm ff}$. The resulting spectrum of bremsstrahlung emission is continuous. Eqn. 4.5 shows that the bremsstrahlung emission spectrum is mainly described by the temperature, T, and density, $n_{\rm e}n_{\rm i}$, of the emitting material. An example of typical thermal bremsstrahlung emitted from Galaxy Clusters at different temperatures is shown in Fig. 4.2.

4.1.3 Cyclotron Emission

Cyclotron radiation is emitted by charged non-relativistic particles accelerated by a magnetic field.[1] The particles are accelerated by the Lorentz force which acts perpendicular to the magnetic field, causing the particles to move in a circular

[1] This phenomenon is known as synchrotron emission for relativistic particles.

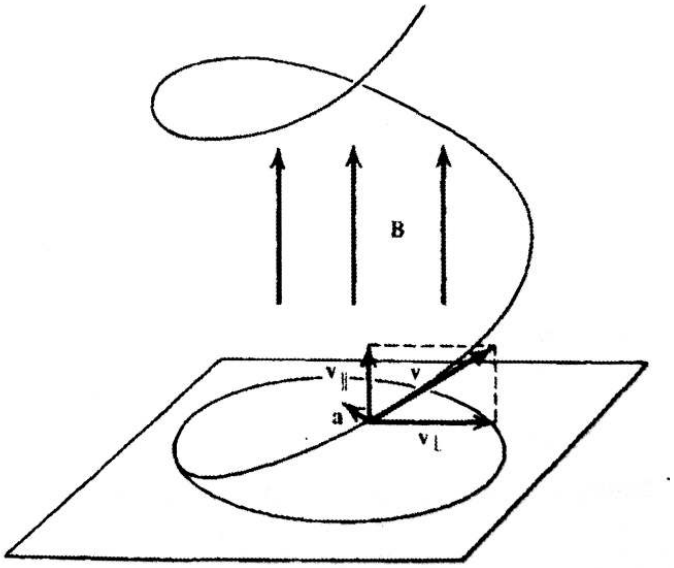

Figure 4.3: Schematic representation the helical motion of an electron in the presence of a uniform magnetic field, B, where a is the acceleration, and v is the electron velocity, which is separated into perpendicular and parallel components, $v_\perp$ and $v_\parallel$, respectively (Rybicki & Lightman, 1979, Fig. 6.1).

motion, or a helical motion if there is a uniform velocity in the direction of the magnetic field lines (see Fig. 4.3). In a thermal plasma in the presence of a magnetic field, cyclotron emission is predominantly created by electrons. As the protons'

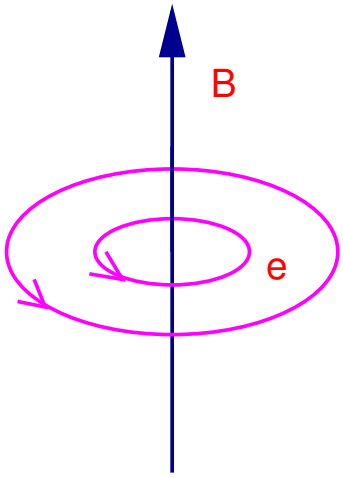

Figure 4.4: Schematic Landau levels for electrons in the presence of a strong magnetic field.

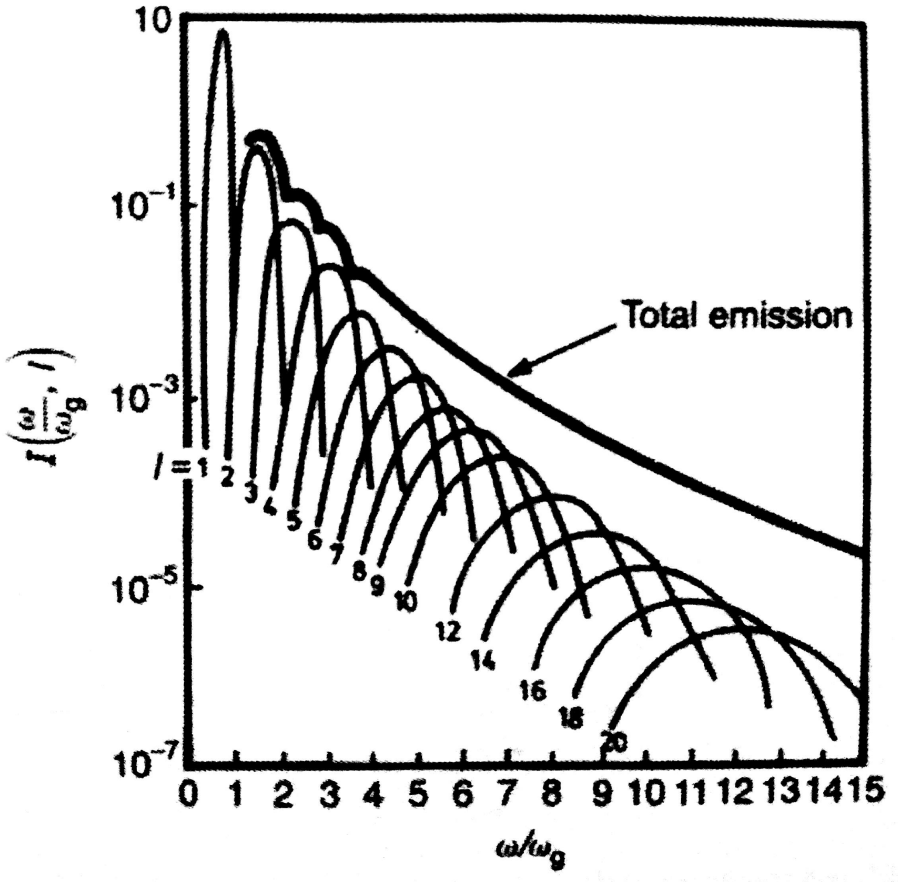

Figure 4.5: Radiated cyclotron spectra of the first 20 gyrofrequency ($\omega_{\rm g}$) harmonics emitted by a plasma with electron speeds $\sim$0.4 c. The total spectrum represents the sum of the spectra of the individual harmonics (Bekefi, 1966; Longair, 2011, Fig. 8.2).

high mass inhibits them from being highly accelerated, the cyclotron emission from protons is negligible.

In the classical approach, an electron of mass $m_{\rm e}$ moves in a circular motion of radius r with a speed $v_\perp$ perpendicular to the magnetic field. From a classical physics perspective, the electron feels a centripetal force $F_c = m_{\rm e} v_\perp^2 / r$, and a Lorentz force $F_{\rm L} = eBv_\perp$ acting as a centrifugal force. The balance of these two forces gives

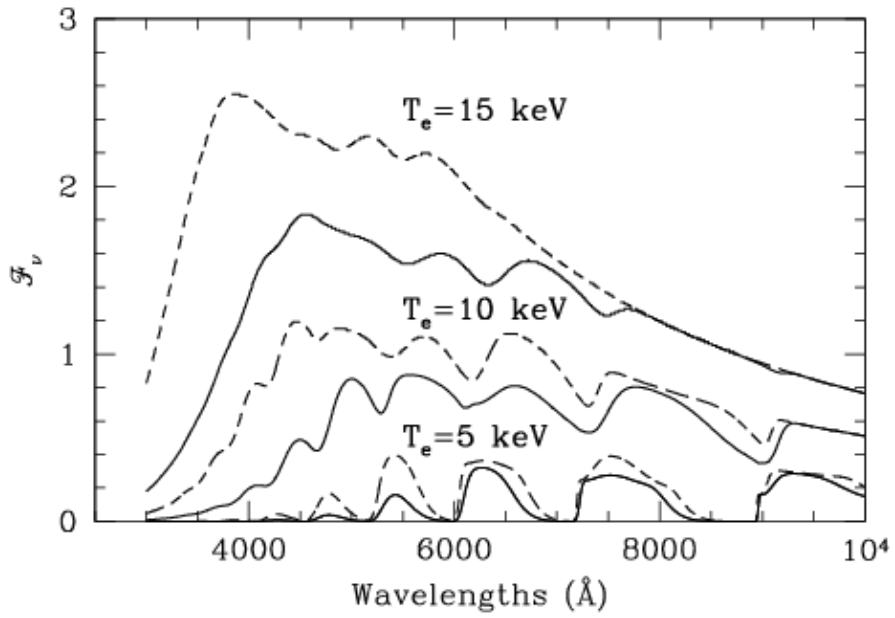

Figure 4.6: Theoretical cyclotron emission spectra for a white dwarf with plasma temperatures T_e =5, 10, and 15 keV, and a magnetic field of 3×10^7 G at a viewing angle of 90°. The solid and dashed curves are for different optical depth values (Wickramasinghe & Ferrario, 2000).

the resulting radius of the electron's stable orbit,

$$r = \frac{m_e v_\perp}{eB}, \tag{4.7}$$

which is known as the gyroradius or Larmor radius. The resulting angular frequency $(v_\perp/r)$ is

$$\omega_g = \frac{eB}{m_e}, \tag{4.8}$$

which is known as the gyrofrequency or cyclotron frequency (Longair, 2011).

Equation 4.7 shows how the gyroradius decreases with increasing magnetic field values. When the gyroradius approaches the electron de Broglie wavelength[2], the electron orbits become quantized. These are known as Landau quantum levels. They are schematically described in Fig. 4.4.

[2]The wavelength associated with a moving particle with momentum p is $\lambda_B = h/p$, which is known as the de Broglie wavelength.

For a thermal plasma in a high magnetic field, the electrons naturally reside at the lowest Landau level, but they can transition to higher levels by interacting with protons and photons. Protons can collisionaly excite an electron to higher Landau levels. The excited electron can then decay back to the ground state and emit cyclotron radiation in the process. Electrons with very low speeds ($v \ll c$) produce an electric field with a frequency equal to the gyrofrequency. As the electron speeds increase to mildly relativistic values, higher gyrofrequency harmonics come into play. Each cyclotron harmonic emits the power

$$\left(\frac{\mathrm{d}E}{\mathrm{d}t}\right)_l = \frac{8\pi^2 e^2 \omega_{\mathrm{g}}^2}{c} \frac{(l+1)l^{2l+1}}{(2l+1)!} \left(\frac{v}{c}\right), \tag{4.9}$$

where $l = 1, 2, 3, ...$ is the harmonic level, and v is the electron speed. Fig. 4.5 shows the cyclotron emission of the first 20 harmonics (and the total spectrum summed over the harmonics) radiating from a plasma of temperature $kT_e = 51.1\,\mathrm{keV}$, where the electron speeds are $\sim 0.4\,\mathrm{c}$. Fig. 4.5 also shows that, as the electron velocities become highly relativistic, the peaks smooth out to form a ,continuous spectral shape, which is known as synchrotron emission (Rybicki & Lightman, 1979, p.181). In addition, examples of theoretical cyclotron emission spectra from a magnetized white dwarf are shown in Fig. 4.6. The interaction between photons and quantized electrons, which results in cyclotron resonant scattering, is discussed in detail in Chapter 5.4.4.

4.2 Comptonization

Compton scattering describes the energy loss of a high-energy photon after interacting with an electron at rest. However, when the electron is in motion, the interacting photon gains energy. The process of a photon increasing in energy as a result of the interaction with a moving electron is known as Comptonization, or inverse Compton scattering. Non-relativistic photon scattering is described by the

Thomson cross-section, $\sigma_{\rm T} = 6.652 \times 10^{-25}{\rm cm}^2$.

In the process of accretion onto a highly magnetic neutron star, two types of Comptonization can occur, thermal and bulk, and these are described in the following.

4.2.1 Thermal Comptonization

Thermal Comptonization describes the process in which photons gain energy by scattering off electrons in a thermal plasma. The average photon energy gain is (Rybicki & Lightman, 1979, p.209)

$$\frac{\Delta E}{E} = \frac{4kT_{\rm e} - E}{m_{\rm e}c^2}, \tag{4.10}$$

where E is the initial energy of the photon and $T_{\rm e}$ is the electron temperature inside the plasma. The total relative energy change of a photon inside a hot plasma with a temperature $kT_{\rm e} \gg E$ is described by the Compton-y parameter,

$$y = \frac{4kT_{\rm e}}{m_{\rm e}c^2} \max(\tau_{\rm e}, \tau_{\rm e}^2), \tag{4.11}$$

where $\tau_{\rm e}$ is the optical depth inside the plasma.

Kompaneets (1957) derived the equation that describes the process of Comptonized diffusion (i.e., repeated inverse Compton scatterings) off non-relativistic electrons through phase-space in a thermal plasma,

$$\frac{\partial n}{\partial y} = \frac{1}{x^2}\frac{\partial}{\partial x} x^4 \left(n + n^2 + \frac{\partial n}{\partial x} \right), \tag{4.12}$$

where n is the photon occupation number, y is the Kompaneets parameter, and x describes the photon energy in terms of the plasma electron temperature as $x = E/kT_{\rm e}$. The photon occupation number depends on the initial photon energy

and the spectral radiative intensity, $I(E)$, as

$$n = I(E)\frac{(hc)^2}{8\pi E^3}. \tag{4.13}$$

The Kompaneets parameter is

$$y = \frac{4kT_{\rm e}}{m_{\rm e}c^2}\sigma_{\rm T}N_{\rm e}ct, \tag{4.14}$$

where $N_{\rm e}$ electron number density, t is the scattering time, and $\sigma_{\rm T}$ is the Thomson cross-section. The $\sigma_{\rm T}N_{\rm e}ct$ term describes the average time between scatterings.

Equation 4.12 can be interpreted as the combination of three physical processes: the recoil effect on the photon (n), stimulated emission (n^2), and the Doppler motion ($\partial n/\partial x$). For details on the derivation of the Kompaneets equation see Rybicki & Lightman (1979, p.213).

4.2.2 Bulk Comptonization

In addition to the thermal Comptonization process, there are also non-thermal Comptonization processes, which describe photons scattered off electrons that have a power-law velocity distribution (in contrast to the Maxwellian electron velocity distribution for thermal Comptonization). The type of non-thermal Comptonization that is relevant for understanding pulsar accretion is known as "bulk (or dynamical) Comptonization". It describes photons being scattered inside a shock wave of highly energetic electrons accelerated by the magnetic field. Moving plasma can experience a shock wave from a converging electron flow. The shock creates inhomogeneities in the magnetic field which act as "mirrors" for the electrons. As electrons are reflected back and forth across the shock by these "magnetic mirrors", they gain high amounts of energies. This electron acceleration process is known as First Order Fermi Acceleration (Krymskii, 1977; Bell, 1978). Photons scattered off these accelerated electrons gain energy through bulk Comptonization. The resulting

radiation spectrum is that of a power-law,

$$F(E) = E^{-\alpha}, \tag{4.15}$$

where the spectral index, α, is $\gtrsim 2$.

4.3 Absorption and Fluorescence

4.3.1 Absorption

Before reaching the observer, X-rays pass through neutral material, such as the Inter-Stellar Medium (ISM) or stellar winds from the optical companions. This can result in absorption and emission features in the observed spectrum.

The amount of neutral material that a photon travels through is described by the number of hydrogen atoms per unit area along the observer's line of sight, known as the equivalent hydrogen column density, $N_{\rm H}$. The interstellar absorption changes the shape of the spectrum at energies lower than 2–3 keV(Eikmann et al., 2012) as shown in Fig. 4.7. How strongly these features influence the spectral continuum depends on the geometry and ionization state of the material (Brandt et al., 1996). Stellar winds typically exhibit "partial covering" absorption due to their inhomogeneous/clumpy structure (Szostek & Zdziarski, 2008).

4.3.2 Fluorescence

Fluorescence lines are also observed in the spectra of accreting pulsar. The X-rays emitted from the accretion column have energies high enough to excite inner-shell electrons, ionizing the neutral material. When the electron vacancy is filled by a different electron transitioning from a higher-energy shell, that electron loses some of its energy in the form of a photon. This phenomenon is known as fluorescence (see left image in Fig. 4.8), which is observed as a narrow spectral

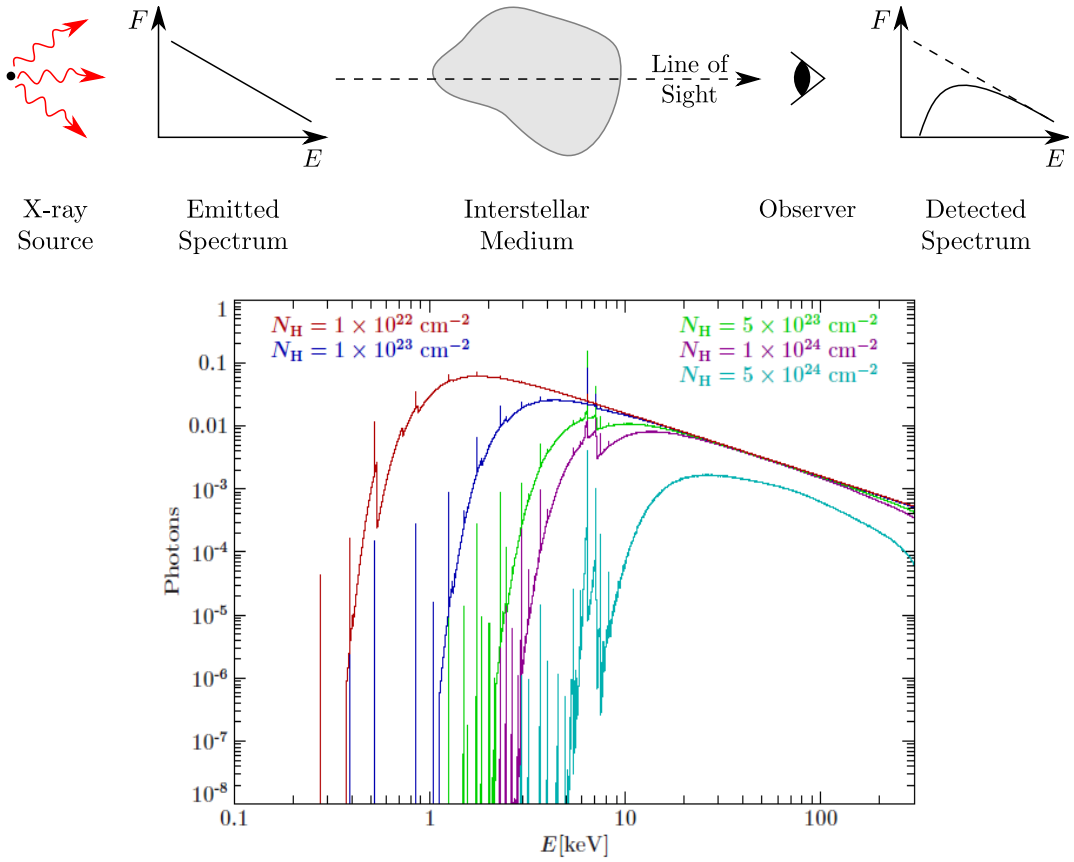

Figure 4.7: Upper panel: Representation of the absorption process and its distorting effect on the X-ray continuum spectrum at low energies (Bissinger, 2016, Fig. 1.24). Lower panel: Example of how the value of the column density (N_{H}) affects the overall shape of the X-ray spectrum. The photo-absorption cross-sections and elemental abundances are provided by Verner & Yakovlev (1995) and Wilms et al. (2000), respectively (Eikmann et al., 2012).

emission line at the energy of the escaping photon (Stokes, 1852). Fluorescence lines are generally modeled with Gaussian functions.

The Siegbahn notation (Siegbahn, 1943) is used for naming fluorescence lines according to the excited level (K, L, or M) from which the second electron transitions and a Greek letter (α or β) to indicate the lower-energy shell with the electron vacancy. The probability that a photoelectric absorption event is followed by fluorescence line emission is known as the fluorescence yield. Generally, in ISM

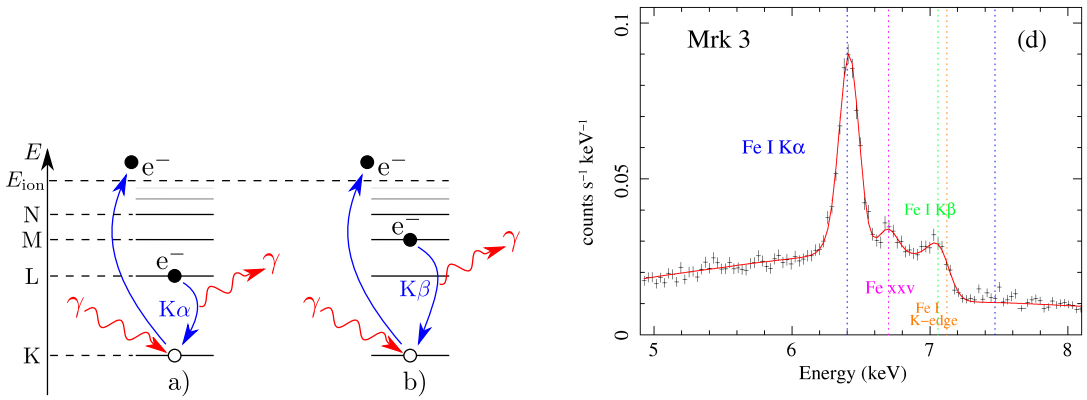

Figure 4.8: Left Image: Representation of fluorescence of (a) Fe Kα and (b) Fe Kβ. As an electron (-e) from the K-shell absorbs an X-ray photon (γ) it transitions to a higher level. An electron from an upper level (L or M) fills the vacancy and emits a photon in the process (Bissinger, 2016, Fig. 1.25). Right Image: Examples of emission lines in X-ray spectra. These are fitted Fe Kα (blue dotted line), Fe Kα (green dotted line), Fe XXV (pink dotted line), and an Fe K-edge. These are lines seen in the *Suzaku* spectrum of the galaxy Mrk 3 (T. Yaqoob, Johns Hopkins University, `http://mytorus.com/mytorus-fits-to-agn-ngc4388-mkn3-circinus-ngc4945.html`).

neutral material, both the iron fluorescence yield and the iron abundance are high (Krause, 1979), leading to strong iron emission lines. A very common and widely studied fluorescence feature for accreting pulsar spectra is the Fe Kα emission line at 6.4 keV (see right image in Fig. 4.8 for examples). This feature is often observed in accreting pulsars, and its studies can be used to determine physical characteristics of the fluorescent material close to the X-ray sources (George & Fabian, 1991). Examples of possible origin locations of the Fe Kα fluorescence line are the low-ionized area in the accretion disk, the stellar wind close to the neutron star, or other unknown locations (Torrejón et al., 2010).

5

Magnetic Field Dominated Accretion

5.1 Alfvén Radius

The magnetic fields ($\sim 10^{12}\,\mathrm{G}$) of accreting pulsars are strong enough to control the movement of the surrounding material, disrupting the originally symmetric disk or spherical inflow (upper panel in Figure 5.1). At a certain distance from the neutron star (bottom left panel in Figure 5.1), the material changes direction and begins to move along the magnetic field lines (Ghosh & Lamb, 1979a,b). This occurs at the Alfvén radius

$$r_A \simeq 6.8 \times 10^8\,\mathrm{cm} \left(\frac{\mu}{10^{30}\,\mathrm{G\,cm^3}}\right)^{4/7} \left(\frac{\dot{M}}{10^{-10}\,M_\odot\,\mathrm{yr^{-1}}}\right)^{-2/7} \left(\frac{M_{\mathrm{NS}}}{1.4\,M_\odot}\right)^{-1/7}, \quad (5.1)$$

where μ is the magnetic dipole moment of the neutron star. At the Alfvén radius, the (outward) magnetic pressure balances out the (inward) ram and gas pressure.

Accretion on a neutron star is possible only when the magnetoshpere's velocity at the Alfvén radius (Eqn. 5.1) is less than or approximately equal to the local Keplerian velocity of the disk plasma. Otherwise, a centrifugal barrier forms that inhibits accretion, the material does not couple with the magnetic field

(Illarionov & Sunyaev, 1975), and the plasma undergoes a propeller effect, i.e., the material is driven/propelled away from the neutron star and accretion does not occur (see also Chapter 3.2).

5.2 X-Ray Luminosity

In X-ray pulsars all the energy liberated through accretion is radiated, powering 10^{34}–$10^{38}\,\mathrm{erg\,s^{-1}}$ luminosities. The emitted X-ray luminosity is

$$L_{\mathrm{X}} = \frac{GM_{\mathrm{NS}}\dot{M}}{R_{\mathrm{NS}}}, \tag{5.2}$$

where M_{NS} and R_{NS} are the mass and radius of the neutron star, and $\dot{M}$ is the mass accretion rate (Frank et al., 2002, p.3).

Material can be accreted only up to the point at which the X-ray radiation pressure force (left-hand side) is in equilibrium with the gravitational force of the compact object (right-hand side),

$$L\frac{\sigma_{\mathrm{T}}}{4\pi cr^2} = \frac{GMm_{\mathrm{p}}}{r^2}\,, \tag{5.3}$$

where M is the mass or the compact object, L is the luminosity, $\sigma_{\mathrm{T}} = 6.652\times10^{-25}\,\mathrm{cm}$ is the Thomson scattering cross section, r is the distance from the center of the compact object, and the constants G, m_{p}, and c are the gravitational constant, proton mass, and the speed of light, respectively (Frank et al., 2002, p.3). The maximum luminosity at which matter can be accreted is known as the Eddington Luminosity,

$$L_{\mathrm{Edd}} = \frac{4\pi cGMm_{\mathrm{p}}}{\sigma_{\mathrm{T}}} = 1.3\times10^{38}\left(\frac{M}{M_{\odot}}\right)\,\mathrm{erg\,s^{-1}}. \tag{5.4}$$

Therefore, the maximum accreting rate associated with this luminosity is the Eddington accretion rate. For example, for a $1.4\,M_{\odot}$ neutron star, the maximum mass accretion rate is $\dot{M}_{\mathrm{edd}} \simeq 1.8\times10^{-8}\,M_{\odot}\,\mathrm{yr^{-1}}$.

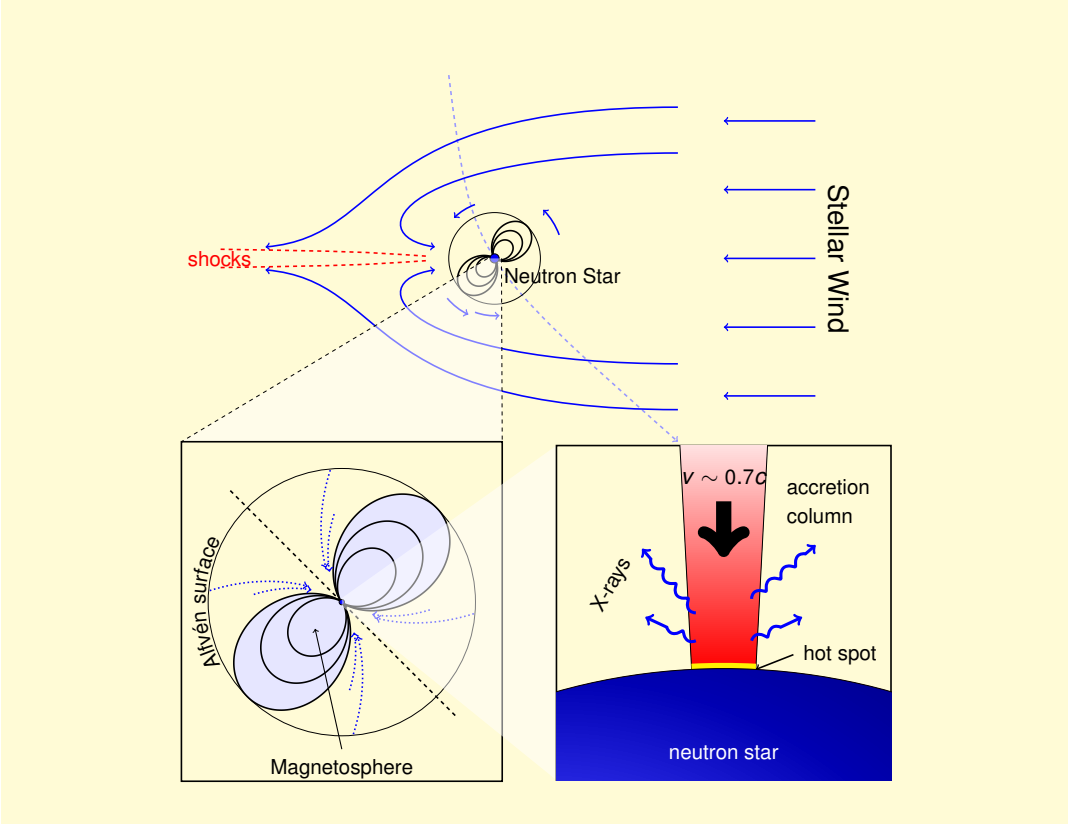

Figure 5.1: Schematic representation of accretion from a wind-emitting star onto a magnetized neutron star. As the material from the strong stellar wind from the optical companion is accreted close to the neutron star, at the Alfvén radius the magnetic field channels the plasma onto the magnetic poles, where an accretion column forms. Inside this accretion column, relativistic plasma is decelerated before coming to a stop at the neutron star surface. Several processes result in the production and emission of X-rays from the accretion column (see Chapter 5.4.1). Figure credit by Jörn Wilms, after Davidson & Ostriker (1973).

5.3 Equilibrium Period

The accretion process can exert torques on the neutron star, leading to spin-up or spin-down phases. At a net torque of zero, the neutron star reaches the equilibrium period (van den Heuvel, 1994),

$$P_{\rm eq} = (2.4\,{\rm ms})(B_9)^{6/7}(R_6)^{16/7}M^{-5/7}\left(\frac{\dot{M}}{\dot{M}_{\rm edd}}\right)^{-3/7}, \qquad (5.5)$$

where B_9 is the dipole magnetic field strength in units of 10^9 G, R_6 is the neutron star radius in units of 10^6 cm, M is the neutron star mass in units of $M_\odot$, and $\dot{M}_{\rm edd}$ is the Eddington accretion rate.

Above the surface of the neutron star at the magnetic poles, the plasma inflow geometry is approximately cylindrical (bottom right panel in Figure 5.1). This is known as an accretion column, inside of which the plasma reaches free-fall velocity. The accreted plasma settles on the bottom of the accretion column where it merges with the neutron star surface forming a thermal mound. It is unclear whether the column is filled, hollow, or has a more complex structure (Mészáros, 1984). Basko & Syunyaev (1975) claim that the material is likely to couple with magnetic field lines of different strengths, possibly forming a hollow accretion column.

At high mass-accretion rates, radiation pressure becomes dominant, and a radiation-dominated radiative shock front forms inside the accretion column (Zel'dovich & Shakura, 1969; Shapiro & Salpeter, 1975; Becker & Wolff, 2007). In high luminosity sources, this is believed to be the main mechanism that decelerates plasma flowing in at relativistic speeds. For low mass accretion rates a radiation-dominated shock does not form and the plasma directly settles on the neutron star surface (Becker et al., 2012).

5.4 Accretion Column

Generally, the broadband spectrum of an accreting pulsar consists of a hard X-ray continuum emitted from the accretion column, with the addition of non-continuum components. The most common of these are: cyclotron lines, interstellar and intrinsic absorption, and fluorescent emission lines. As an example, Figure 5.2 shows the broadband *Suzaku* X-ray spectrum of GX 304−1 and its components. In this section, I describe the physical details of the X-ray production inside the

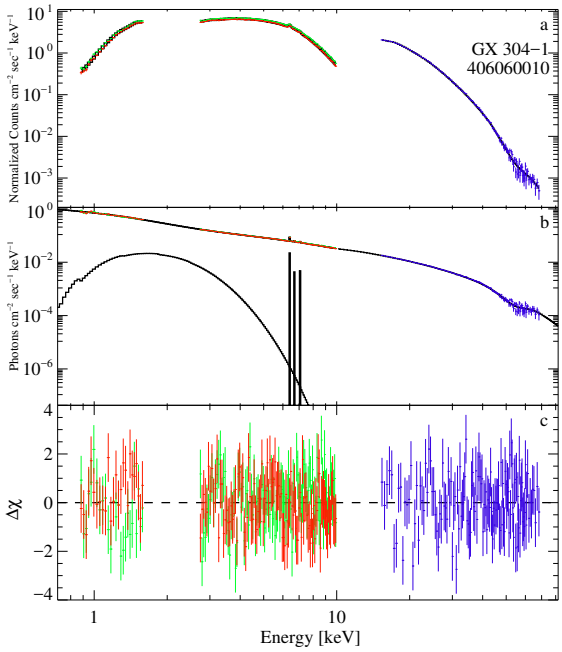

Figure 5.2: This is an example of a broadband spectrum of a pulsar observed with the *Suzaku* satellite. The observed pulsar was GX 304−1. The panels show the following: (a) unabsorbed data and model, (b) unfolded unabsorbed data, full model and model components, and (c) fit residuals. The XIS and PIN models are plotted in black. The data and residuals for each instrument are: XIS0 in red, XIS1 in green, XIS3 in yellow, and PIN in blue. Note in panel (b) the continuum, iron fluorescence, and blackbody emission. The effect of absorption is seen by comparing the spectral shapes in panels (a) and (b) at energies $\lesssim$2 keV.

accretion column. [1]

5.4.1 X-ray Continuum

Inside the accretion column (Figure 5.3) soft X-ray photons (<10 keV) are created from: (1) deflected electrons emitting bremsstrahlung radiation, (2) electrons deflected off the strong magnetic field emitting cyclotron emission, and (3) the hot electrons in the thermal mound at the bottom of the accretion column

[1]Note that a feature of unknown origin was observed at $\sim$ 10 keV in some accreting pulsars, e.g., Cen X-3 (Santangelo et al., 1998; Suchy et al., 2008), 4U 0115+63 (Ferrigno et al., 2009), EXO 2030+375 (Klochkov et al., 2007), Vela X-1 (La Barbera et al., 2003), Her X-1, 4U 1926−67, 4U 1907+09, 4U 1538−52 (Coburn et al., 2002; Mihara, 1995), V0331+53 (Mihara, 1995), MXB 0656−072 (McBride et al., 2006), and XTE J1946+274 (Müller et al., 2012). However, the study of this feature is beyond the scope of this project.

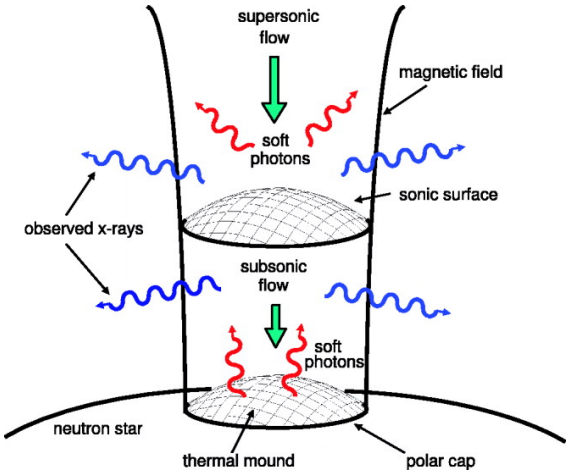

Figure 5.3: Illustration of plasma flowing through the accretion column onto the magnetic pole of a neutron star. The plasma at the top of the column flows in at relativistic speeds and is decelerated by the radiation-dominated radiative shock. Below this shock-front, soft photons are created through, blackbody, bremsstrahlung and cyclotron emission. The soft photons are then Comptonized before exiting the column (Becker & Wolff, 2007).

emitting blackbody radiation. These three types of "seed" photons are subsequently gain energy through inverse Compton scattering, resulting in the hard broadband spectral continuum. The emission and Comptonization processes are described in detail in Chapter 4.

Comptonization can occur dynamically (bulk) or thermally (Becker & Wolff, 2007, and references therein). Bulk Comptonization is the process through which photons gain energy by being scattered back and forth across the radiation-dominated shock. Thermal Comptonization occurs when photons gain energy from diffusion (repeated scatterings), in phase-space, off the hot thermal electrons[2] inside the accretion column.

The standard models generally fit the accreting pulsar spectra well. However, since they do not offer information on the physical properties of the neutron star and the accretion process, there is a high demand for physically descriptive models.

[2]Electrons that have a Maxwell-Boltzmann energy distribution are known as thermal electrons.

The continuum model provided by Becker & Wolff (2007) describes the production, Comptonization, and emission of X-ray radiation from the accretion column of high-luminosity sources where the plasma passes through a radiation-dominated radiative shock. This model can provide a much needed consistent physical description of the accretion mechanism based on the following fundamental parameters that describe the accretion column: the magnetic field in the emitting region, the radius of the accretion column, the plasma temperature, the mass accretion rate, and the degree of thermal and bulk Comptonization. The time-independent, cylindrical, plane-parallel radiation transport equation that describes the photon energy distribution (Becker & Begelman, 1986; Blandford & Payne, 1981; Becker & Wolff, 2007) is shown in Section 8.3.3, along with the implementation and fit procedure of this physical model (based on Becker & Wolff, 2007; Wolff et al., 2016)

5.4.2 Phenomenological Continuum Models

The spectral continua of accreting pulsars generally have a quasi-exponential cut-off power law shape. The commonly used program for X-ray spectral fitting is XSPEC[3]. The phenomenological functions implemented into `xspec` that approximate the spectral shape of the accreting pulsar continuum are: a Power Law with an exponential CUTOFF (CUTOFFPL), a Power Law with a high-energy CUToff (PLCUT), a Fermi-Dirac CUToff model (FDCUT), and a Negative Positive powerlaw times an EXponential function (NPEX).

The simplest pulsar spectral continuum model is CUTOFFPL,

$$\mathrm{CUTOFFPL}(E) = AE^{-\Gamma} \times e^{-E/E_{\mathrm{fold}}} \tag{5.6}$$

where Γ is the photon index and E_{fold} is the folding energy.

[3]http://heasarc.gsfc.nasa.gov/docs/xanadu/xspec/

Pulsars have also been fitted with PLCUT (e.g., White et al., 1983),

$$\mathrm{PLCUT}(E) = AE^{-\Gamma} \times \begin{cases} 1 & (E \leq E_{\mathrm{cut}}) \\ e^{-(E-E_{\mathrm{cut}})/E_{\mathrm{fold}}} & (E > E_{\mathrm{cut}}) \end{cases} , \tag{5.7}$$

where E_{cut} is the cutoff energy and the other parameters are the same as for CUTOFFPL. The observed spectrum is continuous due to bremsstrahlung radiation (see Chapter 5.4.1), however, at E_{cut} the CUTOFFPL model has a discontinuous turnover, which is sometimes a caveat as it can result in an artificial absorption-like feature in the spectral fit.

Tanaka (1986) developed an analytic continuum model with a continuous turnover,

$$\mathrm{FDCUT}(E) = AE^{-\Gamma} \frac{1}{1 + e^{(E-E_{\mathrm{cut}})/E_{\mathrm{fold}}}} . \tag{5.8}$$

Another model with a smooth curvature, developed by Mihara (1995), is the NPEX model,

$$\mathrm{NPEX}(E) = (A_1 E^{-\alpha_1} + A_2 E^{+\alpha_2}) e^{-E/E_{\mathrm{fold}}} , \tag{5.9}$$

where α_1 and α_2 are power law indices. When α_1 is fixed at 2, the model becomes an analytical approximation of a Comptonized continuum spectrum (Sunyaev & Titarchuk, 1980).

In this work, I applied the FDCUT model to describe the continua of the studied accreting pulsars as it provided the overall best fits for the sample spectra.

5.4.3 Pulse Profiles

The accretion column is composed of a "cap" (radiation shock), a "wall" (edge of the accretion column below the shock), and a "hot spot" (thermal mound at the bottom of the column). Radiation emitted from the cap, along the magnetic field lines, is known as pencil-beam emission; whereas radiation emitted from the wall

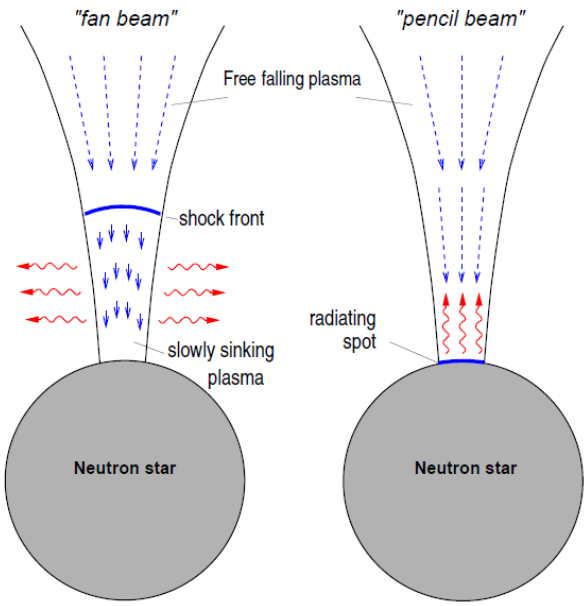

Figure 5.4: Schematic representation of the accretion column for different luminosity regimes and the pencil and fan beam radiation patterns. The left image shows how in the presence of a radiation dominated shock, the radiated emission has a fan-beam pattern (from the side of the column walls) combined with a pencil-beam pattern (from the cap). The image on the right shows the pencil-beam pattern which occurs only in the absence of a radiative shock (Kretschmar et al., 1996).

surface, perpendicular to the magnetic fields lines, is known as fan-beam emission (see Figure 5.4).

The pulse/spin period can be determined from the observed radiation flux modulations as a function of time (lightcurves). One can determine the pulse period of a neutron star by "folding" the lightcurve, i.e., dividing it into equal epochs using trial period values and then adding them over the same phase. Using this method, the most likely period is determined through a χ^2 test of deviations from a constant value. Pulse profiles can also be created through epoch folding. Pulse profiles are generally double-peaked due to the emission from both poles (Kraus et al., 2003; Caballero et al., 2011). The profiles of accreting pulsars are generally complex and they differ from source to source. Usually, the profile structure of accreting pulsars becomes simpler at higher energies and more complex at lower energies. As an

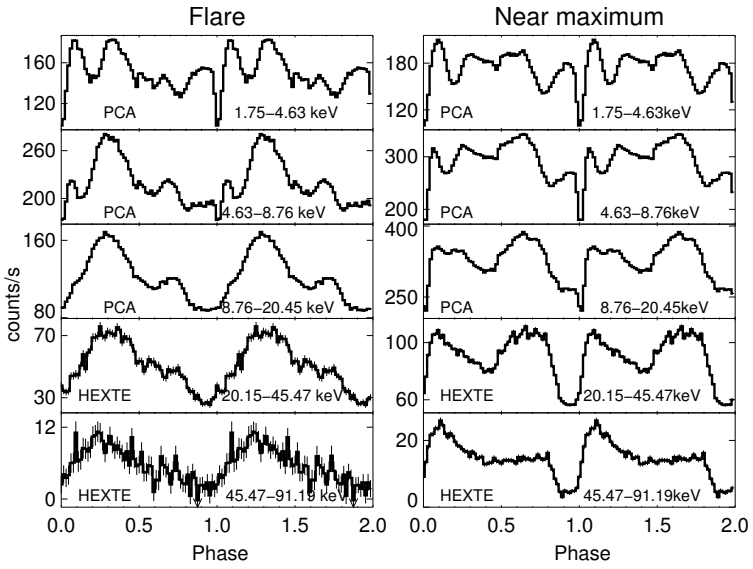

Figure 5.5: Example of a double-peaked pulse profile corresponding to the X-ray pulsar A 0535+26 in different energy bands obtained from *RXTE* observations Caballero et al. (2009, Figure 4).

example, Figure 5.5 by Caballero et al. (2009) shows the energy-dependent pulse profiles of the accreting pulsar A 0535+26.

5.4.4 Cyclotron Resonance Scattering Feature

Inside the neutron star accretion column, electrons that move perpendicular to the magnetic field B have quantized energy differences defined by the "12-B-12 rule",

$$\Delta E = \frac{1}{1+\mathrm{z}} 11.56\mathrm{keV} \times \left(\frac{B}{10^{12}\mathrm{G}} \right), \tag{5.10}$$

where z is the neutron star's gravitational redshift. These quantized energies are known as Landau quantum levels (see Chapter 4.1.3). Photons interact with these quantized electrons and are resonantly scattered out of the line-of-sight. This leads to a broad absorption-like feature in the spectrum known as a Cyclotron Resonance Scattering Feature (CRSF). Using Eqn. 7.1, the observed CRSF energies can be used to calculate the magnetic field strength of accreting pulsars. For typical accreting

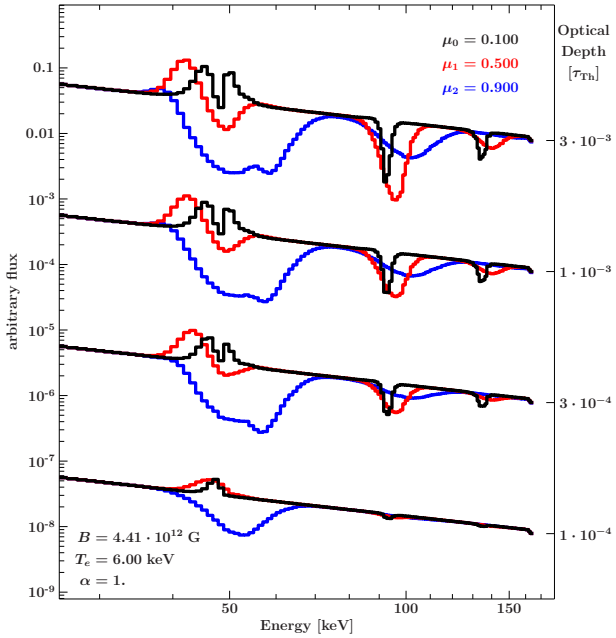

Figure 5.6: Simulated spectra of the Becker & Wolff (2007) continuum model convolved with a physical cyclotron line model developed by Schwarm (2010). The black and blue lines represent the photons that emerge almost perpendicular and parallel to the magnetic field, respectively (Schwarm et al., 2017b).

pulsar magnetic fields of 10^{12}–10^{13} G, cyclotron energies are expected to be found in the ∼12–120 keV, which is consistent with observations.

If the cyclotron energy is equal to the electron rest energy, pair production[4] takes place and CRSFs are not observed (Schönherr et al., 2007). This happens at the critical magnetic field,

$$B_{\mathrm{crit}} = \frac{m_{\mathrm{e}}^2 c^3}{e\hbar} \approx 4.4 \times 10^{13}\,\mathrm{G}. \tag{5.11}$$

The cyclotron feature is created somewhere below the radiation shock in the line-forming region. The height of the line-forming region changes with accretion rate (luminosity). Becker et al. (2012) studied observed correlations between the luminosity of accreting pulsars and their respective CRSF energies (Chapter 5.4.5).

[4]Pair production is the creation of an elementary particle and its antiparticle, e.g., an electron and a positron.

Physically modeling cyclotron features is an ongoing field of study (see, for example, Schönherr et al., 2007; Schwarm et al., 2017b,a). The photon energy due to resonant cyclotron scattering is difficult to derive as it depends on several factors, such as the path of the photon, the scattering cross sections, the optical depth of the outer layer of the accretion column, and the initial and final Landau energy levels of the electron transitions. Figure 5.6 shows the spectral shapes of simulated CRSFs for different optical depths of the outer layer of the accretion column (Schwarm et al., 2017b). Out of the ∼80 known X-ray pulsars, 18 have a cyclotron line feature (Caballero & Wilms, 2012).

Cyclotron lines are commonly fitted with the GABS and CYCLABS analytical functions,

$$M_{\rm CRSF}(E) = \begin{cases} {\rm GABS}(E) = \tau_{\rm c} e^{-(E-E_{\rm c})^2/(2\sigma_{\rm c}^2)} \\ {\rm CYCLABS}(E) = D_{\rm c} \frac{(W_{\rm c}E/E_{\rm c})^2}{(E-E_{\rm c})^2+W_{\rm c}^2} \end{cases} , \tag{5.12}$$

in which $E_{\rm c}$ is the cyclotron resonance energy, $\sigma_{\rm c}$ and $W_{\rm c}$ represent the line width, $\tau_{\rm c}$ is the resonance optical depth, and $D_{\rm c}$ is the line depth. Both functions modify the broadband continuum, $I_0(E)$,

$$I_0(E) \rightarrow I_0(E) e^{-M_{\rm CRSF}(E)} , \tag{5.13}$$

where $M(E)$ can be either 1) GABS(E) resulting in a line with a Gaussian optical depth profile, or 2) CYCLABS(E) resulting in a pseudo-Lorentzian profile. In most cases both models provide acceptable fits to the CRSF feature observed in the pulsar spectra. In this work, I applied the GABS model because, overall, it described the cyclotron resonant scattering features better than the CYCLABS model.

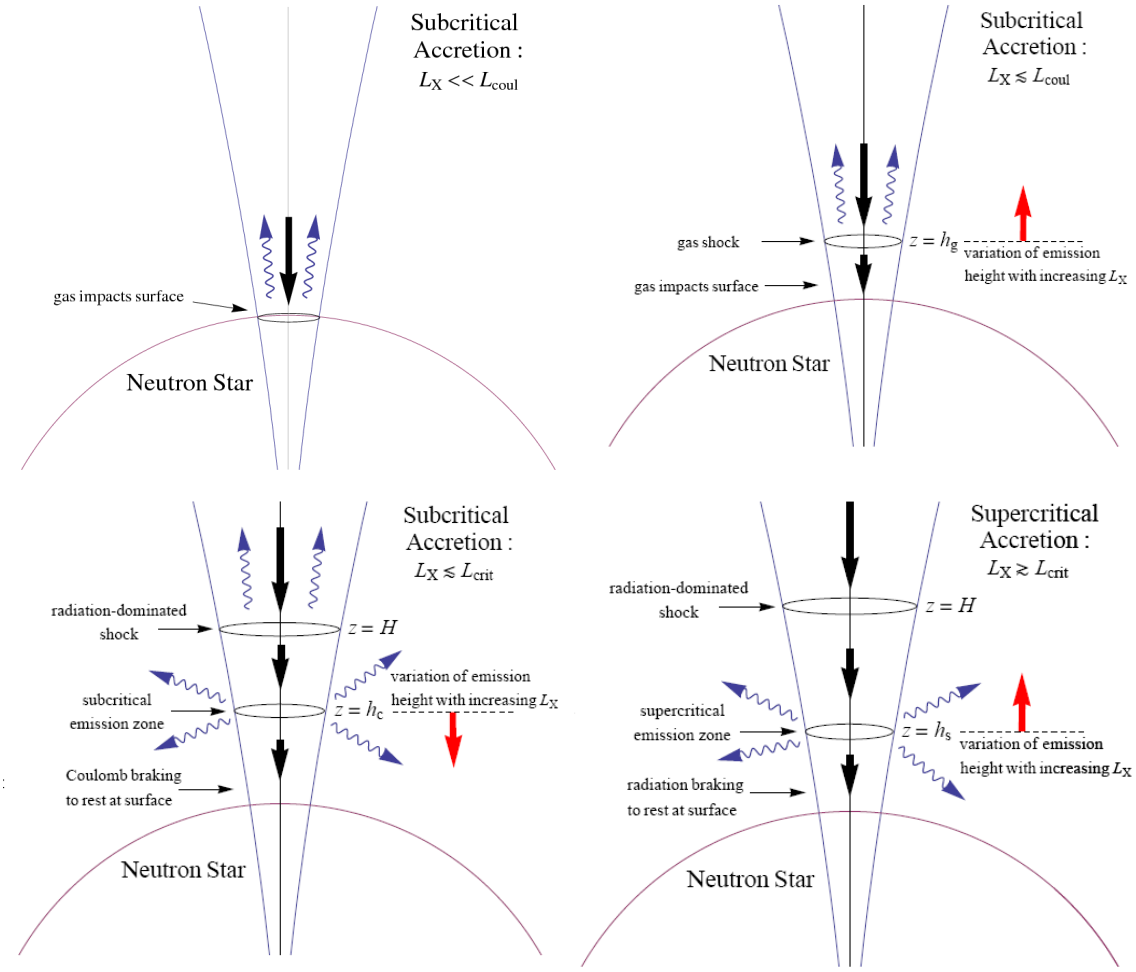

Figure 5.7: Variation of emission height as a function of luminosity in the subcritical (upper panels and lower left panel) and supercritical (lower right panel) regimes (Becker et al., 2012, Figure 1).

5.4.5 Cyclotron Line Energy and Luminosity Correlation

An interesting discovery related to accreting pulsars is the relationship between their X-ray luminosity and fundamental cyclotron line energy. Figure 5.8 shows how the L_X–E_{cycl} correlation was found to be negative for very high-luminosity sources, e.g. V 0332+53 (Tsygankov et al., 2006), 4U 0115+63 (Nakajima et al., 2006) and positive for lower-luminosity sources, e.g. Her X-1 (Staubert et al., 2007). However, there are very low-luminosity sources, e.g., A 0535+26 (Caballero et al.,

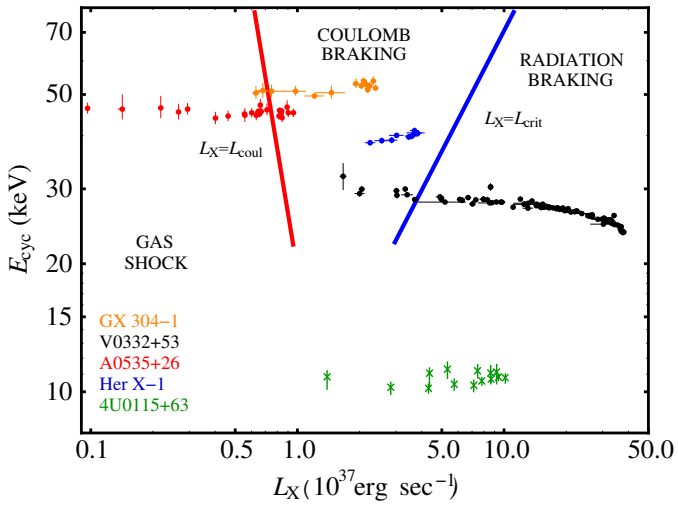

Figure 5.8: Source luminosity and cyclotron centroid energy bimodal correlation for observed sources as described by Becker et al. (2012). The red line is the Coulomb stopping luminosity and the blue line is the critical luminosity.

2007) and XTE J1946+274 (Marcu-Cheatham et al., 2015) which do not show significant variations in the cyclotron line energy. These correlations are believed to be due to different accretion regimes (Becker et al., 2012, and references therein).

Becker et al. (2012) also described how the mechanism via which the plasma in the accretion column is decelerated depends on the amount of in-flowing material. Therefore, the accretion regime is expected to change with luminosity. These regimes are categorized by their X-ray luminosity, L_X, relative to the critical luminosity, L_{crit}[5]:

- Supercritical Accretion ($L_X > L_{crit}$ shown in the bottom-right panel in Figure 5.7 and the "Radiation Braking" region in Figure 5.8) – The in-falling matter is decelerated from relativistic to subsonic speeds by the radiation-dominated radiative shock. Below the shock, the photons are trapped by advection and can escape only through the column walls, i.e., fan-beam emission (left image in Figure 5.4).

- Subcritical Accretion ($L_X < L_{crit}$) – The following accretion regimes depend

[5] L_{crit} is the local Eddington luminosity. See Becker et al. (2012) for more details.

on the source luminosity relative to the Coulomb stopping luminosity, $L_{\rm Coul}$:

- $L_{\rm X} > L_{\rm Coul}$ (top-right and bottom right panels in Figure 5.7 and "Coulomb Breaking" region in Figure 5.8) – The plasma still passes through a radiation-dominated shock, but Coulomb interactions inside the accretion column start contributing to decelerating the flow. Photons can escape through both the accretion column wall and cap (combination of fan- and pencil- beam emission).
- $L_{\rm X} < L_{\rm Coul}$ (top-left panel in Figure 5.7 and "Gas Shock" region in Figure 5.8) – The density of the plasma is too low for Coulomb deceleration. The material is in free fall at non-relativistic velocities and may pass through a gas-mediated shock before coming to a stop at the surface. The emission geometry for this regime is believed to be pencil beam (right image in Figure 5.4).

6

Observational Methods

This chapter contains a description of the instrumentation from which the data analyzed in this work was obtained. The primary telescope presented is the *Suzaku* satellite, while other instruments, such as *Swift*, *RXTE*, *Fermi*, and *INTEGRAL*, are briefly described.

6.1 *Suzaku*

6.1.1 Instruments

The primary data used for this analysis were provided by the *Suzaku* Japanese X-ray satellite (Figure 6.1), which was launched in 2005 July and ended

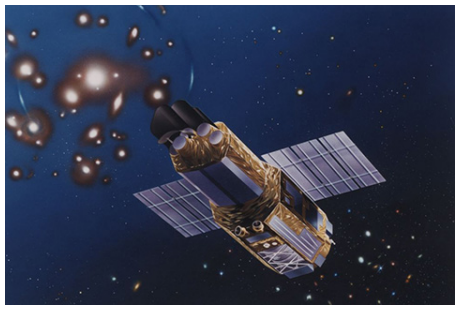

Figure 6.1: Artistic representation of the *Suzaku* satellite. Credit: JAXA.

its mission in 2015 August[1]. The instruments on board were the low-energy X-Ray Spectrometer (XRS Kunieda & Suzaku Team, 2005), the X-Ray Imaging Spectrometer (XIS, Koyama et al., 2007) and the Hard X-ray Detector (HXD, Takahashi et al., 2007). The XRS was initially the primary instrument, but it was shut down in 2006 due to a loss of liquid helium in its cooling system (Mitsuda et al., 2007). *Suzaku*'s instruments had very high sensitivity and provided a broad-band coverage ranging from soft X-rays (0.2 keV) to γ-rays (600 keV). A schematic of the satellite and its instruments is shown in Figure 6.2.

The X-ray Telescopes (XRT, located in front of XIS) had a resolution of 1.8'–2.3'. XIS was the main instrument and its sensitivity lied between 0.2 keV and 12 keV, with a field of view (FOV) of 18'×18'. XIS had four CCD chips (0,1,2,3), but XIS 2 stopped functioning in 2006. Each of these four units had 1024×1024 pixels with a pixel size of 24 μm. The full CCD imaging area was 25 mm^2. XIS 0 and 3 were front-illuminated (FI), while XIS 1 was back-illuminated (BI). The XIS effective areas are 340 cm^2 (FI), 390 cm^2 (BI) at 1.5 keV. In order to minimize the amount of telemetry data, each chip had a 2×2, 3×3 or 5×5 pixel editing mode, for high or low fluxes (see *Suzaku* technical description[2]). The XIS energy resolution was 130 eV at the Mn Kα emission line energy (5.9 keV) from the ^{55}Fe calibration sources present in two corners of each CCD. The XIS is efficient at observing weak and extended X-ray sources due to its low background X-ray emission. Its high broad-band spectral sensitivity and imaging capability make XIS very effective for broad-band spectral analysis. For more details on the XIS instrument, see Koyama et al. (2007).

The XIS CCDs readouts were either full, 1/4, or 1/8 window modes with readout times of 8 s, 4 s and 1 s, respectively. The 1/8 mode was not generally used, the full window was used for dim and moderately bright sources and the 1/4 mode was used for bright sources to reduce pile-up. The pile-up effect occurs in imaging

[1] http://global.jaxa.jp/press/2015/08/20150826_suzaku.html
[2] www.astro.isas.jaxa.jp/suzaku/doc/suzaku_td/

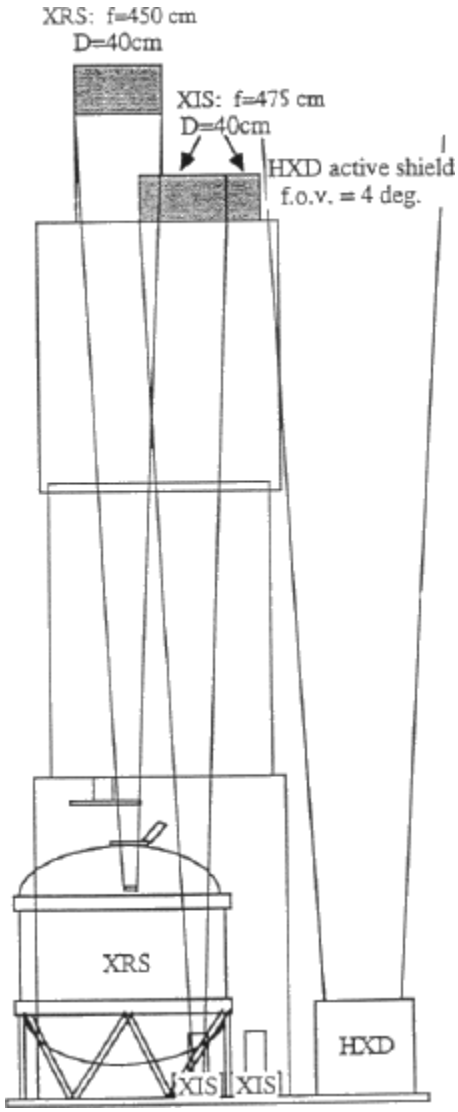

Figure 6.2: Schematic side-view of the *Suzaku* instrument configuration where the three instruments can be seen: XRS -not functional- on the left side, XIS, in the middle, and HXD on the right. Credit: *Suzaku* Team.

instruments when two or more photons hit a detector pixel during one readout cycle. As a result, the pixel reads one photon with a high energy (Davis, 2001). This effect hardens the source spectrum and may lead to incorrect measurements. For further reduction of very bright sources, *Suzaku* had a burst mode option available to avoid pile-up. In burst mode, the exposure time within the readout cycle was reduced. However, we found that in most of the observations (in burst or normal mode), the

sources were bright enough to experience pile-up. Therefore, the employed solution involved the removal of the bright central region of the Point Spread Function (PSF) in the XIS image where the pile-up effect was observed.[3] For more details on the pile-up reduction for each of the observations, see Chapter 8.

The HXD instrument was a collimated detector with a sensitivity range of 10-600 keV. It was composed of 16 units, each with two types of detectors: Positive Intrinsic Negative (PIN) silicon diodes and Gadolinium Silicate crystal scintillators (GSO), for lower and higher energies, respectively. As HXD is not an imaging instrument, the PIN and GSO backgrounds were modeled by the *Suzaku* team[4]. The PIN background consisted of ∼5% Cosmic X-ray Background (CXB) and ∼95% Non X-ray simulated time-variable particle modeled Background (NXB). Since GSO was not very sensitive for sources weak above 40 keV, GSO data were not used in this study. The HXD detectors had a 61 μs time resolution, making them effective for timing analysis (see Chapter 7). The effective are of the PIN instrument (which is used for this analysis) is ∼160 cm^2 at 20 keV, ∼260 cm^2 at 100 keV.

6.1.2 Data Reduction Basics

The *Suzaku* data was extracted and reprocessed following the *Suzaku* Data Reduction Guide[5] and using the HEASOFT analysis package[6]. The event files available were calibrated and screened by the *Suzaku* team. I conducted a recalibration and ran a secondary screening process using the *Suzaku* processing pipeline.

Figure 6.3 shows an example of an XIS CCD image. The source and background events for images, spectra, and light curves were extracted from selected source and background regions. I also performed additional corrections: (1) I

[3]More details about pile-up estimates and extraction can be found at http://space.mit.edu/cxc/software/suzaku/pest.html

[4]ftp://legacy.gsfc.nasa.gov/suzaku/data/background

[5]heasarc.gsfc.nasa.gov/docs/suzaku/analysis/abc/

[6]http://heasarc.gsfc.nasa.gov/docs/software/lheasoft/

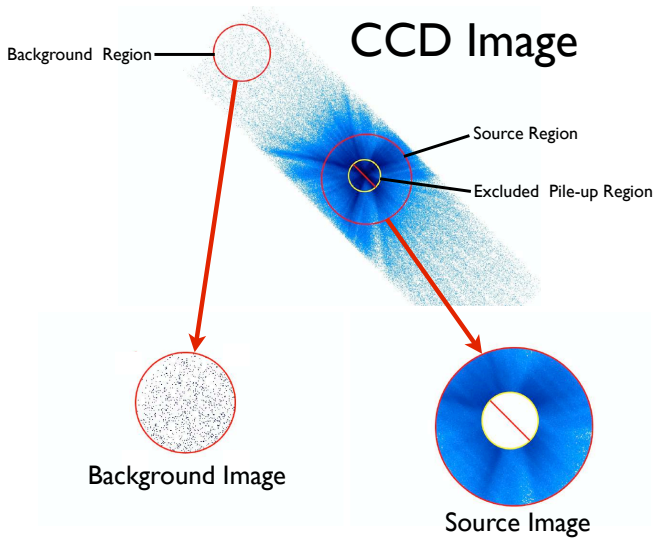

Figure 6.3: Example of an extraction of source and background events from an XIS image of Vela X-1. The original image of the point spread function of the source detected by XIS 0, 3×3 in a 1/4 window mode is shown in the upper half (the diagonal image). From this image, a source region is chosen from which source events are extracted. For bright sources, the pile-up region at the center is excluded, and the final image used for extraction is shown in the bottom right corner. The background image is selected from an area far from the source, and the final image from which background events are extracted is shown in the bottom left corner.

excluded the pile-up in the center of the XIS image where necessary, (2) I corrected for HXD's "dead-time" (the processing time after a detection when no events are being registered) using the count rate of pseudo events that are produced by the HXD analog electronics and are generated every 4 s, and (3) for the timing analysis, I changed the time of the events to the barycenter of the solar system. Binary star corrections[7] were not necessary because, in most cases, the *Suzaku* observation times were significantly shorter than the orbital periods of the observed sources. Therefore, the orbital motion had a negligible effect on the event times. The exceptions were Cen X-3 and Vela X-1 for which the observation times were long compared to their

[7] A binary star correction involves correcting the event times to account for the orbital motion of the neutron star in the binary system. These corrections are necessary when conducting a detailed timing analysis.

orbital periods. However, since I only performed a spectral analysis on Cen X-3 and Vela X-1, the binary star time correction was not necessary.

6.2 Other X-Ray Instruments

Data from other X-ray instruments were also used for the orbital termination of the XRB XTE J1946+274 presented in Chapter 7.3.3. The instruments are described below and the observations studied from each instrument are listed in Table 7.1. In addition to the analysis of XTE J1946+274, data from the *Swift*-BAT instrument were also used to obtain lightcurves for the sources analyzed in Chapter 8 (see Section A.1).

- *Swift* is a NASA satellite, launched in 2004 November, which is mainly focuses on studying X-ray bursts (Gehrels et al., 2004). The *Burst Alert Telescope* (BAT, Barthelmy et al., 2005) detector on board of *Swift* is a detector composed of photo diodes, and its purpose is to monitor sources in the hard X-ray energy band (15–150 keV). The X-Ray Telescope (XRT, Burrows et al., 2005) is a CCD-focusing detector that measures fluxes and spectra in the soft X-ray band (0.2–10 keV).

- *The Rossi X-ray Timing Explorer Mission* (*RXTE*) is also a NASA satellite active between 1995 December and 2012 January. Its *Proportional Counter Array* detector (PCA, Jahoda et al., 2006) consisted of five *Proportional Counter Units* (PCUs), which detected X-rays in the 3–50 keV energy range. *RXTE*'s *High Energy Timing Experiment* (HEXTE, Rothschild et al., 1998) detector was composed of two cluster instruments, each consisting of four scintillators and it observed hard X-ray emission in the 15–250 keV range. PCA and HEXTE had very high timing resolutions, 0.001 ms and 0.0076 ms, which made them ideal for pulsar timing studies.

- The *Fermi Gamma-ray Space Telescope* launched in 2008 June and it is the

result a collaborative project between the U.S. (NASA), Europe, and Japan. The *Gamma-ray Burst Monitor* detector (GBM, von Kienlin et al., 2004; Meegan et al., 2007, 2009) is composed of 12 sodium iodide scintillators and two Bismuth Germanate scintillators. GBM can detect energies as low as 8 keV and has been widely used for the study of the spin period evolution of accreting pulsars (see *Fermi* Pulsar Project[8]).

- The INTErnational Gamma-Ray Astrophysics Laboratory (*INTEGRAL*) is an European Space Agency (ESA) imaging satellite launched in 2002, used for broadband spectroscopy and detection of hard X-rays up to Gamma-rays. The *INTEGRAL Soft Gamma-Ray Imager* (ISGRI, Lebrun et al., 2003) is composed of cadmium telluride semiconductor pixels and observed energies ranging from hard X-rays to soft γ-rays (15 keV–1 MeV).

Published results from data of additional instruments were used for comparions. For the studies of the Fe line and the cylotron line-luminosity correlation, I used *INTEGRAL* data results by Müller et al. (2012), and *RXTE* data results by Heindl et al. (2001), respectively. For the correlations between the empirical parametes, I used *RXTE* results by Coburn et al. (2002), while for the correlations between the physical parameters, I used *BeppoSAX* data results by Farinelli et al. (2016) and *NuSTAR* data results by Wolff et al. (2016), respectively.

[8]https://gammaray.nsstc.nasa.gov/gbm/science/pulsars.html

7

XTE J1946+274

XTE J1946+274 is a transient X-ray binary consisting of a Be-type star and a neutron star with a 15.75 s pulse period in a 172 days orbit with 2–3 outbursts per orbit during phases of activity. This source has been oberved in outburst only twice, in 1998 and 2010.

In this chapter, I present a detailed temporal and spectral analysis of a *Suzaku* observation taken during the 2010 outburst series. Chapter 7.1 contains background information regarding the source, while Chapter 7.2 describes the *Suzaku* observation, the data extraction, and the data processing procedure. Chapter 7.3 presents the temporal analysis: (i) an improved pulse period measurement (using the *Suzaku*-PIN data which has very high timing resolution), (ii) the pulse profile analysis and comparison with *RXTE*-PCA taken at an earlier time during the same outburst series, and (iii) an improved measurement of the orbital parameters using data from multiple instruments. Chapter 7.4 contains the detailed broad-band spectral analysis of XTE J1946+274, where the X-ray continuum is described with a Fermi-Dirac cutoff power-law empirical model. Lastly, in Chapter 7.5 I discuss the results of the temporal analysis and the spectral analysis and how these results provide information regarding the accretion regime.

The material presented in this chapter is based on the paper "The Transient

Accreting X-Ray Pulsar XTE J1946+274: Stability of X-Ray Properties at Low Flux and Updated Orbital Solution" published in the *Astrophysical Journal* (Marcu-Cheatham et al., 2015, ApJ, 815, 44), for which I was the primary investigator. The analysis presented in Chapter 7.3.3 was performed by Dr. Matthias Kühnel (now Matthias Bissinger) at the Dr. Karl Remeis-Observatory at University of Erlangen-Nuremberg (Bamberg, Germany).

7.1 Introduction

The X-ray pulsar XTE J1946+274 was discovered during a three-month long outburst in 1998 September by the All-Sky Monitor (ASM) on the *Rossi X-Ray Timing Explorer* (*RXTE*) (Smith & Takeshima, 1998). Pulsations with a period of 15.83 s were first detected by Wilson et al. (1998) using data from the Burst And Transient Source Experiment (BATSE) on board the *Compton Gamma-Ray Observatory* (*CGRO*). XTE J1946+274 was found to be a High Mass X-ray Binary (HMXB) with a Be IV/IVe stellar companion (Verrecchia et al., 2002). Wilson et al. (2003) determined an orbital period of 169.2 days, an orbital inclination of $\sim 46°$, and a distance of 9.5 ± 2.9 kpc using *RXTE* and BATSE data. Between 1998 and 2001, XTE J1946+274 experienced an outburst approximately every half-orbit: Campana et al. (1999) observed periodic flaring of the X-ray source repeating every $\sim$80 days. Between 1999 September and 2000 July, the outbursts were monitored with the Indian X-ray Astronomy Experiment (IXAE) and the data were analyzed by Paul et al. (2001). Paul et al. (2001) and Wilson et al. (2003) presented pulse profiles with double-peaked structures.

The strong magnetic field ($\sim 10^{12}$ G) of the neutron star enforces collimated accretion along the field lines and quantizes the electron energy states perpendicular to those field lines. When X-ray photons in the column interact through resonant scattering with these quantized electrons they produce an absorption-line-like feature

observed in the spectrum at the energy

$$E \approx \frac{11.56\,\mathrm{keV}}{1+z}\left(\frac{B_{\mathrm{NS}}}{10^{12}\mathrm{G}}\right) \tag{7.1}$$

where B_{NS} is the surface magnetic field, and z is the gravitational redshift, which is ~ 0.3 for typical neutron star parameters, and a line-forming region close to the surface. This is known as a CRSF, which, as can be seen in equation (7.1), can be used to determine the magnetic field strength of highly magnetized pulsars. The first spectral analysis of XTE J1946+274 was performed by Heindl et al. (2001) using pointed *RXTE* data from the first observed outburst in 1998. They found evidence for a CRSF with a centroid energy of $\sim$36 keV corresponding to a B-field of $3.1(1+z)\times 10^{12}$ G.

After 2001 October the source was quiescent until 2010 June. Starting 2010 June 4 the Burst Alert Telescope (BAT) on board of *Swift* and the Gamma-ray Burst Monitor (GBM) on board of *Fermi* observed a new strong outburst (Finger, 2010; Krimm et al., 2010). The BAT light curve (Figure 7.1) shows that this $\sim$140 mCrab outburst was followed by four outbursts at about half the flux at intervals of approximately 82, 75, 73, and 57 days. This behavior is similar to that observed by Campana et al. (1999) for the 1998–2001 outburst series.

Caballero et al. (2010) found no sign of the CRSF at 35 keV in a preliminary analysis of *INTErnational Gamma-Ray Astrophysics Laboratory (INTEGRAL)* data of the first 2010 outburst. Using *RXTE* and *INTEGRAL* data from the first outburst in 2010 June–July and *Swift*, *RXTE*, and *INTEGRAL* data from the third outburst in 2010 November–December, Müller et al. (2012) reported the possible presence of a CRSF at 25 keV (1.81σ significance).

An iron (Fe) Kα fluorescent line at 6.4 keV is present in the spectra. Müller et al. (2012) reported a correlation between the Fe Kα line flux and the 7–15 keV continuum flux.

In this Chapter we present a temporal and spectral analysis of *Suzaku* data

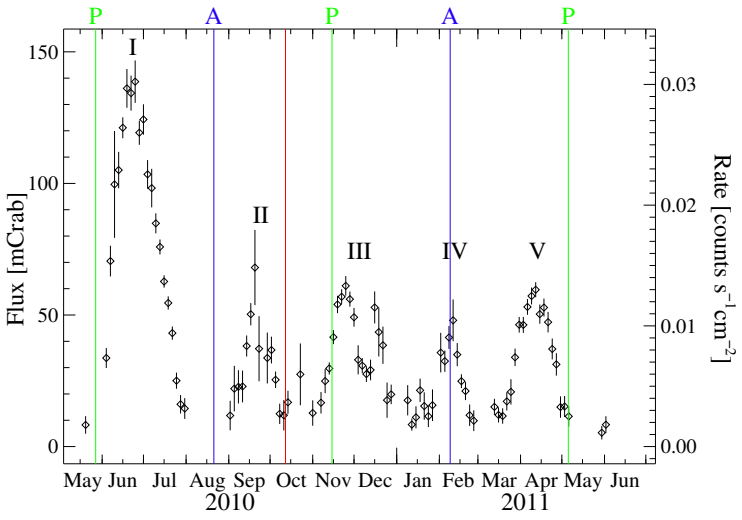

Figure 7.1: *Swift*-BAT 15–50 keV XTE J1946+274 light curve of the series of outbursts in 2010–2011 with a binning of 3 d, showing all bins with S/N$\gtrsim$2; the vertical red line represents the time of the *Suzaku* observation. The apastron (blue lines marked with "A") and periastron (green lines marked with "P") times were determined with the new orbital solution (see §7.3.3). The outbursts are marked I–V. The data were obtained from http://swift.gsfc.nasa.gov/results/transients/.

taken during the end of the second 2010 outburst (red line in Figure 7.1) that allows for a spectral analysis at the lowest flux to date. Due to its high broad-band X-ray sensitivity and its imaging capability, *Suzaku* is an ideal instrument for analyzing broad-band spectra and spectral features (iron lines and CRSFs) for sources at very low fluxes. A first temporal and spectral analysis of the same 2010 *Suzaku* data was conducted by Maitra & Paul (2013a) who reported the presence of a broad CRSF at $\sim$38 keV[1]. The analysis we present here differs significantly from theirs, regarding the spectral analysis itself as well as the breadth of the discussion. The differences between our modeling choices are further explained in §7.4. The CRSF width of $\sim$9 keV found by Maitra & Paul (2013a) is rather broad and could indicate a contribution to modeling the continuum (for a demonstration of this effect see Müller et al., 2013b). In addition the source is not consistently detected above

[1]Note that Maitra & Paul (2013a) quote the resonance energy of a pseudo-Lorentzian line shape, the energy of the minimum of the line shape that is comparable to the CRSF energy values quoted elsewhere in this Chapter is $\sim$40 keV (see page 94 of Mihara, 1995, and Enoto et al. 2008).

38 keV in all spectral bins, even if broadly rebinned (large uncertainties have also been noted by Maitra & Paul, 2013a). This is also the reason why we, contrary to Maitra & Paul (2013a), do not conduct a pulse phase resolved analysis of the CRSF parameters. Though not excluded, the 38 keV line is thus an unlikely CRSF candidate. As we show in §7.4 there is a possibility that a less broad line is present at ∼35 keV instead.

The 2010–2011 outburst series was also monitored by *Fermi*-GBM. Together with the available *RXTE*, *Swift*, and *Suzaku* data, these observations allow us to refine the orbit parameters.

In §7.2 we describe the *Suzaku* data and the data reduction procedure, and provide an overview of the additional multi-instrument data used in our analysis. In §7.3 we first examine the *Suzaku* light curves and hardness ratios. We then determine the local pulse period and the energy resolved pulse profiles which we compare with those observed with *RXTE*-PCA during the bright first outburst of 2010. Last, but not least, we present the improved orbital solution. In §7.4 we present the broad-band *Suzaku* spectral analysis. In §7.5 and §8.5 the results are discussed and summarized, respectively.

7.2 Observation and Data Reduction

We study a ∼50 ks *Suzaku* observation that occurred on 2010 October 11–13 (ObsID 405041010), during a minimum between the second and third outburst of the 2010 outburst series, when the 15–50 keV flux was ∼10 mCrab. We extracted data obtained with the X-ray Imaging Spectrometer (XIS, Koyama et al., 2007), and the PIN instrument from the High X-ray Detector (HXD, Takahashi et al., 2007). The three functional units of the XIS (CCD cameras 0, 1, and 3) were operated in the 1/4 window mode during the observation in order to reduce pile up. Data from the Gadolinium Silicate Crystals (GSO, also part of HXD) were excluded due to the weakness of the source above 40 keV.

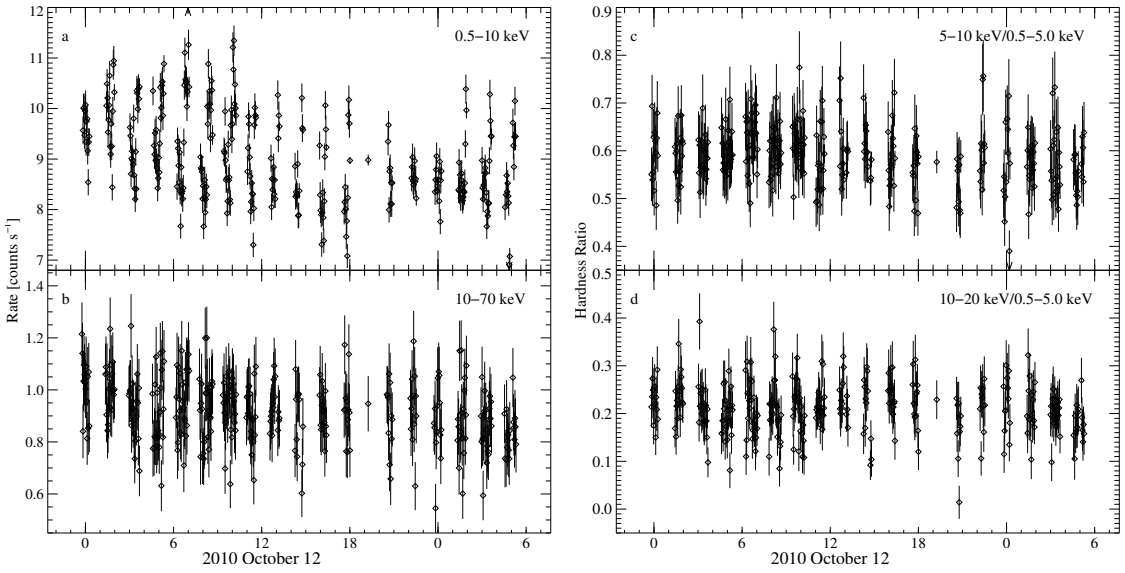

Figure 7.2: (a) Light curve of summed XIS 0, 1, and 3 count rates (0.5–10 keV). (b) Dead-time corrected PIN light curve (10–70 keV). Both light curves are background subtracted and binned to 128 s. (c) Hardness ratio evolution for count rates in the energy bands 5–10 keV and 0.5–5 keV using XIS 3. (d) Hardness ratio evolution for count rates in the energy bands 10–20 keV and 0.5–5 keV using PIN and XIS 3.

We reprocessed the XIS and PIN data and extracted data products following the *Suzaku* Data Reduction (or ABC) Guide (ISAS/JAXA & X-ray Astrophysics Laboratory NASA Goddard Space Flight Center, 2013). The reprocessing was performed using `aepipeline`, applying the newest calibration as well as standard data screening (with the default screening criteria). This was done based on the `HEASOFT` v6.13 software package and the calibration database (`CALDB`) releases HXD-20110913, XIS-20130305 and XRT-20110630. We further filtered the screened XIS events in order to exclude times of telemetry saturation. The events for both XIS and PIN were transferred to the barycenter of the solar system with `aebarycen`.

Using `xselect`, we first extracted XIS images, to which we applied an attitude correction with `aeattcor2`, which further corrects the attitude data for thermal wobbling using mean event positions as a function of time. After comparing the images obtained with and without applying `aeattcor2`, we concluded that the additional attitude correction does not improve the moderate systematic attitude

instability which is visible in the images through an elongated and double-peaked point spread function (PSF, see Maeda, 2010a,b,c, for further discussions of this effect). As we will show in §7.3.1, the systematic attitude wobble has negligible effect on the spectral shape.

XIS source and background event files, light curves and spectra were produced using `xselect` after selecting the extraction regions in the XIS image. For bright sources, this step involves the determination of possibly existing pile-up using `pileest`. For XTE J1946+274 the pileup fraction was $< 4\%$ in the center of the PSF, thus the source was not bright enough to cause strong pile-up during this observation. We used the same source extraction region for the three XIS units and the two editing modes alternately used for event storage ("3×3" and "5×5"): a circle with a radius of 120 pixels ($124\farcs8$) centered on the PSF. The circle is large enough to contain most of the source events but not larger than the window. The background regions were circles with radii of 95 pixels ($98\farcs8$), located within the windows, but as far from the PSFs as possible. XIS 0 has a strip of unusable, masked pixels near the edge of the detector and therefore our XIS 0 background region additionally avoided this zone (Tsujimoto et al., 2010a).

The XIS source and background light curves were extracted with 128 s resolution in the energy bands 0.5–5 keV, 5–10 keV, and 0.5–10 keV. Since the orbital period of the neutron star (172 d) is significantly larger than the duration of the observation (50 ks), we did not perform a binary star orbit correction. The XIS spectra were binned to a resolution close to the half-width half-maximum of the spectral resolution of the instrument (Nowak et al., 2011). To generate the energy and ancillary responses we used the `xisrmfgen` and `xissimarfgen` tools, respectively. The exposure time for each XIS CCD is $\sim$50 ks, while the average source count rates are $\sim$3.05 counts s^{-1} for XIS 0, $\sim$2.80 counts s^{-1} for XIS 1, and $\sim$3.48 counts s^{-1} for XIS 3.

For PIN we applied energy filtering (10–20 keV, 20–40 keV, 40–70 keV and

10–70 keV) to the event files obtained after running `aepipeline`, after which we extracted light curves with `hxdpinxblc` with a time binning of 128 s. This tool produces the total dead-time corrected PIN light curve, the non X-ray background light curve, and the background-subtracted source light curve. We used `hxdpinxbpi` for the PIN spectral extraction which provides the dead-time corrected PIN source spectrum and the Non X-ray Background (NXB) and Cosmic X-ray Background (CXB) spectra. Approximately 5% of the PIN background are CXB and the corresponding spectrum is simulated based on the description by Boldt (1987). The NXB light curve and spectrum produced by the extraction tools are based on modeled events available for each individual observation[2]. For the spectral modeling we used the summed NXB and CXB background. The appropriate response file for the specific calibration epoch was chosen (`ae_hxd_pinhxnome9_20100731.rsp`). For the PIN spectra we applied a binning of a factor of 2 for the energy range 34–40 keV. The exposure time for PIN is ∼43 ks, while the total average source count rate is $\sim 0.90\,\mathrm{counts\,s^{-1}}$.

In addition to these *Suzaku* data we also used XTE J1946+274 data from other instruments. The pulse profile comparison in §7.3.2 presents the *Suzaku*-XIS and *Suzaku*-PIN data together with *RXTE*-PCA data from the peak of the first outburst in 2010. The orbit determination in §7.3.3 is based on the complete 2010 outburst series. The majority of pulse period measurements is provided by the *Fermi*-GBM Pulsar Project[3] while also including *Suzaku*-PIN, all available *RXTE*-PCA, and *Swift*-XRT data. In §7.5 we compare *Suzaku* results with results from Heindl et al. (2001) and Müller et al. (2012) obtained with *RXTE*, *Swift*, and *INTEGRAL*. For all observations used in our analysis, the instruments that performed them, their observation times, and their exposure times are listed in Table 7.1.

[2] `ftp://legacy.gsfc.nasa.gov/suzaku/data/background/pinnxb\_ver2.0\_tuned/2010\_10/ae405041010\_hxd\_pinbgd.evt.gz`

[3] http://gammaray.nsstc.nasa.gov/gbm/science/pulsars/

Table 7.1: XTE J1946+274 Multi-Instrument Observations

Satellite Instrument	Observation time	Number of Observations Total exposure time
Fermi GBM	2010 Dec 16 – 2011 May 1 1^{st} – 5^{th} outbursts in 2010	monitoring
RXTE PCA, HEXTE[a]	1998 Sept 16 – 1998 Oct 14 1^{st} outburst in 1998	12 observations ∼30 ks
RXTE PCA[b]	2010 Jun 20 – 2010 Jul 16 1^{st} outburst in 2010	17 observations ∼60 ks
RXTE PCA[b]	2010 Nov 23 – 2010 Dec 07 3^{rd} outburst in 2010	9 observations ∼23 ks
Swift XRT[b]	2010 Nov 26 – 2010 Dec 28 3^{rd} outburst in 2010	8 observations ∼16 ks
INTEGRAL ISGRI[b]	2010 Jun 20 – 2010 Nov 30 1^{st} & 4^{th} outbursts in 2010	5 observations ∼150 ks
Suzaku XIS, PIN[c]	2010 Oct 11–13 end of 2^{nd} outburst in 2010	1 observation ∼50 ks

[a] Heindl et al. (2001, their Table 1); [b] Müller et al. (2012, first sentence of notes on their Table 1); [c] this work (Chapter 7.2).

7.3 Temporal Analysis

7.3.1 *Suzaku* Light Curves and Hardness Ratios

Figures 7.2a and 7.2b show the background subtracted light curves for the summed count rates of XIS 0, 1 and 3 (0.5–10 keV) and for the PIN count rate (10–70 keV), respectively. According to the *Swift*-BAT light curve in Figure 7.1, the *Suzaku* observation was performed at the end of a decreasing long-term flux trend. This appears to be consistent with the PIN light curve, which might show a moderate decline from $1.06 \pm 0.03\,\mathrm{counts\,s^{-1}}$ in the first satellite orbit of the observation to $0.86 \pm 0.03\,\mathrm{counts\,s^{-1}}$ in the last one. There are no significant flares or dips observed. The XIS light curve displays jumps between two count rate levels for most *Suzaku* orbits. The effect can be observed in all three XIS units individually,

and it is consistent with the systematic attitude instability mentioned in §7.2. This is aggravated by the HXD aim-point used for this observation, since it is slightly off-center on the XIS chips.

Figures 7.2c and 7.2d show hardness ratio evolutions for count rates in the energy bands 5–10 keV and 0.5–5 keV and for count rates in the energy bands 10–20 keV and 0.5–5 keV, respectively. We observe little structure related to the systematic attitude instability in the XIS-PIN band ratios, and no structure in the XIS-XIS band ratios. Since there are no significant source related flux or hardness changes over the observation, we do not perform a time resolved spectral analysis but model the observation averaged spectra in §7.4.

7.3.2 Pulse Period and Pulse Profiles

The XIS has a time resolution of 2 s when in 1/4 window mode, while the PIN has a resolution of 61 μs (ISAS/JAXA & X-ray Astrophysics Laboratory NASA Goddard Space Flight Center, 2015). Therefore, only the PIN data were used for the pulse period determination. Applying epoch folding (Leahy et al., 1983; Schwarzenberg-Czerny, 1989) to the screened, barycenter-corrected, non-background subtracted PIN events, in the 10–40 keV range, we determined a local pulse period of 15.750025(27) s. The uncertainty was estimated using Monte Carlo light curve simulations as described in §7.3.3.

Based on this period and a reference time of MJD 55481.714 for phase 0, we obtained pulse profiles in several energy bands by folding the screened, barycenter-corrected events using 8 phase bins for XIS (0.5–5 keV and 5–10 keV; note that the *Suzaku*-XIS pulse profiles presented by Maitra & Paul (2013a) are oversampled) and 128 phase bins for PIN (10–20 keV, 20–40 keV and 40–70 keV). Figure 7.3 shows that up to 40 keV the pulse profiles are consistent in general structure: they are double-peaked, with a deep ($\phi \sim 0.35$) and a shallow minimum ($\phi \sim 0.9$). In the 10–20 keV range an additional narrow peak feature is visible ($\phi \sim 0.2$) before the

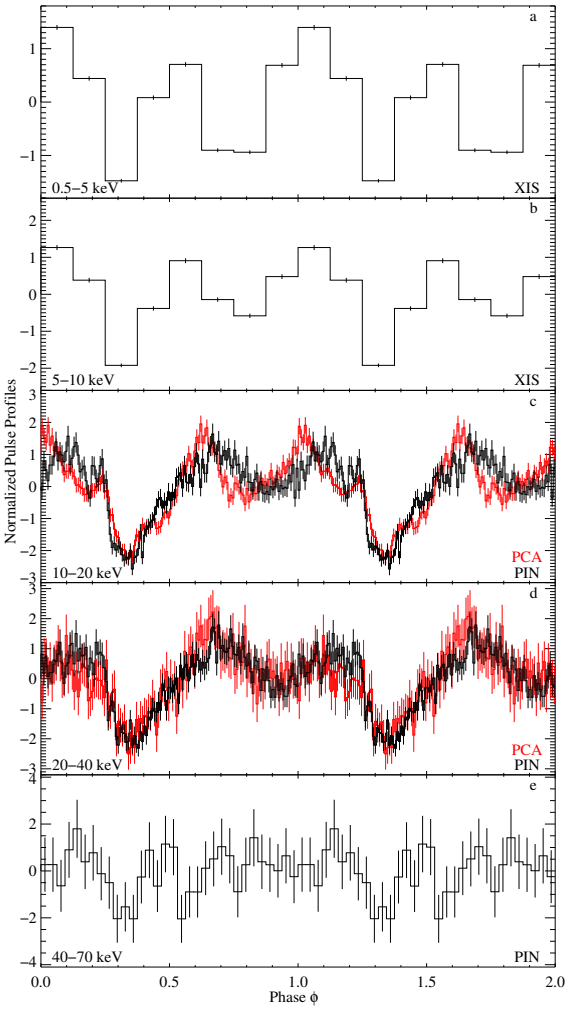

Figure 7.3: Energy resolved *Suzaku* and *RXTE* pulse profiles for the respective instruments and energy rages: (a) XIS 3, 0.5–5 keV, (b) XIS 3, 5–10 keV, (c) PIN (in black) and PCA (in red), 10–20 keV, (d) PIN and PCA, 20–40 keV, (e) PIN, 40–70 keV. The *RXTE*-PCA pulse profiles are from the peak of the bright first outburst in 2010 June (see §7.3.2 for further discussion). The number of phase bins for XIS, PIN and PCA is 8, 128, and 128, respectively, with the exception of 32 for the 40–70 keV PIN range. The period values the *Suzaku* and *RXTE* events were folded on are 15.750025 s (this work) and 15.764 s (Müller et al., 2012), respectively. The profiles were normalized to show standard deviations above the mean.

deep minimum. The shallow minimum is deeper at energies $\lesssim$5 keV than at higher energies. Similar behavior was found by Wilson et al. (2003) during two outbursts observed with *RXTE*-PCA in 1998 and 2001. We determined the pulse fractions

measured with PIN as the difference between the maximum and minimum count rates of the profiles normalized by mean count rate, and obtained values of 1.02 ± 0.09 and 1.04 ± 0.12 for the 10–20 keV and 20–40 keV energy ranges, respectively. Wilson et al. (2003) found pulsed fractions as high as 0.74 in the 2–30 keV range during low-flux outbursts in 2001. No pulsations are visible in the 40–70 keV *Suzaku* profile.

Figures 7.3c and 7.3d include a comparison for the 10–20 keV and 20–40 keV energy bands between the *Suzaku*-PIN pulse profiles from 2010 October 12 (end of the second outburst) and the *RXTE*-PCA pulse profiles from 2010 June 26 (ObsID 95032-12-02-00, peak of the first outburst). The latter were obtained using the same light curve extraction criteria as Müller et al. (2012) used for the full PCA energy band and applying epoch folding with the local period of 15.764 s determined by their analysis. This comparison emphasizes that the shapes of the profiles obtained from the two instruments are very similar, especially at higher energies, despite the large difference in flux:

$$\text{10–20 keV flux} : \begin{cases} 1.57 \times 10^{-9}\,\mathrm{erg\,s^{-1}\,cm^{-2}} & \text{PCA}, \\ 2.10 \times 10^{-10}\,\mathrm{erg\,s^{-1}\,cm^{-2}} & \textit{Suzaku}, \end{cases}$$

$$\text{20–40 keV flux} : \begin{cases} 1.12 \times 10^{-9}\,\mathrm{erg\,s^{-1}\,cm^{-2}} & \text{PCA}, \\ 1.30 \times 10^{-10}\,\mathrm{erg\,s^{-1}\,cm^{-2}} & \textit{Suzaku}. \end{cases}$$

The *Suzaku* fluxes were derived from the spectral best fit model presented in §7.4.1 and the *RXTE*-PCA fluxes from the spectral best fit of the averaged observations during the peak of the first outburst (epoch 1 fit of Müller et al., 2012).

7.3.3 Orbit Determination

The observed pulse period over time as measured by an observer is due to the intrinsic spin-up or spin-down of the neutron star, caused, e.g., by accretion torques, and on due to the Doppler shift by orbital motion. Usually the Doppler shift

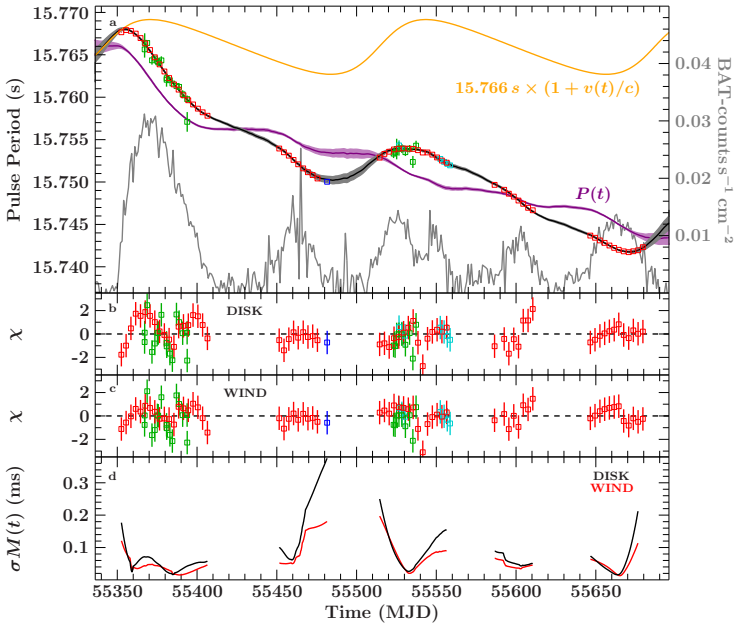

Figure 7.4: Orbit determination: The upper panel (a) shows the observed evolution of barycenter corrected pulse period values obtained with *Fermi*-GBM (red squares), *Suzaku*-PIN (dark blue square), *RXTE*-PCA (green squares), and *Swift*-XRT (light blue squares). It also shows the overall modeled pulse period evolution (black), the modeled intrinsic spin period evolution (purple), and the orbital motion effect (orange) for the DISK model. The BAT 15–50 keV light curve is overplotted in gray. The lower panels show the residuals for fitting (b) the DISK model and (c) the WIND model to the observed evolution. Both models include intrinsic and orbital effects, but differ in the choice of the luminosity exponent α. The model uncertainties are taken into account in the residuals and in the overall model and intrinsic spin period evolution drawn as a band in lighter colors. Panel (d) shows the Monte Carlo simulation of the model uncertainties: As described in the text the *Swift*-BAT light curve was randomized within its uncertainties, resulting in a different best fit of equation (7.4) to the pulse periods during each run. The standard deviation of all calculated pulse period evolutions at the times where period measurements are available is shown for different assumptions of α in black (DISK) and red (WIND). These values are interpreted as model uncertainties for the final fits.

dominates changes in the measured pulse period. For XTE J1946+274, however, the neutron star undergoes a strong spin-up during outbursts such that the orbital parameters of the system could not be constrained well in the past.

Wilson et al. (2003) were able to describe the pulse frequencies as measured by *CGRO*-BATSE and *RXTE*-PCA during the outburst series between 1998 and 2001 using a piece-wise linear approximation of the intrinsic spin-up. Their best fit with a reduced χ^2 of $\chi^2_{\rm red} = 5.94$ for 37 degrees of freedom (d.o.f.) shows that this simplified approximation cannot give a good description of the measured period evolution.

In the most simple model for the angular momentum transfer of the infalling material onto the neutron star (Ghosh & Lamb, 1979b), the period change of the neutron star is connected to the luminosity L via

$$-\dot{P} \propto P^2 L^{\alpha} \tag{7.2}$$

where $\alpha = 1$ for wind and $\alpha = 6/7$ for disk accretion. Assuming that the luminosity of the source is proportional to the measured flux F, the pulse period at the time t is then given by

$$P(t) = P_0 + a(t - t_0) - b \int_{t_0}^{t} \left(\frac{P(t')}{P_0}\right)^2 \left(\frac{F(t')}{F_{\rm ref}}\right)^{\alpha} dt' \tag{7.3}$$

where P_0 is the pulse period at the reference time, t_0, b is the torque strength, and $F_{\rm ref}$ is a reference flux. The model also takes a constant spin-change, a, into account, which could be caused, e.g., the propeller effect (Illarionov & Sunyaev, 1975). We obtain the observed pulse period $P_{\rm obs}(t)$ by applying the Doppler shift caused by the orbital motion to $P(t)$ as defined in equation (7.3):

$$P_{\rm obs} = P(t)(1 + v(t)/c) \tag{7.4}$$

where $v(t)$ the orbital velocity of the neutron star projected on the line of sight and where c is the speed of light. The orbital parameters needed to calculate $v(t)$ are the orbital period, $P_{\rm orb}$, the time of periastron passage, τ, the projected semi-major

axis, $a_{\rm sm} \sin i$, where i is the inclination, the eccentricity e, and the longitude of periastron ω, such that

$$v(t) = \frac{2\pi a_{\rm sm} \sin i}{P_{\rm orb}(1-e^2)^{1/2}} \left(\cos(\theta(t)+\omega) + e\cos\omega\right) \tag{7.5}$$

where $\theta(t)$ is the true anomaly found by solving Kepler's equation, which itself depends on the orbital parameters listed above.

During the activity of XTE J1946+274 in 2010 and 2011, various X-ray and gamma-ray missions observed the source (see §7.2 and Table 7.1 for details), such that the pulse period evolution is known in great detail especially from *Fermi*-GBM. We searched for pulsations near the GBM period for *Suzaku*-PIN, *RXTE*-PCA, and *Swift*-XRT using the epoch folding technique. For the PIN we determined a pulse period of 15.750025(27) s, see §7.3.2. For PCA, we used PCU2 top-layer light curves, extracted in GoodXenon mode with a time resolution of 0.125 s. The XRT data were taken in Windowed Timing mode. The XRT light curves were obtained from a $\sim 0\farcm5$ region centered on the source position and rebinned to a 1 s time resolution. The initial uncertainties of the measured pulse periods were estimated by Monte Carlo simulations, where synthetic light curves of the source based on the observed pulse profile were searched for the pulse period. The uncertainties of the periods measured by *Fermi*-GBM were provided by the GBM Pulsar Project. The measured pulse periods of XTE J1946+274 are shown in Figure 7.4.

In order to compute the pulse periods via equation (7.3), we used the 1 d binned, 15–50 keV *Swift*-BAT light curve of the source as the bolometric flux evolution $F(t)$ and choose $F_{\rm ref} = 1\,{\rm count\,s^{-1}\,cm^{-2}}$. Using the hard BAT flux as a proxy for the bolometric flux is justified since the source does not show strong spectral changes over and between outbursts (Müller et al., 2012, this work). The main source of uncertainty in the predicted pulse period therefore does not come from changes in the spectral shape, but from the overall uncertainty in the BAT flux measurements, which can have uncertainties of up to 15%. In order to take these

uncertainties into account, we use a Monte Carlo approach in which 10000 BAT lightcurves are simulated. For each time with a BAT measurement, t_i, we draw a simulated BAT count rate from a Gaussian distribution with mean and standard deviation given by the measured BAT rate and uncertainty, respectively. For each of the light curve realizations we then derive the best-fit pulse period evolution using equation (7.4). The standard deviation of the resulting simulated pulse periods, $\sigma_{M(t_i)}$, at each t_i is then taken to be representative of the uncertainty of the modeled pulse period evolution.

In order to obtain the final orbit and pulse period model, based on an initial estimate for $\sigma_{M(t_i)}$ we minimize the fit statistics

$$\chi^2 = \sum_i \frac{(P_i - P_{\rm obs}(t_i))^2}{\sigma_{P_i}^2 + \sigma_{M(t_i)}^2} \tag{7.6}$$

where P_i is the measured pulse period at time t_i, $P_{\rm obs}(t_i)$ is the model period (equation [7.4]), and σ_{P_i} and $\sigma_{M(t_i)}$ are the uncertainties of the data and the model as described above. We then iteratively apply the Monte Carlo approach above to refine the estimated model uncertainties. Usually three iterations are sufficient to obtain convergence. Figure 7.4d displays the final estimate for the uncertainty of the pulse period model.

Fits to equation (7.4) are shown in Figure 7.4. The modeled intrinsic spin period $P(t)$ of the neutron star (shown in purple) dominates the period evolution (black) compared to the effect of the orbital motion (orange). The two residual panels show different assumptions for the exponent α of equation (7.2). In order to check the dependency of the orbital parameters on the assumed torque model, we model the data for both, $\alpha = 6/7$ (the DISK model) and for $\alpha = 1$ (the WIND model). As illustrated by Figure 7.4, both models result in a successful description of the measured pulse period evolution and yield *orbital* parameters that are consistent with each other (Table 7.2).

We stress again that for each of the two models the additional uncertainties due to the BAT data have to be calculated separately by the iterative Monte Carlo approach described above. The resulting uncertainties of the model vary between 0.02 and 0.38 ms with a mean of 0.09 ms (see Figure 7.4d). Within the model uncertainties, however, the model pulse periods agree with the measured data. For example, the pulse period predicted by the DISK model for the time of the *Suzaku* observation is 15.750300(380) s, while the observed period is 15.750025(27) s. Unfortunately, the model uncertainty is large enough that it is not possible for us to distinguish between the different torquing models, with both model fits yielding almost the same χ^2. Thankfully, as shown in Table 7.2, the orbital parameters are insensitive to the details of modeling $\dot{P}(t)$. It is only the best fit values for the spin change, a, and the torque strength, b, which differ significantly. Numerical experimenting revealed that this is due to a strong parameter degeneracy of the luminosity exponent α with a and b. Based on the pulse period evolution alone it is therefore not possible to distinguish between the two torquing scenarios.

Table 7.2: Orbital parameters and spin period evolution. The uncertanties are on the 90% confidence level.

	DISK	WIND
$a_{\rm sm} \sin i$ [lt-s]	$471.2^{+2.6}_{-4.3}$	$471.1^{+2.7}_{-2.8}$
$P_{\rm orb}$ [d]	$172.7^{+0.6}_{-0.6}$	$171.4^{+0.4}_{-0.4}$
τ [MJD]	$55514.8^{+0.8}_{-1.1}$	$55515.5^{+0.8}_{-0.7}$
e	$0.246^{+0.009}_{-0.009}$	$0.266^{+0.007}_{-0.007}$
ω [$^\circ$]	$-87.4^{+1.5}_{-1.7}$	$-87.1^{+1.2}_{-1.0}$
t_0	55550 (fixed)	55550 (fixed)
P_0 [s]	$15.749742^{+0.000023}_{-0.000014}$	$15.749753^{+0.000013}_{-0.000013}$
a [s s^{-1}]	$1.67^{+0.16}_{-0.18} \times 10^{-10}$	$0.47^{+0.20}_{-0.10} \times 10^{-10}$
b [s s^{-1}]	$6.52^{+0.06}_{-0.08} \times 10^{-8}$	$10.76^{+0.05}_{-0.04} \times 10^{-8}$
α	6/7 (fixed)	1 (fixed)
$\chi^2_{\rm red}$/dof	1.05/89	1.06/89

Listed are the projected semi major axis, $a_{\rm sm} \sin i$, the orbital period, $P_{\rm orb}$, the time of periastron passage, τ, the eccentricity, e, the longitude of periastron, ω, the reference time, t_0, the spin period at t_0, P_0, the constant spin-change, a, the torque strength, b, and the luminosity exponent, α.

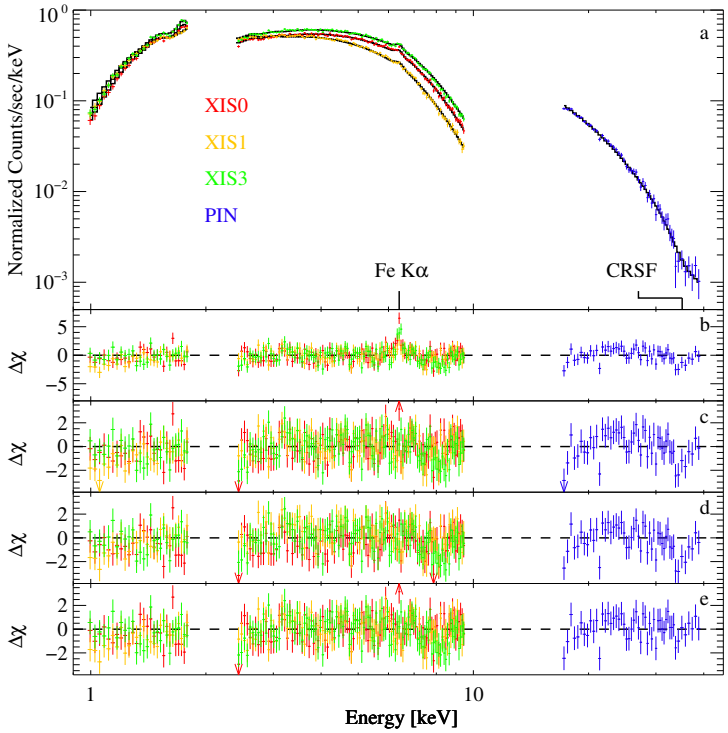

Figure 7.5: Spectra and best fit model for XIS 0, 1, 3 (in red, yellow, and green, respectively) and PIN (in blue). The spectra were fitted simultaneously with the model described by equation (7.10) with an FDCO continuum model. The bottom panels show the residuals as $\Delta\chi$ obtained by (b) fitting only the continuum, (c) fitting the continuum with the Fe Kα line, (d) fitting the continuum with the Fe Kα line and the 35 keV CRSF feature with D_{CRSF} set to 0 *after* fitting, (e) fitting the continuum with the Fe Kα line and the 35 keV CRSF feature.

Table 7.3: XTE J1946+274 Spectral Fit Parameters

	FDCUT I	FDCUT II	FDCUT III	CUTOFFPL	HIGHECUT	NPEX[b]
$N_{\rm H}$ [$\times 10^{22}$cm^{-2}]	$1.14^{+0.01}_{-0.02}$	$1.66^{+0.02}_{-0.03}$	1.67(3)	$1.59^{+0.02}_{-0.04}$	$1.59^{+0.02}_{-0.04}$	$1.58^{+0.03}_{-0.05}$
A_Γ[$\times 10^{-2}$ keV^{-1} cm^{-2} s^{-1}]	$2.04^{+0.03}_{-0.05}$	$2.02^{+0.03}_{-0.05}$	$2.05^{+0.04}_{-0.05}$	0.97(2)	0.97(2)	$0.96^{+0.02}_{-0.04}$
Γ	$0.55^{+0.01}_{-0.02}$	$0.55^{+0.01}_{-0.02}$	0.57(2)	$0.41^{+0.02}_{-0.04}$	$0.41^{+0.02}_{-0.04}$	$0.39^{+0.04}_{-0.08}$
$E_{\rm fold}$ [keV]	$8.6^{+0.2}_{-0.3}$	$8.5^{+0.2}_{-0.3}$	$8.9^{+0.4}_{-0.4}$	$9.6^{+0.4}_{-0.6}$	$9.6^{+0.4}_{-0.6}$	$9.1^{+0.8}_{-1.4}$
$E_{\rm cut}$ [$\times 10^{-2}$ keV]	$0.09^{+0.04}_{-0.09}$	$0.01^{+0.00}_{-0.01}$	$0.05^{+0.03}_{-0.05}$	–	$0.01^{+0.00}_{-0.01}$	–
Γ_2	–	–	–	–	–	-2[a]
α[$\times 10^{-2}$] [keV/keV]	–	–	–	–	–	$0.020^{0.003}_{-0.020}$
$E_{\rm Fe}$ [keV]	–	6.41(3)	6.41(3)	6.41(3)	6.41(3)	6.41(3)
$\sigma_{\rm Fe}$ [keV]	–	0.1[a]	0.1[a]	0.1[a]	0.1[a]	0.1[a]
$A_{\rm Fe}$ [$\times 10^{-5}$ photons cm^{-2} s^{-1}]	–	$8.6^{+1.3}_{-1.4}$	$8.6^{+1.3}_{-1.3}$	$8.7^{+1.3}_{-1.4}$	$8.7^{+1.3}_{-1.4}$	$8.7^{+1.1}_{-1.0}$
$E_{\rm CRSF}$ [keV]	–	–	$35.2^{+1.5}_{-1.3}$	$34.8^{+1.2}_{-1.0}$	$34.8^{+1.2}_{-1.0}$	$34.8^{+1.1}_{-1.0}$
$\sigma_{\rm CRSF}$ [keV]	–	–	2[a]	2[a]	2[a]	2[a]
$D_{\rm CRSF}$ [keV]	–	–	$2.4^{+1.5}_{-1.3}$	$3.5^{+1.5}_{-1.5}$	$3.5^{+1.5}_{-1.5}$	$3.8^{+1.6}_{-1.5}$
$c_{\rm XIS\,0}$	1[a]	1[a]	1[a]	1[a]	1[a]	1[a]
$c_{\rm XIS\,1}$	1.07(1)	1.07(1)	1.07(1)	1.07(1)	1.07(1)	1.07(1)
$c_{\rm XIS\,3}$	0.95(1)	0.95(1)	0.95(1)	0.95(1)	0.95(1)	0.95(1)
$c_{\rm PIN}$	$1.32^{+0.07}_{-0.05}$	$1.35^{+0.07}_{-0.05}$	$1.29^{+0.07}_{-0.06}$	$1.29^{+0.07}_{-0.05}$	$1.29^{+0.08}_{-0.05}$	$1.31^{+0.07}_{-0.06}$
$\chi^2_{\rm red}$/dof	1.38/470	1.19/468	1.17/466	1.12/467	1.12/466	1.12/466

The XIS and PIN spectra were fitted simultaneously with the models described in §7.4.1. The columns are labeled according to the continuum that was used. The uncertainties are given on a 90% confidence level. [a] These parameters were frozen while fitting; [b] for the model $M_{\rm NPEX}(E) \propto (E^{-\Gamma} + \alpha E^{+\Gamma_2})e^{-E/E_{\rm fold}}$ the parameters Γ and Γ_2 are the indices of the falling and rising power law components and α is the normalization of the rising relative to the falling component.

7.4 Spectral Analysis

7.4.1 Best Fit Model

We modeled the 1–9.4 keV XIS and the 17–38 keV PIN spectra using `xspec12` (Arnaud, 1996). The 1.8–2.4 keV range was excluded due to known calibration uncertainties (ISAS/JAXA & X-ray Astrophysics Laboratory NASA Goddard Space Flight Center, 2013). We applied the normalization constants $c_{\mathrm{XIS\,1}}$, $c_{\mathrm{XIS\,3}}$, and c_{PIN} to account for the flux cross-calibration between the respective instruments relative to XIS 0, where $c_{\mathrm{XIS\,0}}$ was fixed at 1 (`xspec` model `constant`). The absorption was modeled with `tbnew`, an updated version of `tbabs`[4], using cross sections by Verner & Yakovlev (1995) and abundances by Wilms et al. (2000). Extending the fit down to 0.8 keV, Maitra & Paul (2013a) included an additional partial covering absorption component. Since they found that its parameters are model dependent and since the hardness ratio evolution over the observation (Figure 7.2c and Figure 7.2d) does not indicate any variability due to partial covering, we used one fully covering absorber alone which is suffient to model the data down to 1 keV well.

Following the spectral analysis of Müller et al. (2012), we first fitted a Fermi-Dirac cutoff model (`power`×`fdcut`, Tanaka, 1986), described by:

$$M_{\mathrm{FDCUT}}(E) \propto E^{-\Gamma} \times \left[1 + \exp\left(\frac{E - E_{\mathrm{cut}}}{E_{\mathrm{fold}}}\right)\right]^{-1} \tag{7.7}$$

where the photon flux at energy E is described by a power law with a photon index Γ, multiplied by an exponential cutoff at energy E_{cut} with a folding energy E_{fold}. The soft Galactic ridge emission seen in the 6–7 keV range, which needed to be taken into account for PCA data modeling by Müller et al. (2012), is not required

[4] `http://pulsar.sternwarte.uni-erlangen.de/wilms/research/tbabs/`

for *Suzaku* due to XIS being an imaging instrument. The results of this fit are listed in Table 7.3 in the column labeled FDCUT I. Figure 7.5b shows the residuals from fitting the continuum model only.

The strongest residuals are seen at 6.41 keV. We interpreted this as a narrow Fe Kα fluorescence line that we proceeded to describe with a Gaussian line model (`gaussian`). The width is unresolved and we fixed it at $\sigma_{\mathrm{Fe}} = 0.1\,\mathrm{keV}$, slightly below the XIS detector resolution. The results of this fit are listed in Table 7.3 in the column labeled FDCUT II and Figure 7.5c shows the fit residuals.

Residuals are still visible in the PIN energy range, especially around 35 keV. We included an absorption-like line with a Gaussian optical depth profile (`gabs`) often used to describe cyclotron lines:

$$M_{\mathrm{CRSF}}(E) = \exp(-\tau(E)) \tag{7.8}$$

with

$$\tau(E) = \tau_{\mathrm{CRSF}} \exp\left[-\frac{1}{2}\left(\frac{E - E_{\mathrm{CRSF}}}{\sigma_{\mathrm{CRSF}}}\right)^2\right] \tag{7.9}$$

where E_{CRSF} is the cyclotron line energy, σ_{CRSF} is the line width, and τ_{CRSF} is the optical depth. Note that the `gabs` implementation provides the line depth $D_{\mathrm{CRSF}} = \tau_{\mathrm{CRSF}}\sigma_{\mathrm{CRSF}}\sqrt{2\pi}$ instead of τ_{CRSF}. The CRSF width was unresolved and we fixed it at $\sigma_{\mathrm{CRSF}} = 2\,\mathrm{keV}$, close to PIN's detector resolution. The results of this fit are listed in Table 7.3 in the column labeled FDCUT III. Figure 7.5a shows the spectra and fitted model and Figure 7.5e shows the fit residuals. The latter do not show any further strong features. In order to illustrate the contribution of the CRSF feature to the best fit Figure 7.5d shows the residuals of the best fit with the CRSF depth set to 0. We tried fixing the PIN cross normalization constant to its canonical value of 1.181 for an HXD-nominal pointing position (Maeda et al., 2008).

This resulted in a worse fit with $\chi^2_{\rm red} = 1.35$, therefore, we left $c_{\rm PIN}$ free.

We then checked whether the presence of a "10 keV feature" is consistent with the data. This is a broad residual that has been observed in the spectra of several accreting pulsars thought to be caused by imperfect modeling of the continuum shape using empirical models (see, e.g., Coburn et al., 2002). It is generally detected as a positive residual (e.g., in Cen X-3, see Suchy et al., 2008) but in some sources, including XTE J1946+274, it appears as a negative one (e.g., in Vela X-1, see Fürst et al., 2014). We applied the deeper of the two detections reported for XTE J1946+274 by Müller et al. (2012) to our model, i.e., following them we included a `gauabs` component (another parametrization of the `gabs` shape) with $E_{10\,\rm keV} = 9.85\,\rm keV$, $\sigma_{10\,\rm keV} = 2.2\,\rm keV$, and $\tau_{10\,\rm keV} = 0.069$. This approach did not significantly change the quality of the fit and fitting $\tau_{10\,\rm keV}$ resulted in a value consistent with 0. We conclude that such a component could be present in the spectrum but is not detected, probably in part due to the lack of data between 9.4 and 17 keV.

Our `fdcut` based best fit model (FDCUT III) thus consists of absorption in the interstellar medium as well as intrinsic to the system, a power law continuum with a rollover, a Gaussian emission line for Fe Kα fluorescence, and an absorption-like line with a Gaussian optical depth profile for the cyclotron line:

$$M_{\rm best}(E) = \texttt{const} \times \texttt{tbnew} \times (\texttt{power} \times \texttt{fdcut} + \texttt{gauss}) \times \texttt{gabs} \tag{7.10}$$

in `xspec` notation. We obtain an unabsorbed 3–60 keV flux of $4.40 \pm 0.01 \times 10^{-10}\,\rm erg\,s^{-1}\,cm^{-2}$.

In the following we present results replacing the `power`×`fdcut` continuum with other continuum models commonly applied to accreting X-ray pulsars (see, e.g., Müller et al., 2013b, for the equations describing these models): a power

law with an exponential cutoff (`cutoffpl`), a power law with a high energy cutoff (`power`×`highecut`, sometimes also called `plcut`), and the sum of a negative and a positive power law with an exponential cutoff (`npex`, Mihara, 1995). The last three columns of Table 7.3 show the best fit spectral parameters using these continuum models. Since the fitted values of the cutoff energy of `highecut` and the normalization of the positive power law of `npex` are consistent with 0 these three models are degenerate and result in the same fit quality and in the same values of their common parameters. The `fdcut` fit has a slightly different rollover shape but its parameters are also qualitatively, and often quantitatively within errors, the same. We note that the `npex` parameters reported by Heindl et al. (2001) for the bright outburst of 1998, which were obtained fitting averaged *RXTE* monitoring spectra above 8 keV can also describe the PIN spectrum, but they do not provide a good description of the XIS spectrum (below 8 keV the spectra were variable between individual monitoring pointings).

Maitra & Paul (2013a) reported `highecut` and `npex` fit of the same *Suzaku* dataset. Their best fit parameters are generally not consistent with ours. For example, their `highecut` cutoff energy of $7.02^{+0.69}_{-0.29}$ keV and their `npex` positive power law normalization are not consistent with 0. A possible explanation for this discrepancy is that the `highecut` model has a break at the cutoff energy, which here is located at the energy of the Fe K edge. In part this approach therefore could be modeling imperfections of the fit in the region of the iron line and edge. No edge component was required in our fits. Using the approach of Maitra & Paul (2013a) by extending the spectrum to 70 keV, i.e., beyond where the source is detected (see next section), and allowing for a 9 keV wide cyclotron line using the `cyclabs` model, did, we were able to reproduce their continuum parameters. Maitra & Paul (2013a) do not quote flux calibration constants. We found a PIN/XIS ratio similar to our

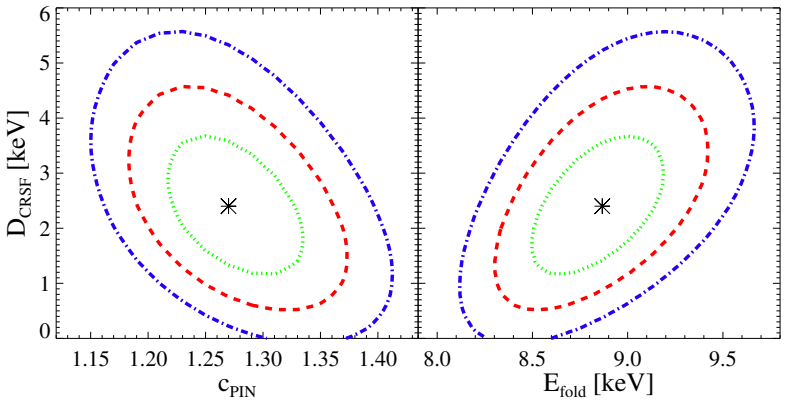

Figure 7.6: Confidence contour plots showing moderate correlations between the depth of the CRSF at 35 keV and the folding energy (top) and between the depth of the CRSF at 35 keV and the PIN flux cross-calibration constant (bottom) for the FDCUT III fit of Table 7.3. Contours for confidence levels of 1, 2, and 3σ are shown in dotted green, dashed red, and dash-dotted blue, respectively.

other fits. We also assumed that their unitless CRSF width values $W_{\rm CRSF}$ were given in keV. As mentioned in §7.1 a 9 keV wide cyclotron line can be expected to in part model the continuum (Müller et al., 2013b). Similar to Maitra & Paul (2013a) we found that thermal Comptonization of soft photons in a hot plasma (`comptt`, Titarchuk, 1994) cannot explain the *Suzaku* spectra, particularly in the PIN range ($\chi^2_{\rm red}$/dof=5.86/464, unconstrained parameters).

7.4.2 Cyclotron Resonance Scattering Feature

The cyclotron line we found in the *Suzaku* spectrum from the end of the second outburst of the 2010 series has an energy of $E_{\rm CRSF} = 35.16^{+1.5}_{-1.3}$ keV, a line depth of $D_{\rm CRSF} = 2.42^{+1.5}_{-1.3}$ keV and a fixed width of $\sigma_{\rm CRSF} = 2$ keV. Heindl et al. (2001) found a CRSF with similar parameters at $E_{\rm CRSF} = 36.2^{+0.5}_{-0.7}$ keV with $D_{\rm CRSF} = 2.79^{+2.14}_{-1.77}$ keV ($\tau_{\rm CRSF} = 0.33^{+0.07}_{-0.06}$) and $\sigma_{\rm CRSF} = 3.37^{+0.92}_{-0.75}$ keV) for the bright outburst in 1998, from *RXTE* data. The CRSF energy obtained with *RXTE* is consistent with the one obtained with *Suzaku*. Müller et al. (2012) did not find a

line at 35 keV, but found marginal evidence (1.8σ) for a CRSF at $\sim$25 keV in the first and third outbursts of the 2010 series.

In order to check the robustness of the *Suzaku* detection of an unresolved cyclotron line at 35 keV with resepct to changes of the continuum model parameters we calculated confidence contours for two parameters of interest, the CRSF depth $D_{\rm CRSF}$ and one continuum parameter at a time. We found no strong correlations. Not unexpectedly, moderate correlations are present with the folding energy $E_{\rm fold}$ and with the flux cross-calibration constant of the PIN spectrum $c_{\rm PIN}$, see Figure 7.6. The confidence contours indicate that the CRSF feature is present independently of the continuum modeling on a $\sim 3\sigma$ level. We further confirmed this picture by determining a significance of 2.81σ for a cyclotron line feature at 35 keV using Monte Carlo simulations. This significance value was obtained by simulating 5000 spectra based on the best fit model parameters without the CRSF (column FDCUT II of Table 7.3) and fitting them with and without including the CRSF (width fixed at 2 keV in the former case). In 25 cases we found a bigger improvement in χ^2 than in the real data, resulting in the quoted significance. For an unresolved line at 25 keV line we determined a 3σ upper limit of $D_{\rm CRSF} \sim 0.9$ for the line depth, based on Monte Carlo simulations including a 25 keV line with different depths and for each depth comparing the χ^2 values obtained from fitting the line to the data and the simulations.

We also investigated the modeled PIN background spectrum and the effect of its uncertainty on the fit parameters, particularly of the cyclotron line. To this end we first included the background normalization as a fit parameter in the FDCUT III model using `recorn`. The uncertainty of the fitted background normalization ranged from a decrease of 20% to an increase of 3%. Repeating the fit fixing the background normalization at either of these values or at the default and adding the expected

systematic uncertainty of 3% to the PIN background spectrum (ISAS/JAXA & X-ray Astrophysics Laboratory NASA Goddard Space Flight Center, 2013, node10) did not significantly change the resulting cyclotron line parameters. We confirm Maitra & Paul (2013a)'s report that the normalization of the background spectrum observed when the source was occulted by the Earth (obtained by setting `ELV` $< -5^\circ$ in `aepipeline`) was about 20% below that of the modeled background spectrum. This result can qualitatively be explained with the anticorrelation between the magnetic field strength and the background flux at a given satellite location (ISAS/JAXA & X-ray Astrophysics Laboratory NASA Goddard Space Flight Center, 2015, node12): A measure for the strength of the Earth's magnetic field – the time resolved magnetic cutoff rigidity of the Earth at the satellite position during the observation – can be obtained from the observation's filter file and we found that it was on average lower during the on-source time (`ELV` > 5) than during the Earth-occultation time (`ELV` < -5) for the XTE J1946+274 observation.

In §7.3.2 we showed that there is no broad-band detection of the pulsar above 40 keV. The background subtracted spectrum generally confirms this. It is consistent with 0 above 38 keV with the exception of two independent spectral bins in the 43–47 keV range that show a marginal source detection (see also Figure 4 of Maitra & Paul, 2013a). The picture stays the same when taking the 3% background uncertainty into account. Using non background subtracted events we detected no pulsations in the 38–45 keV range and marginal ones in the 43–47 keV range, confirming again that the background model is sufficiently accurate. The background spectrum dominates over the source contribution above $\sim$33 keV and declines smoothly with energy with no systematic features around 35 or 40 keV. Above 38 keV the source spectrum might thus show some structure but it is mostly below the detection limit and was therefore excluded from our analysis.

7.5 Discussion

7.5.1 Pulse Period Evolution and Orbit Parameters

We successfully applied the accretion torque theory of Ghosh & Lamb (1979b) to XTE J1946+274 and updated the orbital solution for this source (Table 7.2). Previously Wilson et al. (2003) used three different approaches to model the observed pulse period evolution obtained by *RXTE*-PCA and *CGRO*-BATSE in 1998, which was dominated by a strong spin-up as well. Comparing the resulting orbital parameters to ours we find that the semi-major axis, $a_{\rm sm} \sin i$, agrees best with their 10th-order polynomial model. Extrapolating our derived time of periastron passage, τ, back to 1998, gives times which agree to within 2σ with the result of their model as well. The orbital period, $P_{\rm orb}$, and eccentricity, e, are consistent with their linear model, while the longitude of periastron, ω, is the same as in their piecewise approximation within the uncertainties. As noted by Wilson et al., however, the χ^2 of all three different approaches is not acceptable because the models do "not completely describe the intrinsic torques".

In contrast to other methods such as, e.g., a Fourier series approach (e.g., Kühnel et al., 2013), calculating the spin-up of accreting pulsars using the theory of Ghosh & Lamb (1979b) allows us to model the possibly complex, intrinsic spin period evolution of the neutron star with better accuracy (see also Galloway et al., 2004; Sugizaki et al., 2015). As a result the orbital motion can be properly disentangled from the overall observed pulse period evolution and the derived orbital parameters are generally more reliable. We caution, however, that assuming $P(t')$ is a constant on the right side of equation (7.3) in order to simplify the calculation of this differential equation (see, e.g., Sugizaki et al., 2015) might lead to additional uncertainties when fitting longer time series. If we set $P(t') = P_0$, for example, the

modeled pulse period evolution differs up to 0.01 ms, which is of the same order as the uncertainties of the *Fermi*-GBM period measurements. As soon as more precise flux measurements are used for $F(t)$ or the measured spin-up is even stronger than for XTE J1946+274 the differential equation should thus be solved properly.

This kind of timing analysis would not be possible without regular flux monitoring by all-sky observatories, such as *Fermi*-GBM, *Swift*-BAT, or MAXI.

7.5.2 Mass Function and Orbit Inclination

The accurately determined orbital parameters allow us to derive the value of the mass function of XTE J1946+274 following the same approach as in, e.g., Wilson et al. (2003). The mass function of a binary,

$$f(M) = \frac{(M_{\rm opt} \sin i)^3}{(M_{\rm NS} + M_{\rm opt})^2} = \frac{4\pi^2}{G} \frac{(a_{\rm sm} \sin i)^3}{P_{\rm orb}^2} \tag{7.11}$$

depends on the masses, $M_{\rm opt}$ and $M_{\rm NS}$, of the optical companion and neutron star, respectively, and on the orbital inclination angle, i. However, the mass function can also be calculated using the orbital period, $P_{\rm orb}$, and the projected semi-major axis, $a_{\rm sm} \sin i$. Using the orbital parameters listed in Table 7.2 we derive consistent values of $f(M) = 3.77^{+0.11}_{-0.07}\,{\rm M}_\odot$ for disk-accretion and $f(M) = 3.82^{+0.07}_{-0.07}\,{\rm M}_\odot$ for wind-accretion. Assuming the same mass range for the companion star of 10 $\mathrm{M}_\odot \leq M_{\rm opt} \leq 16$ $\mathrm{M}_\odot$ as used by Wilson et al. (2003) and the canonical neutron star mass $M_{\rm NS} = 1.4\,{\rm M}_\odot$, we can solve equation (7.11) for the inclination angle, i. Using the widest possible range for the mass function as calculated above, 3.70 $\mathrm{M}_\odot \leq f(M) \leq 3.89$ $\mathrm{M}_\odot$, we derive an orbital inclination angle of $41^\circ \leq i \leq 52^\circ$. This is in good agreement with the value of $i \gtrsim 46^\circ$ as found by Wilson et al. (2003).

As already argued by Wilson et al. (2003), the inclination angle of the Be-disk, $i_{\rm disk}$, with respect to the observer is not necessarily aligned with the inclination

angle of the orbit, i. From measurements of the width of the single-peaked Hα line in an optical spectrum, Wilson et al. (2003) concluded that the Be-star is seen nearly pole-on. Thus, the Be-disk and orbital plane might indeed be misaligned in XTE J1946+274. Özbey Arabacı et al. (2015) recently analyzed optical spectra of the system and noted, however, that deriving the Be-disk inclination from the Hα line profile is highly uncertain based on theoretical investigations by Silaj et al. (2010). Assuming that the orbital plane and the Be-disk are aligned ($i_{\rm disk} = i$), Özbey Arabacı et al. (2015) derived the rotational velocity of the Be-star. They concluded that the Be companion of XTE J1946+274 is rotating with 0.50–0.72 times the critical break-up velocity of a typical Be type star ($v_{\rm crit}$∼618 km s^{-1}). Using their initial value of the projected velocity, $v \sin i = 323\,{\rm km\,s^{-1}}$ and our determined inclination angle, i, we find a velocity of 0.66–0.80 times the break-up velocity.

7.5.3 Outburst Behavior

Two outburst series of XTE J1946+274 have been observed, one in 1998 (Wilson et al., 2003) and one in 2010 (Figure7.1) with two to three outbursts per orbit. In order to explain this X-ray activity the companion of XTE J1946+274 has been studied in the optical and IR. Based on observations of permanent Hα emission, Özbey Arabacı et al. (2015) conclude that during X-ray quiescence a large Be disk is present. They observed a brightening in the optical/IR indicating that the Be star experienced a long mass-ejection event from 2006 to 2012, reaching its maximum intensity in 2010, around the time of the outburst series. Özbey Arabacı et al. postulate that this ejection caused an increase in size, perturbations, and warping of the Be disk. They also state that the X-ray activity is triggered by the neutron star coming into contact with the warped areas in the tilted Be disk. This could explain why we observe two to three outbursts per orbit. The presence of Hα

and optical/IR emissions after the X-ray activity indicates that once the material was consumed through accretion, the Be disk quickly and steadily recovered and the system returned to quiescence (Özbey Arabacı et al., 2015).

7.5.4 Continuum and Fe Kα Line

We described the spectral shape of XTE J1946+274 with a Fermi Dirac Cutoff power law together with an Fe Kα fluorescence line and a CRSF at 35 keV. We find $E_{\rm fold} = 8.89(4)$ keV and a hydrogen column density of $N_{\rm H} = 1.67(3) \times 10^{22}{\rm cm}^{-2}$. These parameters are roughly consistent with the ones found by Müller et al. (2012) in PCA data taken during earlier outbursts, namely $E_{\rm fold} = 6.0^{+2.6}_{-1.6}$–$8.1^{+0.7}_{-0.6}$ keV, and $N_{\rm H} = 1.77^{+0.25}_{-0.29}$–$5.1^{+2.5}_{-3.3} \times 10^{22}{\rm cm}^{-2}$. Their measured $\Gamma = 0.74^{+0.12}_{-0.17}$–$1.04^{+0.13}_{-0.18}$ is slightly softer than ours, $\Gamma = 0.57(2)$. The cutoff energy is different as well: It is found here to be zero, while Müller et al. (2012) found $E_{\rm cut} = 14 \pm 4$–$19.4^{+2.1}_{-9.7}$ keV.

In order to study the changes in the spectral shape at different times and luminosities during the outburst series we compared our best fit model and the models fitted in Müller et al. (2012) by eye. The *Suzaku* spectrum is harder at high energies (>12 keV) than the spectra from Müller et al. (2012). This hardness change could be an indication of a higher temperature of the plasma in the accretion column, despite the lower luminosity. At first glance this may seem inconsistent, however, the electron temperature and mass accretion rate cannot be clearly determined without a physical continuum model. The implementation and testing of such a physical model is work in progress (Marcu et al., 2014).

Both, Müller et al. (2012) and we find $N_{\rm H}$ values that are almost twice as large as the Galactic $N_{\rm H}$ in the direction of XTE J1946+274 ($N_{\rm H} = 9.4 \times 10^{21}{\rm cm}^{-2}$; Kalberla et al., 2005). This excess indicates the presence of absorbing material intrinsic to the X-ray binary system. The excitation of such neutral to moderately

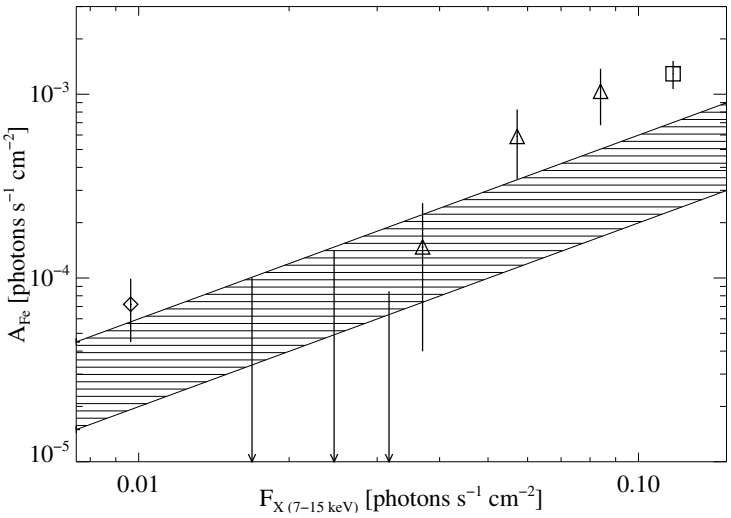

Figure 7.7: Flux of the Fe Kα fluorescence line as a function of the 7–15 keV continuum flux. The diamond represents the *Suzaku*-XIS 0 data. All other data points are from Müller et al. (2012): triangles represent multiple instrument results from the first 2010 outburst (*RXTE, INTEGRAL* – two high-flux triangles) and from the third 2010 outburst (*Swift, RXTE, INTEGRAL* – two low-flux triangles and two upper limits), and the square corresponds to the *RXTE* average spectrum of the 1998 outburst. The hashed region describes the predicted correlation according to Nagase et al. (1986) calculated using $N_{\rm H}$ and continuum normalization values from the *Suzaku* spectral fit and the Müller et al. (2012) fits.

ionized material surrounding the neutron star by the X-rays emitted from the accretion column can produce fluorescent lines from iron and other elements. These lines are a very useful tool for analyzing the properties of the material (e.g., Inoue, 1985; Leahy & Creighton, 1993; Torrejón et al., 2010; Reig & Nespoli, 2013).

We find a narrow ($\sigma_{\rm Fe} = 0.1$ keV) Fe Kα fluorescent emission line at $E_{\rm Fe} = 6.41(3)$ keV, confirming the presence of this neutral to moderately ionized material. The flux was $A_{\rm Fe} \sim 8.6 \times 10^{-5}$ photons cm^{-2} s^{-1} (see Table 7.3). The equivalent width is 32.2 eV for the *Suzaku* observation, consistent with the ∼29 eV found by Maitra & Paul (2013a) in the same data set, but lower than the measured 49–69 eV found in earlier data taken at different fluxes (Heindl et al., 2001; Müller et al., 2012). As shown, e.g., by Inoue (1985), one expects the flux in the flourescence

line to be correlated with the continuum flux above 7 keV. Figure 7.7 shows this relationship using data of all published observations of XTE J1946+274, extending a similar figure by Müller et al. (2012) to lower fluxes. The figure also shows the correlation predicted by equation (4a) of Nagase et al. (1986) which is an estimate for the fluorescent line flux as a function of $N_{\rm H}$ and continuum flux. The hashed region in Figure 7.7 illustrates the range of the expected Fe Kα flux values according to Nagase et al. (1986), taking into account the variation in $N_{\rm H}$ between all published spectral fits. This range is an upper limit to the absorption column of the system. For the values with the lowest uncertainties the observed Fe Kα flux is slightly higher than the one predicted by Nagase et al. (1986). This is especially the case for the high flux data points and is qualitatively consistent with their higher equivalent width compared to the *Suzaku* measurement. A possible reason for this slight excess could be an overabundance of iron in the emitting medium. Alternatively, the excess could also be due to the fact that the ionization structure of the material is more complicated than the purely neutral Fe absorber assumed by Nagase et al. (1986). Finally, it is also likely that the emission is not purely from the line of sight, but from other areas such as fluorescence from a tilted and/or warped Be disk around the neutron star.

7.5.5 Cyclotron Resonance Scattering Feature

Evidence of a $\sim$35 keV cyclotron line line was first seen by Heindl et al. (2001) in *RXTE* data obtained during a time when the source was much brighter than in the observations analyzed here. Our *Suzaku* observation supports the presence of this line: the χ^2 slightly improved from 557 to 545, corresponding to a significance of 2.81σ (obtained using Monte Carlo simulations), between the FDCUT II and FDCUT III fits. Including this line improved the fits with the other

continuum models as well. The centroid energy of $35.2^{+1.5}_{-1.3}$ keV implies a surface magnetic field of $B_{\rm NS} = 3.1^{+0.1}_{-0.1}(1+z) \times 10^{12}$ G.

The CRSF parameters are independent of the continuum model. Furthermore, describing the PIN data only with the `npex` model, we obtain a good fit with $\chi^2_{\rm red} = 0.92$ for 50 d.o.f., for continuum parameters consistent with Heindl et al. (2001). Both the energy of the cyclotron line and its optical depth measured with *Suzaku* are within 1σ of those measured with *RXTE*. Note, however, that due to spectral complexity below 10 keV the *RXTE* based `npex` values do not describe the broad band (XIS and PIN) *Suzaku* data.

We find a lower centroid energy for the CRSF than the effectively $\sim$40 keV previously reported for this dataset by Maitra & Paul (2013a). As explained in §7.4.2, their higher value could be due to in part modeling an artificial feature, as these authors include PIN data above 40 keV, where the source is mostly not detected.

Our spectrum is not consistent with the 25 keV feature discussed by Müller et al. (2012). We tried including a feature with their parameters and the $\chi^2_{\rm red}$ increased to 1.92. When the depth of this 25 keV feature was left free it became consistent with zero.

7.5.6 Accretion Column

It has recently been recognized that different types of correlations between the energy of the CRSF $E_{\rm CRSF}$ and the X-ray luminosity $L_{\rm X}$ are observed for accreting pulsars, probably reflecting different accretion states (Staubert et al., 2007). Studying these correlations allows us to derive constraints on the physical conditions in the accretion column. Becker et al. (2012) presented a model of the different accretion regimes and of how the height (i.e., the B-field and therefore

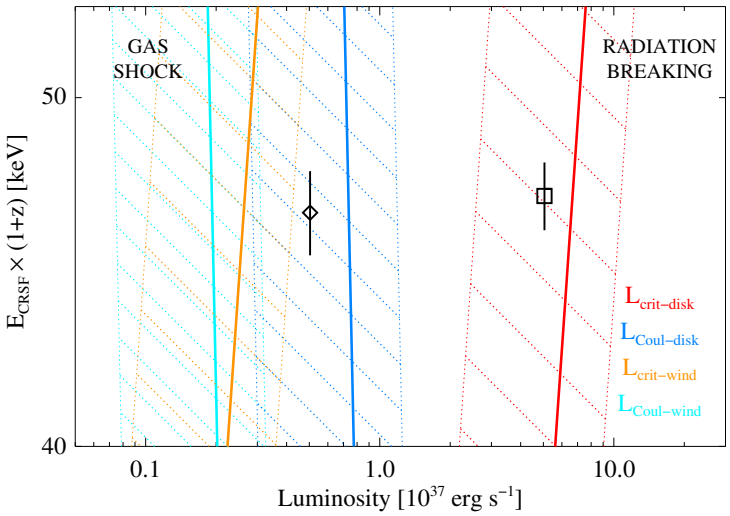

Figure 7.8: Relationship between the intrinsic CRSF energy and the luminosity of XTE J1946+274. The results of the spectral fits from this work (diamond) and Heindl et al. (2001) (square) are shown with respect to the Coulomb and critical luminosities (equations 32 and 45 in Becker et al., 2012) of a neutron star with a standard mass and radius for the cases of disk (dark blue and red solid lines) and wind accretion (light blue and orange solid lines). The hashed luminosity ranges account for the uncertainty of the distance measurement.

$E_{\rm CRSF}$) of the region in the accretion column where the CRSF is produced changes with luminosity for the different regimes (see also Mushtukov et al., 2015): For supercritical sources ($L_{\rm X} \gtrsim L_{\rm crit}$) radiation pressure in a radiative shock in the accretion column is the dominant decelerator for the material inside the accretion column. A source in this regime is expected to show a negative $E_{\rm CRSF}$-$L_{\rm X}$ correlation, as observed for V 0332+53 (Mowlavi et al., 2006). For moderately subcritical sources ($L_{\rm X} \lesssim L_{\rm crit}$) the radiation-dominated shock causes the initial deceleration, followed by Coulomb interactions below the shock which bring the matter to a stop on the neutron star surface. Subcritical sources in this regime are expected to show a positive $E_{\rm CRSF}$-$L_{\rm X}$ correlation, as observed for Her X-1 or GX 304−1 (Staubert et al., 2007; Klochkov et al., 2012). The expected relationship at even lower luminosities ($L_{\rm X} \lesssim L_{\rm Coul}$), where the radiative shock and Coulomb interactions disappear, and

the matter falls through a gas-mediated shock before hitting the stellar surface, is less clear. A 0535+26, for example, is a low-luminosity source that does not show any changes of $E_{\rm CRSF}$ in pulse averaged spectra with luminosity (Caballero et al., 2007, but see Müller et al. 2013a and Sartore et al. 2015).

Where does XTE J1946+274 fit into this picture? In Figure 7.8 we show the Coulomb luminosity $L_{\rm Coul}$ and the critical luminosity $L_{\rm crit}$ for a range of B-fields, i.e., cyclotron line energies (after Becker et al., 2012), separating the different accretion regimes. These luminosities depend among other things on the accretion geometry outside of the Afvén sphere, two cases are presented: disk and wind accretion. Overplotted are the gravitational redshift corrected cyclotron line energies and 3–60 keV luminosities from Heindl et al. (2001) and from our *Suzaku* analysis. We calculated the *Suzaku* luminosity using the unabsorbed flux measurement from the FDCUT III spectral fit. The CRSF energy is consistent within errors between 1998 and 2010, implying that the height of the CRSF emission region is similar for both observations. The luminosities, while both moderate, span a range larger than observed for any other moderate luminosity pulsar (e.g., Her X-1 or GX 304−1) fall in the transition region between low and high luminosity pulsars. In the case of disk accretion, the default assumption for Be-systems, both luminosities are consistent with subcritical accretion, with the 1998 *RXTE* measurement at $L_{\rm X} \lesssim L_{\rm crit}$ and the *Suzaku* measurement at $L_{\rm X} \lesssim L_{\rm Coul}$. Taking the uncertainties of the distance measurement into account, the similarity of the cyclotron line energy measurements is not inconsistent with the Becker et al. (2012) picture. In the case of wind accretion XTE J1946+274 would have been supercritical during both measurements and a negative $E_{\rm CRSF}$-$L_{\rm X}$ correlation would be expected. Calculating the difference in emission heights for supercritical accretion following equation (40) of Becker et al. (2012) and assuming a dipole magnetic field, $\Delta E_{\rm CRSF} \lesssim 1.4\,$keV is expected for

the two luminosities. This is comparable to the uncertainties of the two $E_{\rm CRSF}$ measurements, i.e., though unlikely, we cannot rule out the presence of such a change. We note that wind accretion has so far only been discussed as a possibility for explaining the $E_{\rm CRSF}$-$L_{\rm X}$ relationship of persistent, non-Be, low luminosity sources like Vela X-1 and 4U 1538−522 (Fürst et al., 2014; Hemphill et al., 2014). We did not include the data from Müller et al. (2012) because the presence of a CRSF at 25 keV at fluxes between the 1998 and 2010 extremes is only marginally supported (see §7.4.2). However, a higher emission region at intermediate fluxes in the Coulomb braking regime (disk accretion) is again consistent with the Becker et al. (2012) picture while it is not consistent in the supercritical regime (wind accretion). Using the more precise treatment of the critical luminosity by Mushtukov et al. (2015) is qualitatively in agreement with this picture.

We can calculate the CRSF emission region height for a subcritical source at which the Coulomb interactions start decelerating the plasma using equation (51) of Becker et al. (2012):

$$h_{\rm c} = 1.48\times10^{5}{\rm cm}\left(\frac{\lambda}{0.1}\right)^{-1}\left(\frac{\tau_*}{20}\right)\left(\frac{M_{\rm NS}}{1.4\,M_\odot}\right)^{19/14}\left(\frac{R_{\rm NS}}{10\,{\rm km}}\right)^{1/14} \cdot\left(\frac{B_{\rm NS}}{10^{12}\,{\rm G}}\right)^{-4/7}\left(\frac{L_{\rm X}}{10^{37}\,{\rm erg\,s^{-1}}}\right)^{-5/7} \quad (7.12)$$

where the following parameters are as defined in Becker et al. (2012): $\lambda = 0.1$ describes the disk accretion case, $\tau_* \sim 20$ is the Thomson optical depth in the Coulomb regime, $M_{\rm NS} = 1.4\,M_\odot$ and $R_{\rm NS} = 10\,{\rm km}$ are typical values for the neutron star mass and radius. We obtained $h_{\rm c} = 211\,{\rm m}$ for the emission height using $B_{\rm NS} = 3.1(1+z)\times10^{12}\,{\rm G}$ with $z = 0.3$ and $L_{\rm X} = 5\times10^{37}\,{\rm erg\,s^{-1}}$ (Heindl et al., 2001).

The similarity of the observed pulse profiles at low and high fluxes supports

a scenario where no strong changes in the emission geometry happen over and between outbursts. The 2010 *RXTE* and *Suzaku* pulse profiles of XTE J1946+274 are double-peaked with a deep and a shallow minimum that show weak energy dependence of the depths (Figure 7.3). This structure is strongly similar to what has been observed by Wilson et al. (2003) and Paul et al. (2001) during the 1998 outburst with other instruments at different luminosities. The source even shows a double-peaked profile during quiescence as observed by *Chandra* (Özbey Arabacı et al., 2015). Interestingly the ∼20–40 keV pulse profile of A 0535+26 is very similar to that of XTE J1946+274 (Caballero et al., 2007; Sartore et al., 2015). Modeling the profiles of the 2005 August/September outburst of A 0535+26, Caballero et al. (2011) determined a possible emission pattern by taking into account the contribution of each of the two magnetic poles. They assumed a dipole magnetic field with axisymmetric emission regions. The asymmetry of the pulse profile minima is explained by a small offset of one of the emission regions from being antipodal. The profiles for A 0535+26 were obtained when the source had a luminosity of $L_{3-50\,\mathrm{keV}} \sim 0.8 \times 10^{37}\,\mathrm{erg\,s^{-1}}$ (Caballero et al., 2011), i.e., not unlike the lower range observed for XTE J1946+274.

In summary, for XTE J1946+274 the stability of the pulse profile shape, the lack of strong changes of the spectral shape (§7.5.4), and the possibly constant CRSF energy with luminosity all indicate that there have been no major changes in the accretion column structure and emission geometry over the broad range of moderate luminosities covered by observations.

7.6 Summnay and Conclusions

In this Chapter we analyzed a 50 ks *Suzaku* observation of the accreting pulsar XTE J1946+274 taken at the end of the second outburst in an outburst series

in 2010. We performed a detailed temporal and spectral analysis and compared our results to data available from other instruments and outbursts. In the following we summarize the results of our analysis:

1. We determined a new orbital solution based on *Fermi*-GBM and other data. Its parameters and possible intrinsic pulse period evolutions are listed in Table 7.2 and shown in Figure 7.4.

2. We observed no strong changes between the *Suzaku* spectrum and previously analyzed spectra for different luminosities and outbursts.

3. The *Suzaku* observation allowed us to extend the correlation between the continuum X-ray flux and the flux of the narrow Fe Kα line to lower fluxes than observed before. Comparing the observed correlation with the theoretically expected values for fluorescence emission shows a possible slight elevation of the line flux. This could indicate either an overabundance of iron, a more complex ionization structure, or a more complex spatial structure of the emitting medium than assumed by the simplest model.

4. The *Suzaku* spectrum shows a feature that can be modeled with a cyclotron line component at $35.2^{+1.5}_{-1.3}$ keV at a significance of 2.81σ.

5. The unchanging cyclotron line energy and similar pulse profile shape with luminosity between 1998 and 2010 suggest that the source does not experience strong changes in emission geometry and that XTE J1946+274 has been consistently accreting in the subcritical regime.

6. There are similarities between XTE J1946+274 and A 0535+26 regarding their pulse profile structure and a possibly unchanging cyclotron energy with luminosity. A more detailed study of these similarities could prove useful for better understanding accreting X-ray pulsars in Be systems.

XTE J1946+274 is rarely in outburst, with its two known episodes of activity having occurred approximately a decade apart. It remains a source with many unanswered questions. In particular, monitoring of possible future outbursts with sensitive instruments such as *NuSTAR* could fill the gap in the cyclotron line energy versus X-ray luminosity correlation and shed new light on the accretion mechanism of this source.

8

Pulsar Sample Analysis

This chapter builds on the single source study of XTE J1946+274 presented in the previous chapter, by expanding the spectral analysis to a sample of diverse accreting pulsars. In addition to the empirical spectral modeling, I applied a newly implemented physical continuum model and performed a first self-consistent spectral study and comparison of a larger sample of sources.

I present a detailed spectral analysis of a sample of nine luminous accreting pulsars observed with the *Suzaku* satellite. Chapters 8.1 and 8.2 introduce the sample, the *Suzaku* data used, and the data reduction process. Chapter 8.3 presents the detail of the empirical and physical fitting procedures and results for the individual sources. In Chapter 8.4, I discuss the empirical and physical results in the context of the sample. I also present the first observationally confirmed connections between the physical and empirical modeling.

This chapter is based on the manuscript, "Comprehensive Empirical and Physical Study of the X-ray Spectra of Accreting Pulsars with Suzaku" which is being prepared to be submitted for publication in the *Monthly Notices of the Royal Astronomical Society*, for which I am the primary inverstigator (Marcu-Cheatham et al. 2017, MNRAS, in prep.).

8.1 Introduction

Accreting pulsars are highly magnetic neutron stars that emit X-rays created through the gradual accumulation of matter (White et al., 1983; Nagase, 1989; Bildsten et al., 1997). They are predominantly found in High Mass X-ray Binary (HMXB) systems. They are very compact objects with strong gravitational fields. Their high magnetic (B) fields of $\sim 10^{12}$ G (Coburn et al., 2002) play a critical role in the accretion mechanism (Ghosh et al., 1977; Ghosh & Lamb, 1979a,b; Anzer & Boerner, 1983; Aly, 1986).

The accretion process on to a compact object is a particularly complex phenomenon. In the general picture of a neutron star X-ray binary, the compact object accretes material from a donor star via (i) Roche Lobe overflow (Dewi & Pols, 2003), (ii) a stellar wind (Giménez-García et al., 2016), or (iii) a circumstellar disc around the optical companion (Rappaport et al., 1978). Historically, Davidson & Ostriker (1973) provided the first picture of accretion on to a highly magnetic neutron star. The material transferred by the donor star spirals in towards the pulsar forming an accretion disc. The presence of the high magnetic field disrupts the accretion disc at the Alfvén radius, where the ram gas pressure is surpassed by the neutron star's magnetic energy density (Elsner & Lamb, 1977). Past the Alfvén radius, plasma is channeled along the magnetic field lines on to one or both of the neutron star's magnetic poles. As a result, an *accretion column* forms above the surface. Inside the accretion column the plasma flows at relativistic speeds ($\sim 0.7c$). If the radiation pressure inside the column becomes sufficiently high (Shapiro & Salpeter, 1975), a radiative shock may form. For high-luminosity sources ($\geq 10^{37}\,\mathrm{erg\,s^{-1}}$, Basko & Sunyaev, 1976), a radiation-dominated radiative shock is assumed to be the main mechanism through which the plasma flow is decelerated before settling on to the surface of the pulsar (Becker, 1998). This deceleration

process and the Compton up-scattering of photons inside the accretion column produce the broadband X-ray spectra that we observe (Becker & Wolff, 2007).

One goal of this work is to create an observational foundation that can be used to further improve our theoretical understanding of accreting pulsars. Observational similarities and differences among several sources can provide insight into properties of accreting pulsars which are not apparent from studying individual sources. Here we therefore study the broadband spectra of a set of nine accreting pulsars observed with the *Suzaku* satellite. We focus on characterizing the continuum emission and also investigate additional spectral components such as interstellar and system-intrinsic absorption, blackbody emission, iron line emission, and cyclotron resonant scattering features. We first describe the spectra of the sample with commonly applied empirical models. This provides a reference for comparison to earlier studies of the individual sources as well as to the few exsiting studies of similar samples. In particular we build on the analysis performed by Coburn et al. (2002, hereafter C02) who studied a set of accreting pulsars using *Rossi X-ray Timing Explorer (RXTE)* data and investigated the influence of the magnetic field on the spectral continuum emission. Our main goal for the sample, however, is the application of a physically descriptive continuum model, surpassing the current standard spectral fitting with empirical continua. Modelling the broadband X-ray spectra with a physical model is critical for understanding the accretion process for highly magnetic pulsars. Thus, we apply the physical Radiation-Dominated Radiative Shock model, introduced by Becker & Wolff (2007) and recently fitted by Wolff et al. (2016) to *NuSTAR* data of the accreting pulsar Her X-1, to the spectra of the sample. We further evaluate whether comparison between the empirical and physical results can provide a basis for physically interpreting the former.

In Section 8.2 we introduce the pulsar sample and the individual source

properties, the *Suzaku* observations, and the data reduction process. In Section 8.3 we describe the empirical and physical continuum models that we applied and our spectral fit results. Section 8.3.1 focuses on the empirical continuum modelling and the additional spectral components, while Section 8.3.2 contains the detailed results of our best empirical spectral fits and compares them with those of previous studies for the individual sources. Section 8.3.3 focuses on the description of the physical continuum model, along with the fit procedure for the new model implementation, while Section 8.3.4 contains the physical fit results. In Section 8.4 we discuss our results. Section 8.4.1 and Section 8.4.2 address the empirical fit results regarding the continuum and the additional components, respectively. Section 8.4.3 presents a comparison with the previous work by C02 and others. Section 8.4.4 discusses the physical fit results and their relationship to the empirical ones. In Section 8.5 we summarize the conclusions of this study.

Table 8.1: Properties of the pulsar sample.

Source	Discovery Satellite & Year	Distance [kpc]	Optical Companion	Orbital Period [d]	Pulse Period [s]	CRSF Fundamental [keV]	B-field[a] [$\times 10^{12}$ G]
LMC X-4	*Uhuru* 1971[b]	50.0[c]	O8 III[d]	$\sim$1.4[e]	$\sim$3.5[e]	-	unknown
Cen X-3	*Uhuru* 1971[f,g]	5.7(15)[h]	O 6-8 III[i]	$\sim$2.1[g]	$\sim$4.8[j]	$\sim$30[k]	3.4
1A 1118−61	*Ariel V* 1974[l]	5 ± 2[m]	O9.5IV–Ve[n]	24 ± 0.4[o]	407.72[p]	$\sim$55[p]	6.2
4U 0115+63	*Uhuru* 1971[b]	7–8[q]	B 0.2 Ve[q]	$\sim$24.3[r]	3.61[s]	12.7[t]	1.4
GX 304−1	Balloon 1967[u]	2.4(5)[v]	B2 Vne[v,w]	$\sim$132.5[x]	$\sim$272[y]	$\sim$52[z]	5.9
4U 1626−67	*Uhuru* 1972[b]	5–13[aa]	KZ TrA[ab]	0.0292[aa,ac]	7.66[ad]	$\sim$37[ae]	4.2
A 0535+26	*Ariel V* 1975[af]	1.8(6)[ag]	B0 IIIe[ah]	$\sim$111[ai]	$\sim$103.3[aj]	$\sim$45[aj,ak]	5.1
XTE J1946+274	*RXTE*-ASM 1998[al]	9.5(29)[am]	Be-IV-IVe[an]	172.7(6)[ao]	15.75[ao]	$\sim$36[ao,ap]	4.03
Vela X-1	Rocket 1967[aq]	1.9(2)[ar]	B 0.5Ib[as]	$\sim$9[at]	283[au]	$\sim$25[av]	2.86

[a] This is the magnetic field strength calculated using Equation 8.2 with the observed CRSF energies listed in the preceding column, and the neutron star gravitational redshift $z = 0.3$. [b] Giacconi et al. (1972). [c] Contopoulos et al. (1987). [d] van der Meer et al. (2007). [e] White (1978). [f] Schreier et al. (1972). [g] Giacconi et al. (1971). [h] Thompson & Rothschild (2009). [i] Ash et al. (1999). [j] Bildsten et al. (1997). [k] Santangelo et al. (1998). [l] Eyles et al. (1975). [m] Janot-Pacheco et al. (1981). [n]Chevalier & Ilovaisky (1975). [o] Staubert et al. (2011). [p] Doroshenko et al. (2010). [q] Negueruela & Okazaki (2001), we adopt a value of 7.5(5) kpc. [r] Rappaport et al. (1978). [s] Cominsky et al. (1978). [t] Santangelo et al. (1999). [u] McClintock et al. (1977). [v] Parkes et al. (1980). [w] Mason et al. (1978). [x] Priedhorsky & Terrell (1983); Manousakis et al. (2008). [y] McClintock et al. (1977). [z] Yamamoto et al. (2011). [aa] Chakrabarty (1998), we adopt a value of 9(4) kpc. [ab] McClintock et al. (1977). [ac] Middleditch et al. (1981). [ad] Levine et al. (1988). [ae] Orlandini et al. (1998). [af] Rosenberg et al. (1975). [ag] Giangrande et al. (1980), consistent with this early measurement we adopt a value of 1.86(60) keV based on the recent *Gaia* parallax (Gaia Collaboration et al., 2016). [ah] Steele et al. (1998). [ai] Finger et al. (1996). [aj] Caballero et al. (2007). [ak] Caballero et al. (2013). [al] Smith & Takeshima (1998). [am] Wilson et al. (2003). [an] Verrecchia et al. (2002). [ao] Marcu-Cheatham et al. (2015). [ap] Heindl et al. (2001). [aq] Chodil et al. (1967). [ar] Sadakane et al. (1985). [as] Hiltner et al. (1972). [at] Kreykenbohm et al. (2008). [au] McClintock et al. (1976). [av] Kendziorra et al. (1992); Kretschmar et al. (1996, 1997).

8.2 Pulsar Sample and Data Reduction

8.2.1 Sample Selection

Accreting pulsars show considerable variety. For example, the type of donor star and the system geometry determine the material transfer mechanism (via Roche-Lobe overflow, stellar wind capture, or circumstellar disc crossing). These types of systems can be persistent or transient, with fluxes ranging from being undetectable in quiescence to outbursts brighter than the Crab. Accreting pulsars also cover a wide range of pulse periods and magnetic fields. Our choice of accreting pulsars is motivated by covering a broad range of accreting pulsar properties to account for their diversity. The pulsars studied are: LMC X-4, Cen X-3, 1A 1118−61, 4U 0115+63, GX 304−1, 4U 1626−67, A 0535+26, XTE J1946+274, and Vela X-1. Table 8.1 shows source properties of interest: discovery instrument and year, distance to the source, optical companion type, orbital and pulse periods, observed cyclotron resonant scattering feature (CRSF) fundamental line energy, and magnetic field strength. Eight of the sources are High Mass X-ray Binaries (HMXB), with LMC X-4, Cen X-3, and Vela X-1 being persistent sources with O and B stellar companions, and 1A 1118−61, 4U 0115+63, GX 304−1, A 0535+26, and XTE J1946+274 being transients with Oe and Be stellar companions. 4U 1626−67 is a persistent source and the only Low Mass X-ray Binary (LMXB) in the sample. The sources cover a wide range of pulse periods (∼3.5–407 s), as well as observed fundamental CRSF energies (∼10–55 keV) and corresponding intrinsic magnetic field ranges (∼1.4–6.2 G). LMC X-4 is the only source in the sample that does not have a confirmed cyclotron line (Tsygankov & Lutovinov, 2005). However, LMC X-4 is very luminous and makes for an ideal candidate to study the continuum. All sources have been observed with *Suzaku*. We chose observations with luminosities

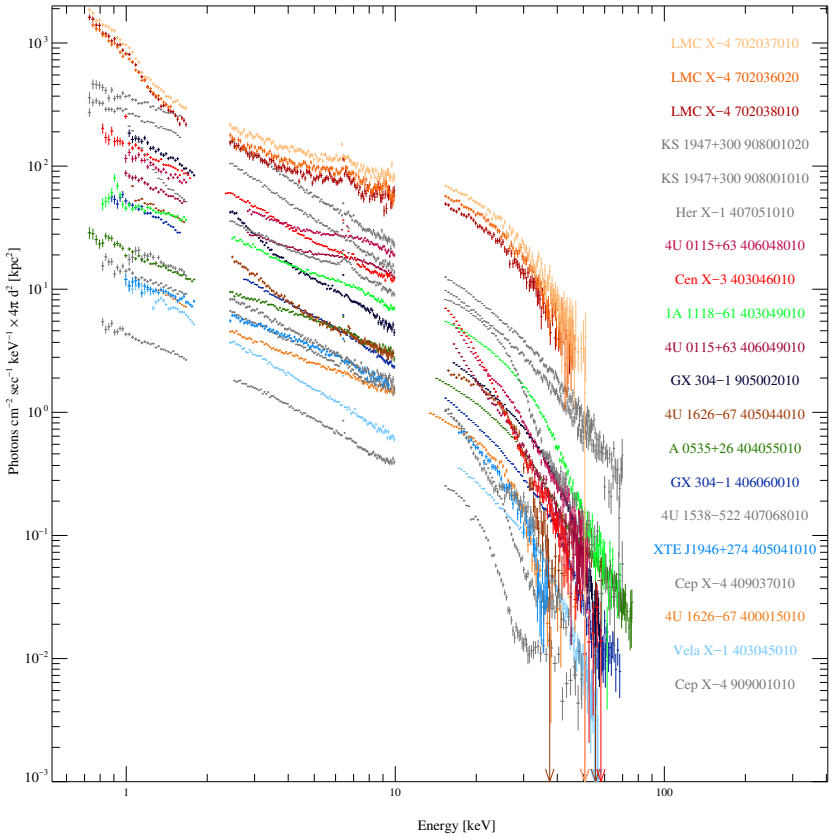

Figure 8.1: Luminosity-sorted *Suzaku* spectra of several accreting pulsars, corrected for absorption. See Table 8.1 for the adopted distances. XIS 3 data are shown for <10 keV and PIN data are shown for >10 keV. The sources in color are those from the sample studied in this work.

of $\sim 10^{36}\,\mathrm{erg\,s^{-1}}$ and higher because the physical model we are testing applies to sources with luminosities high enough to form a radiative shock inside the accretion column. Note that since we analyse time-averaged spectra, we extracted data for times of constant hardness (see Section 8.2.2 for more details). Figure 8.1 shows an overview of luminosity-sorted *Suzaku* spectra of accreting pulsars, including those from our sample.

Table 8.2: *Suzaku* observation log.

Source	Sequence	Start Time [MJD]	Start Day [yyyy-mm-dd]	Exposure[a] [ks]	Window & Burst	Aim Point	Exclusion[b] [arcsec]
LMC X-4	702036020[c]	54561.554	2008-04-05	20.5	1/8:Normal	XIS	15
LMC X-4	702037010[c]	54507.064	2008-02-11	17.0	1/8:Normal	XIS	10
LMC X-4	702038010[c]	54480.564	2008-01-15	19.9	1/8:Normal	XIS	-
Cen X-3	403046010[d]	54808.290	2008-12-08	34.2	1/4:Burst	HXD	30
1A 1118−61	403049010[e]	54846.575	2009-01-15	29.0	1/4:Burst	HXD	50
4U 0115+63	406048010[f]	55747.045	2011-07-05	16.8	1/4:Burst	XIS	60
4U 0115+63	406049010[f]	55750.056	2011-07-08	38.5	1/4:Normal	XIS	60
GX 304−1	406060010[g]	55957.561	2012-01-31	12.6	1/4:Burst	XIS	60
GX 304−1	905002010[g,h]	55421.691	2010-08-13	3.7	1/4:Burst	HXD	60
4U 1626+67	400015010[i]	53803.054	2006-03-09	102.7	1/8:Normal	XIS	-
4U 1626+67	405044010[i]	55445.541	2010-09-06	20.0	1/4:Normal	XIS	30
A 0535+26	404055010	55292.514	2010-04-06	2.4	1/4:Burst	HXD	20
XTE J1946+274	405041010[j,k]	55481.204	2010-10-12	42.0	1/4:Normal	HXD	-
Vela X-1	403045010[l]	54634.198	2008-06-17	77.5	1/4:Normal	XIS	70

[a] XIS 3 exposure. [b] Radius of the circular region excluded from the centre of the source region in order to reduce pile-up. The *Suzaku* observations listed in this table were previously studied by: [c] Hung et al. (2010); [d] Naik et al. (2011); [e] Suchy (2011); Maitra et al. (2012); [f] Iyer et al. (2015); [g] Jaisawal et al. (2016); [h] Yamamoto et al. (2011); [i] Camero-Arranz et al. (2012); [j] Maitra & Paul (2013b); Marcu-Cheatham et al. (2015); [k] Doroshenko et al. (2011); Maitra & Paul (2013c); Odaka et al. (2013).

8.2.2 Observations and Data Reduction

In order to create a relevant comparison among sources, the extraction process of the *Suzaku* data was kept as consistent as possible between all the observations. We extracted data obtained with the X-ray Imaging Spectrometer (XIS, Koyama et al., 2007) and the PIN instrument from the Hard X-ray Detector (HXD, Takahashi et al., 2007).

At the time of these observations the CCD cameras 0, 1, 3 of the XIS were functional and were operated with a 1/4 window sub-array option for the observations in question, with two exceptions where the 1/8 window sub-array option was used: all LMC X-4 observations and one of the 4U 1626−67 observations. Depending on the brightness of the source during the observation, the XIS CCDs operated in either burst or normal mode, i.e., taking partial of full exposures per read-out cycle, respectively, in order to reduce pile-up.

The observation properties are given in the *Suzaku* observation log (Table 8.2). The times of the *Suzaku* observations for each source can be seen in the context of the long-term light curves observed by *Swift*-BAT shown in Appendix A.1. Due to the large distance, LMC X-4 generally has a low flux, therefore, *Suzaku* observed it in normal mode during different super-orbital cycle phases. XTE J1946+274 had a strong outburst series in 2010. *Suzaku* observed it at the end of the second outburst in the series at low flux, in normal mode. Vela X-1 had high pile-up due to the fact that it was observed at high flux in normal mode. The Cen X-3 observation took place in burst mode since the source is known to be persistent and bright. Both GX 304−1 observations were performed in burst mode, due to the fact that they were taken close to the peak of two different outbursts during a 2010–2012 outburst series. The two 4U 0115+63 observations took place during an outburst decline: the first one in burst mode and the second one in normal mode. 1A 1118−61 was

also observed twice by *Suzaku* during an outburst. For this work, we use only data from the higher luminosity observation. Similarly, we use the highest luminosity observation of A 0535+26, taken in burst mode during the decline of a 2009 outburst. Note also that the A 0535+26 observation was performed in burst mode with one of the smallest partial exposures (0.135 s in a 2 s readout cycle) and may have been affected by out-of-time events, i.e., events recorded during charge transfer[1].

We reprocessed and extracted XIS and PIN data according to the *Suzaku* Data Reduction/ABC Guide (ISAS/JAXA & X-ray Astrophysics Laboratory NASA Goddard Space Flight Center, 2013) using the `HEASOFT` v6.16 software package. We used the *Suzaku* reprocessing tool `aepipeline` with the default screening parameters and the most recent (and final) calibration database (`CALDB`) releases HXD-20110913, XIS-20160607, and XRT-20110630. We further filtered the screened XIS events, in order to exclude times of telemetry saturation. We transferred the XIS and PIN events to the barycenter of the solar system with `aebarycen`.

Initial XIS images were extracted with `xselect`. We used the tool `aeattcor2`[2], which corrected the data for remaining thermal attitude uncertainties by using mean event positions as a function of time. Some images still show a moderate systematic attitude instability, which appears as a double-peaked, elongated point spread function (PSF, Maeda, 2010c,b,a). Note, however, that the spectral analysis is not expected to be affected by this effect (Maeda, 2010b,a). For data taken in burst mode the events were further filtered using the corresponding burst Good Time Intervals (GTI).

We then determined the XIS regions to be used for the extractions. For most observations, the source extraction regions are circles with radii of 120.″0

[1] `ftp://legacy.gsfc.nasa.gov/suzaku/nra\_info/suzaku\_td\_xisfinal.pdf`

[2] The `aeattcor2` tool is based on the ISIS script aeattcor.sl by John Davis, see `http://space.mit.edu/cxc/software/suzaku/aeatt.html`.

centered on the PSFs. These regions were used for all XIS units and editing modes used for event storage ("2×2","3×3", and "5×5"). LMC X-4 and one of the 4U 1626−67 observations require a smaller source region radius of 70.″0 due to the 1/8 window sub-array option. These circular regions are large enough to contain most of the source events, but are confined within their respective windows. For bright sources a pile-up effect occurs in imaging instruments when two or more photons hit a detector pixel during one readout cycle (Davis, 2001; Yamada et al., 2012). As a result the pixel reads one photon with a high energy. This effect hardens the source spectrum and may lead to incorrect results. Therefore, we selected circular regions to exclude pile-up fractions $\gtrsim 3\%$ from the centre of the source extraction regions.[3] The radii for the pile-up regions for each observation are listed in Table 8.2. The background was extracted from circular regions with the same radii as the respective source region: 70.″0 for LMC X-4 and one of the 4U 1626−67 observations and 120.″0 for all the other observations. The background regions are located within the windows, but as far from the PSFs as possible. The dead zone of XIS 0 (Tsujimoto et al., 2010b) was avoided during the background region selection. The XIS source and background event files, images, light curves, and spectra were then generated using `xselect`.

We extracted XIS source and background light curves in the $0.5 - 10$ keV, $0.5 - 5$ keV, and $5 - 10$ keV energy ranges with a resolution of 128 s. For PIN we extracted light curves in the $10 - 60$ keV range with a time binning of 128 s. We used `hxdpinxblc`, which produces the total dead-time corrected PIN light curve, the non X-ray background light curve, and the background-subtracted source light curve.

We used these XIS and PIN light curves to obtain hardness ratios (5–

[3]More details about pile-up estimates and extraction can be found at `http://space.mit.edu/cxc/software/suzaku/pest.html`.

10 keV/0.5–5 keV and 10–60 keV/0.5–5 keV). LMC X-4, 1A 1118−61, 4U 0115+63, GX 304−1, 4U 1626−67, A 0535+26, and XTE J1946+274 showed approximately constant hardness ratios. Therefore, we extracted observation-averaged spectra for these sources. Cen X-3 and Vela X-1 showed changing hardness patterns during the *Suzaku* observations (Fig. 8.2). Therefore, we extracted spectra for the times when the hardness was comparatively constant: 54808.64–54809.07 MJD for Cen X-3 and 54634.25–54634.83 MJD for Vela X-1. Note that during this time period, Vela X-1 experienced 'low states', which have been studied by Odaka et al. (2013) and Doroshenko et al. (2011). These short low flux periods were excluded from our extraction.

We applied the XIS binning suggested by Nowak et al. (2011), which corresponds to a resolution close to the half-width half-maximum of the spectral resolution of the instrument. We used the `xisrmfgen` and `xissimarfgen` tools to generate the energy and ancillary responses. The XIS 3 exposure times for all the observations are listed in Table 8.2.

Using `hxdpinxbpi`, we extracted the dead-time corrected PIN source spectrum and the total background spectrum, i.e., the sum of cosmic X-ray background (CXB - ∼5% of the PIN background flux) and non X-ray modeled background (NXB - ∼95% of the PIN background flux).[4] We chose the appropriate PIN response files of the calibration epoch for each observation.[5] The PIN spectra were extracted with 256 bins and rebinned at high energies ($\gtrsim$ 30 keV) for better signal-to-noise ratios.

[4] `ftp://legacy.gsfc.nasa.gov/suzaku/data/background/`
[5] `http://heasarc.gsfc.nasa.gov/docs/suzaku/analysis/pinepochs.html`

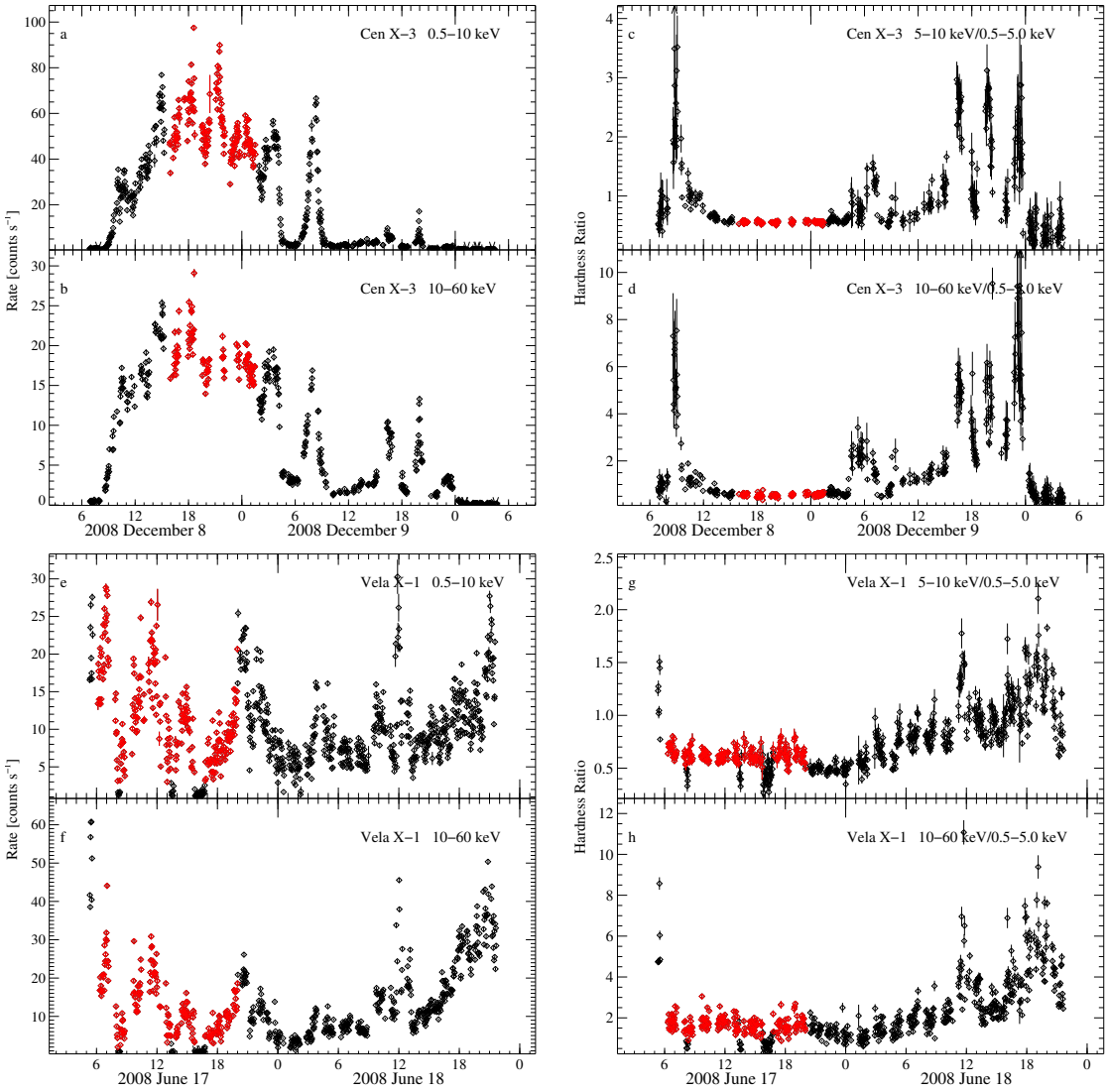

Figure 8.2: *Suzaku* light curves and hardness ratios for Cen X-3 (a–d), ObsID 403046010, and Vela X-1 (e–h), ObsID 403045010. We extracted spectra from times of approximately constant hardness. The corresponding data are highlighted in red.

Table 8.3: Best fit continuum parameters obtained with the `fdcut` model, cross-calibration constants and goodness of fit.

Source	Sequence	L_{37}^{a} [erg s^{-1}]	Γ	$E_{\rm fold}$ [keV]	$E_{\rm cut}$ [keV]	A_Γ [keV^{-1} cm^{-2} s^{-1}]	$c_{\rm XIS\,1}$	$c_{\rm XIS\,3}$	$c_{\rm PIN}$	$\chi^2_{\rm red}$/dof
LMC X-4	702037010	31.4(1)	0.67(2)	8.1(6)	27(1)	$1.01(2)\times10^{-2}$	1.091(9)	1.079(8)	1.39(5)	1.25/521
LMC X-4	702036020	25.44(8)	0.66(2)	$7.7^{+0.7}_{-0.6}$	27(1)	$0.78(2)\times10^{-2}$	1.16(1)	1.080(9)	$1.43^{+0.06}_{-0.05}$	1.06/491
LMC X-4	702038010	20.63(7)	0.70(2)	$7.2^{+0.7}_{-0.6}$	26(1)	$0.70(2)\times10^{-2}$	1.16(1)	1.11(1)	$1.49^{+0.07}_{-0.06}$	1.26/496
Cen X-3	403046010	4.0(21)	$1.06^{+0.18}_{-0.09}$	$6.8^{+0.8}_{-0.6}$	19^{+3}_{-4}	$0.37^{+0.12}_{-0.06}$	-[c]	0.965(3)	$0.96^{+0.10}_{-0.11}$	1.23/355
1A 1118−61	403049010	4.0(32)	$0.63^{+0.07}_{-0.21}$	$10.1^{+0.2}_{-1.1}$	$21.6^{+2.4}_{-0.6}$	$0.125^{+0.009}_{-0.035}$	-[c]	0.980(3)	$1.21^{+0.06}_{-0.03}$	1.18/395
4U 0115+63	406048010	3.973(6)	$1.0^{+0.1}_{-0.2}$	$9.7^{+0.6}_{-0.5}$	12^{+6}_{-8}	$0.23^{+0.03}_{-0.02}$	1.036(4)	1.009(4)	1.40	1.26/459
4U 0115+63	406049010	2.746(4)	$1.1^{+0.1}_{-0.2}$	$8.9^{+0.8}_{-0.6}$	17^{+5}_{-6}	0.14(1)	1.046(3)	1.012(3)	1.40	1.18/455
GX 304−1	905002010	2.0(9)	$0.915^{+0.002}_{-0.155}$	$16.4^{+2.6}_{-0.2}$	0.0[b]	$1.684^{+0.336}_{-0.003}$	-[c]	0.940(4)	$1.012^{+0.033}_{-0.003}$	1.09/371
4U 1626−67	405044010	1.36(120)	1.04(2)	4^{+3}_{-2}	45^{+4}_{-6}	0.030(1)	0.973(6)	0.987(6)	1.26(4)	1.09/448
A 0535+26	404055010	1.2(4)	$0.61^{+0.02}_{-0.04}$	$15.0^{+0.2}_{-0.4}$	8^{+3}_{-4}	$0.55^{+0.05}_{-0.03}$	-[c]	-[c]	$0.900^{+0.013}_{-0.005}$	1.15/299
GX 304−1	406060010	0.9(4)	$0.93^{+0.07}_{-0.08}$	$13.8^{+0.6}_{-0.4}$	0.0[b]	$0.90^{+0.11}_{-0.05}$	-[c]	1.014(3)	$1.02^{+0.09}_{-0.08}$	1.16/380
4U 1626−67	400015010	0.58(52)	$0.75^{+0.02}_{-0.03}$	8^{+2}_{-1}	24^{+1}_{-2}	$0.89^{+0.03}_{-0.02}\times10^{-2}$	1.020(5)	1.009(4)	$0.96^{+0.03}_{-0.02}$	1.28/423
XTE J1946+274	405041010	0.5(3)	0.59(2)	9.1(4)	0.0[b]	$2.11^{+0.05}_{-0.02}\times10^{-2}$	1.052(7)	0.945(6)	$1.28^{+0.06}_{-0.05}$	1.17/449
Vela X-1	403045010	0.30(6)	$1.22^{+0.06}_{-0.08}$	10^{+2}_{-1}	29^{+3}_{-6}	0.26(3)	1.032(4)	0.973(4)	$1.24^{+0.07}_{-0.08}$	1.22/506

[a] 1–80 keV unabsorbed luminosities during the respective *Suzaku* observation in units of 10^{37} erg s^{-1}. [b] The $E_{\rm cut}$ value for these fits were consistent with zero. [c] We removed data from these instruments due to calibration issues predominanty in the back-illuminated XIS unit.

Table 8.4: Best fit fully ($N_{\rm H1}$) and partially ($N_{\rm H2}$ and covering fraction f) covering absorption parameters compared to the interstellar absorption along the line of sight (Galactic $N_{\rm H}$, Dickey & Lockman, 1990).

Source	Sequence	$N_{\rm H1}^{\rm FDCUT}$ $[\times10^{22}{\rm cm}^{-2}]$	$N_{\rm H2}^{\rm FDCUT}$ $[\times10^{22}{\rm cm}^{-2}]$	$f^{\rm FDCUT}$	$N_{\rm H1}^{\rm BWSIM}$ $[\times10^{22}{\rm cm}^{-2}]$	$N_{\rm H2}^{\rm BWSIM}$ $[\times10^{22}{\rm cm}^{-2}]$	$f^{\rm BWSIM}$	21 cm $N_{\rm H}$ $[\times10^{22}{\rm cm}^{-2}]$
LMC X-4	702037010	0.057	-	-	0.057	-	-	0.057
LMC X-4	702036020	0.057	-	-	0.057	-	-	0.057
LMC X-4	702038010	0.057	-	-	0.057	-	-	0.057
Cen X-3	403046010	$1.63^{+0.08}_{-0.06}$	6^{+3}_{-2}	$0.26^{+0.10}_{-0.07}$	$1.0^{+0.3}_{-0.2}$	13^{+10}_{-3}	$0.25^{+0.10}_{-0.09}$	0.100
1A 1118−61	403049010	1.26(4)	13(2)	0.5(1)	$1.29^{+0.05}_{-0.04}$	12^{+3}_{-2}	0.4(1)	1.200
4U 0115+63	406048010	$1.72^{+0.10}_{-0.26}$	2^{+2}_{-1}	$0.30^{+0.24}_{-0.07}$	-	-	-	0.860
4U 0115+63	406049010	$1.6^{+0.2}_{-0.7}$	$1.5^{+1.1}_{-0.5}$	$0.5^{+0.4}_{-0.2}$	-	-	-	0.860
GX 304−1	905002010	$1.71^{+0.05}_{-0.01}$	$9.6^{+1.1}_{-0.1}$	$0.761^{+0.056}_{-0.002}$	1.69(6)	10(1)	$0.76^{+0.04}_{-0.07}$	1.060
4U 1626−67	405044010	0.10	-	-	0.10	-	-	0.100
A 0535+26	404055010	$0.74^{+0.06}_{-0.12}$	-	-	$0.41^{+0.07}_{-0.08}$	-	-	0.450
GX 304−1	406060010	$1.71^{+0.05}_{-0.06}$	5(1)	$0.59^{+0.07}_{-0.11}$	$1.62^{+0.07}_{-0.04}$	$7.5^{+1.7}_{-0.8}$	$0.64^{+0.05}_{-0.09}$	1.060
4U 1626−67	400015010	0.10	-	-	0.10	-	-	0.100
XTE J1946+274	405041010	1.75(3)	-	-	0.9(2)	-	-	0.940
Vela X-1	403045010	$2.75^{+0.05}_{-0.06}$	$8.6^{+1.0}_{-1.1}$	$0.29^{+0.04}_{-0.05}$	2.35(2)	14^{+2}_{-1}	0.16(1)	0.410

Table 8.5: Best fit `gauss` parameters for the 10 keV feature.

Source	Sequence	$E_{10\,\mathrm{keV}}^{\mathrm{FDCUT}}$ [keV]	$\sigma_{10\,\mathrm{keV}}^{\mathrm{FDCUT}}$ [keV]	$A_{10\,\mathrm{keV}}^{\mathrm{FDCUT}}$ [ph cm^{-2} s^{-1}]	$L_{10\,\mathrm{keV}}^{\mathrm{FDCUT}}$ [$\times 10^{35}$ erg s^{-1}]	$E_{10\,\mathrm{keV}}^{\mathrm{BWSIM}}$ [keV]	$\sigma_{10\,\mathrm{keV}}^{\mathrm{BWSIM}}$ [keV]	$A_{10\,\mathrm{keV}}^{\mathrm{BWSIM}}$ [ph cm^{-2} s^{-1}]	$L_{10\,\mathrm{keV}}^{\mathrm{BWSIM}}$ [$\times 10^{35}$ erg s^{-1}]
Cen X-3	403046010	13.4(7)	$3.4^{+1.0}_{-0.6}$	$0.06^{+0.03}_{-0.01}$	21.55	$13.0^{+0.7}_{-1.4}$	$3.4^{+1.2}_{-0.6}$	$0.05^{+0.04}_{-0.02}$	19.04
4U 0115+63	406048010	$7.86^{+0.10}_{-0.09}$	2.9(2)	0.13(2)	87.54	-	-	-	-
4U 0115+63	406049010	7.8(1)	$3.2^{+0.3}_{-0.2}$	0.10(2)	67.15	-	-	-	-
GX 304−1	905002010	$10.0^{+0.2}_{-0.5}$	$1.5^{+0.2}_{-0.1}$	$-0.036^{+0.004}_{-0.015}$	-2.47	$10.0^{+0.9}_{-0.6}$	$1.5^{+0.5}_{-0.6}$	−0.03(2)	-2.23
GX 304−1	406060010	9.16[a]	$1.4^{+0.9}_{-0.6}$	$-0.008^{+0.009}_{-0.011}$	-0.57	$9.3^{+1.2}_{-0.4}$	$0.8^{+0.8}_{-0.4}$	$-0.003^{+0.001}_{-0.003}$	-0.17
Vela X-1	403045010	8.3(5)	$1.0^{+0.6}_{-0.5}$	$-0.001^{+0.001}_{-0.002}$	-0.06	10^{+1}_{-2}	$0.8^{+0.6}_{-0.8}$	$0.002^{+0.040}_{-0.001}$	0.08

[a] Frozen - parameter could not be constrained.

Table 8.6: Best fit `bbody` parameters for the blackbody components and their luminosities.

Source	Sequence	$kT_{\rm BB}^{\rm FDCUT}$ [keV]	$\rm Norm_{BB}^{FDCUT,a}$ [$\times10^{-3}$]	$L_{\rm BB}^{\rm FDCUT}$ [$\times10^{35}$]	$kT_{\rm BB}^{\rm BWSIM}$ [keV]	$\rm Norm_{BB}^{BWSIM}$ [$\times10^{-3}$]	$L_{\rm BB}^{\rm BWSIM}$ [$\times10^{35}$]
LMC X-4	702037010	0.169(3)	0.51(1)	128.17	0.159(2)	0.53(2)	131.82
LMC X-4	702036020	0.178(3)	0.40(1)	100.24	$0.169^{+0.005}_{-0.003}$	$0.39^{+0.02}_{-0.04}$	98.54
LMC X-4	702038010	0.179(3)	0.44(1)	110.46	$0.173^{+0.004}_{-0.002}$	$0.46^{+0.02}_{-0.04}$	114.56
1A 1118−61	403049010	$0.65^{+0.15}_{-0.07}$	4^{+3}_{-2}	8.85	$0.6^{+0.6}_{-0.2}$	1^{+2}_{-1}	2.98
GX 304−1	905002010	$0.414^{+0.003}_{-0.015}$	$59.0^{+0.5}_{-14.3}$	33.97	0.41(2)	59^{+9}_{-8}	33.76
4U 1626−67	405044010	$0.485^{+0.009}_{-0.008}$	1.16(5)	9.42	$0.471^{+0.009}_{-0.008}$	1.51(7)	12.27
A 0535+26	404055010	$0.21^{+0.02}_{-0.03}$	2^{+1}_{-2}	0.69	0.30(1)	$2.4^{+0.8}_{-0.3}$	0.76
GX 304−1	406060010	$0.3^{+1.3}_{-0.3}$	8^{+3}_{-4}	4.62	$0.41^{+0.06}_{-0.03}$	11^{+5}_{-7}	6.28
4U 1626−67	400015010	0.30(2)	$0.141^{+0.007}_{-0.006}$	1.15	0.28(1)	$0.17^{+0.05}_{-0.01}$	1.37

[a] In `xspec` the normalization of the `bbody` model is defined as L_{39}/D_{10}^2, where L_{39} is the source luminosity in units of $10^{39}\,\rm erg\,s^{-1}$ and D_{10} is the distance to the source in units of 10 kpc.

Table 8.7: Best fit `gauss` parameters for the iron fluorescence lines and their luminosities in the empirical `fdcut`-based fits. See text and references therein for additional narrow emission lines included in the fits.

Source	Sequence	Spectral Line	E [keV]	σ [eV]	A [$\times 10^{-4}$ ph s^{-1} cm^{-2}]	$L_{\rm Fe}$ [$\times 10^{33}$ erg s^{-1}]	EW [eV]
LMC X-4	702037010	Fe Kα	$6.35^{+0.03}_{-0.04}$	1.0	0.5(2)	141.24	14.8
		Broad Fe	$6.62^{+0.07}_{-0.06}$	456^{+97}_{-89}	4.8(9)	1430.07	137.7
LMC X-4	702036020	Fe Kα	$6.44^{+0.03}_{-0.04}$	1.0	0.5(2)	148.93	19.8
		Broad Fe	6.58(7)	516^{+138}_{-129}	$3.9^{+0.9}_{-0.8}$	1175.51	160.7
LMC X-4	702038010	Fe Kα	$6.39^{+0.02}_{-0.03}$	1.0	0.6(2)	173.70	24.3
		Broad Fe	$6.55^{+0.06}_{-0.05}$	382^{+98}_{-81}	$3.5^{+0.7}_{-0.6}$	1052.81	155.0
Cen X-3	403046010	Fe Kα	$6.407^{+0.006}_{-0.004}$	1.0	31^{+2}_{-3}	120.99	62.4
		Fe XXV	$6.658^{+0.010}_{-0.008}$	1.0	21(3)	80.80	41.7
		Fe XXVI	6.97(2)	90^{+30}_{-35}	15^{+4}_{-5}	58.52	34.6
1A 1118−61	403049010	Fe Kα	$6.397^{+0.006}_{-0.005}$	1.0	17(1)	51.70	50.8
4U 0115+63	406048010	Fe Kα	$6.34^{+0.04}_{-0.03}$	1.0	$3.5^{+0.9}_{-1.0}$	23.31	8.9
		Fe XXV	$6.65^{+0.02}_{-0.03}$	1.0	5.1(10)	34.64	13.5
4U 0115+63	406049010	Fe Kα	$6.41^{+0.04}_{-0.05}$	1.0	$3.0^{+0.6}_{-0.7}$	19.88	11.4
		Fe XXV	$6.68^{+0.06}_{-0.07}$	1.0	2.3(6)	15.26	8.9
GX 304−1	905002010	Fe Kα	$6.41^{+0.01}_{-0.02}$	1.0	38(5)	26.23	33.8
4U 1626−67	405044010	Broad Fe	6.75(5)	129^{+56}_{-61}	1.5(4)	14.89	37.4
A 0535+26	404055010	Fe Kα	6.39(3)	1.0	20(5)	7.84	23.5
GX 304−1	406060010	Fe Kα	6.41(1)	1.0	17(2)	11.93	26.8
		Fe XXV	$6.70^{+0.04}_{-0.05}$	1.0	3(2)	2.30	6.1
		Fe XXVI & Fe Kβ	7.03(4)	1.0	4(2)	2.75	6.9
4U 1626−67	400015010	Broad Fe	6.7(1)	300^{+159}_{-117}	0.5(2)	4.54	19.8
XTE J1946+274	405041010	Fe Kα	6.40(2)	1.0	0.7(1)	7.60	30.0
Vela X-1	403045010	Fe Kα	$6.409^{+0.006}_{-0.005}$	1.0	13.4(8)	5.77	53.8
		Fe Kβ	7.06(5)	1.0	1.6(8)	0.71	7.6

Table 8.8: Best fit `gabs` parameters for the CRSF lines.

Source	Sequence	$E_{\rm CRSF}^{\rm FDCUT}$ [keV]	$\sigma_{\rm CRSF}^{\rm FDCUT}$ [keV]	$D_{\rm CRSF}^{\rm FDCUT,a}$	$E_{\rm CRSF}^{\rm BWSIM}$ [keV]	$\sigma_{\rm CRSF}^{\rm BWSIM}$ [keV]	$D_{\rm CRSF}^{\rm BWSIM}$
Cen X-3	403046010	$29.8^{+1.3}_{-0.9}$	4.00[d]	4(1)	$30.1^{+1.0}_{-0.8}$	$5.8^{+1.1}_{-1.0}$	9^{+5}_{-4}
1A 1118−61	403049010	52^{+2}_{-3}	9^{+8}_{-3}	11(7)	49^{+2}_{-1}	7(1)	7(2)
4U 0115+63	406048010	$21.1^{+0.5}_{-0.4}$ [b]	2.5(5)[b]	$1.3^{+0.5}_{-0.4}$ [b]	-	-	-
		33(2)[c]	7.00[c,d]	4.00[c,d]	-	-	-
4U 0115+63	406049010	$21.7^{+0.8}_{-0.7}$ [b]	2.5(8)[b]	$1.1^{+0.7}_{-0.5}$ [b]	-	-	-
		32(3)[c]	7.00[c,d]	4.00[c,d]	-	-	-
GX 304−1	905002010	$58.4^{+0.3}_{-21.1}$	$9.6^{+-15.9}_{-0.2}$	32^{+240}_{-6}	59^{+12}_{-4}	8^{+8}_{-2}	18^{+41}_{-9}
4U 1626−67	405044010	39(1)	$6.0^{+0.6}_{-0.7}$	37^{+9}_{-10}	$38.1^{+0.8}_{-0.7}$	$5.2^{+0.6}_{-0.5}$	26^{+5}_{-4}
A 0535+26	404055010	$44.9^{+0.6}_{-0.8}$	$10.3^{+1.2}_{-0.8}$	13(2)	$44.9^{+0.3}_{-0.1}$	$10.3^{+0.6}_{-0.3}$	$15.2^{+0.9}_{-0.4}$
GX 304−1	406060010	53(1)	$6.1^{+0.9}_{-0.8}$	$9.7^{+2.1}_{-1.0}$	53(1)	$5.7^{+1.0}_{-0.8}$	8^{+3}_{-2}
4U 1626−67	400015010	36(1)	$4.1^{+1.2}_{-0.9}$	13^{+7}_{-4}	$37.1^{+1.0}_{-0.8}$	$4.7^{+0.8}_{-0.6}$	18^{+4}_{-3}
XTE J1946+274	405041010	36^{+2}_{-1}	2.00[d]	4^{+4}_{-2}	35.61	2.00[d]	3(2)
Vela X-1	403045010	26[e]	3.5[e]	$0.9^{+0.8}_{-0.6}$	30.0[e]	4.5[e]	0.0[f]
		52(2)[b]	7.00[b,d]	9.00[b,d]	59.9(2)[b]	9(7)[b]	9.00[b,d]

[a] Note that the `gabs` implementation provides the line depth $D_{\rm CRSF} = \tau_{\rm CRSF}\sigma_{\rm CRSF}\sqrt{2\pi}$ instead of $\tau_{\rm CRSF}$. [b] Values for the CRSF first harmonic. [c] Values for the CRSF second harmonic. [d] Fixed. [e] Values for the CRSF fundamental line for which $E_{\rm CRSF}$ and $\sigma_{\rm CRSF}$ were fixed at 1/2 the value of the first harmonic's $E_{\rm CRSF}$ and $\sigma_{\rm CRSF}$ shown right below. [f] Consistent with zero.

Table 8.9: Best `fdcut`-based fit models.

Source	Sequence	Model
LMC X-4	702037010	const × tbnew × (powerlaw × fdcut + bbody + 3× gauss)
LMC X-4	702036020	const × tbnew × (powerlaw × fdcut + bbody + 3× gauss)
LMC X-4	702038010	const × tbnew × (powerlaw × fdcut + bbody + 3× gauss)
Cen X-3	403046010	const × tbnew × tbnew_pcf × (powerlaw × fdcut + 7× gauss) × gabs
1A 1118−61	403049010	const × tbnew × tbnew_pcf × (powerlaw × fdcut + bbody + 3× gauss) × gabs
4U 0115+63	406048010	const × tbnew × tbnew_pcf × (powerlaw × fdcut + 3× gauss) × gabs × gabs
4U 0115+63	406049010	const × tbnew × tbnew_pcf × (powerlaw × fdcut + 3× gauss) × gabs × gabs
GX 304−1	905002010	const × tbnew × tbnew_pcf × (powerlaw × fdcut + bbody + 2× gauss) × gabs
4U 1626−67	405044010	const × tbnew × (powerlaw × fdcut + bbody + 9× gauss) × gabs
A 0535+26	404055010	const × tbnew × edge × (powerlaw × fdcut + bbody + gauss) × gabs
GX 304−1	406060010	const × tbnew × tbnew_pcf × (powerlaw × fdcut + bbody + 4× gauss) × gabs
4U 1626−67	400015010	const × tbnew × (powerlaw × fdcut + bbody + 9× gauss) × gabs
XTE J1946+274	405041010	const × tbnew × (powerlaw × fdcut + gauss) × gabs
Vela X-1	403045010	const × tbnew × tbnew_pcf × (powerlaw × fdcut + 3× gauss) × gabs × gabs

Table 8.10: Best fit fundamental CRSF and continuum parameters obtained with the `mplcut` model, and goodness of fit.

Source	Sequence	$E_{\rm CRSF}$ [keV]	$\sigma_{\rm CRSF}$ [keV]	$D^{\rm a}_{\rm CRSF}$	Γ	$E_{\rm fold}$ [keV]	$E_{\rm cut}$ [keV]	$\chi^2_{\rm red}$/dof
Cen X-3	403046010	29.1(7)	4.00	2.5(5)	$1.08^{+0.04}_{-0.02}$	7.8(2)	18^{+3}_{-1}	1.40/503
1A 1118−61	403049010	54^{+2}_{-1}	$8.8^{+3.2}_{-1.0}$	15^{+6}_{-3}	$0.6^{+0.1}_{-0.3}$	$12.3^{+1.5}_{-0.5}$	$9.7^{+0.6}_{-0.4}$	1.23/393
4U 0115+63	406048010	9.9[b]	-	-	$1.15^{+0.10}_{-0.25}$	12^{+2}_{-1}	14^{+2}_{-5}	1.24/459
4U 0115+63	406049010	10.3[b]	-	-	$1.22^{+0.14}_{-0.08}$	$10.4^{+1.9}_{-0.9}$	$17.2^{+1.1}_{-0.8}$	1.15/455
GX 304−1	905002010	$60.3^{+0.4}_{-0.6}$	$9.0^{+0.6}_{-0.3}$	30.00	0.292(6)	$12.99^{+0.22}_{-0.03}$	0.0[c]	1.20/520
4U 1626−67	405044010	$37.8^{+0.9}_{-0.8}$	$4.6^{+0.9}_{-0.8}$	19^{+14}_{-4}	1.04(2)	14(2)	$22.7^{+0.9}_{-0.8}$	1.14/457
A 0535+26	404055010	$45.1^{+0.9}_{-0.8}$	$9.0^{+1.3}_{-0.9}$	9^{+1}_{-2}	0.69(2)	$16.9^{+0.5}_{-0.4}$	$8.1^{+0.5}_{-0.3}$	1.18/297
GX 304−1	406060010	54(1)	$6.8^{+0.8}_{-0.7}$	12(2)	$0.65^{+0.04}_{-0.03}$	$13.6^{+0.4}_{-0.3}$	$5.3^{+0.3}_{-0.5}$	1.15/519
4U 1626−67	400015010	37^{+3}_{-1}	4^{+3}_{-1}	16^{+24}_{-6}	$0.61^{+0.09}_{-0.08}$	12^{+18}_{-3}	$9.8^{+0.5}_{-0.3}$	1.30/429
XTE J1946+274	405041010	35(1)	2.00	4^{+3}_{-2}	$0.40^{+0.19}_{-0.08}$	$9.3^{+1.0}_{-0.7}$	$0.6^{+0.3}_{-1.4}$	1.13/447
Vela X-1	403045010	26.5[d]	4.05[d]	$3.81^{+0.95}_{-0.75}$	$1.27^{+0.05}_{-0.07}$	12(1)	26(1)	1.22/508

[a] Note that the `gabs` implementation provides the line depth $D_{\rm CRSF} = \tau_{\rm CRSF}\sigma_{\rm CRSF}\sqrt{2\pi}$ instead of $\tau_{\rm CRSF}$. [b] This is half the energy of the first harmonic (also show in in Fig. 8.4c). The fundamental was not fitted due to the XIS-PIN gap. [c] Consistent with zero. [d] Fixed to half the values of the first harmonic.

8.3 Spectral Modelling and Results

Since the discovery of accreting pulsars, their X-ray continua have been described with phenomenological (empirical) models which have some form of a (quasi-)exponential cut-off power law shape, e.g., a simple cutoff power law (`cutoffpl`)[6], a power law with a high energy cutoff (`plcut`, White et al., 1983)[7], a Fermi-Dirac cutoff power law (`fdcut`, Tanaka, 1986), and a combination of negative and positive exponentially cutoff power laws (`npex`, Mihara, 1995). See Müller et al. (2013b) for a summary of the empirical continuum models commonly used for describing the accreting pulsar spectral continuum. Although these models are successfully reproducing the broadband spectra of accreting pulsars, their biggest caveat is that they provide almost no information about the physical processes that result in the observed X-ray emission. Therefore, in recent years, a significant amount of work has been put into building physically descriptive continuum models for accreting pulsars (Becker & Wolff, 2005a,b, 2007; Ferrigno et al., 2009; Farinelli et al., 2012, 2016; Wolff et al., 2016). In our spectral modelling approach we first fitted the sample spectra with phenomenological models, as described in Section 8.3.1. Based on those fits, we applied the physical model introduced in Section 8.3.3. Results of the empirical and physical modelling are presented in Sections 8.3.2 and 8.3.4, respectively. Note that, unless stated otherwise, the fit results for all observations are listed in order of decreasing luminosity in the relevant tables. All uncertainties are given at the 90% level for one parameter of interest ($\Delta\chi^2 = 2.71$, Lampton et al., 1976).

[6] `https://heasarc.gsfc.nasa.gov/xanadu/xspec/manual/XSmodelCutoffpl.html`

[7] Note that, in `xspec` notation, the `plcut` model is defined as `power` × `highecut`.

8.3.1 Empirical Models

Using `xspec12` (Arnaud, 1996), we modelled the $\sim 1 - 10\,\mathrm{keV}$ XIS and $\sim 15 - [40 - 80]\,\mathrm{keV}$ PIN spectral ranges, with the exact limits depending on the source. The upper and lower XIS boundaries, as well as the lower PIN boundaries were determined by calibration uncertainties. In addition, the $\sim 1.7 - 2.4\,\mathrm{keV}$ range was excluded due to known XIS calibration uncertainties (ISAS/JAXA & X-ray Astrophysics Laboratory NASA Goddard Space Flight Center, 2013). See Fig. 8.1 for the XIS and PIN selected energy ranges for each observation. We applied the normalization constants $c_{\mathrm{XIS\,1}}$, $c_{\mathrm{XIS\,3}}$, and c_{PIN} to account for the flux cross-calibration of the respective instruments relative to XIS 0, where $c_{\mathrm{XIS\,0}}$ was fixed at 1 for all sources. Absorption and partial covering (where present) were modelled with `tbnew` and `tbnew_pcf`, updated versions of `tbabs` and `pcfabs`[8]. We used cross sections by Verner & Yakovlev (1995) and abundances by Wilms et al. (2000).

All source spectra were first fitted with empirical models. We tested continuum models commonly applied for fitting accreting X-ray pulsars: `cutoffpl`, `plcut`, `fdcut`, and `npex`. The model that consistently describes the spectra of all sources and observations in our sample is the Fermi-Dirac cutoff model (`power`×`fdcut` in `xspec`) defined as

$$M_{\texttt{fdcut}}(E) \propto E^{-\Gamma} \times \left[1 + \exp\left(\frac{E - E_{\mathrm{cut}}}{E_{\mathrm{fold}}}\right)\right]^{-1} \tag{8.1}$$

where the photon flux at energy E is described by a power law with a photon index, Γ, multiplied by an exponential cutoff at energy E_{cut} with a folding energy, E_{fold}. The best fit parameters for the continuum are listed in Table 8.3 and the absorption and the partial covering parameters are listed in Table 8.4.

[8] `http://pulsar.sternwarte.uni-erlangen.de/wilms/research/tbabs/`

In a few sources, residuals are present at low energies ($< 5\,\mathrm{keV}$), which we describe with a blackbody component (`xspec` model `bbody`). All blackbody best fit parameters are listed in Table 8.6.

All spectra show residuals that are indicative of the presence of fluorescence emission lines from iron in the 6–7 keV range. We describe these lines with Gaussian emission line models (`xspec` model `gaussian`). The best fit parameters for all the fluorescence lines are listed in Table 8.7. Most of the lines are too narrow to be resolved. Their widths were fixed at $\sigma_{\mathrm{Fe}} = 1\,\mathrm{eV}$.

Some sources show broad residuals around 8–13 keV, which we interpret as a "10 keV bump". This is a feature of unknown origin, which has been observed in the spectra of several accreting pulsars, e.g., Cen X-3 (Santangelo et al., 1998; Suchy et al., 2008), 4U 0115+63 (Ferrigno et al., 2009), XTE J1946+274 (Müller et al., 2012), Vela X-1 (La Barbera et al., 2003), and other pulsars that are not in our sample, such as Her X-1, 4U 1907+09, 4U 1538−52 (Coburn et al., 2002; Mihara, 1995), V 0331+53 (Mihara, 1995), and MXB 0656−072 (McBride et al., 2006). In our analysis, this feature is modelled with a Gaussian line model as a broad emission feature ($\sigma\sim3\,\mathrm{keV}$) or absorption feature ($\sigma\sim1\,\mathrm{keV}$). The best fit parameters of the "10 keV bump" are listed in Table 8.5.

In some sources, characteristic residuals are visible in the PIN band. These are generally representative of cyclotron lines, i.e., inelastic resonant scattering of photons off of electrons quantized on Landau levels (Makishima & Mihara, 1992). This scattering process produces an absorption-line-like feature observed at the energy

$$\Delta E \approx \frac{1}{1+z} 11.56\,\mathrm{keV} \times \left(\frac{B}{10^{12}\mathrm{G}}\right) \tag{8.2}$$

where z is the gravitational redshift. This is known as a Cyclotron Resonance Scattering Feature (CRSF), which can be used to directly determine the magnetic

field strength in the scattering region as shown by Eqn. 8.2. To model the cyclotron line, we include an absorption-like line with a Gaussian optical depth profile (`xspec` model `gabs`) often used to describe cyclotron lines,

$$M_{\texttt{gabs}}(E) = \exp(-\tau(E)) \tag{8.3}$$

where

$$\tau(E) = \tau_{\rm CRSF} \times \exp\left[-\frac{1}{2}\left(\frac{E - E_{\rm CRSF}}{\sigma_{\rm CRSF}}\right)^2\right]. \tag{8.4}$$

In this equation $E_{\rm CRSF}$ is the cyclotron line energy, $\sigma_{\rm CRSF}$ is the line width, and $\tau_{\rm CRSF}$ is the optical depth. Note that the `gabs` implementation in `xspec` provides the line depth $D_{\rm CRSF} = \tau_{\rm CRSF}\sigma_{\rm CRSF}\sqrt{2\pi}$ instead of $\tau_{\rm CRSF}$. All CRSF parameters are listed in Table 8.8.

Depending on the source, additional narrow lines (e.g., the emission line complex at $\sim$1 keV in 4U 1626−67) or comparatively weak broad components (e.g., the emission line at $\sim$2 keV in Cen X-3) are required, which are described in the results sections (see also Table 8.9). Figures that show the individual empirical spectral fits can be found in Appendix A.2. In Figures A.10–A.23 the upper panels show the absorbed data and best fit model, the middle panels show the unfolded unabsorbed data, full best fit model and model components, and the bottom panels show the fit residuals.

In order to compare our results to those found by C02, we also fitted the continua using a power law with a modified high-energy cutoff, `mplcut`,

$$M_{\texttt{mplcut}}(E) = M_{\texttt{plcut}}(E) \times M_{\texttt{gabs}}(E) \tag{8.5}$$

where

$$M_{\texttt{plcut}}(E) = AE^{-\Gamma} \begin{cases} 1 & \text{for } E \leq E_{\rm cut} \\ e^{-(E-E_{\rm cut})/E_{\rm fold}} & \text{for } E > E_{\rm cut}. \end{cases} \tag{8.6}$$

Following C02, we applied the `gabs` model to smooth the spectral cutoff,

$$M_{\texttt{gabs}}(E) = \exp\left\{-\tau \times \exp\left[-\frac{1}{2}\left(\frac{E-E_{\rm cut}}{\sigma}\right)^2\right]\right\}. \tag{8.7}$$

Although C02 found that when applying the `fdcut` model, the continuum and CRSF parameters are not completely orthogonal, this did not affect our results because we mainly focus on studying the continuum emission. However, since C02 applied the `mplcut` continuum model to investigate cyclotron-continuum correlations, we also fitted this model in order to compare with their results (Section 8.4.3). We find that the fitted `mplcut` parameters are similar to the `fdcut` parameters. Table 8.10 lists the `mplcut` fit parameters relevant for the comparison with C02. The additional model components are also similar to those found with `fdcut`. We use the `mplcut` fits only to compare with the C02 results. For the rest of the analysis, we use the results from the `fdcut`-based fits, since: (i) `fdcut` provides a comparably good fit with fewer fit parameters than `mplcut`, (ii) when fitting `mplcut`, the `gabs` component that is used for modelling the roll-over requires a fixed width for uncertainty calculations, whereas for `fdcut` none of the continuum parameters needed to be fixed, and (iii) `fdcut` smooths the rollover in the X-ray continuum without the need for an additional `gabs` component.

8.3.2 Empirical Fit Results

We obtained the overall best empirical fits for our *Suzaku* broad-band spectra by applying the `fdcut` model to the continuum. The complete fitted models for each observation are listed in Table 8.9. All the best fit parameters for

the continuum and non-continuum components are listed in Tables 8.3-8.8. All uncertainties are given on a 90% confidence level. In this section, the fit results for each source are discussed and compared to previous studies.

LMC X-4

LMC X-4 is an accreting X-ray pulsar located in the Large Magellanic Cloud. It is the only source in our sample with no confirmed CRSF. Using *BeppoSAX* data, La Barbera et al. (2001) claim to have found a CRSF at $E_{\mathrm{CRSF}}{\sim}100\,\mathrm{keV}$ with a width of $\sigma_{\mathrm{CRSF}}{\sim}60\,\mathrm{keV}$. They also state that the measurement is consistent with the theoretically predicted magnetic field, assuming LMC X-4 was spinning in equilibrium. However, the cyclotron line at 100 keV has yet to be confirmed: see analysis of *INTEGRAL* data by Tsygankov & Lutovinov (2005). In addition, no CRSF was found in the recent *NuSTAR* study by Shtykovsky et al. (2017), who conclude that the magnetic field of LMC X-4 is $B < 3 \times 10^{11}\,\mathrm{G}$ or $B > 6.5 \times 10^{12}\,\mathrm{G}$.

LMC X-4 is much more luminous than the other sources chosen for this study, reaching more than $10^{38}\,\mathrm{erg\,s^{-1}}$. It also shows superorbital variations, on a time scale of ∼30 d (Lang et al., 1981; Ilovaisky et al., 1984; Hung et al., 2010). These variations are assumed to be caused by a precessing accretion disc that periodically obscures the neutron star (Heemskerk & van Paradijs, 1989). Hung et al. (2010) used 13 years of *RXTE* All Sky Monitor data to improve the superorbital measurements. They measure a superorbital period of $30.32 \pm 0.04\,\mathrm{d}$, and define the beginning of the high state (JD 2454560.0) to be the zero phase ($\phi = 0$). They also determined that the three *Suzaku* observations were taken at different superorbital phases ($\phi_{702038010} = 0.39$, $\phi_{702037010} = 0.27$, and $\phi_{702036020} = 0.07$). Fig. A.1 shows an illustration of the times of the *Suzaku* observations in the context of the superorbital cycle in the hard X-ray flux. The luminosities at the times of the observations cover

a range of $\sim (21-31) \times 10^{37}\,\mathrm{erg\,s^{-1}}$ (see Table 8.3). Hung et al. (2010) were the first to study these observations and, similarly to us, they used `fdcut` to model the continuum. We compare our results to theirs as well as to those found by Paul et al. (2002), who studied *ASCA* data of LMC X-4, applying the `cutoffpl` and `plcut` continuum models.

Our `fdcut`-based best fit model for all the LMC X-4 observations consists of interstellar absorption, a power law continuum with a rollover, a low-temperature blackbody, three Gaussian emission lines from fluorescence of Ne IX and Fe Kα and describing a broad Fe component.

All fitted parameter values are consistent with those found by Hung et al. (2010), with the exception of the PIN cross-normalization constant, which we left free. Compared to Paul et al. (2002) we obtain a lower photon index, but similar cutoff and folding energies. Freezing $c_{\mathrm{PIN}} = 1.16$ like Hung et al. (2010) significantly worsens our fits (χ^2_{red}>1.4).[9] We fixed the absorption to $N_{\mathrm{H}} = 0.057$ as Paul et al. (2002) and Hung et al. (2010). The continuum parameters show only small differences between the three observations. The blackbody component is consistent with Hung et al. (2010), and its low temperatures shows a slight increase with decreasing luminosity. These temperatures are in agreement with the blackbody temperature fitted by Paul et al. (2002) in their `plcut`-based fit. The Fe Kα line is too narrow to be resolved so we fixed $\sigma_{\mathrm{Fe\,K}\alpha} = 1\,\mathrm{eV}$. We also included a broad Fe emission component, which Hung et al. (2010) interpreted as possibly being produced by the reflection of the Fe Kα line off of the accretion disc. The energy and width of the broad Fe line are consistent with those found by Paul et al. (2002) as well, but the line flux they measured is about double the values we measure. In

[9] The nominal values of the PIN cross-normalization constant for the XIS and HXD aim points (see 'Aim Point' column in Table 8.2) are 1.16 and 1.18, respectively. However, the best fit values usually vary around these values for different sources (see 'c_{PIN}' column in Table 8.3).

addition to the narrow Ne IX emission line at ∼0.9 keV Hung et al. (2010) also fitted an O VIII Lyα line at ∼0.6 keV, which is outside the energy range we consider.

Cen X-3

Cen X-3 was the first X-ray pulsar ever discovered (Giacconi et al., 1971). It is a persistent and eclipsing HMXB known for having three Fe fluorescence lines and a CRSF at ∼30 keV. The iron lines were first resolved by *ASCA* (Ebisawa et al., 1996). The source exhibits aperiodic long term variability reminiscent of state changes. While the origin of this variability has not been firmly established, it has been suggested to be caused by obscuration through a precessing accretion disc, similar to the superorbital cycle of LMC X-4 (Raichur & Paul, 2008). The *Suzaku* observation spans one binary orbit, from eclipse to eclipse, and the hardness-selected XIS and PIN spectra correspond to the central part of the first half of the orbit, which shows comparatively high flux and low absorption (Fig. 8.2 a–d). This observation was first studied by Naik et al. (2011), who separated the observation time into segments and described the spectrum of each segment with the `plcut` continuum model.

Our `fdcut`-based best fit model consists of fully and partially covering absorption, a power law continuum with a rollover, three Gaussian emission lines for Fe fluorescence, a Gaussian emission line for the "10 keV bump", three miscellaneous Gaussian emission lines, and an absorption-like line with a Gaussian optical depth profile for the CRSF. The miscellaneous lines are: a possible Compton shoulder at 6.3(2) keV, possible Fe L shell or Ne X (Ne Lyα) emission at 1.015(9) keV that was also reported by Ebisawa et al. (1996), and a broad feature of unknown origin at 2.7(1) keV. Ebisawa et al. (1996) resolved several emission lines between 1.25 keV and 2.64 keV that might contribute to the flux of this broad component.

We find strong intrinsic absorption that is both fully and partially covering. From their time-resolved study of the varying absorption parameters Naik et al. (2011) concluded that clumps of dense material pass through the line of sight to the neutron star, in particular during the second half of the orbit. The continuum parameters are consistent with those found by Suchy et al. (2008) for *RXTE* data, who also applied an `fdcut`-based model, with those found by Burderi et al. (2000) for *BeppoSAX* data, who applied a `plcut`-based model, and with those from similar orbital phases of the Naik et al. (2011) study. Despite the 10–13 keV energy gap between XIS and PIN, we were able to fit a broad and relatively well-constrained 10 keV feature, with parameters similar to those found by Suchy et al. (2008). We also fitted the three Fe fluorescence lines: Fe Kα at $6.407^{+0.006}_{-0.004}$ keV, He-like Fe (Fe XXV Kα) at $6.658^{+0.010}_{-0.008}$ keV, and H-like Fe (Fe XXVI Kα) at 6.97(2) keV. Naik et al. (2011) studied the orbital phase dependence of these lines and infered that the Fe Kα line is produced by cold dense material close to the compact object, and the He- and H-like lines may originate from a region further from the neutron star. We find a CRSF with a width that could not be constrained and that we fixed at $\sigma_{\rm CRSF} = 4$ keV (Suchy et al., 2008, found $\sigma_{\rm CRSF} \sim 4 - 7$ keV). The remaining cyclotron line parameters are consistent with those found by Suchy et al. (2008) as well. We confirm that the continuum can also be well fitted with the `plcut` continuum model.

1A 1118−61

The X-ray binary 1A 1118−61 was serendipitously discovered by *Ariel-V* in 1974 (Eyles et al., 1975) during an observation of Cen X-3. Its companion is HEN 3-640 (='Wray 793'), a highly reddened Be-type star, O9.5IV-Ve (Chevalier & Ilovaisky, 1975). 1A 1118−61 has since experienced three major outbursts: in

1974 when it was detected, in 1992 (Coe et al., 1994), and in 2009 (Mangano, 2009). Doroshenko et al. (2010) and Suchy (2011) discovered a CRSF line at ∼55 keV *RXTE* and *Suzaku* data of the 2009 outburst, respectively. *Suzaku* observed 1A 1118−61 twice during this outburst. For this analysis, we are using only the higher-luminosity observation.

Our `fdcut`-based best fit model for this source consisted of fully and partly covering absorption, a power-law continuum with a rollover, a blackbody component, a Gaussian optical depth profile for the cyclotron line. Three Gaussian emission lines were also included for (i) a narrow line at ∼0.93 keV due to Ni K edge (Suchy, 2011) or Ne IX (simialrly to LMC X-4), (ii) the Fe Kα line, and (iii) a broad feature at 6.4 keV resembling the 10 keV feature observed in other sources (e.g., Cen X-3).

This observation was studied previously by Suchy (2011) and Maitra et al. (2012). Suchy (2011) used `cutoffpl` and `comptt`[10] to model the continuum. Maitra et al. (2012) used the `npex` continuum model. We found that the `fdcut` model resulted in a better fit with $\chi^2_{\rm red} = 1.18$. We find strong partially covering absorption, both consistent with those found by Suchy (2011) and Maitra et al. (2012). Devasia et al. (2011) found even higher partial covering in *RXTE* data. A high-energy cutoff-powerlaw model (`plcut`) was used by Doroshenko et al. (2010); Devasia et al. (2011) to model *RXTE* data. Compared to our results, they fit a similar photon index, lower cutoff energies, but slightly higher folding energies. Similarly to Suchy (2011); Devasia et al. (2011); Maitra et al. (2012), we fitted a low-temperature blackbody. We also fitted an Fe Kα emission line. Unlike Suchy (2011), but similarly to Maitra et al. (2012), we do not find Fe Kβ emission, nor a 10 keV absorption-like feature. Instead, we included a broad Gaussian line at 6.4(2) keV (in addition to the narrow Fe Kα line), which accounts for ∼2.7% of the total spectral flux. This feature

[10] `https://heasarc.gsfc.nasa.gov/xanadu/xspec/manual/node155.html`

broader than broad Fe lines such as the ones found for LMC X-4 and 4U 1626−67, it rather shows a resemblance to the broad 10 keV features in other sources. The CRSF parameters we obtain are consistent with those found by Suchy (2011) in their `comptt` fit ($E_{\rm CRSF} = 54.5^{+2.4}_{-2.1}$ keV, $\sigma_{\rm CRSF} = 10.3^{+3.6}_{-0.1}$ keV, and $D_{\rm CRSF} = 23.6^{+10.4}_{-6.9}$), but differed from those of the much deeper and broader CRSF they found at a higher energy in their `cutoffpl`-based fit ($E_{\rm CRSF} = 58.2^{+0.8}_{-0.5}$ keV, $\sigma_{\rm CRSF} = 14.1^{+3.5}_{-3.1}$ keV, and $D_{\rm CRSF} = 60.1^{+5.9}_{-1.5}$). This is not unexpected as the use of different continuum models influences the CRSF parameters (Müller et al., 2013b).

4U 0115+63

4U 0115+63 is an HMXB well known for having up to 5 CRSF harmonics (Heindl et al., 2000). These lines were first seen in the *BeppoSAX* data taken during a giant outburst in 1999, when the energy of the fundamental was found at 12.7 keV. 4U 0115+63 was the first cyclotron line source to show more than one harmonic (Santangelo et al., 1999). During its outburst in 2008, Müller et al. (2013b) studied this pulsar with multiple instruments and found a positive correlation between the cyclotron line energy and the source luminosity. Iyer et al. (2015) analyzed *Suzaku* and *RXTE* data and used a low-temperature blackbody and high energy cutoff power law and found absorption-like residuals at ∼15 keV.

Suzaku observed 4U 0115+63 twice during the decline of a giant outburst in 2011. For both these observations, the `fdcut`-based best fit model consisted of absorption in the interstellar medium as well as intrinsic to the system, partial covering, a power law continuum with a rollover, two Gaussian emission lines for Fe fluorescence, a Gaussian emission line for the '10 keV bump'. We also fitted two absorption-like lines with a Gaussian optical depth profile for the cyclotron line first and second harmonics.

We obtained the best fits with the PIN cross-normalization constant was fixed $c_{\rm PIN} = 1.4$. We found that the absorption and partial covering models had higher hydrogen column densities and a lower covering fraction in the first observation than in the second observation, possibly indicative of small changes in the absorbing material along our line of sight between observations.

The photon index and the cutoff and folding energy were relatively similar between the two observations, indicating that the accretion regime did not experience strong changes between observations. The folding energy was consistent with that fitted by Müller et al. (2013b) at similar luminosities, but we fitted higher photon indexes and cutoff energies.

For both observations we fitted narrow emission lines: Fe Kα and He-line Fe (XXV). The lines were too narrow to be resolved, therefore, their widths were fixed at 1 eV. The line fluxes were larger in the high-luminosity observation. The presence of the He-like iron suggests that the material surrounding the neutron star may be slightly ionized.

4U 0115+63 generally has a '10 keV bump', and this feature was present in both *Suzaku* spectra. Our fitted parameters for this feature were close to those found by Müller et al. (2013b). We did not find the absorption-like feature at 15 keV claimed by Iyer et al. (2015).

Due to the gap between XIS and PIN, we were unable to fit the fundamental cyclotron line which is normally found in the 10–12 keV range. However, we fitted the first and second harmonics in both observations, for which the parameters were fixed due to low signal to noise (Müller et al., 2013b).

GX 304−1

The pulsar GX 304−1 was in quiescence until it went into outburst in 2008. Since then, GX 304−1 has been widely studied with several instruments. The first *Suzaku* observation, Yamamoto et al. (2011) found a CRSF at ∼52 keV. Following that, Klochkov et al. (2012) found a positive correlation between the luminosity and the cyclotron line energy in *INTEGRAL* data.

Suzaku observed GX 304−1 twice. The first observation (Obs 1) was taken at a high luminosity right before the peak of the first outburst in a series. The second observation (Obs 2) was taken at about half the luminosity of Obs 1, during the decline of the fifth outburst of the same series. The first observation was studied previously by Yamamoto et al. (2011), and both observations were studied by Jaisawal et al. (2016).

Our `fdcut`-based best fit model consisted of absorption in the interstellar medium as well as absorption intrinsic to the system, a partial covering model in Obs 2, a power law continuum with a rollover, Gaussian emission lines for Fe fluorescence (two in in Obs 1 and three in Obs 2) a low-temperature blackbody, and an absorption-like line with a Gaussian optical depth profile for the cyclotron line.

The absorption in our *Suzaku* fits is lower than that found by Yamamoto et al. (2011) in Obs 1 and by Rothschild et al. (2017) in *RXTE* data. On the other hand, we found high partial covering, similarly to Jaisawal et al. (2016). Our values differ from theirs likely due to the use of different continuum models (Jaisawal et al. (2016) applied the `npex` continuum model). For consistency, we tested the `npex` model, but we found that this resulted in artificial an absorption-line-like feature at the cutoff energy, which did not exist in the `fdcut` based fits.

In our best fits we found that Γ was higher in the high-luminosity observation, but $E_{\rm fold}$ was lower, while the cutoff energies were consistent with zero. In

both observations we fitted low-temperature blackbodies, with a possible positive correlation between the blackbody temperature and source X-ray luminosity.

We found higher cyclotron energies than both Yamamoto et al. (2011) and Jaisawal et al. (2016). This was likely due to the use of different continuum models (Fürst et al., 2014).[11] However, our measured cyclotron energies showed a positive correlation with luminosity, consistent with what Klochkov et al. (2012) found in *INTEGRAL* data.

4U 1626−67

4U 1626−67 is the only low-mass X-ray binary in our sample. In this system, the pulsar orbits a dwarf star in a short orbital period of 42 min (Middleditch et al., 1981). This source has had steady spin-ups and spin-downs with two torque reversals in 1991 and 2008 (Bildsten et al., 1994; Camero-Arranz et al., 2010). 4U 1626−67 regularly experiences Quasi-Periodic Oscillations (QPOs) and has the lowest observed pulsar mass-function (Levine et al., 1988). Like in most LMXBs, in 4U 1626−67 the material is transferred from the donor star to the compact object via Roche-lobe overflow. A cyclotron line was first found at ∼37 keV by Orlandini et al. (1998). The *Suzaku* observations were previously studied by Camero-Arranz et al. (2012) and Iwakiri et al. (2012).

We reproduced the spectral fit model by Camero-Arranz et al. (2012), by applying `fdcut` instead of `plcut` to describe the continuum. Our best fit model consisted of interstellar absorption, a power-law continuum with a high rollover and a low-temperature blackbody. We also fitted a Gaussian-emission-line complex at ∼1 keV (see Camero-Arranz et al., 2012, for more details), a Gaussian emission line for a broad Fe fluorescence feature, and an absorption line with a Gaussian optical

[11] Fürst et al. (2014) studied in detail how different continuum models influence the shape and fit parameters of the cyclotron lines.

depth profile for the cyclotron line.

We fixed the absorption to the Galactic value, $N_{\rm H} = 0.1 \times 10^{22}\,{\rm cm}^{-2}$. The photon index and folding energy were consistent with those found by Iwakiri et al. (2012) and Camero-Arranz et al. (2012). The cutoff energy was also consistent with that found by Iwakiri et al. (2012), but higher than that found by Camero-Arranz et al. (2012). We fitted the same emission-complex component at $\sim$1 keV as in Camero-Arranz et al. (2012). In addition, our blackbody parameters were also consistent with Camero-Arranz et al. (2012). Iwakiri et al. (2012) did not find a blackbody in their `plcut`-based fit, but in their `npex`-based fit they fitted very high temperature blackbody components ($kT_{\rm BB}\sim$5.0 – 7.2 keV). Consistent with Camero-Arranz et al. (2012), we fitted a broad Fe line. Iwakiri et al. (2012) described this component with three Gaussian emission lines: Fe Kα, Fe XXV, and Fe XXVI. Lastly, our cyclotron line parameters were consistent with those found by both Camero-Arranz et al. (2012) and Iwakiri et al. (2012).

A 0535+26

A 0535+26 is a HMXB which it exhibits two different types of outbursts (Stella et al., 1986). The type I outbursts are normal, periodic, occur at periastron, and characterized by an increase in luminosity of up to 100 times its minimum. The type II outbursts are giant, sporadic, last several days, occur at any orbital phase, and show an increase in luminosity of up to 1000 times its minimum. A 0535+26 has a cyclotron line at $\sim$45 keV, energy which has not shown significant changes with luminosity (Becker et al., 2012; Caballero et al., 2013).

The *Suzaku* observation of A 0535+26 used in this study was taken during the peak of the second outburst in the 2009–2011 outburst series. There are two other *Suzaku* observations that were taken when the luminosity of the source was

much lower. The first one was taken at the end of a normal outburst in September 2005 and was studied by Naik et al. (2008); Doroshenko et al. (2014). The second observation took place during the main outburst in 2009, and it was studied by Caballero et al. (2013) who fitted the continuum with a `cutoffpl` model.

Our `fdcut`-based best fit model consisted of absorption in the interstellar medium as well as absorption intrinsic to the system, a power law continuum with a rollover, an absorption edge due to Fe, a low-energy blackbody, a Gaussian emission line for Fe Kα fluorescence, and an absorption-like line with a Gaussian optical depth profile for the cyclotron line. We excluded data from XIS 1, the back-illuminated instrument, due to calibration issues.

We fitted an absorption model with a hydrogen column density higher than the $N_{\rm H} = 0.70(3) \times 10^{22}{\rm cm}^{-2}$ found by Caballero et al. (2013) at a lower luminosity.

Our continuum parameters were similar to those found in earlier studies of A 0535+26 by Sartore et al. (2015) in *INTEGRAL* data taken during a later outburst in 2011. The folding energy we fitted was much lower than the $E_{\rm fold}$∼31–44 keV found by Caballero et al. (2013) at a lower luminosity. We fitted a low-temperature blackbody in contrast to a high-temperature ($\sim 1.2-1.5$ keV) blackbody found by Naik et al. (2008) and Caballero et al. (2013) in the lower luminosity observations. We confirmed that the blackbody temperature difference was not artificially caused by the use of different continuum models, because when we tested the `cutoffpl` continuum model (similarly to Caballero et al., 2013), we again found a low temperature of kT∼0.34 keV. We fitted an Fe Kα fluorescence line, with a lower equivalent width than the EW=70 eV found by Caballero et al. (2013) at lower luminosities. This is unexpected, as the amount of iron fluorescence along the line of sight is generally positively correlated with the amount of X-ray emission (see, for example, Marcu-Cheatham et al., 2015). We also fitted an Fe absorption edge.

A possible explanation is that the low equivalent width and the presence of the absorption edge are due to slight ionization in the fluorescing material surrounding the neutron star. Lastly, despite the differences in the continuum parameters, our CRSF fitted parameters were consistent with values previously found in A 0535+26 spectra (Caballero et al., 2007, 2013; Sartore et al., 2015).

XTE J1946+274

XTE J1946+274 is an HMXB that is generally in quiescence. It experienced two outburst series since its discovery: in 1998 (Smith & Takeshima, 1998) and in 2010 (Campana et al., 1999; Müller et al., 2012; Marcu-Cheatham et al., 2015). The source is known for showing two outbursts per orbit during a series: one at periastron and one at apastron (Campana et al., 1999; Müller et al., 2012; Marcu-Cheatham et al., 2015).

Heindl et al. (2001) found evidence for a CRSF at ∼36 keV. Caballero et al. (2010) found no signature of the CRSF at 35 keV in a preliminary analysis of the first 2010 outburst. In a previous study of the same *Suzaku* observation (Marcu-Cheatham et al., 2015), we presented the most recent orbital solution, pulse period, and pulse period evolution of XTE J1946+274.

For XTE J1946+274 we reproduced the same `fdcut`-based fit from Marcu-Cheatham et al. (2015). This fit consisted of absorption in the interstellar medium as well as absorption intrinsic to the system, a power law continuum with a rollover, a Gaussian emission line for Fe Kα fluorescence, and an absorption-like line with a Gaussian optical depth profile for the cyclotron line.

The *Suzaku* results are consistent with the previously observed positive correlation between the iron fluorescence flux and the amount of X-ray emission (Müller et al., 2012). As described in more detail in Marcu-Cheatham et al. (2015),

we observed no strong changes between the *Suzaku* spectrum and previously analyzed spectra for different luminosities and outbursts by Heindl et al. (2001) and Müller et al. (2012).

Vela X-1

Vela X-1 is the most studied HMXB from the sample, and one of the most well known wind accretors (Fürst et al., 2014). Its strong flux variability (Kreykenbohm et al., 2008; Staubert et al., 2004) is assumed to be caused by structures or clumps in the stellar wind formed as a result of instabilities induced by the neutron star (Oskinova et al., 2012; Fürst et al., 2010). Vela X-1 generally has a weak fundamental CRSF line at ∼25 keV and a strong harmonic at ∼55 keV (Kendziorra et al., 1992; Kretschmar et al., 1996, 1997; Kreykenbohm et al., 2002; Maitra & Paul, 2013c).

We extracted *Suzaku* data during constant hardness (Fig. 8.2). These data were studied previously by Maitra & Paul (2013c) who fit the continuum with the `plcut` and `compttt` models.

Our `fdcut`-based best fit model consisted of absorption in the interstellar medium as well as absorption intrinsic to the system, a partial covering model, a power law continuum with a rollover, a two Gaussian emission line for Fe fluorescence, a Gaussian absorption line for the '10 keV bump', and two absorption-like line with a Gaussian optical depth profile for the cyclotron line fundamental and first harmonic. Despite the fact that Vela X-1 is known to exhibit spectral changes with phase, we successfully model the average spectrum obtained during times of constant hardness.

We found higher N_{H} values but a lower fraction for the partial covering than those found by Maitra & Paul (2013c). We fitted consistent Γ and E_{cut}, but lower E_{fold} compared to Maitra & Paul (2013c). We found a better fit using the

`fdcut` continuum model compared to the `plcut`-based fit by Maitra & Paul (2013c), who obtained a goodness of fit of $\chi^2_{\rm red} = 2.03$ for 831 d.o.f.[12] We also fitted an Fe Kα line consistent with that found my Maitra & Paul (2013c), but in addition, we also found residuals at $\sim$7 keV, illustrative of Fe Kβ emission. We added a shallow absorption-like 10 keV feature, which was also found previously by Fürst et al. (2014) in *NuSTAR* data.

Vela X-1's fundamental cyclotron line is generally shallow and difficult to detect, possibly due to photon spawning (Fürst et al., 2014). We fitted the first cyclotron harmonic by leaving all the parameters free, but we froze the energy and width of the fundamental at half of those of the harmonic (see Table 8.8). We fitted a shallow CRSF fundamental line at $E = 26$ keV and a deep and broad harmonic at $E = 52(2)$ keV. The harmonic was unconstrained, so we fixed $\sigma = 7$ keV and $\tau = 9.0$. Our CRSF parameters were relatively similar to those found by Maitra & Paul (2013c).

8.3.3 Physical Model

In the general picture of high-luminosity accretion on to a strongly magnetic neutron star (Becker & Wolff, 2007, 2005a,b) most of the X-ray emission we observe originates from the accretion column. As mentioned in Section 8.1, the accretion column forms above the surface of the neutron star as a result of the matter flow being channeled along the B-field lines from the accretion disc (or wind) on to the magnetic poles. The accretion column model was first developed by Davidson & Ostriker (1973). It describes geometry of the column as being cylindrical, in which, for high-luminosity sources, at a certain height inside the accretion column, a radiation-dominated radiative shock front forms as a result of the high radiation

[12] The large difference in degrees of freedom between our analysis and that by Maitra & Paul (2013c) is due to the different binning of XIS data.

pressure caused by the large amount of in-flowing matter. Before reaching the shock, the plasma free-fall velocities are supersonic ($\sim 0.7\,c$). The shock decelerates the plasma to subsonic velocities before it settles on the surface of the neutron star. The shock front has a thickness of only a few electron scattering lengths and is dominated by radiation pressure as gas pressure is negligible in these high-luminosity regimes. As the matter flow reaches the surface, it merges with the neutron star interior and forms a hot thermal mound.

Due to the high electron temperature inside the accretion column ($kT_{\rm e} \sim 3-6\,{\rm keV}$), low-energy X-ray seed photons are produced via three mechanisms: bremsstrahlung and cyclotron emissions which both originate inside all throughout the accretion column, and blackbody emission from the hot thermal mound. Before escaping the accretion column, these photons are further up-scattered by the hot in-falling plasma via bulk and thermal Comptonization processes. Thermal Comptonization is the process by which photons gain energy through diffusion/repeated scattering off the hot thermal electrons inside the accretion column. In the photon transport equation, this process is described by the Kompaneets term (Kompaneets, 1957). The observed high-energy cutoff in the more luminous sources is an indication of thermal Comptonization (for more details see Becker & Wolff, 2007; Wolff et al., 2016). Bulk or dynamic Comptonization describes photons being scattered back and forth across the radiation shock. In the radiation transport equation, the energy gained by the seed photons through bulk Comptonization is described by first-order Fermi acceleration (for more details see Becker & Wolff, 2005a,b). The final X-ray broadband spectrum can, thus, be modelled by using a transport equation that describes the energy gained by the low-energy X-ray 'seed' photons through their interactions with the hot plasma in the column (thermal Comptonization) and the rapidly compressing gas in the radiation shock (bulk Comptonization).

For a monochromatic source with photon energy ϵ, at a fixed height z above the stellar surface, i.e., a photon distribution $f(z,\epsilon)$, the time-independent, cylindrical, plane-parallel radiation transport equation is

$$v\frac{\partial f}{\partial z} = \frac{dv}{dz}\frac{\epsilon}{3}\frac{\partial f}{\partial \epsilon} + \frac{\partial}{\partial z}\left(\frac{c}{3n_e\sigma_\parallel}\frac{\partial f}{\partial z}\right) - \frac{f}{t_{\rm esc}} + \frac{n_e\bar{\sigma}c}{m_ec^2}\frac{1}{\epsilon^2}\frac{\partial}{\partial \epsilon}\left[\epsilon^4\left(f + kT_e\frac{\partial f}{\partial \epsilon}\right)\right] + \frac{Q(z,\epsilon)}{\pi r_0^2}, \quad (8.8)$$

where v is the plasma velocity, r_0 is the radius of the column, and n_e is the electron number density. The two parameters, $\sigma_\parallel$ and $\bar{\sigma}$ are related to the electron scattering cross sections perpendicular to the magnetic field and angle-averaged, respectively. The accretion column electron temperature, T_e, is assumed to be constant throughout the column. The left-hand side of the equation denotes advection across the column. The right-hand side terms describe bulk Comptonization, spatial diffusion along the column axis, photon escape, and thermal Comptonization, in that order. In the last term, $Q(z,\epsilon)$, describes the injected low-energy X-ray 'seed' photons. The term includes all three emission types: bremsstrahlung, blackbody, and cyclotron. All types of seed photons are injected continuously, but at different locations and energies. Bremsstrahlung seed photons are created at all energies all throughout the column. Blackbody seed photons are also injected at all energies, but only from the height of the thermal mound, close to the stellar surface. Cyclotron seed photons are created throughout the column, but only at the cyclotron energy.

BW provided the first analytical solution to the radiation transport equation. They made the assumption that the velocity of the in-falling matter, v, is proportional to the optical depth inside the column, τ,

$$v(\tau) = -\alpha c\tau \quad (8.9)$$

where $\alpha \sim 1$ is a constant (Wolff et al., 2016; Lyubarskii & Syunyaev, 1982; Becker, 1998). With this assumption, the transport equation becomes solvable separately in energy and in space and the total observable flux is the sum of the Comptonized bremsstrahlung, blackbody, and cyclotron emission components (see Wolff et al., 2016; Becker & Wolff, 2007).

Unlike the empirical models, fitting this model renders physical parameters that describe the accretion column.[13] The mass accretion rate, $\dot{M}$, the column radius, r_0, the electron temperature inside the column, T_e, and the electron angle-averaged, B-field parallel and perpendicular cross sections, $\bar{\sigma}$, $\sigma_\parallel$ and $\sigma_\perp$, respectively, are all fitted parameters of the model.

An alternative spectral fitting approach that we adopt is the use of the 'similarity parameters', δ and ξ. These parameters are dimensionless variables that can be related to the physical processes inside the column. These parameters are described by

$$\delta = \frac{\alpha}{3}\frac{\sigma_\parallel}{\bar{\sigma}}\frac{m_e c^2}{kT_e} = 4\frac{y_{\rm bulk}}{y_{\rm thermal}} \tag{8.10}$$

and

$$\xi = \frac{\pi r_0 m_p c}{\dot{M}\sqrt{\sigma_\parallel \sigma_\perp}} \approx 4.1\frac{t_{\rm shock}}{t_{\rm escape}} \tag{8.11}$$

where α is the constant from the velocity profile in Equation 8.9. Specifically, δ represents the ratio between the bulk and thermal Comptonization processes, $y_{\rm bulk}$ and $y_{\rm thermal}$. Previous tests of the model have found δ to be close to unity (Becker & Wolff, 2007; Ferrigno et al., 2009; Wolff et al., 2016). The second similarity parameter, ξ describes the balance between the timescales of the photon escape, $t_{\rm escape}$, and the dynamical accretion $t_{\rm shock}$. BW and Becker (1998) show that, assuming the plasma passes through a filled accretion column, in order for it to come to a complete stop

[13] Note that in this model: (i) the plasma velocity, pressure and density only vary with height and are constant across the column; (ii) the electrons are assumed to have a Maxwell-Boltzmann velocity distribution in their frame of rest.

at the neutron star surface ξ must be relatively close to unity.

The details of the fit procedure are described in Section 8.3.3. The physical fit parameters for all the observations are listed in Table 8.11.

The analytical BW physical model was implemented into `xspec` by M. T. Wolff and was first successfully applied a *NuSTAR* spectrum of Her X-1 (Wolff et al., 2016). We used the same implementation to test the model's applicability to our pulsar sample.

With our current knowledge of the accretion mechanism, we were able to constrain some of the fit parameters and avoid possible degeneracies. By studying the thermal broadening effect on the cyclotron scattering feature, we found that the electron temperature inside the accretion column lies in the $\sim$3-7 keV rage (see also Section 8.4.3 for more details). The mass-accretion rate was measured from the model flux. We assume the magnetosphere structure constrains the accretion column to values of a couple of kilometers or lower (Becker & Wolff, 2007; Ferrigno et al., 2009; Farinelli et al., 2016). The magnetic field itself can be tied to the cyclotron line energy. As mentioned in Section 8.3.3, the similarity parameters are close to unity.

Although the model does not automatically account for conservation of energy, we implemented a routine that ensures that the measured X-ray luminosity is equal to the model's accreted luminosity.

In our best `fdcut` fit we then replaced the `power` $\times$ `fdcut` with the similarity-parameter interface of the BW physical model (`BWsim` in `xspec`). Note that we found the *Suzaku* XIS response files to be oversampled in energy causing the fits to have a very long processing time. In order to minimize the fitting time, we first ran test fits after compressing the energy bins in the XIS response files by 79 using the ftool `rbnrmf`. Once the BW model was loaded, we initialized the

fit parameters. We first calculated the mass accretion rate value, $\dot{M}_{\rm acc}$, from the 1–80 keV continuum luminosity of our best `fdcut` fits using

$$L = \frac{GM_{\rm NS}\dot{M}}{R_{\rm NS}}, \tag{8.12}$$

where $M_{\rm NS}$ and $R_{\rm NS}$ are the canonical mass and radius of the neutron star, $1.4\,M_{\odot}$ and 10 km, respectively, and G is the gravitational constant. We initialized the electron column temperature, to values between 3–6 keV. We found that reasonable starting values for the accretion column radius were ∼200–300 km. The neutron star mass and radius were fixed to their canonical default values. The cross section for the electrons moving perpendicular to the B-field, $\sigma_{\perp}$, was fixed to the Thomson scattering cross section, $\sigma_{\rm T}$ (for more details see Wolff et al., 2016). The similarity parameters, δ and ξ, were initialized to unity. From previous tests we found negligible contributions from the Comptonized blackbody emission. Therefore, we included only Comptonized bremsstrahlung and cyclotron emissions in our fits.

Initially, we froze the parameters of the additional model components (absorption, fluorescence lines, blackbody, and CRSFs). This step decreased the fitting time and ensured that the parameters of these components stayed confined within their expected values. We initially froze the similarity parameters. We first ran a `fit` command [14] with only two free parameters: T_e and r_0. Once `xspec` found better values for T_e and r_0, we freed δ and ran another `fit`. We repeated this process for ξ. Then, we proceed by freeing the parameters of the rest of the model components, one by one, while subsequently running `fit` commands. Once a good fit was found, we replaced the compressed response file with the original, non-binned response file, and ran a final fit.

Once the best test fit was found (after applying the non-binned response

[14] If the `fit` did not find reasonable values we used the `steppar` command.

file), we followed with a procedure that ensured the energy conservation between the model luminosity and the accreted luminosity. We measured the 0.1-100 keV continuum flux. With this new flux measurement, we recalculated the luminosity and the mass accretion rate, $\dot{M}_{\rm model}$, using Equation 8.12. We replaced the $\dot{M}_{\rm acc}$ in the fit with the newly calculated $\dot{M}_{\rm model}$ and refitted. This process was repeated until $\dot{M}_{\rm model} = \dot{M}_{\rm acc}$, i.e., the accretion luminosity and the model luminosity were equal (conserved energy). Lastly, for the uncertainty calculations we used the `steppar` command.

8.3.4 Physical Fit Results

In this subsection we discuss our best physical model fit results, which are listed in Table 8.11. Using these parameters, we also determined other relevant physical properties (see Table 8.12) such as the accretion luminosity, the temperature of the thermal mound at the bottom of the accretion column, $\sigma_{\parallel}$ and $\bar{\sigma}$ (see Section 8.3.3).

In Table 8.12 we also specify qualitatively which regime describes the source at in therms of the model accretion luminosity. Becker et al. (2012) described how the plasma deceleration mechanism in the accretion column depends on the amount of in-flowing material. Therefore, the accretion regime is expected to change with luminosity. These regimes are categorized by the source X-ray luminosity, $L_{\rm X}$, relative to the critical luminosity, $L_{\rm crit}$.[15] Supercritical Accretion ($L_{\rm X}>L_{\rm crit}$) occurs when the in-falling matter is decelerated from relativistic to subsonic speeds by the radiation-dominated radiative shock at the top of the accretion column. Subcritical Accretion ($L_{\rm X}<L_{\rm crit}$) can be separated in two categories depending on the X-ray luminosity relative to the Coulomb stopping luminosity, $L_{\rm coul}$. For $L_{\rm X}>L_{\rm Coul}$ the

[15] $L_{\rm crit}$ is the local Eddington luminosity. See Becker et al. (2012) for more details.

plasma still passes through a radiation-dominated shock, but Coulomb interactions inside the accretion column start contributing to the plasma flow deceleration. For $L_{\rm X}<L_{\rm Coul}$ the density of the plasma is too low for Coulomb deceleration, and the material is likely in free fall at non-relativistic velocities and possibly passes through a gas-mediated shock before coming to a stop the surface.

Most of the observations analyzed in this work are taken at times when the mass accretion rates were sufficiently high for the radiation pressure to become dominant and form a radiation-dominated radiative shock. We wanted to test the applicability of the model at different luminosities, therefore the chosen *Suzaku* observations ranged from highly supercritical luminosities (e.g., LMC X-4) to close to the Coulomb luminosity (e.g., Vela X-1).

Lastly, Table 8.12 also contains the calculated height of the radiation shock, $z_{\rm sonic}$, and the maximum height which the physical model is integrated over, $z_{\rm max}$. These parameters are defined by BW as

$$z_{\rm sonic} = \frac{r_0}{2\sqrt{3}} \left(\frac{\sigma_\perp}{\sigma_\parallel}\right)^{1/2} \ln\frac{7}{3} \tag{8.13}$$

and

$$z_{\rm max} = \frac{R_{\rm NS}}{2} \left\{ \left[1 + \frac{4GM_{\rm NS} r_0 \xi}{\alpha c^2 R_{\rm NS}^2} \left(\frac{\sigma_\perp}{\sigma_\parallel}\right)^{1/2} \right]^{1/2} - 1 \right\}. \tag{8.14}$$

In the following, we describe the physical fit results for each source.

Table 8.11: Best Fit `BWsim`-Based Continuum Fit Parameters

Source	Sequence	$\dot{M}$ [$\times 10^{17}\,\mathrm{g\,s^{-1}}$]	T_e [keV]	r_0 [m]	B-field [$\times 10^{12}\,\mathrm{G}$]	D [kpc]	ξ	δ	χ^2_red/dof
LMC X-4	702037010	18.81	$6.17^{+0.43}_{-0.46}$	$1295.70^{+779.07}_{-229.65}$	10.00	50.00	$2.32^{+3.44}_{-0.67}$	$0.44^{+0.32}_{-0.30}$	1.15/520
LMC X-4	702036020	14.45	$5.59^{+0.48}_{-0.43}$	$801.33^{+199.00}_{-89.31}$	10.00	50.00	$1.67^{+0.74}_{-0.35}$	$0.81^{+0.37}_{-0.36}$	1.00/489
LMC X-4	702038010	11.52	$5.07^{+0.46}_{-0.40}$	$575.67^{+101.97}_{-55.38}$	10.00	50.00	$1.44^{+0.45}_{-0.24}$	$1.09^{+0.40}_{-0.41}$	1.12/494
Cen X-3	403046010	2.04	$3.16^{+0.27}_{-0.15}$	$60.62^{+6.76}_{-3.60}$	3.39	5.70	$1.41^{+0.18}_{-0.08}$	$3.68^{+0.64}_{-0.86}$	1.21/353
1A 1118−61	403049010	1.93	$6.44^{+0.05}_{-0.29}$	$131.87^{+16.11}_{-10.65}$	5.56	5.00	$2.91^{+0.65}_{-0.39}$	$0.45^{+0.12}_{-0.11}$	1.21/395
GX 304−1	905002010	1.31	$6.81^{+0.36}_{-0.32}$	$79.00^{+16.33}_{-8.04}$	6.60	2.40	$3.31^{+1.40}_{-0.59}$	$0.77^{+0.30}_{-0.29}$	1.05/371
4U 1626−67	405044010	0.82	$5.15^{+0.66}_{-0.60}$	$33.13^{+0.83}_{-0.67}$	4.28	9.00	$1.38^{+0.30}_{-0.16}$	$2.67^{+0.24}_{-0.24}$	1.15/430
A 0535+26	404055010	$0.19^{+0.03}_{-0.05}$	$7.67^{+0.05}_{-0.11}$	$8.12^{+0.55}_{-0.78}$	5.06	1.86	$5.80^{+3.67}_{-1.48}$	0.28(12)	1.21/291
GX 304−1	406060010	0.57	$7.14^{+0.26}_{-0.22}$	$42.04^{+23.78}_{-7.14}$	5.95	2.40	$5.73^{+10.73}_{-1.49}$	$0.52^{+0.31}_{-0.33}$	1.17/379
4U 1626−67	400015010	0.35	$6.22^{+0.06}_{-0.06}$	$39.36^{+3.13}_{-2.51}$	4.18	9.00	$8.15^{+1.08}_{-0.95}$	$0.15^{+0.03}_{-0.02}$	1.27/417
XTE J1946+274	405041010	0.32	$4.50^{+0.14}_{-0.11}$	$12.80^{+1.15}_{-0.69}$	4.00	9.50	$2.38^{+0.31}_{-0.16}$	$0.96^{+0.12}_{-0.17}$	1.07/448
Vela X-1	403045010	0.14	$5.01^{+0.02}_{-0.02}$	$15.51^{+0.04}_{-0.41}$	3.37	1.90	$12.33^{+8.78}_{-4.79}$	$0.17^{+0.01}_{-0.002}$	1.30/506

Table 8.12: Calculated Physical Parameters

Source	Sequence	$L_{\rm acc}$ $[\times 10^{37}\,{\rm erg\,s^{-1}}]$	Luminosity (Accretion Regime)	$z_{\rm max}$ [km]	$z_{\rm sonic}$ [km]	$\sigma_{\parallel}$ $[\times 10^{-5}\sigma_{\rm T}]$	$\bar{\sigma}$ $[\times 10^{-4}\sigma_{\rm T}]$	$T_{\rm Mound}$ [keV]
LMC X-4	702037010	34.95	$L_{\rm X} \gg L_{\rm crit}$	32	45	4.9	19.9	1.6
LMC X-4	702036020	26.85	$L_{\rm X} \gg L_{\rm crit}$	23	25	6.1	10.9	2.0
LMC X-4	702038010	21.4	$L_{\rm X} \gg L_{\rm crit}$	18	17	6.7	8.2	2.2
Cen X-3	403046010	3.79	$L_{\rm X} > L_{\rm crit}$	5.8	3.0	2.5	1.4	5.0
1A 1118−61	403049010	3.6	$L_{\rm X} > L_{\rm crit}$	9.2	5.8	3.1	14.6	2.9
GX 304−1	905002010	2.4	$L_{\rm X} > L_{\rm crit}$	7.7	4.5	1.9	5.5	3.5
4U 1626−67	405044010	1.5	$L_{\rm X} > L_{\rm crit}$	2.8	1.2	4.8	2.1	5.2
A 0535+26	404055010	0.35	$L_{\rm crit} \gg L_{\rm X} \approx L_{\rm coul}$[a]	2.73	1.1	0.3	3.9	7.5
GX 304−1	406060010	1.06	$L_{\rm X} \approx L_{\rm crit}$	6.3	3.4	0.9	6.7	3.9
4U 1626−67	400015010	0.65	$L_{\rm crit} > L_{\rm X} \gg L_{\rm coul}$	5.7	2.9	1.1	43.8	3.3
XTE J1946+274	405041010	0.59	$L_{\rm crit} > L_{\rm X} \gg L_{\rm coul}$	2.0	0.8	1.6	4.1	6.8
Vela X-1	403045010	0.26	$L_{\rm crit} \gg L_{\rm X} \approx L_{\rm coul}$[b]	3.9	1.8	0.5	30.8	4.3

[a] $L_{\rm coul}$ calculated for disc accretion ($\lambda = 0.5$ Becker & Wolff, 2007). [b] $L_{\rm coul}$ calculated for wind (spherical) accretion ($\lambda = 1$ Becker & Wolff, 2007).

LMC X-4

LMC X-4 is generally highly supercritical, making it the only super-Eddington source. This source was an ideal candidate for testing the physical model because of its high signal to noise ratio. We successfully fitted the physical model for all three observations, with slightly better $\chi^2_{\rm red}$ values than their respective `fdcut`-based fits, with consistent Fe Kα, broad Fe, and blackbody emission components.

We fitted a very large accretion column with average electron temperatures. Both the column radius and temperature showed a positive correlation with luminosity (or mass accretion rate). The accretion column r_0 and T_e values are consistent with those claimed by BW. We fitted low δ values, which showed an increase with decreasing luminosity. This could indicate that there was less bulk Comptonization than thermal Comptonization inside the accretion column, and that the amount of bulk Comptonization may have increased with decreasing luminosity.

We found that, in the more luminous observations, the height of the radiation shock was higher than $z_{\rm max}$, which seemed unphysical. However, these measurements were qualitative due to their large degree of uncertainty (e.g., due to distance, unknown magnetic field, etc.). We also calculated relatively low thermal mound temperatures, which seem to increase at lower luminosities.

Although LMC X-4 does not have a confirmed CRSF, we tested the physical model fits with both B=10^{13} G and B=0 G and found no difference in the fit results. The cyclotron emission flux is expected to decrease with increasing magnetic field as $Q_{\rm cycl}{\sim}B^{-7/2}$ (Becker & Wolff, 2007). We confirmed that the cyclotron emission is negligible for very high magnetic fields: for LMC X-4, the cyclotron emission flux was $\lesssim$0.004% of the total flux when setting the magnetic field to B=10^{13} G.

Cen X-3

Cen X-3 was also in a supercritical accretion regime. We successfully reproduced the `fdcut`-based fit with the physical model. All the additional model components, including the 10 keV feature and the broad 2 keV emission line, were needed for a good fit. The parameters of these features were mostly consistent with the empirical fit. The absorption, $H_{\rm H1}$, was lower, while the partial covering, $H_{\rm H2}$, was higher in the physical fit. The electron temperature was lower than that of the other sources. The column radius was, also, relatively low compared to sources of similar luminosities. The δ value indicated that there was about an equal amount of bulk and thermal Comptonization processes inside the accretion column. We also found a relatively high thermal mound temperature, about twice the temperature of the accretion column. Most of the fitted parameters ($\dot{M}$, T_e, similarity parameters) were similar to those predicted by BW, with the exception of r_0, which was much lower in our fits. Farinelli et al. (2016) also fitted the BW model with a different implementation.[16] They fitted a lower column temperature ($\sim 1.4 - 1.8$ keV) and a much larger column radius ($\sim 1.0 - 1.7$ km). With their implementation, they claim a much higher contribution of cyclotron emission (28% and 78% of the total flux in their high- and low-luminosity observations, respectively) than what we find (13% of the total flux). However, West et al. (2017) tested a similar accretion column model on the same *BeppoSAX* data that Farinelli et al. (2016) uses, and they found a cyclotron emission contribution closer to what we fitted.

1A 1118−61

1A 1118−61 was also supercritical during the time of the *Suzaku* observation. We successfully reproduced the `fdcut`-based fit with the physical model.

[16] `compmag` is an implemented a numerical solution of the BW model into `xspec` by Farinelli et al. (2012).

Similarly, to the `fdcut`-based fits, we found signatures of high partial covering and a low-temperature blackbody. The absorption, partial coverer, blackbody, and cyclotron line parameters were consistent within uncertainties. The broad Gaussian emission-like feature at ∼6.4 had a slightly lower flux than in the empirical fit and was still needed for a good fit. We fitted a low δ, indicative of a high amount of thermal Comptonization compared to bulk. The thermal mound temperature was about half of the accretion column temperature. After LMC X-4, 1A 1118−61 had the highest $z_{\rm sonic}$, which in this case (and in all other sources with the exception of LMC X-4) was lower than $z_{\rm max}$.

4U 0115+63

4U 0115+63 was the only source we were unable to describe with the physical model. Ferrigno et al. (2009) fitted a continuum model composed of `comptt` and the physical model. The `comptt` described most of the soft X-ray emission, while the physical model described the hard X-ray tail of the spectrum. We also tried fitting the continuum with `comptt+BWsim`. Although the fit was successful, with a goodness of fit of $\chi^2_{\rm red}$∼1.25, we found that the `comptt` model dominated the spectrum at soft and harder energies, while there was negligible contribution from the physical model at very high energies. We also tested a combination of two physical models, however we were unable to accurately constrain the mass accretion rate. 4U 0115+63 has the lowest magnetic field out of all the sources in the sample, and it is still unclear how this low B-field affects the accretion column geometry.

GX 304−1

Both *Suzaku* observations of GX 304−1 were taken when the source was accreting in a supercritical regime. In both cases, we successfully reproduced the

`fdcut`-based fit with the physical model. We measured an increasing accretion column electron temperature, but a decreasing column radius with luminosity. We still found signatures of partial covering, the 10 keV (absorption) feature, and a low-temperature blackbody in each observation, all consistent with the empirical fits. We fitted high ξ values, which appeared to increase with decreasing luminosity. We found low values for δ, indicative of a larger amount of thermal Comptonization compared to bulk. In addition, δ decreased with luminosity (opposite correlation than that of LMC X-4), indicating that, for GX 304−1, thermal Comptonization was more dominant at lower luminosities.

4U 1626−67

Suzaku observed 4U 1626−67 when the source was supercritical (ObsID: 405044010) and subcritical (ObsID: 400015010). In both cases, we successfully reproduced the `fdcut`-based fit with the physical model. We fitted narrow emission lines, low-temperature blackbody, and CRSF lines consistent with the empirical fit. The accretion column temperature and radius did not show strong changes between observations. The value of δ decreased with luminosity, indicating that the amount of bulk Comptonization may be decreasing with luminosity. The ξ value fitted in the low luminosity observation was very high and it is unclear whether this value is physical.

A 0535+26

We successfully reproduced the A 0535+26 `fdcut`-based fit with the physical model. The blackbody and CRSF parameters were consistent with the empirical fit, but the absorption was slightly lower in the physical fit. A 0535+26 was the only source for which we could not obtain a good fit with the mass accretion

rate calculated from the empirical continuum flux. Therefore, we left the mass accretion rate free. The fitted value was much lower than what we predicted. The A 0535+26 observed *Suzaku* data may have been affected by the out-of-times events (see Section 8.2.2), which could explain why we measure a higher flux, and, therefore, a higher accretion luminosity than that fitted by the physical model. The fitted accretion luminosity was very subcritical, close the Coulomb luminosity. We fitted a very hot, yet narrow accretion column, in which thermal Comptonization was dominant. Similarly to the low-luminosity observation of 4U 1626−67, we found that the ξ value is very high.

XTE J1946+274

XTE J1946+274 was in a subcritical regime during its *Suzaku* observation. However, its luminosity was closer to $L_{\rm crit}$ than $L_{\rm coul}$. Therefore, it is not entirely unexpected that we were able to successfully reproduce the `fdcut`-based fit with the physical model. The absorption in the physical fit was lover ($\sim$21 cm $N_{\rm H}$ compared to the empirical fit. In addition, the CRSF was difficult to detect, therefore we constrained it by freezing both the energy, $E_{\rm CRSF}$ and the width, $\sigma_{\rm CRSF}$. In the physical fit we found an Fe edge component that we did not find in the `fdcut` fit. Compared to the other sources in the study, for XTE J1946+274 we fitted a relatively cold and narrow accretion column. We found average values for ξ and δ. In addition to Cen X-3, this is the only other source where we found the thermal mound temperature to be higher than the accretion column temperature.

Vela X-1

Vela X-1's luminosity during its *Suzaku* observation was very subcritical, close to the Coulomb luminosity. We found slightly larger inconsistencies between

the empirical and physical fit compared to other sources. The absorption was slightly lower, while the partial covering showed a higher $N_{\rm H}$ with a lower partial covering fraction. In the empirical fit we fitted a narrow and shallow 10 keV feature, while in the physical fit we found a feature with similar parameters, but as an emission line and with little effect on the goodness of fit. The CRSF harmonic was fitted at a higher energy, while the fundamental was undetectable. We fitted a medium-temperature, narrow accretion column. Similarly to the empirical fit, we found high partial covering. Also the physical model fit of Vela X-1 was slightly worse than it respective `fdcut`-based fit. The fitted ξ value was very high, likely because the source luminosity was too low for the physical model to apply.

8.4 Discussion

In this section we discuss the *Suzaku* spectral fit results. We interpret the best fit continuum parameters (see Table 8.3) and their relationship to the sources' luminosities. We also discuss the non-continuum model components, i.e., intrinsic absorption, iron fluorescence, the blackbody emission from the accretion disc, and the 10keV feature. We present comparisons between our results and those found by C02, specifically, we discuss the possible correlations between the cyclotron line and continuum parameters. Lastly, we discuss our physical fit results, we evaluate and interpret the fitted physical paramters, and we present the first confirmed connections between the physical and empirical fits.

8.4.1 Empirical Continuum and 10 keV Feature

Figure 8.1 shows a qualitative comparison among the luminosity-ordered brad-band X-ray spectral continue of several accreting pulsars observed with *Suzaku*. For decades, these spectra have been successfully described using power-law-type

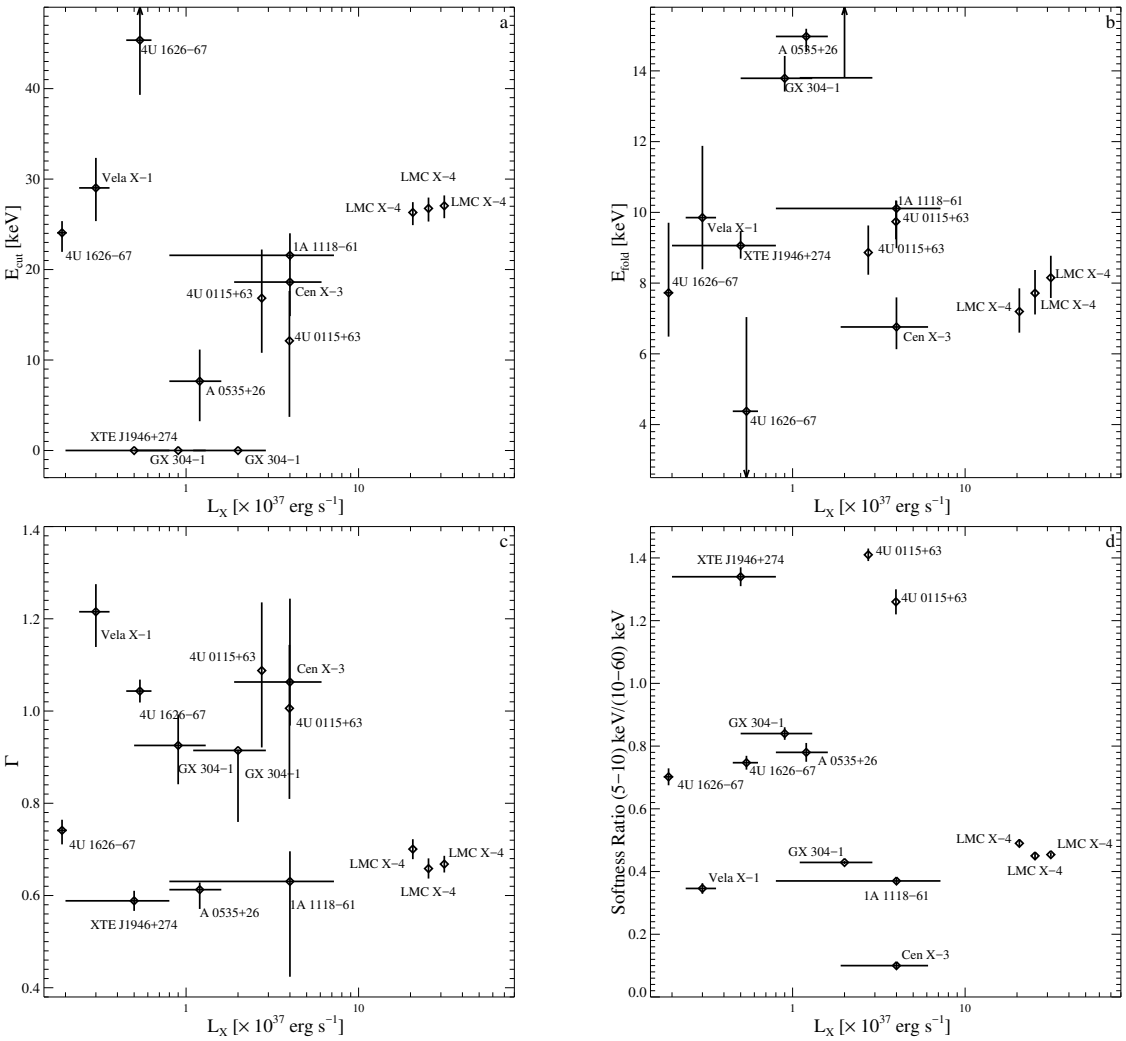

Figure 8.3: Correlations between `fdcut` continuum parameters and luminosity: (a) Continuum cutoff energy as a function of source luminosity. We see a correlation between LMC X-4, Cen X-3, 4U 0115+63, GX 304−1 1A 1118−61, A 0535+26, and XTE J1946+274 (Pearson correlation coefficient is 0.77). 4U 1626−67 and Vela X-1 lie outside this correlation (see text for more details). (b) Continuum folding energy as a function of source luminosity. (c) Continuum photon index as a function of source luminosity. (d) Spectral hardness (5–10 keV/10–60 keV) measured from the sources' XIS3 and PIN light curves as a function of source luminosity. We do not find any correlations in panels b,c, and d.

phenomenological models, with the caveat that these models provide no physical description of the X-ray emission process. For the sources in our sample, we tested the different empirical continuum models commonly used to describe the accreting

pulsar spectra: `plcut`, `cutoffpl`, `npex`, `fdcut`, and `comptt`. [17] We found that `fdcut` provided the overall best fits for all the sources. In some cases, other models also provided good fits for some sources, but not for others.

We found that the photon index and folding energy lie in the $0.53 \lesssim \Gamma \lesssim 1.2$ and $6.8 \lesssim E_{\rm fold} \lesssim 15.2$ ranges. As it is theorized that the folding energy is related to the electron temperature (Mihara et al., 1998), there are likely no large differences in the electron temperatures inside the accretion columns of the sources.

We searched for correlations between the X-ray luminosity and the continuum fit parameters, Γ, $E_{\rm cut}$, $E_{\rm fold}$, and the spectral hardness, respectively. In Fig. 8.3a the continuum cutoff energy was plotted as a function of source luminosity, in which the non-wind accreting HMXBs, i.e., LMC X-4, Cen X-3, 4U 0115+63, GX 304−1, 1A 1118−61, A 0535+26, and XTE J1946+274 showed a possible correlation. For these sources we measured a Pearson correlation coefficient of 0.77. 4U 1626−67 and Vela X-1 lie outside this correlation, which may be related to the type of donor stars: Vela X-1 has the strong wind donor and 4U 1626−67 has a low-mass donor.

As shown in Fig. 8.3b, c, and d we did not find a correlation for the continuum folding energy, photon index, and the source softness and the X-ray luminosity. Generally the photon index is thought to be an indication of the hardness of the spectrum Torres & Rea (2011). However, Fig. 8.3c and d show that Γ is not a direct indication of the spectral hardness. Reig & Nespoli (2013) found that accreting pulsars may show hardness states similar blackholes in XRBs. They found that accreting pulsars may show two distinct hardness-intensity states. In each state, the photon index shows a distinct correlation with hardness.

Some of the sources in our sample required an additional component around

[17] A list of `xspec` models can be found at `https://heasarc.gsfc.nasa.gov/xanadu/xspec/manual/Models.html`.

10 keV for a good fit. In Cen X-3 and 4U 0115+63 we fitted this 10 keV feature as a broad emission line, and as a narrow absorption line in Vela X-1 and GX 304−1. Currently the 10 keV line is thought to originate from the cyclotron emission (Ferrigno et al., 2009), however, we did not find any connection between the cyclotron line and this feature. However, a closer look revealed that the HMXBs without a 10 keV feature (LMC X-4, 1A 1118−61, A 0535+26, and XTE J1946+274) show a possible linear correlation between the photon index and the X-ray luminosity, while the other sources occupy a separate region on the plot. It is yet unclear whether this is a physical interpretation, or it is just an artificial effect due the 10 keV line influencing the continuum description. We did not find any distinguishable properties of the HMXBs without a 10 keV feature in the physical fits.

8.4.2 Intrinsic absorption, iron fluorescence, and blackbody emission

Due to *Suzaku*'s high spectral resolution in the lower energy bands, we were able to study the X-ray absorption and fluorescence emission of the neutron star surrounding medium along the line of sight. Using the improved model (`tbnew`) we successfully described the absorption in our spectra and searched for signatures of intrinsic absorption and other properties of the surrounding material. Table 8.4 shows our fitted hydrogen column densities compared to the interstellar 21 cm $N_{\rm H}$ for each source. In LMC X-4, and 4U 1626−67, we find no indication of intrinsic absorption along the line of sight. However, we found fluorescence emission, predominantly Fe Kα, which indicates that there is a cold neutral (or near-neutral) fluorescent material somewhere in the system, that is illuminated by the X-rays from the accretion column. This material may be located further from the neutron star, possibly around or close to the accretion disc. For example, Hung et al. (2010) claimed that the broad Fe line in LMC X-4 may be a reflection of the Fe Kα line

off the accretion disc. The fluorescent material in 4U 1626−67 material may be slightly ionized as Iwakiri et al. (2012) found that the broad Fe component may be an emission complex of higher ionization lines, i.e., He-like and H-like emission lines (Fe XXV and XXVI).

In the other sources we generally found moderate intrinsic absorption, which was relatively high in Cen X-3 and very high in Vela X-1 (the measured $N_{\rm H}$ almost 8 times higher than the Galactic value), which is not expected due to the presence of the strong stellar wind engulfing the neutron star. In Cen X-3, 4U 0115+63, and GX 304−1 we found He-like and H-like emission lines, indicative of slightly ionized fluorescent material. For GX 304−1, the Fe Kβ had a higher flux than that expected for a neutral material, i.e., 13% of the Fe Kα flux (Palmeri et al., 2003). In A 0535+26 and XTE J1946+274 we only found Fe Kα emission. In Vela X-1, the Fe Kβ flux was 13% of the Fe Kα flux, implying that, in A 0535+26, XTE J1946+274, and Vela X-1. the fluorescent material is likely neutral or very near-neutral.

For Cen X-3, 1A 1118−61, 4U 0115+63, GX 304−1, and Vela X-1 we fitted partial covering absorption modes, which can indicate the degree of clumpiness of the stellar winds from the optical companion that the X-rays pass through before reaching the observer. Specifically, we conclude that there are large but few clumps in Cen X-3, 1A 1118−61, and Vela X-1, i.e., large column densities but low partial covering fractions. In contrast, 4U 0115+63 showed a larger number of smaller clumps, especially in the lower-luminosity observation. 1A 1118−61 and GX 304−1 appeared to have a higher amount of large clumps in the stellar wind.

For several sources, a low-temperature blackbody component was required for a good fit and we investigated the possible origins of this emission, i.e., (i) from the stellar surface, (ii) from the accretion disc due to reprocessed X-rays, (iii) directly

from the accretion disc, or (iv) from the accretion curtain around the neutron star.

For the first case, we assumed a circular blackbody emitting region (with an area $A = \pi R_{\rm BB}$) at the polar caps, from which the emitted blackbody luminosity, $L_{\rm BB}$ is

$$L_{\rm BB} = A\sigma T_{\rm BB}^4 \tag{8.15}$$

where $T_{\rm BB}$ is the fitted blackbody temperature and σ is the Stefan-Boltzmann constant. With that assumption we found radii for the blackbodies higher than the neutron star radii ($R_{\rm BB}{\sim}13 - 60\,{\rm km}$), which may indicate that the blackbody forms further from the neutron star surface.

We then investigated the possible reprocessing of the X-ray emission from the accretion disc by comparing the blackbody radii with the Alfvén radii (R_A) or magnetosphere radii ($R_m{\sim}R_A/2$) of each source. Assuming a thick partial spherical shell centreed on the neutron star (see Fig. 9 and equation in Hickox et al., 2004), the equation for the blackbody radius would be

$$R_{\rm BB} = \sqrt{\frac{L_{\rm X}}{4\pi\sigma T_{\rm BB}^4}} \tag{8.16}$$

where $L_{\rm X}$ is the source luminosity. With this we obtained estimates of the locations of the blackbody emissions. Note that these are rough estimates as there are large uncertainties in the measured distances that transfer over to the calculated luminosities. Consistent with Hung et al. (2010), the we calculated a blackbody radius of ${\sim}1500\,{\rm km}$, which is close to the magnetosphere radius $R_m{\sim}2000\,{\rm km}$, but much lower than the Alfvén radius of $R_m{\sim}4000\,{\rm km}$. Even though these are rough estimates, it is an indication that the blackbody may originate from X-rays reprocessing off the accretion disc, very far away from the neutron star. For the other sources, 1A 1118−61, GX 304−1, 4U 1626−67, and A 0535+26, we calculated

much smaller blackbody radii, in the range of $R_{\rm BB}{\sim}40-200\,{\rm km}$, which are much lower than the Alfvén radii or the magnetosphere radii of their respective sources ($R_m{\sim}R_A/2{\sim}1000-3000\,{\rm km}$).

We considered direct emission from the thin accretion disc (Frank et al., 2002, p.91), where the blackbody temperature at radius $R_{\rm BB}$ is

$$T_{\rm BB}=\left\{\left(\frac{3GM_{\rm NS}\dot{M}}{8\pi R_{\rm NS}^3\sigma}\right)^{1/4}\left[1-\left(\frac{R_{\rm NS}}{R_{\rm BB}}\right)^{1/2}\right]\right\}^{1/4}, \tag{8.17}$$

where $R_{\rm NS}$ and $M_{\rm NS}$ are the radius and mass of the neutron star, $\dot{M}$ is the mass accretion rate derived from the luminosities listed in Table 8.3, and G is the gravitational constant. However, this also resulted in blackbody radii of a few kilometers or less, much lower than the Alfvén or the magnetosphere radii.

We conclude that the blackbody components observed in 1A 1118−61, GX 304−1, 4U 1626−67, and A 0535+26 likely do not originate from the neutron star surface, nor from the accretion disc. The alternate explanation is that the blackbody emission originates from the accretion curtain.

8.4.3 CRSF and Continuum Correlations

In addition to studying the continua of the accreting pulsar sample, we also investigated the possible influence of the magnetic field on the continuum emission by expanding on the study of the continuum-cyclotron line fit parameter correlations found by C02. In order to do so, we made addition fits for our *Suzaku* spectra by replacing `fdcut` with the same continuum model as used by C02, `mplcut`. Figure 8.4 contains three correlation plots based on Fig. 7, 8, and 9 in C02 with the original *RXTE* results plotted in gray and the added *Suzaku* results plotted in black. The panels in Fig. 8.4 describe (a) fundamental cyclotron line width vs.

energy, (b) fundamental cyclotron relative width vs. depth, and (c) the continuum cutoff energy vs. the fundamental CRSF energy.

The fundamental cyclotron line parameters of the sources with both *RXTE* and *Suzaku* data (Cen X-3, XTE J1946+274, Vela X-1 and 4U 1626−67) were overall similar, despite the fact that for each source the *RXTE* and *Suzaku* observations were taken at different times during different outbursts. For these sources, $E_{\rm CRSF}$ showed consistent values between the different observations. A 0535+26 also appears in Fig. 9 in C02, however, they originally plotted the first harmonic value instead of the fundamental (quoted from Kendziorra et al., 1994). The width and depths of the measured CRSFs for each source showed some differences between observations. For Vela X-1 the fundamental is very shallow and we were not able to constrain it. Instead we tied it to the parameters of the harmonic. The CRSFs for Cen X-3 and XTE J1946+274 were also difficult to constrain and we fixed some of the parameters. We found differences between the cutoff energies compared with C02, particularly for XTE J1946+274 and one of the 4U 1626−67 observations. Since we used the same continuum model as they do and changes in the accretion mechanism generally affect the shape of the continuum, such large differences may be explained by variations intrinsic to the source. Note that we did not show the X Per data from C02 as the absorption feature initially interpreted as a CRSF was found to be a 'break' between two soft and hard spectral components that compose the continuum (Doroshenko et al., 2012). Also, results from 4U 0115+63 were not included in Fig. 8.4a and b since we were unable to fit a fundamental CRSF line due to the XIS–PIN gap. The 4U 0115+63 $E_{\rm CRSF}$ plotted in Fig. 8.4c was at half of the energy of the fitted first harmonic.

We measured a Pearson correlation coefficient of 0.86. We note that, for 1A 1118−61, GX 304−1, and XTE J1946+274, the CRSF energies were at the

high-energy end of the sources' PIN range (see Fig. A.14, Fig. A.17, Fig. A.18 and Fig. A.22 in Appendix A.2), which may increase the uncertainty in the CRSF fit parameters.

Based on C02, we compared the width and energy of the cyclotron line measurements. As we show in Fig. 8.4a, the *Suzaku* results agree and strengthen the previously observed correlation. As described by C02, the observed correlation is likely due to the thermal broadening effect. Based on Meszaros & Nagel (1985), the observed CRSF width due to thermal broadening, $\sigma_{\rm CRSF}$, is

$$\sigma_{\rm CRSF} \approx E_{\rm CRSF}\sqrt{8\ln 2\frac{kT_{\rm e}}{m_{\rm e}c^2}} \times |\cos\theta|, \tag{8.18}$$

where $E_{\rm CRSF}$ is the cyclotron line energy, θ is the observer viewing angle relative to the magnetic moment, and $kT_{\rm e}$ is the electron temperature. Therefore, the width of the correlation shown in Fig. 8.4a is likely due to the range of viewing angles, while the linearity of the correlation may indicate that the electron temperature of the accretion columns does not differ greatly between sources.

In Fig. 8.4b we see that the previously claimed linear correlation between $\sigma_{\rm CRSF}/E_{\rm CRSF}$ and $\tau_{\rm CRSF}$ is not supported by our *Suzaku* results. This linear correlation was also found for 4U 1538−52 by Rodes-Roca et al. (2008) from *RXTE* and *INTEGRAL* studies. Both C02 and Rodes-Roca et al. (2008) find that the linear relationship they see is opposite of what the Monte Carlo simulations (Araya & Harding, 1999) give in terms of relativistic cross sections. Despite previous claims, the *Suzaku* results indicate that there is no clear correlation. This is not an unexpected result as both C02 and Araya & Harding (1999) emphasize how the shape of the CRSF fundamental line is highly complex.

Although we did not find a correlation, we noticed that the data points occupy a relatively well defined space within the diagram, possibly covering the

total range of observable angles, with the *RXTE* Cen X-3 observation possibly taken at or close to $\cos\theta\sim1$. We used the results from Fig. 8.4b to obtain an estimate for the characteristic electron temperature ($T_{\rm char}$). Assuming that the accretion column temperatures between sources do not show strong differences (as described by the linearity of the correlation in Fig. 8.4a) and assuming that the maximum $\sigma_{\rm CRSF}/E_{\rm CRSF}\sim0.3$ measurement may correspond to $\cos\theta\sim1$, we calculated $T_{\rm char}\sim6\,$keV. In Section 8.4.4, we checked the consistency of our results by comparing this calculated characteristic temperature to the electron temperature parameters fitted with the physical model.

Fig. 8.4a and b show that $\sigma_{\rm CRSF}/E_{\rm CRSF}\lesssim0.25$. Assuming $|\cos\theta|\sim1$, we can calculated an approximate upper limit to the electron temperatures inside the column $kT\lesssim6\,$keV. Remarkably, this result is consistent with the plasma temperatures obtained by fitting the physical model to the pulsar sample and to *NuSTAR* data of Her X-1 (Wolff et al., 2016).

We investigated the relationship between the cyclotron line energy and the spectral cutoff energy, as shown in Fig. 8.4c. Originally, Makishima & Mihara (1992) and Makishima et al. (1999) claimed a possible correlation $E_{\rm CUT}\propto E_{\rm CRSF}^{0.7}$, which was later supported by C02. In some cases, our *Suzaku* results were in relative agreement with this correlations, i.e., 4U 0115+63, Cen X-3, Vela X-1, and one 4U 1626−67 observation. However, all our other sources and observations, as well as 4U 1626−67 and GX 301-2 in the C02 sample, lie outside this correlation. From Fig. 8.4c we can conclude that our *Suzaku* results are not in agreement with the previously found correlation between the magnetic field and the spectral cutoff.

We also searched for a possible correlation between the spectral folding energy and cyclotron energy, similar to what Makishima et al. (1999) investigated using `npex`-based continuum fits. In Fig. 8.4d we plotted ours and the C02's *RXTE*

results in this context. We conclude that the fundamental cyclotron energy and spectral roll-over do not show a clear correlation.

8.4.4 Physical Modelling

General Results

We have successfully reproduced the empirical continuum model fits with the physical model for 8 out of the 9 sources in our accreting pulsar sample. The power-law shaped continua were fitted with roughly the same goodness of fit with both the `fdcut` and the physical model. The fitted physical parameters were plausible and consistent within the context of our current understanding of the processes that occur inside the accretion columns of X-ray pulsars.

The only source we unable to fit with the physical model was 4U 0115+63. However, we assume this might be due to the very low magnetic field of the neutron star. The magnetic field lines define the quasi-cylindrical geometry of the accretion column, therefore, it is not unexpected that, for higher magnetic fields, the plasma is better confined within that geometry. However, a lower magnetic field may result in an overall different accretion geometry, which can be a possible explanation for why we were unable to describe the continuum of 4U 0115+63 with the physical model, which assumes a cylindrical column.

For A 0535+26 we obtained a good physical fit, however, we were unable to tie the mass accretion rate parameter to the measured continuum flux, i.e., for A 0535+26, we were unable to follow the procedure described in Section 8.3.3 that ensures conservation of energy between the model and observation. Instead, the fit required a much lower mass accretion rate than expected. However, the spectrum of A 0535+26 may have been affected by the possible out-of-time events during the observation (see Section 8.2.2). As these out-of-time events may result in higher

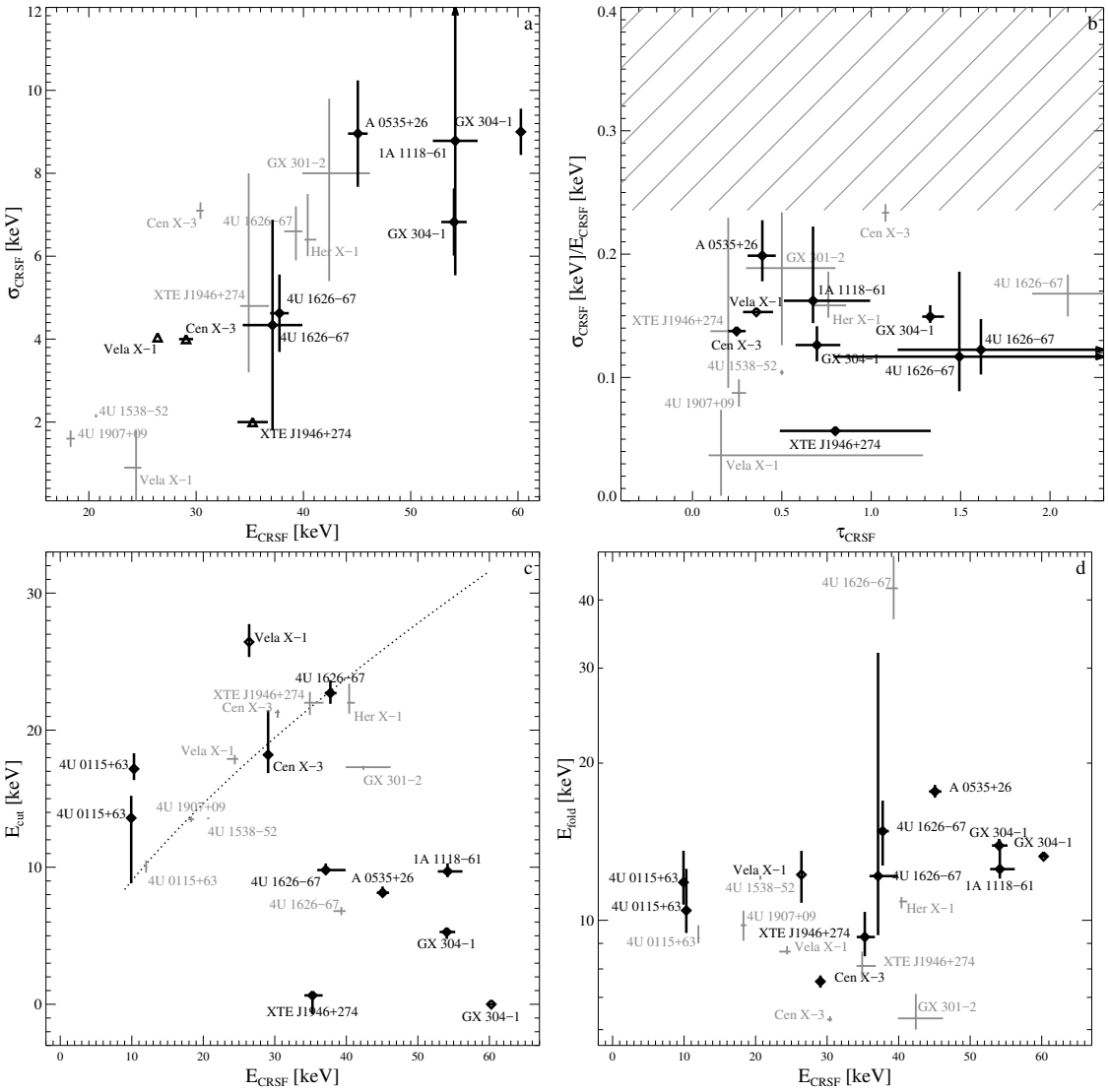

Figure 8.4: Figure based on C02 for which the data points are shown in gray. The data points in black are results form this analysis and were obtained by fitting the continuum with an `mplcut` model. (a) CRSF width as a function of its centroid energy. We measure a Pearson correlation coefficient of 0.78. (b) CRSF relative width as a function of depth. We measure a Pearson correlation coefficient of 0.14. (c) Continuum cutoff energy as a function of the cyclotron energy. Our results do not confirm the previously found correlation $E_{\rm CUT} \propto E_{\rm CRSF}^{0.7}$ found by Makishima et al. (1999) shown by the dotted line (see text for more details). (d) Continuum folding energy as a function of the cyclotron energy.

flux measurements, this could explain why the physical model required a lower mass accretion rate than that derived from the spectral flux measurements. Note,

however, that this explanation is uncertain. The out-of-time events were not studied in detail, therefore, it is unclear the exact effect they have on the observed spectral shape.

We investigated whether the 10 keV feature originates from the accretion column by not including them in our initial fit trials. However, in the expected sources (Cen X-3, GX 304−1, and Vela X-1) the feature was still necessary for a good fit. The parameters of this component in the physical fits are consistent with those in the empirical fits (see Table 8.4–8.8).

For all the fitted spectra, most of the continuum flux is from Comptonized bremsstrahlung emission. The Comptonized cyclotron emission had an overall lower flux contribution, however, it accounted for a higher amount of the flux at the hard X-ray energies. This is not unexpected, as the cyclotron lines form in the emission region at those high energies. The Comptonized cyclotron emission was negligible in LMC X-4, source which likely has a very large magnetic field. Unexpectedly, for all sources the Comptonized blackbody emission was negligible and did not effect the goodness of fit. This was the case even for the sources that appeared to have higher thermal-mound temperatures, such as Cen X-3, 4U 1626−67, A 0535+26, and XTE J1946+274.

For most of the sources, the accretion columns show predominantly thermal Comptonization (i.e., $\delta \gg 4$). Only Cen X-3 and the high luminosity observation of 4U 1626−67 showed about equal contributions from both thermal and bulk Comptonization.

We find that the column electron temperature fitted with the physical model showed a strong correlation with the folding energy. Specifically, the electron temperatures seem to be are equivalent to $\approx 1/2$ of the respective folding energies. A possible connection between these two variables has been assumed before, e.g.,

Mihara et al. (1998) claimed a connection between the folding energy and the Thomson optical depth and temperature. However, this is the first time that the correlation has been confirmed through observations and the application of a physical model. This is also the first connection ever confirmed between the empirical and physical accreting pulsar X-ray continuum description.

The luminosity and accretion column temperatures showed no correlation. This is not unexpected, as the luminosity/mass accretion rate is not a direct indication of the source hardness. Rather, the amount of hard X-ray photons produced is related to the electron temperature, which depends on the physical properties and geometric structure of the accretion column.

For this project we chose high-luminosity sources that were likely to be at least above the Coulomb luminosity and would form an radiation-dominated shock in the accretion column. We confirmed that most of the sources have fitted accretion luminosities that lie in the supercritical regime (see Table 8.12). Only A 0535+26 and Vela X-1 were close to the Coulomb luminosity, while XTE J1946+274 and the low-luminosity observation of 4U 1626−67 were slightly subcritical. Even at the lower luminosities, the physical model provided good fit results. Vela X-1 was the source with the lowest accretion luminosity, and the only source where the physical fit was not as good as the empirical fit.

For all the sources except LMC X-4, the height of the radiation-dominated shock is at approximately half of the height of the accretion column. For Cen X-3, the emission region height is consistent with that found by Farinelli et al. (2016), who used an alternate implementation of the physical model to *BeppoSAX* data from 1997.

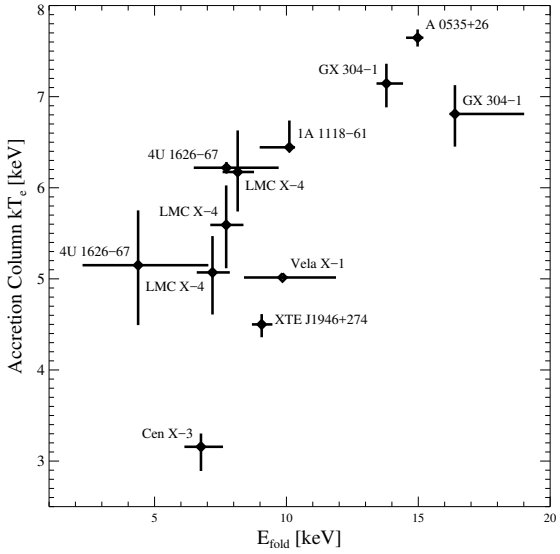

Figure 8.5: The electron temperature inside the accretion column as a function of the folding energy. The electron temperatures are from the spectral fits where the continuum was described with the physical model. The folding energies are from the empirical spectral fits, where the continuum was modelled with the `fdcut` model. This is the first time the correlation between the folding energy from empirical fits is confirmed to be related to the electron temperature inside the accretion column. This is also the first confirmed correlation between the physical model and the phenomenological models.

Physical Correlations

We compared the physical and empirical continuum fit parameters and found a linear correlation between the electron temperature (fitted with the physical model) and the spectral curvature/roll-over ($E_{\rm fold}$) fitted with the empirical models. This relationship holds for $E_{\rm fold}$ values obtained in both the `fdcut`- and `mplcut`-based fits. Although this correlation has been theorized before (see, e.g., Makishima & Mihara, 1992; Farinelli et al., 2016), this is the first time it has been confirmed with systematic physical and empirical modeling of a sample of sources. We see that the folding energy values are around double the electron temperature values. This is also the first confirmed connection between the physical and empirical models. This linear correlation can further be used in providing more physical interpretations to

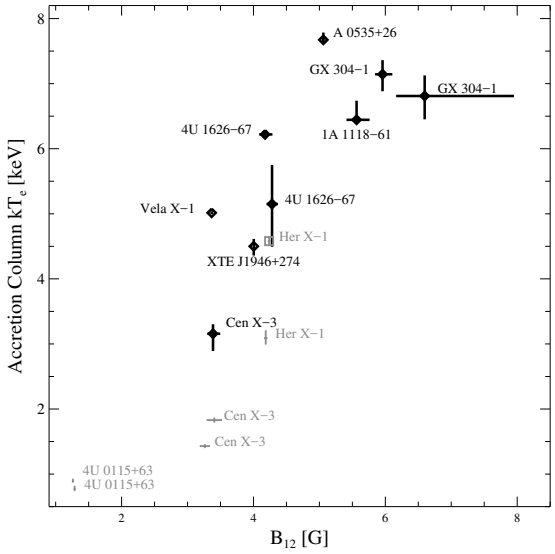

Figure 8.6: The electron temperature inside the accretion column as a function of the magnetic field strength (in units of 10^{12} G) at the emission region as measured by the fundamental CRSF. Both the electron temperatures and magnetic field strengths are from the spectral fits where the continuum was described with the physical model. LMC X-4 was not included in the plot as its CRSF and magnetic field have not yet been confirmed (see text for details). The grey crosses are *BeppoSAX* results from Farinelli et al. (2016) and the grey square is the *NuSTAR* result from Wolff et al. (2016).

past results obtained with empirical spectral fits

We note a remarkable self-consistency between the electron temperature values fitted with the physical model and the characteristic electron temperature calculated from the observed thermal broadening effect of the cyclotron line described in Section 8.4.3.

We see a possible linear correlation between the accretion column electron temperature and the magnetic field (Fig. 8.6). This trend was also found by Farinelli et al. (2016), who fit a different implementation of the radiation-dominated radiative shock model, and their results are shown by the grey crosses in Fig. 8.6. They argue that cyclotron cooling explains the observed correlation based on the theory by Arons et al. (1987) that cyclotron cooling is an efficient cooling mechanism for the

accretion column. However, we and Wolff et al. (2016) find that the Comptonized cyclotron emission fluxes (including those in Cen X-3 and Her X-1) are only a few percent of the total continuum flux (see Fig. A.27). The Comptonized cyclotron emission flux we measure for Cen X-3 is also in agreement with that found by West et al. (2017). In contrast, Farinelli et al. (2016) measure a much larger relative cyclotron emission flux (28%–78%) for similar cyclotron line (magnetic field) values of Cen X-3 and Her X-1 compared to those fitted by us and Wolff et al. (2016). However, note that the cyclotron seed photons are calculated differently in the two model implementations. Therefore, it is not clear if the linear correlation observed between the electron temperature and magnetic is due to cyclotron cooling or other physical or even observational effects. Therefore, in order to obtain a better understanding of this, further testing of the physical model on more sources is needed.

8.5 Summary and Conclusions

In this paper we analyzed the high-luminosity *Suzaku* observations of a sample of nine accreting pulsars. We performed a detailed X-ray broad-band spectral analysis of each source by applying phenomenological models and a new physical model implementation (Becker & Wolff, 2007; Wolff et al., 2016). For individual sources, we compared our results with previous studies. In addition, we conducted a comprehensive comparative study of the sample en masse. In the following we summarize the results of our analysis.

We successfully described the continua of all the accreting pulsars in our sample with the Fermi Dirac Cutoff Power Law empirical model. Describing all the sources and observations consistently with one model made it possible to make a for a meaningful comparison between them. We also studied the non-broad-band-

continuum spectral components (absorption, partial covering, iron fluorescence, low-temperature blackbody emissions, 10 keV features, and cyclotron lines) and compared the fit parameters (Tables 8.3–8.8) with previous studies for each source. We found a possible correlation between the cutoff energy and luminosity for the non-wind HMXBs (Fig. 8.3a), and a possible correlation between the photon index and luminosity for the sources without the 10 keV feature. We also studied the structure and ionization level of the surrounding medium for each source from absorption, partial covering, and fluorescence iron emission measurements. We also studied the low-temperature blackbody component in the sources in which it was present. We confirm the previous claim by Hung et al. (2010) that the blackbody emission in LMC X-4 is likely due to the reprocessing of the X-ray emission from the column off the accretion disc. For the other sources (1A 1118−61, GX 304−1, 4U 1626−67, and A 0535+26), the data indicate that the blackbody may originate from the hot plasma in the accretion "curtain".

We also compared our sample results with previous studies, particularly with the correlations between the CRSF and continuum parameters found by C02. We confirmed the thermal broadening observed for the cyclotron line found by C02. We also found that the CRSF thermal broadening information can provide an approximate upper limit to the accretion column electron temperature ($\sim$6 keV from Fig. 8.4b). We disclaimed the previous claimed correlation between the cutoff and CRSF energies originally claimed by Makishima & Mihara (1992) and Makishima et al. (1999).

We successfully fitted the physical model to all the sources in our sample, except 4U 0115+63, which we assume may have a different accretion column geometry due to its low magnetic field. The physical model reproduced the empirical `fdcut`-based fits. We obtained physically descriptive parameters of the accretion column

structure and geometry, e.g., radius, electron temperature, ratio between bulk and thermal Comptonization, and height of the radiation-dominated radiative shock (see Tables 8.11 and 8.12). All the additional model components applied in the `fdcut`-based fits (absorption, blackbody emission, 10 keV feature, fluorescence lines, and cyclotron lines) were needed in the physical model-based fits as well.

We found two connections between the physical model- and the empirical model-based fits fits. First, we confirm a correlation between the folding energy of the empirical model and the electron temperature fitted with the physical model (Fig. 8.5). Although this has been previously theorized, this is the first confirmation obtained by using a physical continuum description. The folding energy values are approximately double the electron temperature values. Second, we find a self-consistency in our spectral results, as the physically fitted accretion column temperatures are in agreement with the $\sim$6 keV characteristic electron temperature calculated from the thermal boradening effect of the CRSF. This information can now allow us to provide better physical interpretations to empirical fits and make fewer assumptions.

The electron temperature also showed a linear correlation with the magnetic field (i.e., with the fitted cyclotron line energy), however, the physical interpretation is not clear. Cyclotron cooling may be one possible explanation, yet it is not confirmed, therefore, this correlation requires further investigation.

Accreting pulsars are a rich laboratory for astrophysical studies, which continue challenge our current understanding of extreme physical phenomena. A major breakthrough is the transition from phenomenological spectral modelling to a description that carries physical information about these systems, which has been a highly anticipated step since their discovery. Future tests and studies of physical models with improved spectral data from current and upcoming X-ray missions will

further build upon and improve our current understanding of accreting pulsars and neutron stars in general.

9

Summary and Outlook

9.1 Summary

Neutron stars are the post-supernova remnants of the evolution of intermediate/high mass stars. They are remarkable laboratories for extreme physics, a blend of physical phenomena that go beyond what we can reproduce in our laboratories. They have incredibly high gravitational fields, and the highest magnetic fields and matter densities in the universe, properties which have raised many questions in the physics and astrophysics communities regarding our current understanding of the behavior of matter at densities higher than the nuclear density.

Pulsars, neutron stars with high magnetic fields, show periodic fluctuations of radiation. Pulsars in binary systems emit high-energy radiation when they accrete mass from their companion star. The transferred material is channeled along the magnetic field lines in a cylindrical geometry onto the magnetic poles of the neutron star. Inside this accretion column, the accreted plasma reaches temperatures around 10^7 K and soft X-ray bremsstrahlung, blackbody, and cyclotron photons are produced. Before exiting the column, these seed photons gain energy via thermal and bulk Comptonization processes, resulting in the observed hard X-ray emission. This

dissertation focused on the study of the X-ray continuum emission from the hot accretion column at the neutron star poles using data from the *Suzaku* satellite.

The first part of the analysis (Chapter 7) was a temporal and spectral study of the accreting pulsar XTE J1946+274. The temporal analysis consistent of updating the pulse-period measurement using the high timing resolution PIN data.[1]. The X-ray spectrum was described by an absorbed FermiDirac cut-off power-law model. I also found a narrow Fe Kα line and a weak cyclotron line. The iron flux measured in the *Suzaku* spectrum was consistent with the previously observed continuum flux versus iron line flux correlation expected from fluorescence. The iron line flux was slightly higher than that expected from fluorescent emission along the line of sight, possibly indicating higher iron abundance or a non-uniform structure of the surrounding material. The unchanging pulse profiles and cyclotron energy ofXTE J1946+274 were strong indicators that the source did not experience strong changes in the accretion regime at different luminosities, rather it was observed only in the subcritical state.

Building and expanding on the single-source study of XTE J1946+274 presented in Chapter 7, I conducted a detailed spectral analysis of a sample of nine high-luminosity accreting pulsars (LMC X-4, Cen X-3, 1A 1118−61, 4U 0115+63, GX 304−1, 4U 1626−67, A 0535+26, XTE J1946+274, and Vela X-1) observed with *Suzaku* (Chapter 8). I mainly focused on the empirical and physical modeling of the continuum, but also studied additional spectral features, and compared with previous studies.

I described properties of the pulsar surrounding material of each source, the location (along or outside the line of sight), structure (level of clumpiness), and ionization level (neutral or near-neutral), by measuring the intrinsic absorption,

[1]This pulse period measurement was later used by Matthias Kühnel to improve determination of the orbital parameters using data from multiple instruments (*Suzaku*, *RXTE*, *Swift*, and *Fermi*)

the partial covering, and the iron fluorescent lines, respectively. In some sources, a 10 keV line feature was present, yet its origins remain unknown, as although it has been theorized that it may be related to the cyclotron emission (Ferrigno et al., 2009), the *Suzaku* data do not show any such indication.

In terms of the continuum, I studied the sources individually and en masse in the context of the sample.

First, I applied the standard empirical continuum models, and obtained good fits for all sources with the Fermi Dirac Cutoff Power-Law. For the individual sources, I found that the continuum parameters and the additional components were generally consistent with previous studies. In the context of the sample, I compared the *Suzaku* cyclotron line and continuum fit parameters with those found by Coburn et al. (2002) in a similar pulsar sample analysis performed using *RXTE* data. The *Suzaku* results disagree with the previously claimed correlation between the CRSF energy and the continuum cutoff and folding energies found by Makishima & Mihara (1992); Makishima et al. (1999); Coburn et al. (2002). The cyclotron line measurements from this work and the Coburn et al. (2002) study reveal a thermal broadening effect, which provided an estimate of a characteristic electron temperature of $\sim$6 keV in the accretion columns.

Second, I tested a new implementation of the physical model developed by Becker & Wolff (2007) and implemented by Wolff et al. (2016). I successfully reproduced the empirical continuum model-based fits with the physical model for all sources, except 4U 0115+63 (which was likely due to the low magnetic field of the source). The model provides a physical description of the geometry and structure of accretion columns with radiation-dominated radiative shock of high-luminosity pulsars. The model fit parameters are: the mass accretion rate, the column radius, the plasma temperature, and similarity parameters related to photon travel time and

the bulk and thermal Comptonization effects (Table 8.11). Additional properties were derivable from these fit results, e.g., the shock height, the accretion column height, and characteristic parameters related to the cross sections (Table 8.12). In the context of the sample, the physical fit results confirm that the electron temperature is correlated with the spectral roll-over (the folding energy in empirical models). Although this has been theoretically assumed, this is the first time this correlation has been confirmed by systematically applying both empirical and physical models to observed data. The electron temperature and magnetic field also showed a possible linear trend, which has been theorized to be due to cyclotron cooling (Farinelli et al., 2016). However, this is currently not numerically supported by our results and further studies are needed.

Lastly, a self-consistency between the empirical and physical spectral fits is confirmed by the fact that the plasma temperature fitted with the physical model is in agreement with the $\sim$6 keV characteristic electron temperature determined from the thermal broadening of the cyclotron line.

9.2 Outlook

Since their discovery, accreting pulsars have been studied in detail because they are generally bright sources, and the accretion process is depended on the neutron star properties. Pulsar accretion is complex as it involves a combination of extreme temperatures, magnetic fields, and gravitational forces. For this reason, physically descriptive models have become available only in recent years, and making them available for testing on observations has been a long anticipated step. Increasingly accurate measurements of pulsar properties will be obtained with better data from current and upcoming instruments, as well as future improvements to the physically descriptive model, such as accounting for relativistic light-bending

effects of the emission from both magnetic poles (see, for example, work in progress by Falkner et al., 2016) .

Appendix A

Long-Term Light Curves and Spectral Fits

A.1 Plots of the *Swift*-BAT Light Curves

This appendix section presents plots of the *Swift*-BAT 15–50 keV light curves from 2005 to 2015 of all sources in the pulsar sample as well as close-up views around the times of the *Suzaku* observations considered in this work. The BAT light curves are displayed with a binning of 3 d, and show all bins with a signal to noise ratio $\geq$2. The vertical red lines represent the times of the *Suzaku* observations. In the close-ups the thickness of the red lines corresponds to the *Suzaku* exposure time. The BAT data were obtained from `http://swift.gsfc.nasa.gov/results/transients/`.

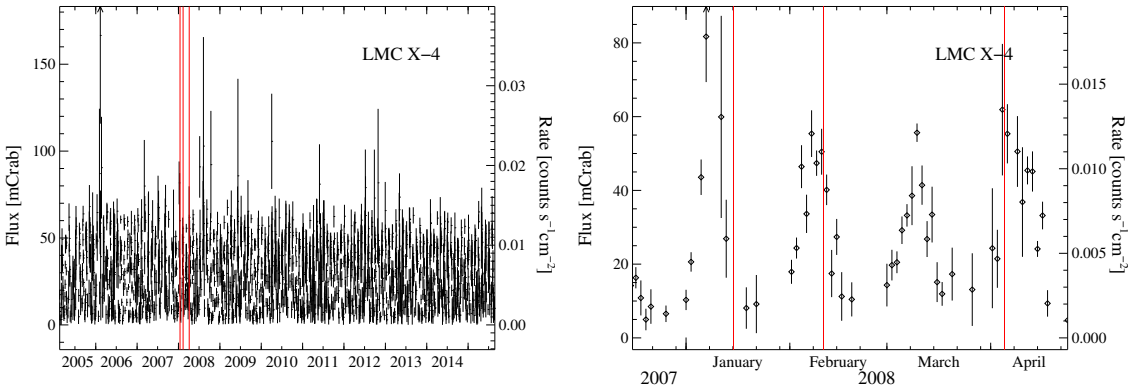

Figure A.1: BAT light curve with times of the *Suzaku* observations analysed in this work highlighted for LMC X-4 with, in chronological order, *Suzaku* ObsIDs 702038010, 702037010, and 702036020.

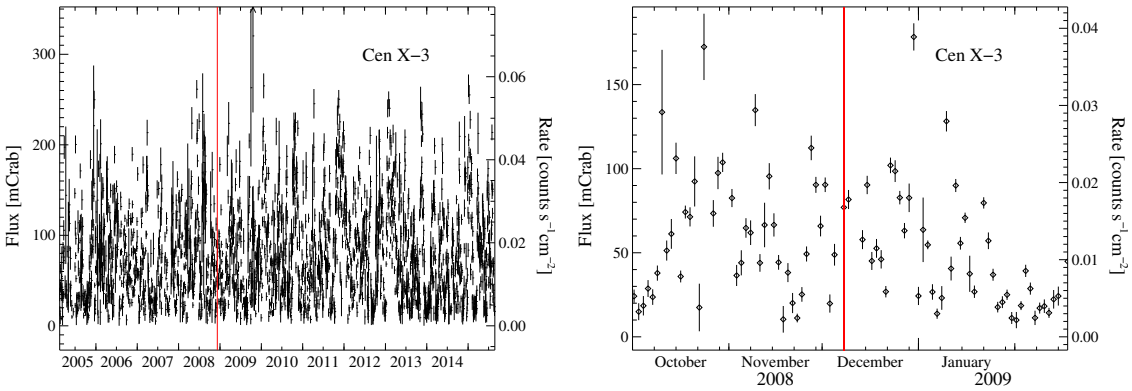

Figure A.2: Figure A.1 for Cen X-3 with ObsID 403046010.

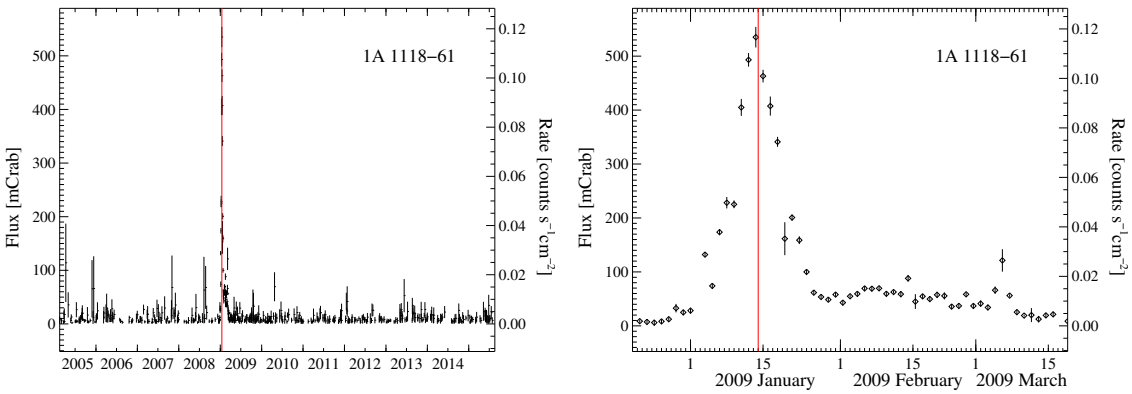

Figure A.3: Figure A.1 for 1A 1118−61 with ObsID 403049010.

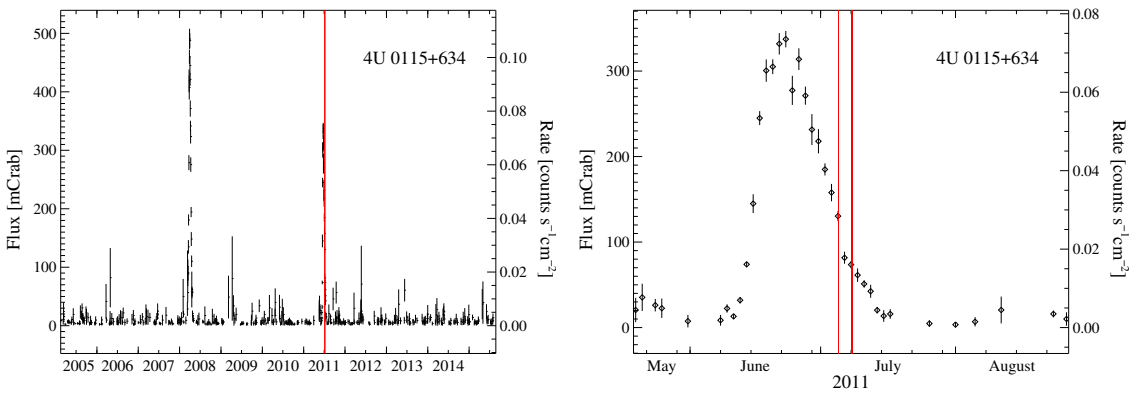

Figure A.4: Figure A.1 for 4U 0115+63 with ObsIDs 406048010 and 406049010.

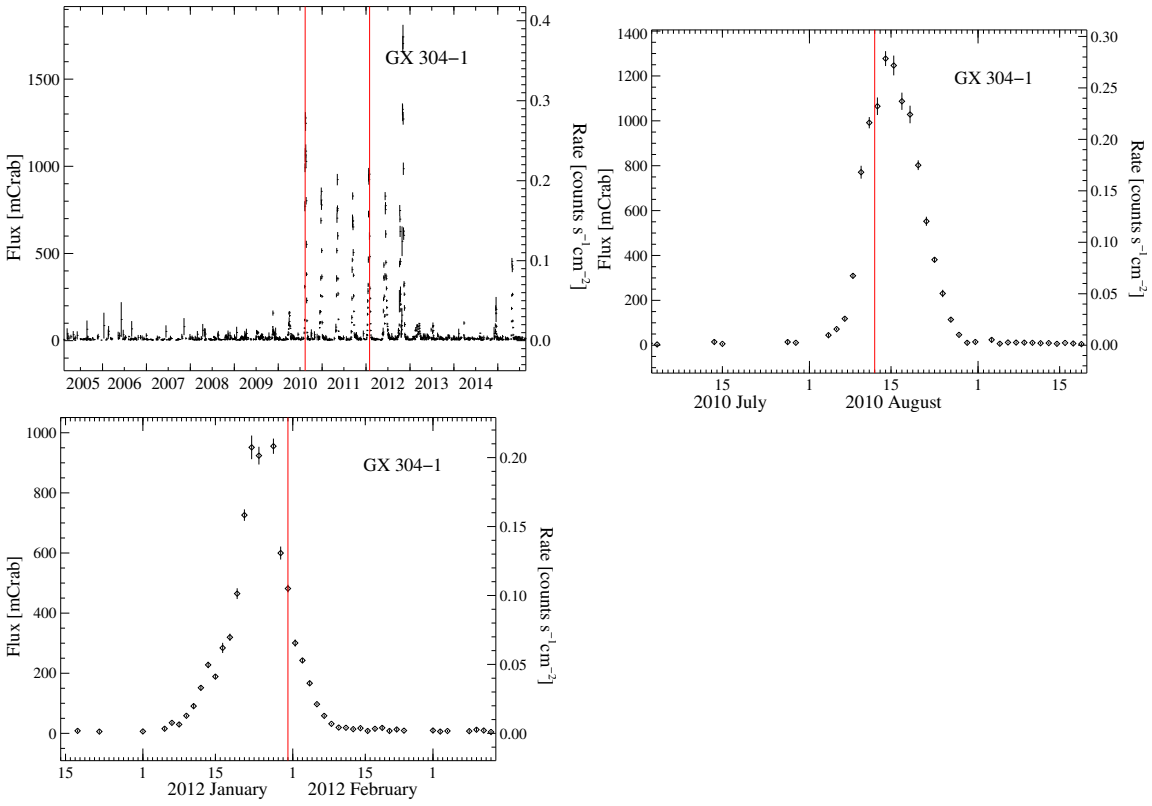

Figure A.5: Figure A.1 for GX 304−1 with ObsIDs 905002010 and 406060010.

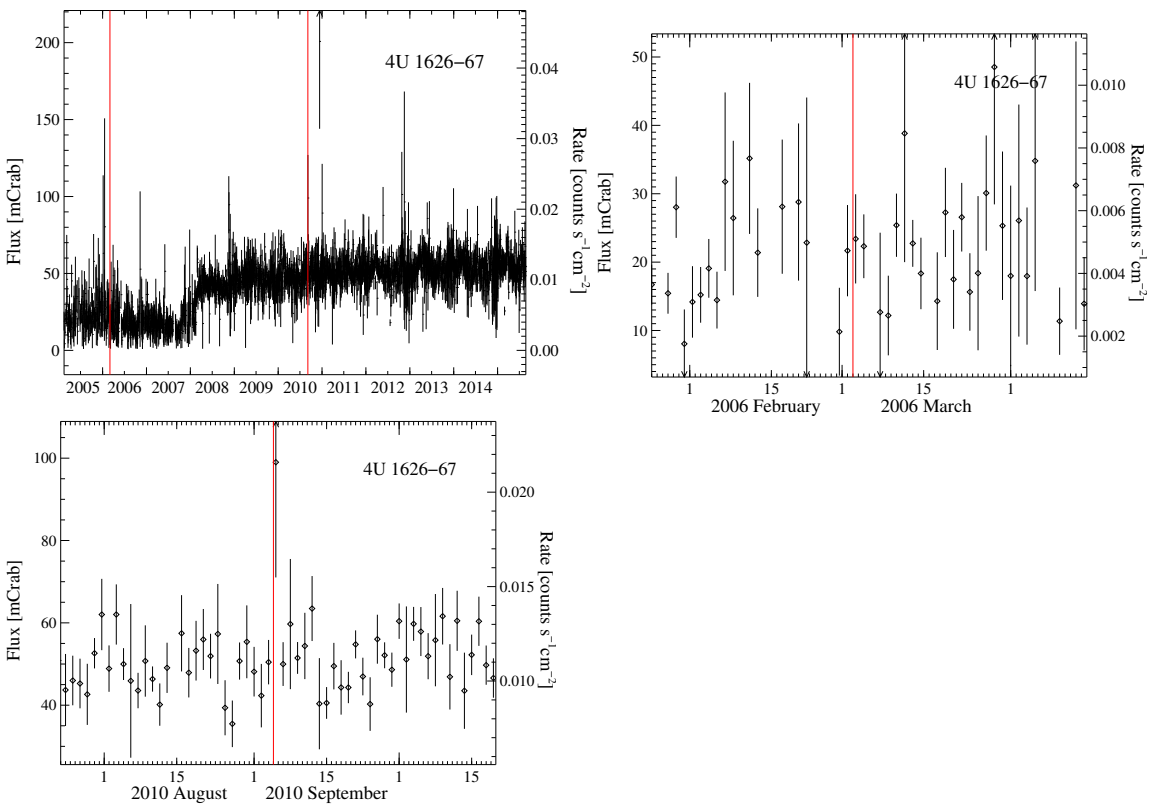

Figure A.6: Figure A.1 for 4U 1626−67 with ObsIDs 400015010 and 405044010.

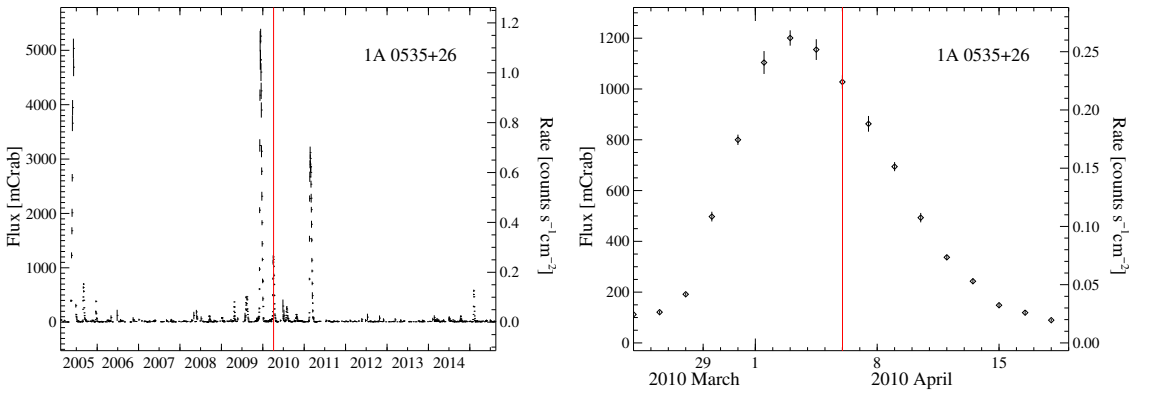

Figure A.7: Figure A.1 for A 0535+26 with ObsID 404055010.

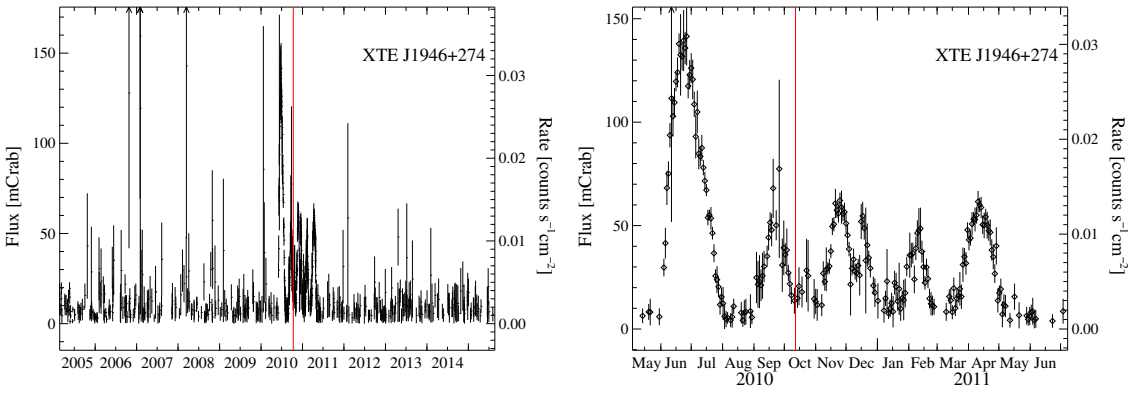

Figure A.8: Figure A.1 for XTE J1946+274 with ObsID 405041010.

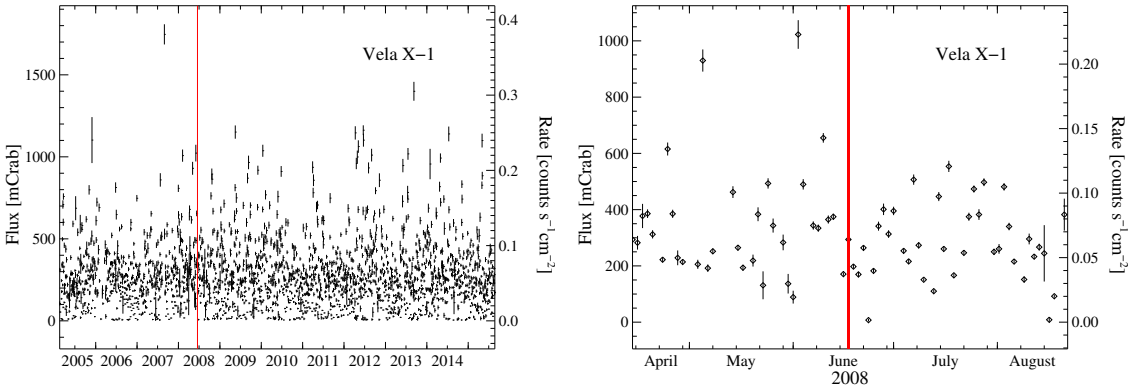

Figure A.9: Figure A.1 for Vela X-1 with ObsID 403045010.

A.2 Plots of the Empirical Spectral Fits

This appendix section presents plots of the best spectral fits obtained with the `fdcut` continuum model for all *Suzaku* observations analysed in this work. The fits are discussed in detail in Section 8.3.2. The upper panel of each figure shows the absorbed *Suzaku* spectrum in counts space together with the full model, the middle panel shows the unfolded *Suzaku* spectrum, corrected for absorption, together with the full model and the model components, and the bottom panel shows the fit residuals. The data and the residuals are plotted in red for XIS0, in green for XIS1, in yellow for XIS3, and in blue for PIN. The full model and the model components are plotted in black.

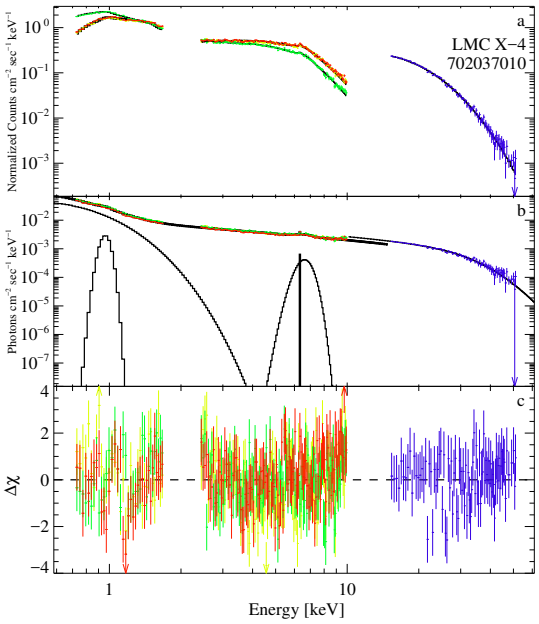

Figure A.10: Empirical spectral fit for LMC X-4, ObsID 702037010.

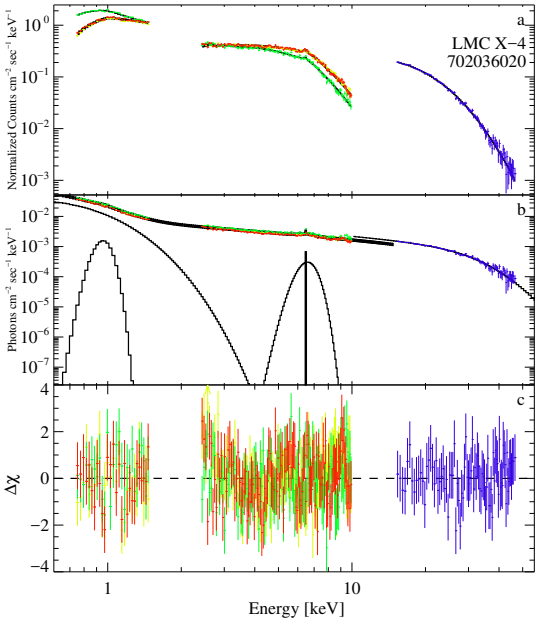

Figure A.11: Empirical spectral fit for LMC X-4, ObsID 702036020.

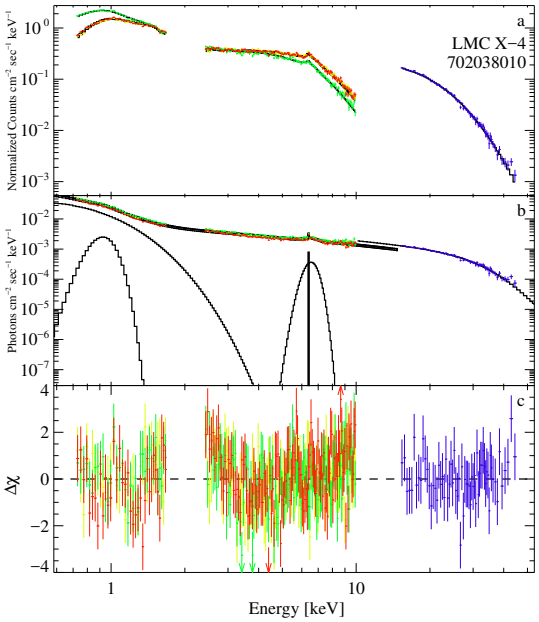

Figure A.12: Empirical spectral fit for LMC X-4, ObsID 702038010.

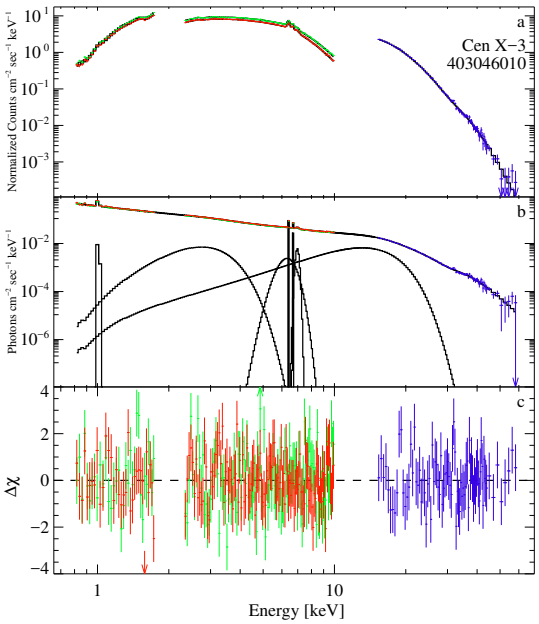

Figure A.13: Empirical spectral fit for Cen X-3, ObsID 403046010.

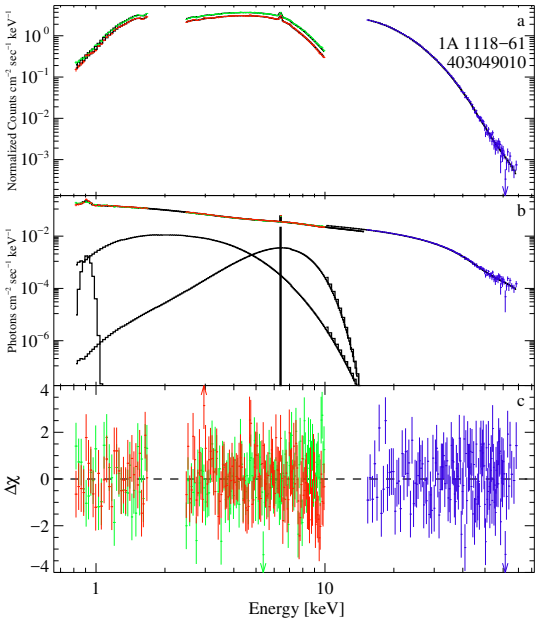

Figure A.14: Empirical spectral fit for 1A 1118−61, ObsID 403049010.

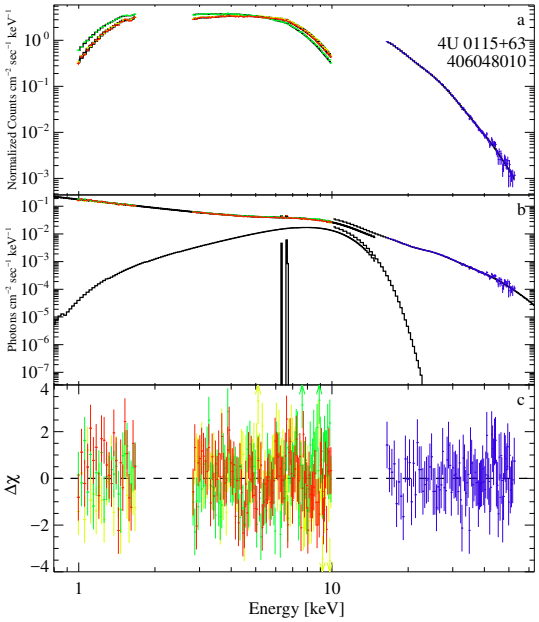

Figure A.15: Empirical spectral fit for 4U 0115+63, ObsID 406048010.

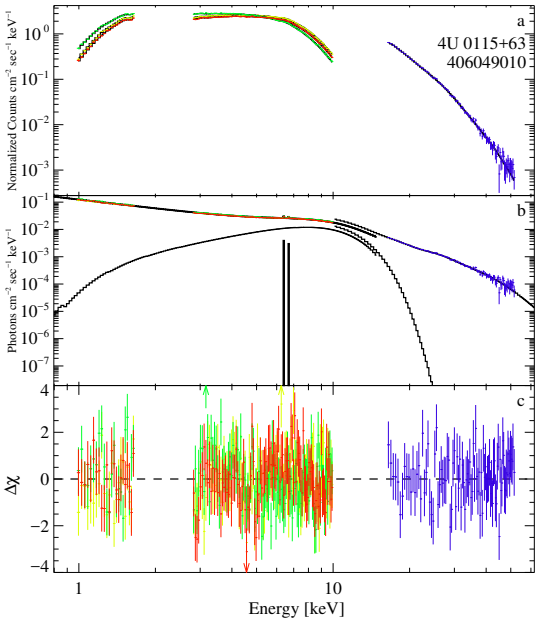

Figure A.16: Empirical spectral fit for 4U 0115+63, ObsID 406049010.

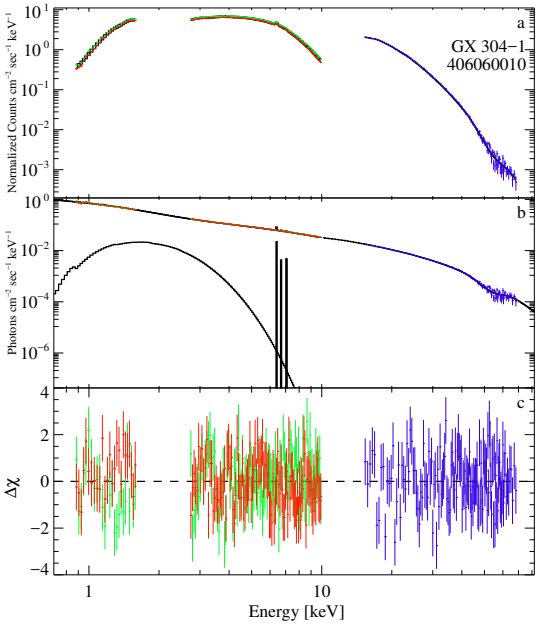

Figure A.17: Empirical spectral fit for GX 304−1, ObsID 406060010.

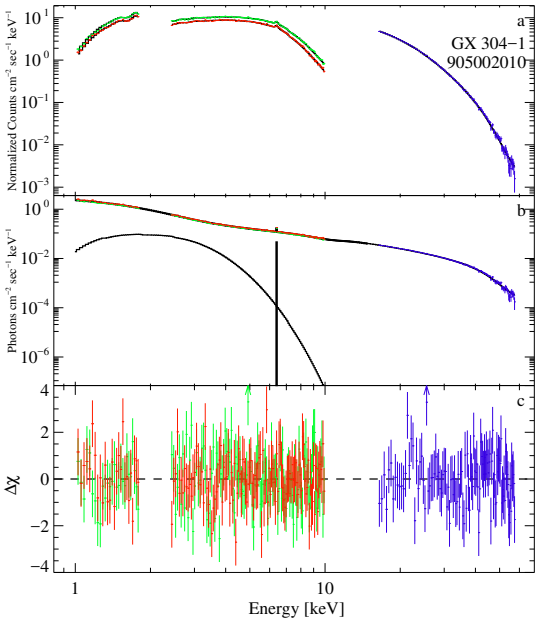

Figure A.18: Empirical spectral fit for GX 304−1, ObsID 905002010.

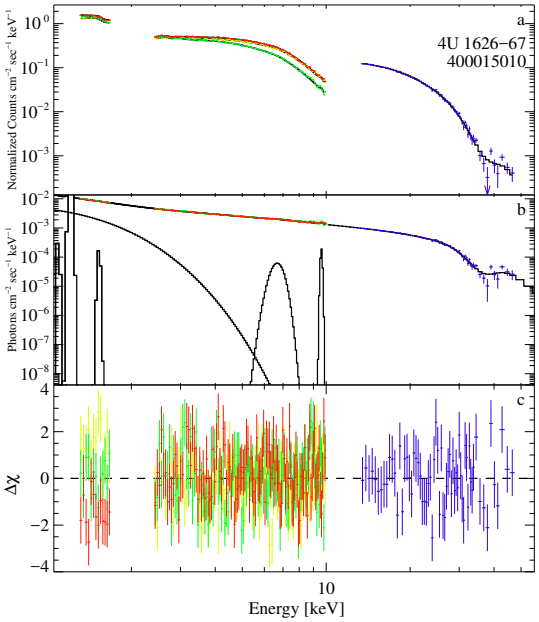

Figure A.19: Empirical spectral fit for 4U 1626−67, ObsID 400015010.

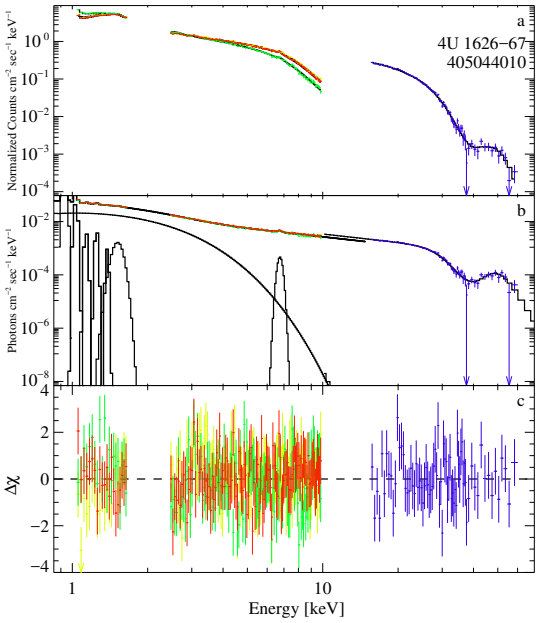

Figure A.20: Empirical spectral fit for 4U 1626−67, ObsID 405044010.

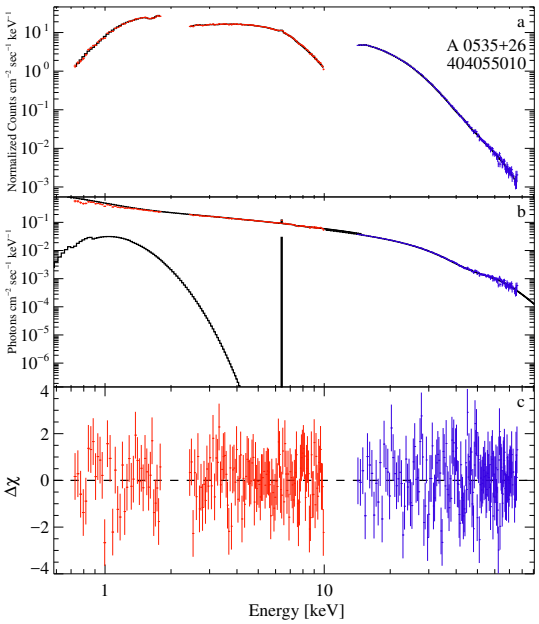

Figure A.21: Empirical spectral fit for A 0535+26, ObsID 404055010.

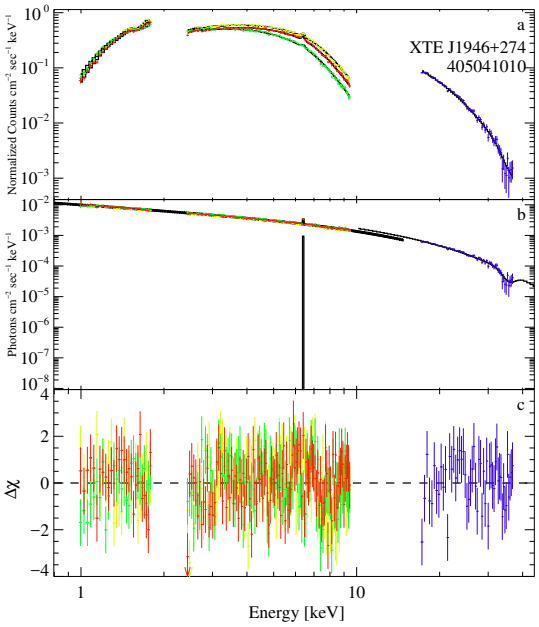

Figure A.22: Empirical spectral fit for XTE J1946+274, ObsID 405041010.

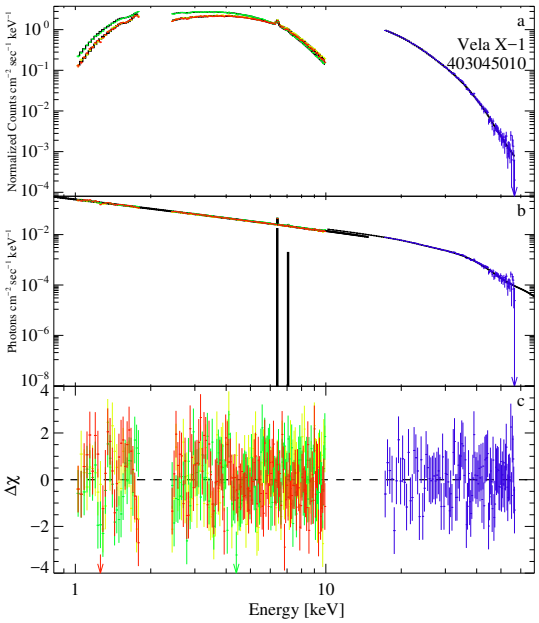

Figure A.23: Empirical spectral fit for Vela X-1, ObsID 403045010.

A.3 Plots of the Physical Spectral Fits

This appendix section presents plots of the best spectral fits obtained with the `bwsim` continuum model for all *Suzaku* observations analysed in this work (with exception of the 4U 0115+63 observations for which we did not obtain good fits with this model). The fits are discussed in detail in Section 8.3.4. The upper panel of each figure shows the absorbed *Suzaku* spectrum in counts space together with the full model, the middle panel shows the unfolded *Suzaku* spectrum, corrected for absorption, together with the full model and the model components, and the bottom panel shows the fit residuals. The data and the residuals are plotted in red for XIS0, in green for XIS1, in yellow for XIS3, and in blue for PIN. The full model and the model components are plotted in black, with the exception of the Comptonized bremsstrahlung and cyclotron emission contributions which are plotted in pink and light blue, respectively.

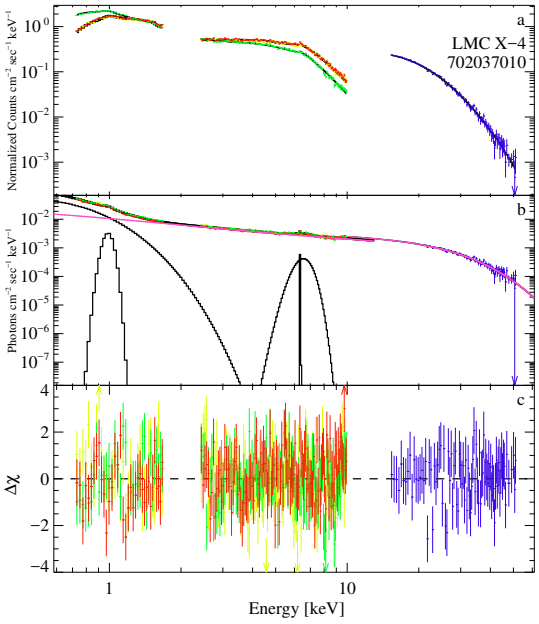

Figure A.24: Physical spectral fit for LMC X-4, ObsID 702037010.

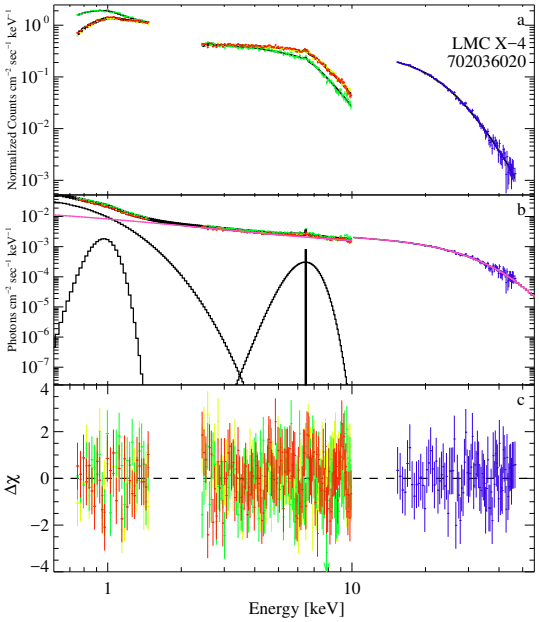

Figure A.25: Physical spectral fit for LMC X-4, ObsID 702036020.

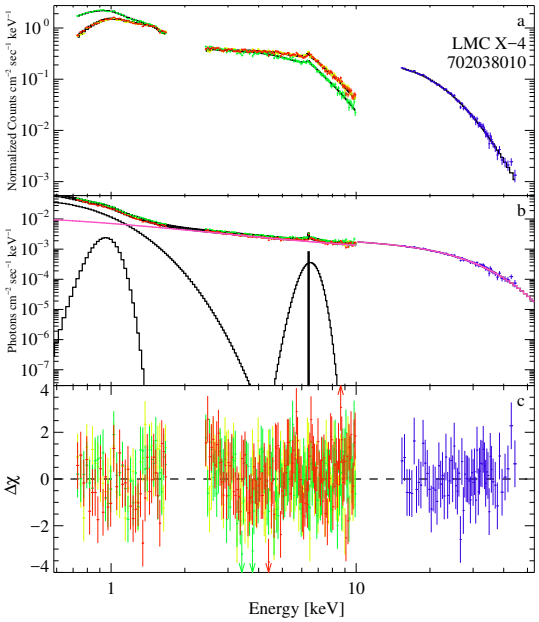

Figure A.26: Physical spectral fit for LMC X-4, ObsID 702038010.

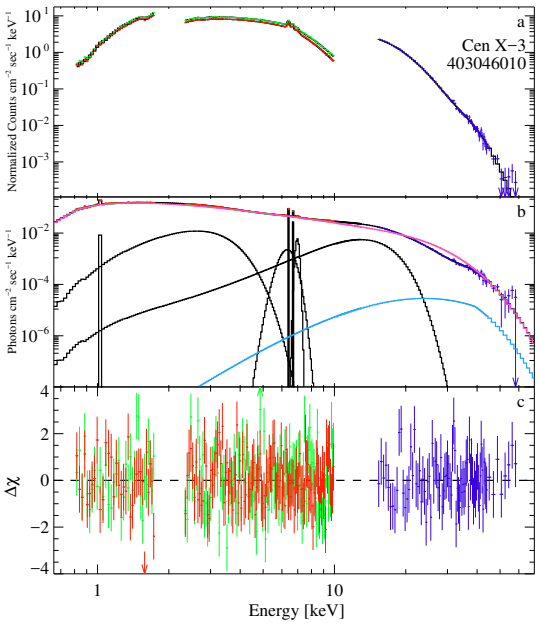

Figure A.27: Physical spectral fit for Cen X-3, ObsID 403046010.

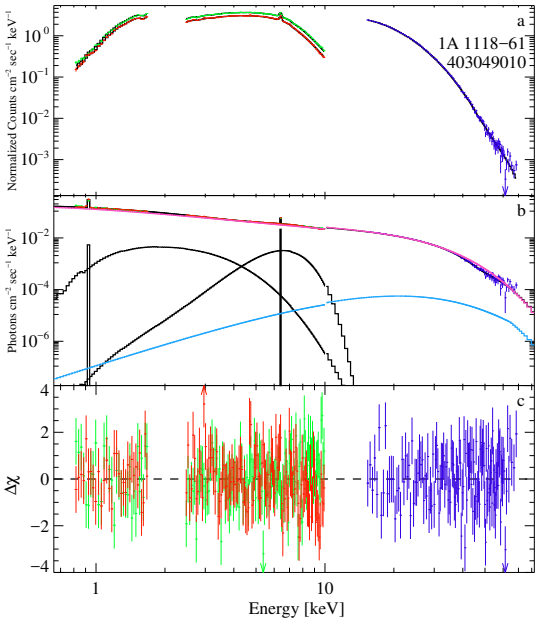

Figure A.28: Physical spectral fit for 1A 1118−61, ObsID 403049010.

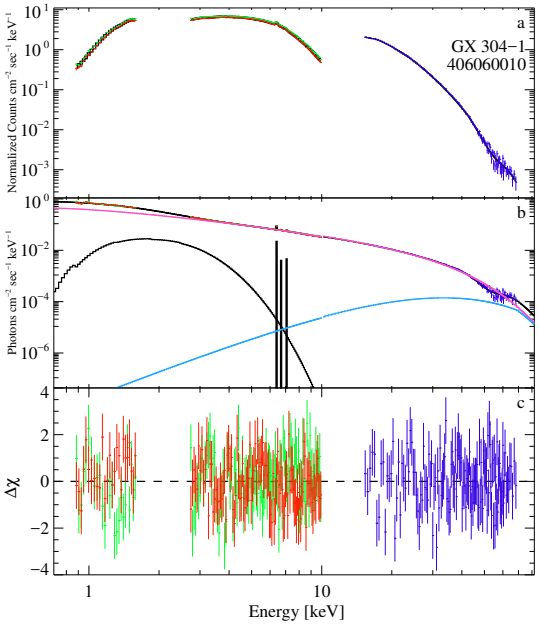

Figure A.29: Physical spectral fit for GX 304−1, ObsID 406060010.

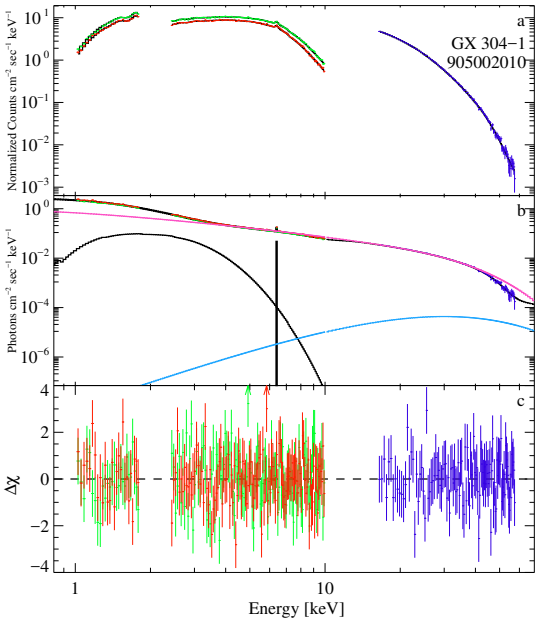

Figure A.30: Physical spectral fit for GX 304−1, ObsID 905002010.

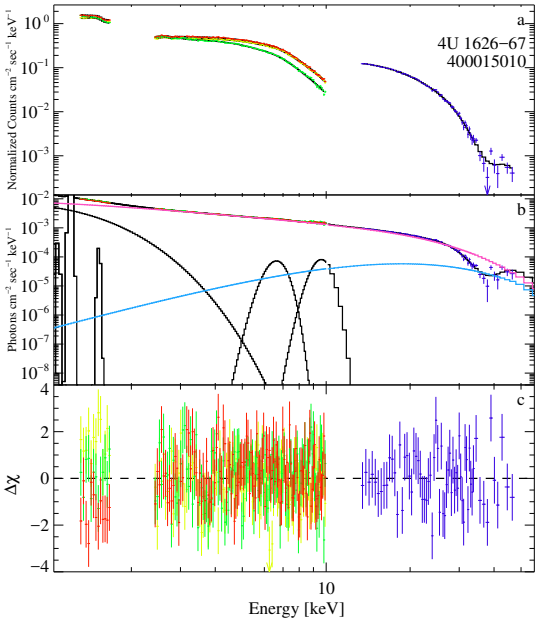

Figure A.31: Physical spectral fit for 4U 1626−67, ObsID 400015010.

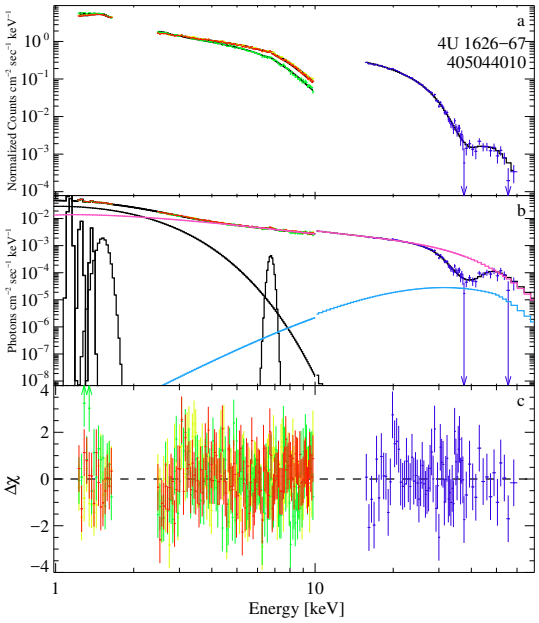

Figure A.32: Physical spectral fit for 4U 1626−67, ObsID 405044010.

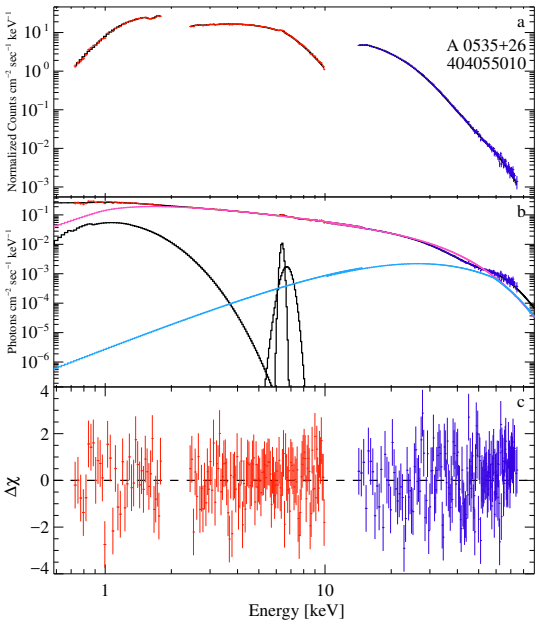

Figure A.33: Physical spectral fit for A 0535+26, ObsID 404055010.

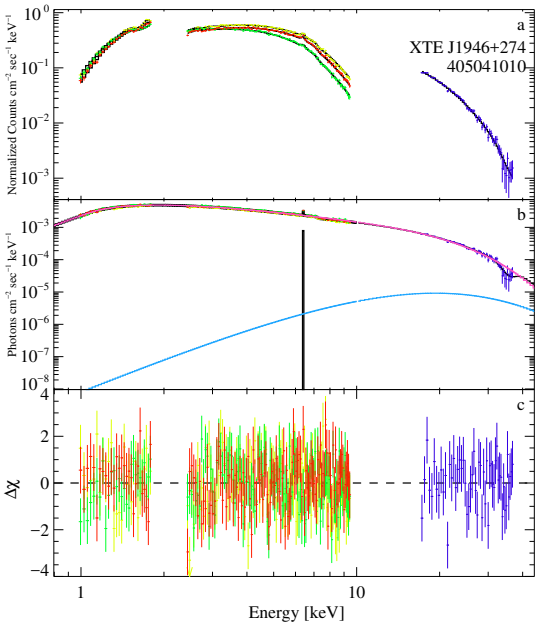

Figure A.34: Physical spectral fit for XTE J1946+274, ObsID 405041010.

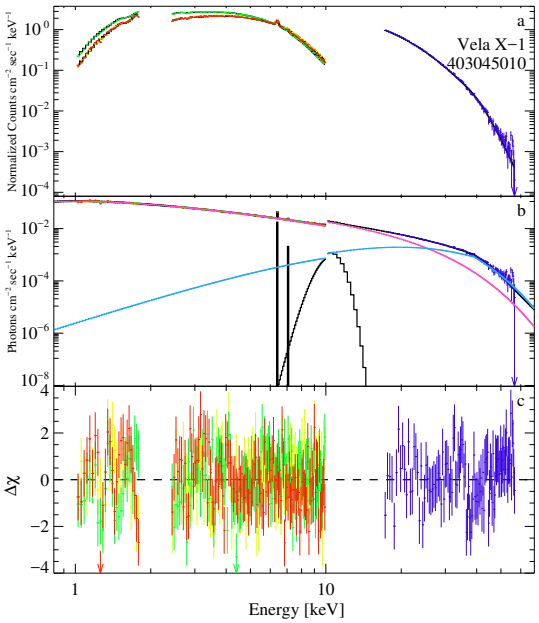

Figure A.35: Physical spectral fit for Vela X-1, ObsID 403045010.

Bibliography

Aly, J. J., 1986, in Magnetospheric Phenomena in Astrophysics, ed. R. I. Epstein, W. C. Feldman, Vol. 144, American Institute of Physics Conference Series, 45

Anzer, U., & Boerner, G. 1983, Astron. Astrophys., 122, 73

Araya, R. A., & Harding, A. K. 1999, ApJ, 517, 334

Arnaud, K. A., 1996, in Astronomical Data Analysis Software and Systems V, ed. G. H. Jacoby, J. Barnes, Vol. 101, Astronomical Society of the Pacific Conference Series, 17

Arnaud, M., 2005, in Background Microwave Radiation and Intracluster Cosmology, ed. F. Melchiorri, Y. Rephaeli, Vol. 2005937974, 77

Arnett, D., 1996, Supernovae and nucleosynthesis. an investigation of the history of matter, from the Big Bang to the present, (Princeton, NJ: Princeton University Press)

Arons, J., Klein, R. I., & Lea, S. M. 1987, ApJ, 312, 666

Ash, T. D. C., Reynolds, A. P., Roche, P., et al. 1999, MNRAS, 307, 357

Baade, W., & Zwicky, F. 1934, Contributions from the Mount Wilson Observatory, vol. 3, pp.79-83, 3, 79

Baaquie, B. E., & Willeboordse, F. H. 2015, Exploring the Invisible Universe: From Black Holes to Superstrings, (Hackensack, NJ: World Scientific Publishing Co. Pte. Ltd.)

Baron, E., & Cooperstein, J. 1990, ApJ, 353, 597

Barthelmy, S. D., Barbier, L. M., Cummings, J. R., et al. 2005, SSRv, 120, 143

Basko, M. M., & Sunyaev, R. A. 1976, MNRAS, 175, 395

Basko, M. M., & Syunyaev, R. A. 1975, Soviet Journal of Experimental and Theoretical Physics, 41, 52

Becker, P. A., 1998, ApJ, 498, 790

Becker, P. A., & Begelman, M. C. 1986, ApJ, 310, 534

Becker, P. A., Klochkov, D., Schönherr, G., et al. 2012, Astron. Astrophys., 544, A123

Becker, P. A., & Wolff, M. T. 2005a, Astrophys. J., Lett., 621, L45

Becker, P. A., & Wolff, M. T. 2005b, ApJ, 630, 465

Becker, P. A., & Wolff, M. T. 2007, ApJ, 654, 435

Becker, W., & Aschenbach, B. 1995, in NATO Advanced Science Institutes (ASI) Series C, ed. M. A. Alpar, U. Kiziloglu, J. van Paradijs, Vol. 450, NATO Advanced Science Institutes (ASI) Series C, 47

Bekefi, G., 1966, Radiation processes in plasmas, Wiley series in plasma physics, (New York: JohnWiley)

Belczynski, K., & Ziolkowski, J. 2009, ApJ, 707, 870

Bell, A. R., 1978, MNRAS, 182, 147

Bethe, H. A., 1990, Reviews of Modern Physics, 62, 801

Bhattacharya, D., & van den Heuvel, E. P. J. 1991, Phys. Rep., 203, 1

Bildsten, L., Chakrabarty, D., Chiu, J., et al. 1994, in American Institute of Physics Conference Series, ed. C. E. Fichtel, N. Gehrels, J. P. Norris, Vol. 304, American Institute of Physics Conference Series, 294

Bildsten, L., Chakrabarty, D., Chiu, J., et al. 1997, ApJS, 113, 367

Bissinger, M., 2016, Ph.D. thesis, Naturwissenschaftliche Fakultät der Friedrich-Alexander-Universität Erlangen-Nürnberg

Blandford, R. D., & Payne, D. G. 1981, MNRAS, 194, 1041

Blondin, J. M., & Owen, M. P. 1997, in IAU Colloq. 163: Accretion Phenomena and Related Outflows, ed. D. T. Wickramasinghe, G. V. Bicknell, L. Ferrario, Vol. 121, Astronomical Society of the Pacific Conference Series, 361

Boldt, E., 1987, in IAU Symp. 124, Observational Cosmology, ed. A. Hewitt, G. Burbidge, L. Z. Fang, (Cambridge: Cambridge Univ. Press), 611

Boltzmann, L., 1884, Annalen der Physik, 258, 291

Bonanno, A., Urpin, V., & Belvedere, G. 2005, Astron. Astrophys., 440, 199

Bondi, H., & Hoyle, F. 1944, MNRAS, 104, 273

Braithwaite, J., & Spruit, H. C. 2004, Nature, 431, 819

Brandt, W. N., Fabian, A. C., Dotani, T., et al. 1996, MNRAS, 283, 1071

Burbidge, E. M., Burbidge, G. R., Fowler, W. A., & Hoyle, F. 1957, Reviews of Modern Physics, 29, 547

Burderi, L., Di Salvo, T., Robba, N. R., La Barbera, A., & Guainazzi, M. 2000, ApJ, 530, 429

Burrows, D. N., Hill, J. E., Nousek, J. A., et al. 2005, SSRv, 120, 165

Caballero, I., Kraus, U., Postnov, K., et al. 2009, in Proc. of the 10th INTEGRAL Workshop, A Synergistic View of the High Energy Sky, PoS(Integral08)110

Caballero, I., Kraus, U., Santangelo, A., Sasaki, M., & Kretschmar, P. 2011, Astron. Astrophys., 526, A131

Caballero, I., Kretschmar, P., Santangelo, A., et al. 2007, Astron. Astrophys., 465, L21

Caballero, I., Pottschmidt, K., Bozzo, E., et al. 2010, The Astronomer's Telegram, 2692, 1

Caballero, I., Pottschmidt, K., Marcu, D. M., et al. 2013, Astrophys. J., Lett., 764, L23

Caballero, I., & Wilms, J. 2012, Mem. Soc. Astron. Ital., 83, 230

Camero-Arranz, A., Finger, M. H., Ikhsanov, N. R., Wilson-Hodge, C. A., & Beklen, E. 2010, ApJ, 708, 1500

Camero-Arranz, A., Pottschmidt, K., Finger, M. H., et al. 2012, Astron. Astrophys., 546, A40

Campana, S., Israel, G., & Stella, L. 1999, Astron. Astrophys., 352, L91

Carroll, B. W., & Ostlie, D. A. 1996, An Introduction to Modern Astrophysics, (New York: Pearson)

Ceccobello, C., Farinelli, R., & Titarchuk, L. 2014, Astron. Astrophys., 562, A99

Chadwick, J., 1932, Nature, 129, 312

Chakrabarty, D., 1998, ApJ, 492, 342

Chandra X-Ray Observatory, 2003, A Cocoon Found Inside the Black Widow's Web, http://adsabs.harvard.edu/abs/2003cxo..pres....2.

Chandrasekhar, S., 1931, ApJ, 74, 81

Charles, P. A., & Seward, F. D. 1995, Exploring the X-ray Universe, (Cambridge, NJ: Cambridge University Press)

Chaty, S., 2008, Chinese Journal of Astronomy and Astrophysics Supplement, 8, 197

Chaty, S., 2013, Advances in Space Research, 52, 2132

Chen, H.-L., Chen, X., Tauris, T. M., & Han, Z. 2013, ApJ, 775, 27

Cheng, Z.-Q., Shao, Y., & Li, X.-D. 2014, ApJ, 786, 128

Chevalier, C., & Ilovaisky, S. A. 1975, IAU Circ., 2778

Chodil, G., Mark, H., Rodrigues, R., Seward, F. D., & Swift, C. D. 1967, ApJ, 150, 57

Coburn, W., Heindl, W. A., Rothschild, R. E., et al. 2002, ApJ, 580, 394

Coe, M. J., 2000, in IAU Colloq. 175: The Be Phenomenon in Early-Type Stars, ed. M. A. Smith, H. F. Henrichs, J. Fabregat, Vol. 214, Astronomical Society of the Pacific Conference Series, 656

Coe, M. J., Roche, P., Everall, C., et al. 1994, Astron. Astrophys., 289, 784

Coley, J. B., 2015, Ph.D. thesis, University of Maryland, Baltimore County

Colgate, S. A., 1971, ApJ, 163, 221

Colgate, S. A., & White, R. H. 1966, ApJ, 143, 626

Cominsky, L., Clark, G. W., Li, F., Mayer, W., & Rappaport, S. 1978, Nature, 273, 367

Contopoulos, G., Kotsakis, D., Petrou, M., & Palmer, P. L. 1987, Cosmology. The Structure and Evolution of the Universe, (New York: Springer)

Corbet, R. H. D., 1986, MNRAS, 220, 1047

Davidson, K., & Ostriker, J. P. 1973, ApJ, 179, 585

Davis, J. E., 2001, ApJ, 562, 575

Demorest, P. B., Pennucci, T., Ransom, S. M., Roberts, M. S. E., & Hessels, J. W. T. 2010, Nature, 467, 1081

Devasia, J., James, M., Paul, B., & Indulekha, K. 2011, MNRAS, 414, 1023

Dewi, J. D. M., & Pols, O. R. 2003, MNRAS, 344, 629

Dickey, J. M., & Lockman, F. J. 1990, ARA&A, 28, 215

Doroshenko, V., Santangelo, A., Doroshenko, R., et al. 2014, Astron. Astrophys., 561, A96

Doroshenko, V., Santangelo, A., Kreykenbohm, I., & Doroshenko, R. 2012, Astron. Astrophys., 540, L1

Doroshenko, V., Santangelo, A., & Suleimanov, V. 2011, Astron. Astrophys., 529, A52

Doroshenko, V., Suchy, S., Santangelo, A., et al. 2010, Astron. Astrophys., 515, L1

Duncan, R. C., & Thompson, C. 1992, Astrophys. J., Lett., 392, L9

Ebisawa, K., Day, C. S. R., Kallman, T. R., et al. 1996, PASJ, 48, 425

Eikmann, W., Wilms, J., & Lee, J. 2012, in Proc. of "An INTEGRAL view of the high-energy sky (the first 10 years)", PoS(INTEGRAL 2012)145

Elsner, R. F., & Lamb, F. K. 1977, ApJ, 215, 897

Enoto, T., Makishima, K., Terada, Y., et al. 2008, PASJ, 60, 57

Enoto, T., Sasano, M., Yamada, S., et al. 2014, ApJ, 786, 127

Esposito, P., Israel, G. L., Sidoli, L., et al. 2013, MNRAS, 433, 3464

Eyles, C. J., Skinner, G. K., Willmore, A. P., & Rosenberg, F. D. 1975, Nature, 254, 577

Falkner, S., Schwarm, F.-W., Wolff, M. T., Becker, P. A., & Wilms, J. 2016, in AAS/High Energy Astrophysics Division, Vol. 15, AAS/High Energy Astrophysics Division, 201.08

Farinelli, R., Ceccobello, C., Romano, P., & Titarchuk, L. 2012, Astron. Astrophys., 538, A67

Farinelli, R., Ferrigno, C., Bozzo, E., & Becker, P. A. 2016, Astron. Astrophys., 591, A29

Ferrigno, C., Becker, P. A., Segreto, A., Mineo, T., & Santangelo, A. 2009, Astron. Astrophys., 498, 825

Finger, M. H., 2010, The Astronomer's Telegram, 2847, 1

Finger, M. H., Wilson, R. B., & Harmon, B. A. 1996, ApJ, 459, 288

Fraga, E. S., Kurkela, A., & Vuorinen, A. 2016, European Physical Journal A, 52, 49

Frank, J., King, A., & Raine, D. J. 2002, Accretion Power in Astrophysics: Third Edition, (Cambridge, NJ: Cambridge University Press)

Fürst, F., Kreykenbohm, I., Pottschmidt, K., et al. 2010, Astron. Astrophys., 519, A37

Fürst, F., Pottschmidt, K., Wilms, J., et al. 2014, ApJ, 780, 133

Gaia CollaborationBrown, A. G. A., Vallenari, A., et al. 2016, Astron. Astrophys., 595, A2

Galloway, D. K., Morgan, E. H., & Levine, A. M. 2004, ApJ, 613, 1164

Gehrels, N., Chincarini, G., Giommi, P., et al. 2004, ApJ, 611, 1005

George, I. M., & Fabian, A. C. 1991, MNRAS, 249, 352

Ghosh, P., 2007, Rotation And Accretion Powered Pulsars. Series: World Scientific Series in Astronomy and Astrophysics, Edited by Pranab Ghosh, vol. 10, 10

Ghosh, P., & Lamb, F. K. 1979a, ApJ, 232, 259

Ghosh, P., & Lamb, F. K. 1979b, ApJ, 234, 296

Ghosh, P., Pethick, C. J., & Lamb, F. K. 1977, ApJ, 217, 578

Giacconi, R., Gursky, H., Kellogg, E., Schreier, E., & Tananbaum, H. 1971, Astrophys. J., Lett., 167, L67

Giacconi, R., Murray, S., Gursky, H., et al. 1972, ApJ, 178, 281

Giangrande, A., Giovannelli, F., Bartolini, C., Guarnieri, A., & Piccioni, A. 1980, Astron. Astrophys. Suppl., 40, 289

Giménez-García, A., Shenar, T., Torrejón, J. M., et al. 2016, Astron. Astrophys., 591, A26

Ginzburg, V. L., 1964, Soviet Physics Doklady, 9, 329

Gregory, P. C., & Fahlman, G. G. 1981, Vistas in Astronomy, 25, 119

Habets, G. M. H. J., & Heintze, J. R. W. 1981, Astron. Astrophys. Suppl., 46, 193

Hansen, C. J., Kawaler, S. D., & Trimble, V. 2004, Stellar interiors : physical principles, structure, and evolution, 0941-7834, (New York: Springer), 2 edition

Heemskerk, M. H. M., & van Paradijs, J. 1989, Astron. Astrophys., 223, 154

Heindl, W. A., Coburn, W., Gruber, D. E., et al. 2000, in American Institute of Physics Conference Series, ed. M. L. McConnell, J. M. Ryan, Vol. 510, American Institute of Physics Conference Series, 173

Heindl, W. A., Coburn, W., Gruber, D. E., et al. 2001, Astrophys. J., Lett., 563, L35

Hemphill, P. B., Rothschild, R. E., Markowitz, A., et al. 2014, ApJ, 792, 14

Hertzsprung, E., 1909, Astronomische Nachrichten, 179, 373

Hewish, A., Bell, S. J., Pilkington, J. D. H., Scott, P. F., & Collins, R. A. 1968, Nature, 217, 709

Hewish, A., & Okoye, S. E. 1965, Nature, 207, 59

Hickox, R. C., Narayan, R., & Kallman, T. R. 2004, ApJ, 614, 881

Hilditch, R. W., 2001, An Introduction to Close Binary Stars, (Cambridge: Cambridge University Press)

Hiltner, W. A., Werner, J., & Osmer, P. 1972, Astrophys. J., Lett., 175, L19

Hung, L.-W., Hickox, R. C., Boroson, B. S., & Vrtilek, S. D. 2010, ApJ, 720, 1202

Iben, Jr., I., 1965, ApJ, 141, 993

Iben, Jr., I., 1991, ApJS, 76, 55

Iben, Jr., I., & Tutukov, A. V. 1996, Astron. Astrophys. Suppl., 105, 145

Illarionov, A. F., & Sunyaev, R. A. 1975, Astron. Astrophys., 39, 185

Ilovaisky, S. A., Chevalier, C., Motch, C., et al. 1984, Astron. Astrophys., 140, 251

Inoue, H., 1985, SSRv, 40, 317

ISAS/JAXA& X-ray Astrophysics Laboratory NASA Goddard Space Flight Center 2013, The Suzaku Data Reduction Guide, Version 5, http://heasarc.gsfc.nasa.gov/docs/suzaku/analysis/abc/

ISAS/JAXA& X-ray Astrophysics Laboratory NASA Goddard Space Flight Center 2015, The Suzaku Technical Description, http://heasarc.gsfc.nasa.gov/docs/suzaku/prop_tools/suzaku_td/

Iwakiri, W. B., Terada, Y., Mihara, T., et al. 2012, ApJ, 751, 35

Iyer, N., Mukherjee, D., Dewangan, G. C., Bhattacharya, D., & Seetha, S. 2015, MNRAS, 454, 741

Jahoda, K., Markwardt, C. B., Radeva, Y., et al. 2006, ApJS, 163, 401

Jaisawal, G. K., Naik, S., & Epili, P. 2016, MNRAS, 457, 2749

Janot-Pacheco, E., Ilovaisky, S. A., & Chevalier, C. 1981, Astron. Astrophys., 99, 274

Jeans, J. H., 1902, Philosophical Transactions of the Royal Society of London Series A, 199, 1

Kalberla, P. M. W., Burton, W. B., Hartmann, D., et al. 2005, Astron. Astrophys., 440, 775

Kaspi, V. M., Roberts, M. S. E., & Harding, A. K. 2006, Isolated neutron stars, 279–339

Keenan, P. C., 1985, The MK Classification and its Calibration, (Dordrecht: Springer Netherlands)

Kendziorra, E., Kretschmar, P., Pan, H. C., et al. 1994, Astron. Astrophys., 291, L31

Kendziorra, E., Mony, B., Kretschmar, P., et al. 1992, in Frontiers Science Series, ed. Y. Tanaka, K. Koyama, 51

Kippenhahn, R., & Weigert, A. 1990, Stellar Structure and Evolution, (New York: Springer)

Klochkov, D., Doroshenko, V., Santangelo, A., et al. 2012, Astron. Astrophys., 542, L28

Klochkov, D., Horns, D., Santangelo, A., et al. 2007, Astron. Astrophys., 464, L45

Kochhar, R. K., 1991, Journal of the British Astronomical Association, 101, 95

Kompaneets, A. S., 1957, Sov.Phys.-JETP, 4, 730

Koyama, K., Hoshi, R., & Nagase, F. 1987, PASJ, 39, 801

Koyama, K., Tsunemi, H., Dotani, T., et al. 2007, PASJ, 59, 23

Kraus, U., Zahn, C., Weth, C., & Ruder, H. 2003, ApJ, 590, 424

Krause, M. O., 1979, Journal of Physical and Chemical Reference Data, 8, 307

Kretschmar, P., Pan, H. C., Kendziorra, E., et al. 1996, Astron. Astrophys. Suppl., 120, C175

Kretschmar, P., Pan, H. C., Kendziorra, E., et al. 1997, Astron. Astrophys., 325, 623

Kreykenbohm, I., Coburn, W., Wilms, J., et al. 2002, Astron. Astrophys., 395, 129

Kreykenbohm, I., Wilms, J., Kretschmar, P., et al. 2008, Astron. Astrophys., 492, 511

Krimm, H. A., Barthelmy, S. D., Baumgartner, W., et al. 2010, The Astronomer's Telegram, 2663, 1

Krymskii, G. F., 1977, Akademiia Nauk SSSR Doklady, 234, 1306

Kühnel, M., Müller, S., Kreykenbohm, I., et al. 2013, Astron. Astrophys., 555, A95

Kunieda, H., & Suzaku Team 2005, in American Astronomical Society Meeting Abstracts, Vol. 37, Bulletin of the American Astronomical Society, 1413

Kuśmierek, K., Madej, J., & Kuulkers, E. 2011, MNRAS, 415, 3344

La Barbera, A., Burderi, L., Di Salvo, T., Iaria, R., & Robba, N. R. 2001, ApJ, 553, 375

La Barbera, A., Santangelo, A., Orlandini, M., & Segreto, A. 2003, Astron. Astrophys., 400, 993

Lampton, M., Margon, B., & Bowyer, S. 1976, ApJ, 208, 177

Lang, F. L., Levine, A. M., Bautz, M., et al. 1981, Astrophys. J., Lett., 246, L21

Lattimer, J. M., 2012, Annual Review of Nuclear and Particle Science, 62, 485

Lattimer, J. M., & Prakash, M. 2001, ApJ, 550, 426

Leahy, D. A., & Creighton, J. 1993, MNRAS, 263, 314

Leahy, D. A., Elsner, R. F., & Weisskopf, M. C. 1983, ApJ, 272, 256

Lebrun, F., Leray, J. P., Lavocat, P., et al. 2003, Astron. Astrophys., 411, L141

Levine, A., Ma, C. P., McClintock, J., et al. 1988, ApJ, 327, 732

Lewin, W. H. G., van Paradijs, J., & van den Heuvel, E. P. J. 1995, X-Ray Binaries, (Cambridge, NJ: Cambridge University Press)

Longair, M. S., 2011, High Energy Astrophysics, (Cambridge: Cambridge University Press)

Lorimer, D. R., 2008, Living Reviews in Relativity, 11

Lovelace, R. B. E., Sutton, J. M., & Craft, H. D. 1968, IAU Circ., 2113

Lyne, A. G., Manchester, R. N., & Taylor, J. H. 1985, MNRAS, 213, 613

Lyubarskii, Y. E., & Syunyaev, R. A. 1982, Soviet Astronomy Letters, 8, 330

Maeda, Y., 2010a, Photometry using the XIS-1 data taken with the narrow window modes, Document JS-ISAS-SUZAKU-MEMO-2010-06, ftp://legacy.gsfc.nasa.gov/suzaku/doc/xis/suzakumemo-2010-06.pdf

Maeda, Y., 2010b, A possible flux variation of the XIS data taken after Dec. 18th, 2009, Document JS-ISAS-SUZAKU-MEMO-2010-05, ftp://legacy.gsfc.nasa.gov/suzaku/doc/xis/suzakumemo-2010-05.pdf

Maeda, Y., 2010c, A possible pointing determination error between Dec. 18th, 2009 and June 15th, 2010, Document JS-ISAS-SUZAKU-MEMO-2010-04, ftp://legacy.gsfc.nasa.gov/suzaku/doc/xis/suzakumemo-2010-04.pdf

Maeda, Y., Someya, K., Ishida, M., et al. 2008, Recent update of the XRT response. III. Effective Area, Document JS-ISAS-SUZAKU-MEMO-2008-06, http://www.astro.isas.jaxa.jp/suzaku/doc/suzakumemo/suzakumemo-2008-06.pdf

Maitra, C., & Paul, B. 2013a, ApJ, 771, 96

Maitra, C., & Paul, B. 2013b, ApJ, 771, 96

Maitra, C., & Paul, B. 2013c, ApJ, 763, 79

Maitra, C., Paul, B., & Naik, S. 2012, MNRAS, 420, 2307

Makishima, K., & Mihara, T. 1992, in Frontiers Science Series, ed. Y. Tanaka, K. Koyama, 23

Makishima, K., Mihara, T., Nagase, F., & Tanaka, Y. 1999, ApJ, 525, 978

Manchester, R. N., & Taylor, J. H. 1977, Pulsars, (San Francisco: W. H. Freeman)

Mangano, V., 2009, The Astronomer's Telegram, 1896

Manousakis, A., Beckmann, V., Bianchin, V., et al. 2008, The Astronomer's Telegram, 1613, 1

Marcu, D. M., Fürst, F., Pottschmidt, K., et al. 2011, Astrophys. J., Lett., 742, L11

Marcu, D. M., Pottschmidt, K., Gottlieb, A. M., et al. 2014, in Proc. of 7th INTEGRAL Workshop in Copenhagen, High Energy Astrophysical Phenomena, PoS(INTEGRAL 2014)065

Marcu-Cheatham, D. M., Pottschmidt, K., Kühnel, M., et al. 2015, ApJ, 815, 44

Martínez-Núñez, S., Kretschmar, P., Bozzo, E., et al. 2017, SSRv

Masetti, N., Orlandini, M., Palazzi, E., Amati, L., & Frontera, F. 2006, Astron. Astrophys., 453, 295

Mason, K. O., Murdin, P. G., Parkes, G. E., & Visvanathan, N. 1978, MNRAS, 184, 45P

McBride, V. A., Wilms, J., Coe, M. J., et al. 2006, Astron. Astrophys., 451, 267

McClintock, J. E., Bradt, H. V., Doxsey, R. E., et al. 1977, Nature, 270, 320

McClintock, J. E., Rappaport, S., Joss, P. C., et al. 1976, Astrophys. J., Lett., 206, L99

Meegan, C., Bhat, N., Connaughton, V., et al. 2007, in The First GLAST Symposium, ed. S. Ritz, P. Michelson, C. A. Meegan, Vol. 921, American Institute of Physics Conference Series, 13

Meegan, C., Lichti, G., Bhat, P. N., et al. 2009, ApJ, 702, 791

Mészáros, P., 1984, Vol. 115, American Institute of Physics Conference Series, 165

Mészáros, P., 1992, High-energy radiation from magnetized neutron stars, (Chicago: University of Chicago Press)

Meszaros, P., & Nagel, W. 1985, ApJ, 298, 147

Middleditch, J., Mason, K. O., Nelson, J. E., & White, N. E. 1981, ApJ, 244, 1001

Mihara, T., 1995, Ph.D. thesis, Univ. of Tokyo

Mihara, T., Makishima, K., & Nagase, F. 1998, Advances in Space Research, 22, 987

Mitsuda, K., Bautz, M., Inoue, H., et al. 2007, PASJ, 59, 1

Morgan, W. W., Keenan, P. C., & Kellman, E. 1943, An atlas of stellar spectra, with an outline of spectral classification, (Chicago: The University of Chicago Press)

Mowlavi, N., Kreykenbohm, I., Shaw, S. E., et al. 2006, Astron. Astrophys., 451, 187

Müller, D., Klochkov, D., Caballero, I., & Santangelo, A. 2013a, Astron. Astrophys., 552, A81

Müller, S., Ferrigno, C., Kühnel, M., et al. 2013b, Astron. Astrophys., 551, A6

Müller, S., Kühnel, M., Caballero, I., et al. 2012, Astron. Astrophys., 546, A125

Mushtukov, A. A., Suleimanov, V. F., Tsygankov, S. S., & Poutanen, J. 2015, MNRAS, 447, 1847

Nagase, F., 1989, PASJ, 41, 1

Nagase, F., Hayakawa, S., Sato, N., Masai, K., & Inoue, H. 1986, PASJ, 38, 547

Naik, S., Dotani, T., Terada, Y., et al. 2008, ApJ, 672, 516

Naik, S., Paul, B., & Ali, Z. 2011, ApJ, 737, 79

Nakajima, M., Mihara, T., Makishima, K., & Niko, H. 2006, ApJ, 646, 1125

Negueruela, I., & Okazaki, A. T. 2001, Astron. Astrophys., 369, 108

Negueruela, I., Smith, D. M., Reig, P., Chaty, S., & Torrejón, J. M. 2006, in The X-ray Universe 2005, ed. A. Wilson, Vol. 604, ESA Special Publication, 165

Newton, W. G., 2013, Nature Physics, 9, 396

Nowak, M. A., Hanke, M., Trowbridge, S. N., et al. 2011, ApJ, 728, 13

Odaka, H., Khangulyan, D., Tanaka, Y. T., et al. 2013, ApJ, 767, 70

Oppenheimer, J. R., & Volkoff, G. M. 1939, Physical Review, 55, 374

Orlandini, M., Dal Fiume, D., Frontera, F., et al. 1998, Astrophys. J., Lett., 500, L163

Oskinova, L. M., Feldmeier, A., & Kretschmar, P. 2012, MNRAS, 421, 2820

Özbey Arabacı, M., Camero-Arranz, A., Zurita, C., et al. 2015, Astron. Astrophys., 582, A53

Özel, F., 2006, Nature, 441, 1115

Pacini, F., 1967, Nature, 216, 567

Palmeri, P., Mendoza, C., Kallman, T. R., Bautista, M. A., & Meléndez, M. 2003, Astron. Astrophys., 410, 359

Parkes, G. E., Murdin, P. G., & Mason, K. O. 1980, MNRAS, 190, 537

Paul, B., Agrawal, P. C., Mukerjee, K., et al. 2001, Astron. Astrophys., 370, 529

Paul, B., Nagase, F., Endo, T., et al. 2002, ApJ, 579, 411

Planck, M., 1900, Annalen der Physik, 306, 69

Prialnik, D., 2000, An Introduction to the Theory of Stellar Structure and Evolution, (Cambridge, NJ: Cambridge University Press)

Priedhorsky, W. C., & Terrell, J. 1983, ApJ, 273, 709

Raichur, H., & Paul, B. 2008, MNRAS, 387, 439

Rappaport, S., Clark, G. W., Cominsky, L., Li, F., & Joss, P. C. 1978, Astrophys. J., Lett., 224, L1

Reid, I. N., & Hawley, S. L. 2005, New light on dark stars : red dwarfs, low-mass stars, brown dwarfs, (New York: Springer - Praxis Publishing Ltd.)

Reig, P., 2007, MNRAS, 377, 867

Reig, P., & Nespoli, E. 2013, Astron. Astrophys., 551, A1

Rodes-Roca, J., Torrejón, J. M., & Bernabéu, J. G. 2008, Lecture Notes and Essays in Astrophysics, 3, 189

Rosenberg, F. D., Eyles, C. J., Skinner, G. K., & Willmore, A. P. 1975, Nature, 256, 628

Rothschild, R. E., Blanco, P. R., Gruber, D. E., et al. 1998, ApJ, 496, 538

Rothschild, R. E., Kühnel, M., Pottschmidt, K., et al. 2017, MNRAS, 466, 2752

Russell, H. N., 1914, Popular Astronomy, 22, 275

Rybicki, G. B., & Lightman, A. P. 1979, Radiative processes in astrophysics, (New York: Wiley-VCH)

Sadakane, K., Hirata, R., Jugaku, J., et al. 1985, ApJ, 288, 284

Salaris, M., & Cassisi, S. 2005, Evolution of Stars and Stellar Populations, (Hoboken, NJ: John Wiley & Sons)

Santangelo, A., del Sordo, S., Segreto, A., et al. 1998, Astron. Astrophys., 340, L55

Santangelo, A., Segreto, A., Giarrusso, S., et al. 1999, Astrophys. J., Lett., 523, L85

Sartore, N., Jourdain, E., & Roques, J. P. 2015, ApJ, 806, 193

Savonije, G. J., 1978, Astron. Astrophys., 62, 317

Schönherr, G., Wilms, J., Kretschmar, P., et al. 2007, Astron. Astrophys., 472, 353

Schreier, E., Levinson, R., Gursky, H., et al. 1972, Astrophys. J., Lett., 172, L79

Schwarm, F., 2010, Diploma thesis, Dr. Karl Remeis-Sternwarte Bamberg & ECAP, FAU Erlangen-Nürnberg

Schwarm, F.-W., Ballhausen, R., Falkner, S., et al. 2017a, Astron. Astrophys., 601, A99

Schwarm, F.-W., Schönherr, G., Falkner, S., et al. 2017b, Astron. Astrophys., 597, A3

Schwarzenberg-Czerny, A., 1989, MNRAS, 241, 153

Sguera, V., Bazzano, A., Bird, A. J., et al. 2006, ApJ, 646, 452

Shakura, N. I., 1975, Soviet Astronomy Letters, 1, 223

Shapiro, S. L., & Salpeter, E. E. 1975, ApJ, 198, 671

Shapiro, S. L., & Teukolsky, S. A. 1983, Black holes, white dwarfs, and neutron stars: The physics of compact objects, (New York: Wiley-Interscience)

Shklovsky, I. S., 1967, Astrophys. J., Lett., 148, L1

Shtykovsky, A. E., Lutovinov, A. A., Arefiev, V. A., et al. 2017, Astronomy Letters, 43, 175

Sidoli, L., Paizis, A., Fürst, F., et al. 2015, MNRAS, 447, 1299

Siegbahn, M., 1943, Nature, 151, 502

Silaj, J., Jones, C. E., Tycner, C., Sigut, T. A. A., & Smith, A. D. 2010, ApJS, 187, 228

Smith, D. A., & Takeshima, T. 1998, The Astronomer's Telegram, 36, 1

Staelin, D. H., & Reifenstein, III, E. C. 1968, Science, 162, 1481

Staubert, R., Kreykenbohm, I., Kretschmar, P., et al. 2004, in 5th INTEGRAL Workshop on the INTEGRAL Universe, ed. V. Schoenfelder, G. Lichti, C. Winkler, Vol. 552, ESA Special Publication, 259

Staubert, R., Pottschmidt, K., Doroshenko, V., et al. 2011, Astron. Astrophys., 527, A7

Staubert, R., Shakura, N. I., Postnov, K., et al. 2007, Astron. Astrophys., 465, L25

Steele, I. A., Negueruela, I., Coe, M. J., & Roche, P. 1998, MNRAS, 297, L5

Steiner, A. W., Lattimer, J. M., & Brown, E. F. 2010, ApJ, 722, 33

Stella, L., White, N. E., & Rosner, R. 1986, ApJ, 308, 669

Stokes, G. G., 1852, Annalen der Physik, 163, 480

Struve, O., 1931, ApJ, 73, 94

Suchy, S., 2011, Ph.D. thesis, Univ. of Calif. San Diego

Suchy, S., Pottschmidt, K., Wilms, J., et al. 2008, ApJ, 675, 1487

Sugizaki, M., Yamamoto, T., Mihara, T., Nakajima, M., & Makishima, K. 2015, PASJ, 67, 73

Sunyaev, R. A., & Titarchuk, L. G. 1980, Astron. Astrophys., 86, 121

Szostek, A., & Zdziarski, A. A. 2008, MNRAS, 386, 593

Takahashi, T., Abe, K., Endo, M., et al. 2007, PASJ, 59, 35

Tanaka, Y., 1986, in IAU Colloq. 89: Radiation Hydrodynamics in Stars and Compact Objects, ed. D. Mihalas, K.-H. A. Winkler, Vol. 255, Lecture Notes in Physics, Berlin Springer Verlag, 198

Tauris, T. M., & van den Heuvel, E. P. J. 2006, Formation and evolution of compact stellar X-ray sources, 623–665

Thompson, T. W. J., & Rothschild, R. E. 2009, ApJ, 691, 1744

Thomson, W., 1871, Nature, 4, 261

Titarchuk, L., 1994, ApJ, 434, 570

Tolman, R. C., 1939, Physical Review, 55, 364

Tomsick, J. A., Heinke, C., Halpern, J., et al. 2011, ApJ, 728, 86

Torrejón, J. M., Schulz, N. S., Nowak, M. A., & Kallman, T. R. 2010, ApJ, 715, 947

Torres, D. F., & Rea, N. 2011, Astrophysics and Space Science Proceedings, 21

Tsujimoto, M., et al. 2010a, Anomaly of XIS0 in June 2009, Document JS-ISAS-SUZAKU-MEMO-2010-01, ftp://legacy.gsfc.nasa.gov/suzaku/doc/xis/suzakumemo-2010-01.pdf

Tsujimoto, M., et al. 2010b, Anomaly of XIS0 in June 2009, Document JS-ISAS-SUZAKU-MEMO-2010-01, ftp://legacy.gsfc.nasa.gov/suzaku/doc/xis/suzakumemo-2010-01.pdf

Tsygankov, S. S., & Lutovinov, A. A. 2005, Astronomy Letters, 31, 380

Tsygankov, S. S., Lutovinov, A. A., Churazov, E. M., & Sunyaev, R. A. 2006, MNRAS, 371, 19

Turolla, R., Zane, S., & Watts, A. L. 2015, Reports on Progress in Physics, 78, 116901

van den Heuvel, E. P. J., 1994, in Saas-Fee Advanced Course 22: Interacting Binaries, ed. S. N. Shore, M. Livio, E. P. J. van den Heuvel, H. Nussbaumer, A. Orr, 263

van der Meer, A., Kaper, L., van Kerkwijk, M. H., Heemskerk, M. H. M., & van den Heuvel, E. P. J. 2007, Astron. Astrophys., 473, 523

Verner, D. A., & Yakovlev, D. G. 1995, Astronomy and Astrophysics Supplement Series, 109, 125

Verrecchia, F., Israel, G. L., Negueruela, I., et al. 2002, Astron. Astrophys., 393, 983

von Kienlin, A., Meegan, C. A., Lichti, G. G., et al. 2004, in UV and Gamma-Ray Space Telescope Systems, ed. G. Hasinger, M. J. L. Turner, Vol. 5488, Proceedings of SPIE, 763

Walter, R., Lutovinov, A. A., Bozzo, E., & Tsygankov, S. S. 2015, A&ARv, 23, 2

West, B. F., Wolfram, K. D., & Becker, P. A. 2017, ApJ, 835, 130

White, N. E., 1978, Nature, 271, 38

White, N. E., Swank, J. H., & Holt, S. S. 1983, ApJ, 270, 711

Wickramasinghe, D. T., & Ferrario, L. 2000, PASP, 112, 873

Wien, W., 1897, Philosophical Magazine Series 5, 43, 214

Wilms, J., Allen, A., & McCray, R. 2000, ApJ, 542, 914

Wilson, C. A., Finger, M. H., Coe, M. J., & Negueruela, I. 2003, ApJ, 584, 996

Wilson, C. A., Finger, M. H., Wilson, R. B., & Scott, D. M. 1998, IAU Circ., 7014, 2

Wolff, M. T., Becker, P. A., Gottlieb, A. M., et al. 2016, ApJ, 831, 194

Woltjer, L., 1964, ApJ, 140, 1309

Yamada, S., Uchiyama, H., Dotani, T., et al. 2012, PASJ, 64, 53

Yamamoto, T., Sugizaki, M., Mihara, T., et al. 2011, PASJ, 63, 751

Zavlin, V. E., & Pavlov, G. G. 2002, in Neutron Stars, Pulsars, and Supernova Remnants, ed. W. Becker, H. Lesch, J. Trümper, 263

Zavlin, V. E., Pavlov, G. G., & Shibanov, Y. A. 1996, Astron. Astrophys., 315, 141

Zel'dovich, Y. B., & Novikov, I. D. 1971, Relativistic astrophysics. Vol.1: Stars and relativity, (Chicago: University of Chicago Press)

Zel'dovich, Y. B., & Shakura, N. I. 1969, Soviet Journal of Experimental and Theoretical Physics, 13, 175

Zhang, B., Xu, R. X., & Qiao, G. J. 2000, Astrophys. J., Lett., 545, L127